AVERTISSEMENT

Ce document est le fruit d'un long travail approuvé par le jury de soutenance et mis à disposition de l'ensemble de la communauté universitaire élargie.

Il est soumis à la propriété intellectuelle de l'auteur. Ceci implique une obligation de citation et de référencement lors de l'utilisation de ce document.

D'autre part, toute contrefaçon, plagiat, reproduction illicite encourt une poursuite pénale.

Contact : ddoc-theses-contact@univ-lorraine.fr

LIENS

Code de la Propriété Intellectuelle. articles L 122. 4
Code de la Propriété Intellectuelle. articles L 335.2- L 335.10
http://www.cfcopies.com/V2/leg/leg_droi.php
http://www.culture.gouv.fr/culture/infos-pratiques/droits/protection.htm

Université de Lorraine **École doctorale C2MP**

THÈSE

présentée et soutenue publiquement le **28 Février 2020**

pour l'obtention du grade de

Docteur de l'Université de Lorraine

(**Spécialité : Sciences des matériaux**)

par

Komlavi Sényo ELOH

FFT-based modelling of X-Ray Diffraction peaks : application to dislocation loops

Composition du jury

Olivier THOMAS	Professeur, Université Aix-Marseille	Rapporteur
Djimédo KONDO	Professeur, Université Pierre et Marie Curie	Rapporteur
Laurent CAPOLUNGO	Directeur de Recherche, Los Alamos National Laboratory, USA	Examinateur
Istvàn GROMA	Professeur, Eötvös Loránd University, Budapest, Hongrie	Examinateur
Lionel GELEBART	Ingénieur de recherche HDR, CEA Saclay	Examinateur
Marie-Ingrid RICHARD	Ingénieur de recherche HDR, CEA et ERSF	Examinateur
Alain JACQUES	Directeur de Recherche CNRS, Université de Lorraine	Directeur
Stéphane BERBENNI	Directeur de Recherche CNRS, Université de Lorraine	Co-directeur

Labex-DAMAS, Institut Jean Lamour — UMR CNRS 7198, LEM 3- UMR CNRS 7239
Pôle M4 : Matière, Matériaux, Métallurgie, Mécanique

Acknowledgements

The work presented in this manuscript was carried out at "Institut Jean Lamour" (IJL UMR CNRS 7198) and "Laboratoire d'Etudes de Microstructure et de Mécanique des Matériaux" (LEM3 UMR CNRS 7239) of University of Lorraine. It was financed by the ANR (Agence Nationale de Recherches) through LABEx DAMAS : "Laboratoire d'Excellence Design d'Alliages Métalliques pour l'Allègement des Structures"

Firstly, I would like to express my sincere gratitude to my advisors Dr Alain JACQUES and Dr Stéphane BERBENNI , senior researchers at CNRS "Centre National de Recherches Scientifiques" for the continuous support of my Ph.D study and related research, for their patience and motivation, and immense knowledge. Their guidance helped me in all the time of research and writing of this thesis. I could not have imagined having a better advisor and mentor for my Ph.D study. Additionally thanks you for all your advice which will be infinitely useful to me in my professional and personal career.

I would also like to thank Sébastian ALLAIN and Stéphane ANDRE for having accepted to be in my monitoring committee. Your advice during the various discussion and meeting allowed me to organize myself during the thesis and to prepare my defense.

I gratefully acknowledge professors Olivier THOMAS and Djimédo KONDO for having accepted to report my thesis. Many thanks to Lionel GELEBART, Laurent CAPOLUNGO, Istvàn GROMA and Marie-Ingrid RICHARD for having accepted to participate to my thesis jury.

I am also very grateful to IJL and LEM3 staff for giving me a warm working ambience. My sincere thanks to all the members of team 304 at IJL and team APPLI at LEM3 for all useful exchanges during the meetings and also in the offices. I do not forget the IT department of both labs. I thanks all my doctoral colleagues. The discussions about our individual experiences were very instructive for me.

Finally I thank all my family : my father, my mother, my brothers and sisters

and all my relatives for their advice, their encouragement and their presence at my side during the most difficult moments.

Abstract

In this work, we propose and test an original numerical method of simulation of X-ray diffraction peaks by single crystals. This method is based on the use of Fast Fourier Transform (FFT) algorithms for the calculation of mechanical fields resulting from external loading and / or linear defects such as dislocation loops. These defects are modeled by stress-free strain fields (eigenstrains) in a periodic microstructure subjected to thermomechanical loadings.

In the first part, we present an improved approach by FFT-type algorithms which allows to accurately obtain the local mechanical fields without numerical oscillation at material's discontinuities. This improvement is due to the use of a discrete and periodic Green operator. This is obtained by solving the Lippmann-Schwinger equation in the Fourier space and using an appropriate spatial discretization. The fourth order modified Green operator allows to calculate the values of the strain and stress fields at all voxels. We also propose a third order periodic green operator to compute the displacement field. The computed displacement field is then corrected by a sub-voxelization method which removes the artifacts appearing in the case of dislocation loops inclined with respect to the reference grid. Numerical examples on reference cases show the effect of the Green operators for the calculation of local mechanical fields without oscillation and the efficiency of the sub-voxellization method. The final displacement field obtained is the input data of the simulation of X-ray diffraction patterns.

The method of simulation of X-ray diffraction peaks of FCC (Face-Centered Cubic) single crystals is then presented. The diffracting material is modelled by a representative volume containing dislocation loops in (111) slip planes. We calculate the amplitude then the intensity of the diffracted beam near a node of the reciprocal lattice. This 3D distribution of the diffracted intensity is processed to obtain 1D diagrams that will be analyzed.

The simulations demonstrate foremost the elimination of the artifacts on the diffraction diagrams which are due to the oscillations of the uncorrected mechanical fields. The diffraction peaks are analyzed by different statistical methods (Fourier transform of intensity, method of moments, etc.) which allow to evaluate the dis-

tribution parameters of dislocations (density, polarization factor, etc.) and compare them with their theoretical values.

Résumé

Dans ce travail, nous proposons et testons une méthode numérique originale de simulation de diagrammes de diffraction des Rayons X par des monocristaux. Cette méthode repose sur l'utilisation d'algorithmes numériques de type Transformée de Fourier rapide (fast Fourier transform (FFT) en anglais) pour le calcul des champs mécaniques provenant de chargement extérieurs et/ou des défauts linéaires comme des boucles de dislocations. Ces défauts sont modélisés par des champs de déformation libres de contraintes (eigenstrains) dans une microstructure périodique soumise à des chargements thermomécaniques.

Dans la première partie, nous présentons une approche améliorée du calcul des champs mécaniques par les algorithmes de types FFT qui permet d'obtenir les champs mécaniques locaux de manière précise et sans oscillation numérique aux discontinuités. Cette amélioration est due à l'utilisation d'un opérateur de Green discret consistent et périodique. Celui-ci est obtenu en résolvant l'équation de Lippmann-Schwinger dans l'espace de Fourier et en faisant une discrétisation spatiale appropriée. L'opérateur de Green modifié de degré quatre permet de calculer pour tous les voxels les valeurs du champ de déformations et de contraintes. Nous proposons aussi un opérateur de Green périodique d'ordre trois qui permet de calculer le champ de déplacement. Le champ de déplacement calculé est ensuite corrigé par une méthode de sous voxélisation qui supprime les artefacts apparaissant dans le cas des boucles de dislocations inclinées vis-à-vis de la grille de référence. Des exemples numériques sur des cas de références montrent l'effet des opérateurs de Green pour le calcul des champs mécaniques locaux sans oscillation et l'efficacité de la méthode de sous voxélisation. Le champ de déplacements final obtenu est la donnée d'entrée de la simulation de diagrammes de diffraction aux rayons X.

La méthode de simulation des diagrammes de diffraction des Rayons X de monocristaux CFC est ensuite présentée. Le matériau diffractant est modelisé par un volume représentatif contenant des boucles de dislocations qui glissent dans des plans de types (111). Nous calculons l'amplitude puis l'intensité du faisceau diffracté au voisinage d'un noeud du réseau réciproque. La distribution 3D de l'intensité diffractée est ensuite traitée pour obtenir des diagrammes 2D et 1D qui seront analysés.

Les premières simulations démontrent tout d'abord la suppression des artefacts sur les diagrammes de diffraction qui sont dus aux oscillations des champs mécaniques non corrigés. Les pics de diffraction sont analysés par différentes méthodes statistiques (transformée de Fourier de l'intensité, méthode des moments statistiques d'ordres supérieurs) qui permettent d'évaluer les paramètres de la distribution des dislocations (densité, facteur de polarisation, etc.) et de les comparer avec les valeurs théoriques.

Table des matières

Remerciements i

Abstract v

Résumé vii

Table des matières xii

Introduction 1

1 Bibliographic study on X-ray diffraction and FFT-based calculation methods 6
- 1.1 Introduction . . . 6
- 1.2 X-ray diffraction . . . 7
  - 1.2.1 In situ XRD on Ni-based superalloy single crystals . . . 7
  - 1.2.2 Basics of X-ray diffraction theory . . . 11
  - 1.2.3 Analysis method based on the profiles moment . . . 18
  - 1.2.4 X-ray diffraction simulations . . . 20
  - 1.2.5 Conclusions . . . 29
- 1.3 FFT-based method for computed mechanical fields . . . 30
  - 1.3.1 Introduction and advantage of the numerical method . . . 30
- 1.4 Conclusions . . . 60

2 Development of a new consistent discrete Green operator for FFT-based methods to solve heterogeneous problems with eigenstrains 63
- 2.1 Introduction . . . 63
- 2.2 The Lippmann-Schwinger equation and its numerical spectral resolution 64
  - 2.2.1 The Lippmann-Schwinger equation for eigenstrained heterogeneous materials . . . 64
  - 2.2.2 Fourier space resolution . . . 66
  - 2.2.3 Numerical Algorithm . . . 67
  - 2.2.4 Some numerical examples . . . 67
- 2.3 Suppression of numerical oscillations . . . 72
- 2.4 Development of consistent periodized discrete Green operators (DGO) 73
  - 2.4.1 One-dimensional case . . . 73
  - 2.4.2 Consistent periodized discrete Green operators $\widehat{\boldsymbol{\Gamma}^D}(\boldsymbol{\xi}_{ijq})$ . . . 77

2.4.3 Symetries and convergence of $\widehat{\boldsymbol{\Gamma}^D}(\boldsymbol{\xi}_{ijq})$ . . . 77
2.4.4 Comparison with the consistent periodized discrete Green operator introduced by Brisard and Dormieux [16, 17] . . . 78
2.5 Applications to references cases . . . 79
2.5.1 Cubic-shaped eigenstrained inclusion in a homogeneous isotropic elastic periodic medium . . . 80
2.5.2 Spherical inclusion problem with eigenstrains in a homogeneous isotropic elastic periodic medium . . . 86
2.5.3 Spherical inhomogeneity problem with eigenstrains . . . 88
2.6 Conclusions . . . 92

3 FFT-based Computation of the displacement field and applications to dislocations 95
3.1 Objectives . . . 95
3.2 Green operator for the displacement field and application . . . 96
3.2.1 Green operator for the displacement field . . . 96
3.2.2 Discrete Green operator to compute the displacement field . . . 98
3.2.3 Discrete operator to compute displacement fields at voxels corners . . . 99
3.2.4 Application to the computation of displacement field . . . 100
3.3 Voxelization artifacts and proposition of sub-voxelization method . . . 105
3.3.1 Displacement field due to an inclined dislocation loop . . . 105
3.3.2 Origin of the voxelization artifacts . . . 107
3.3.3 Sub-voxelization method . . . 108
3.3.4 Numerical applications . . . 112
3.4 Conclusion . . . 113

4 X-ray diffraction peaks modeling using the displacement field 121
4.1 Objectives . . . 121
4.2 Numerical model to simulate X-ray diffraction intensity peaks . . . 122
4.2.1 Amplitude and intensity . . . 122
4.2.2 1D projections . . . 124
4.2.3 Applications to reference cases . . . 125
4.3 X-ray diffraction analysis . . . 135
4.3.1 Fourier transform of the 1D diffraction peak . . . 136
4.3.2 Analysis method based on the momentum . . . 140
4.4 Results . . . 142
4.4.1 Effect of the diffraction vector $\mathbf{g}$ . . . 142
4.4.2 Effect of the dislocation loop's sizes . . . 142
4.4.3 Effect of the dislocation density . . . 147
4.4.4 Dislocation dipoles . . . 151
4.4.5 Analysis of the results . . . 152
4.5 Conclusion . . . 159

Conclusion générale et perspectives 163

A Crystalline material and X-ray diffraction **181**
A.1 Crystalline material 181
A.2 Diffraction basis 183

B Equivalence between DGO_k on a set of N points and CGO on a set of $2kN$ points **194**

C Analytical stress and displacement components for periodic distributions of cubic-shaped inclusions with eigenstrains in isotropic elasticity **196**

D Peaks analysis results **199**

Table des figures

1.1 Setup of a triple-crystal diffractometer. 8
1.2 Reciprocal-space mapping using the ω (specimen) and α (analyser) rotations. A ω rotation scans the mosaicity, and an α scan gives the distribution of lattice parameters [61]. K, K_0 represent the incident and the diffracted beam respectively. G is the reciprocal lattice vector and Q correspond to the exact Bragg position 9
1.3 TCD $\theta/2\theta$ scan diffraction peak for an Ni-base single-crystal superalloy [25] 10
1.4 Setup of a double crystal diffractometer. 10
1.5 Far-field DCD technique [130, 129]. The diffracted beam is recorded by a far field camera and the γ and γ phases are separated. 11
1.6 Schematic representation of the diffraction by two Young's holes . . . 13
1.7 The mean square strain computed in a $50nm \times 50nm$ crystal box containing 10 randomly distributed edge dislocations. Logarithmic scale in x-axis. The dashed line shows that the computed mean square strain is well described by a logarithmic dependence for small values of L 15
1.8 The function $f^*(\eta)$ and two of its approximations : for small and large values of L 16
1.9 (a) Line profile measured on a tensile deformed Cu single crystal. (b) Fitted second-order variance. (c) Fitted third-order variance divided by q^2. (d) Fitted Fourth-order variance [51]. 20
1.10 (a) High-resolution X-ray Bragg peaks. (b) Characteristic behavior of the fourth order moment divided by q^2. [13]. 21
1.11 Comparison of normalized unfiltered and filtered, i.e. with instrumental broadening (IB), intensity from the Fourier average-strain (Fourier ε^L) and Fourier displacement (Fourier $\Delta\mathbf{u}$) methods, and the PDF of strain from the Stokes Wilson approximation for an RRD of 32 screw dislocations for diffraction vectors (a), (b) $\mathbf{g} = [11\bar{3}]$ and (c), (d) $\mathbf{g} = [31\bar{3}]$ 25
1.12 Example : computing the diffracted intensity of a synthetic diffraction spot on the virtual detector [160] 27
1.13 Illustration of the setup for 90° reflection Laue experiment [125] . . . 27

1.14 (a) Experimental Laue diffraction pattern from 2% plastically deformed Ni. (b) Simulated Laue pattern. (c) *Streaking* of the Laue spot (006) in the experiment. (d) *Streaking* of the Laue spot (006) in the simulation [125] 28
1.15 Results of simulations of the rolling of an aluminum polycrystal containing 100 grains and discretized in $32 \times 32 \times 32$ elements (voxels in the case of the FFT). Left : distributions of accumulated plastic deformations (a) and stresses (c) obtained by FFT. On the right : distributions of accumulated plastic deformations (b) and stresses (d) obtained by FE. Comparisons were made on the same scale, only the maximum and minimum values differ. Calculation times are 3 hours for the FFT and 5 days for the FE method [107]. 32
1.16 Stress field along a center line parallel to x-axis due to a dilatational eigenstrain contained in a spherical inclusion. The resolution is $128 \times 128 \times 128$ with 14 voxel radius. The dangling voxels leads to a large deviations at the interface between inclusion and matrix [3] 39
1.17 Stress field along a center line parallel to x-axis due to a dilatational eigenstrain contained in a spherical inclusion. (a) the component σ_{11} and (b)σ_{33}. The resolution is $1024 \times 1024 \times 1024$ with 14 voxel radius [3]. 40
1.18 Comparison of the computational cost between regular DDD method and the DDD-FFT approach [12]. 41
1.19 Schematic view of the representation of a pair of dislocations on a FFT grid [49] 42
1.20 Comparisons of the shear stress contours for a screw dislocation calculated with static FFT FDM and with static FEM FDM 43
1.21 2D maps of normalized stress components σ_{11} (a) and σ_{22} (b) obtained with edge dislocation interacting with a circular hole [30] 43
1.22 Numerical error on the stress equilibrium for different resolution and different contrast with a viscoplastic FFT polycrystalline formulation [75] 44
1.23 (a) Effective response predicted with the EVP-FFT model for the copper polycrystal ($A = 2.2$) and the artificial FCC random polycrystal ($A = 0.5$) deformed in uni axial tension up to 0.2% . (b) and (c) Predicted fields of normalized fluctuations of the von Mises stress, for the copper polycrystal (b) and the artificial FCC polycrystal (c), in different stages of the loading. [73] 46
1.24 Transient creep experiments. Comparison between the experimental results and the full-field simulations performed on the configuration on the left with the CP-EVP-FFT solver [127] 47

1.25 Grain size effect reported on the overall flow stress at 0.2% overall plastic strain ($E^p = 0.2\%$) and comparison with a Hall-Petch type scaling law (linear fits : dotted lines). The numerical simulations were performed with the MFDM EVPFFT formulation with a RVE of 100 grains and128 × 128 × 128 voxels and with a RVE of 27 grains and 64 × 64 × 64 voxels 48
1.26 Spatial distribution of equivalent cumulated plastic strain ε_p^{eq} recorded at $E^p = 0.2\%$ for three average grain sizes (MFDM-EVPFFT) with same scale range : 0.25μm (a), 1μm (b),10μm (c). Simulation results with conventional CP-EVPFFT (d) with same scale range. 49
1.27 Iterations of the FFT-based schemes for 10% compression. MS is the Moulinec Suquet basic algorithm and NE,NR,NK and NK2 are other FFT methods based on the Newton-Krylov algorithm [65] 50
1.28 Comparisons of the number of iteration with the classic FFT-based method [98, 99] (FFTH) and the accelerated method proposed in [163] (CG) 51
1.29 Convergence properties as a function of the inclusion behavior [47]. The parameter β stands as the mechanical contrast between matrix and inclusion. 52
1.30 Comparison between the number of iterations at convergence for the strain-based and the stress-based algorithms [95] 53
1.31 Comparison between the number of iterations at convergence of the strain-based, the stress-based, and the polarization based [95] 54
1.32 Comparison of the number of iterations at convergence for different schemes. The studied material is a periodic microstructure with one spherical inclusion [92] 55
1.33 Illustration of the Gibbs phenomenon with a square wave approximated by harmonics. The Gibbs phenomenon is more important when the order of the partial sum of the Fourier series increases. 57
1.34 The continuous function shown in (a) is nonzero only for a finite interval of the period T. It follows that its Fourier transform, whose modulus is shown schematically in (b), is not bandwidth limited but has finite amplitude for all frequencies. If the original function is sampled with a sampling interval $\triangle$, as in (a), then the Fourier transform (c) is defined only between plus and minus the Nyquist critical frequency. Power outside that range is folded over or "aliased" into the range. The effect can be eliminated only by low-pass filtering the original function before sampling 58
1.35 Stress component σ_{12} predicted by the various FFT schemes at three resolutions. G (using partial derivative $i\xi_j$), G^C (using $i\xi_j^C$), G^W(using $i\xi_j^w = exp^{i\frac{2\pi m_j}{T_j}} - 1$), G^R (using ξ_j^R) [156] 60

2.1 The normalized stress component σ_{33} along the z-axis through the center of the unit cell for the cubic-shaped inclusion configuration with eigenstrain, given by FFT-method and analytical solution (see Appendix C). 68
2.2 The normalized stress component σ_{12} along the z-axis through the center of the unit cell for the cubic-shaped inclusion configuration with eigenstrain, given by FFT-method and analytical solution (see Appendix C). 69
2.3 Normalized stress field component σ_{11}/E_m along a centered line parallel to the x-axis for the spherical inclusion with eigenstrain, given by the Eshelby's analytical solution and computed with FFT-method. Here, the classic spatial discretization is used : $x_i = i\frac{d}{N}$. 70
2.4 Normalized stress field components σ_{11}/E_m (figure (a)) and σ_{33}/E_m (figure (b)) along a centered line parallel to the x-axis for the spherical inclusion with eigenstrain, given by the Eshelby's analytical solution and computed with CGO and DGO_{81}. Here, the following spatial discretization is used : $x_i = i\frac{d}{N} + \frac{d}{2N}$ 71
2.5 Normalized stress field component $\sigma_{12}/(2\nu)$ along a centered line parallel to the x-axis for the spherical inclusion with eigenstrain, given by the Eshelby's analytical solution and computed with FFT-method. 72
2.6 Definition of $t^d(x_i)$ with respect to $t(x)$. This configuration is consistent with the spatial discretization explained in the text. 74
2.7 Representation of the cubic-shaped inclusion. The line d_1 is defined as parallel to the x-axis through the center of the unit cell, the line d_2 is defined as parallel to the x-axis through an edge line, the line d_3 is defined as paralle to the z-axis through the center of the unit cell. Materials points O, A, B, C are some specific points used in analysis of numerical results. 81
2.8 The normalized stress component σ_{33} along d_1 (figures (a) and (b)) and along d_2 (figures (c) and (d)) for he cubic-shaped inclusion configuration with eigenstrain, given by analytical solution ((see Appendix C)), and computed with CGO and DGO_k for different k (DGO_1, DGO_6, DGO_{21}, DGO_{51}, DGO_{81}, DGO_{101}). 82
2.9 The normalized stress components σ_{11} (figures (a) and (b)) and σ_{12} (figures (c) and (d)) along the line d_1 for the cubic-shaped inclusion configuration with eigenstrain, given by the analytical solution (see Appendix C), and computed with CGO and DGO_k for different k (DGO_1, DGO_6, DGO_{21}, DGO_{51}, DGO_{81}, DGO_{101}). 83
2.10 Relative difference ϵ computed at some specific points O (figure (a)), B (figure (b)), A (figure (c)), C (figure (d)). The specific points were defined in Fig. 2.7 of the cubic-shaped inclusion with CGO and DGO_k (for different values of k). Solid lines represent the CGO solution and dotted lines represent the DGO_k solutions. 84

2.11 The shear stress component σ_{12} normalized with $2\mu_m$ (where μ_m is the elastic shear modulus) for the cubic-shaped inclusion configuration with homogeneous isotropic elasticity computed with CGO, DGO_{81} and FFT-solution with CGO "truncated" at the highest frequencies [99] (named "modified CGO" in the figure). 85
2.12 Normalized stress field components σ_{11}/E_m (figure (a)) and σ_{33}/E_m (figure (b)) along a centered line parallel to the x-axis for the spherical inclusion with eigenstrain, given by the Eshelby's analytical solution and computed with CGO and DGO_{81}. Here, the following spatial discretization is used : $x_i = i\frac{d}{N} + \frac{d}{2N}$ 86
2.13 Normalized stress field component $\sigma_{12}/(2\mu_m)$ along a centered line parallel to x-axis for the spherical inhomogeneity problem with eigenstrain, given by analytical solutions and numerically computed with CGO and DGO_{81}. 87
2.14 Normalized stress field components σ_{11}/E_m (figure (a)) and σ_{33}/E_m (figure (b)) along a centered line parallel to the x-axis for the spherical inhomogeneity problem with eigenstrain, given by analytical solutions [104, 64] and numerically computed with CGO and DGO_{81}. Here, $R = K_m/K_i = 2$. 88
2.15 The convergence error computed with the strain field criterion for both CGO and DGO_{81} methods as a function of iteration number up to 50 iterations for two mechanical contrasts : $R = K_m/K_i = 2$ and $R = K_m/K_i = 0.5$. 89
2.16 Normalized stress field component $\sigma_{12}/(2\mu_m)$ along a centered line parallel to x-axis for the spherical inhomogeneity problem with eigenstrain, given by analytical solutions [104, 64] and numerically computed with CGO and DGO_{81}. 90
2.17 2D sections of the stress component σ_{12} normalized by $2\mu_m$ computed with CGO and DGO_{81}. Using the visualization software ParaView [138], *Point Data* are used to represent the result of CGO on figure (a) and DGO_{81} on figure (b) ; *Cell Data* are used to represent the result of CGO on figure (c) and DGO_{81} on figure (d). 91

3.1 The displacement field component u_3 (figures (a) et (b)) and u_1 (figures (c) et (d)) along a centered z-axis for a flat cubic-shaped inclusion (Eshelby-like squared prismatic dislocation loop), given by the analytical solution (see Appendix C) and computed with CGO, DGO_k for different k (DGO_1, DGO_6, DGO_{21}, DGO_{51}, DGO_{81}, DGO_{101}). 101
3.2 Relative error ϵ_1 (figure (a)) and ϵ_3 (figure (b)) computed at the center of the inclusion (point O) for different values of k with displacement field components u_1 and u_3. Solid lines represent the CGO solution and dotted lines represent the DGO_k solutions. 102

3.3 The displacement field component u_3 along a centered z-axis for a flat cubic-shaped inclusion (Eshelby-like squared prismatic dislocation loop. (a) With discrete Green operator (eq. 3.10). (b) With shift discrete Green operator (eq. 3.12). 103
3.4 Effect of the discretization level (Fourier grid resolution) on the accuracy of the displacement field component u_3/b along d_3 for a flat cubic-shaped inclusion (Eshelby-like squared prismatic dislocation loop) given by CGO, and DGO_{21} for two resolutions : $32 \times 32 \times 32$ voxels ($8\times8\times1$ voxels for the inclusion) and $128\times128\times128$ voxels ($32\times32\times1$ voxels for the inclusion). 104
3.5 Schematic reprsentation of slip planes and different square loops. On the left, a (001) plane consistent with the FFT grid and on the right (111) plane, not consistent with the FFT grid 105
3.6 Displacement field due to an inclined dislocation loop. The displacement field is represented along a centered line parallel to the $z-axis$ 106
3.7 Schematic representation of deformed voxels containing in (111) plane and voxels along which the displacement field is represented 107
3.8 Local oscillation of the phase due to artifacts (the representation is made for 32 voxels centered in the unit cell along z direction). The red line is approximately equal to the phase expected for this displacement field 108
3.9 2D representation of a dislocation loop in a tilted plane on a (8×8 FFT grid. (a) With a homogeneous eigenstrain in the voxels occupied by the dislocation loop. (b) With each voxel subdivided into 4×4 sub-voxels, 4 of which have a non zero eigenstrain 109
3.10 2D representation of the computational grid. Black dots correspond to the voxels center. (a) A voxel with center O is discretized in 4×4 in 2D ($4 \times 4 \times 4$) sub-voxels. Some sub-voxels contain an eigenstrain (red sub-voxels). We want to compute the displacement field at voxel centered at point A, due to these deformed sub-voxels centered at B_j. (b) Effect of one deformed sub-voxel centered at O on a row of sub-voxels centered at B_j such as $OA_j = B_j$ A. The sum of these effects is equal to the previous displacement field. 110
3.11 Effect of deformed voxels of the usual grid centered at O on a row of voxels (computed at corners A'_j using a shifted Green operator) such as $OA'_j = nB_jA$. This sum is equal to previous wanted sum. 111
3.12 (a) Plot of the displacement field u_3 (normalized by b_3) along the $z-axis$ for inclined dislocation loop. Artifacts are removed by sub-voxel method described above 113
3.13 Plot of the periodic displacement field u_1^* (normalized by a) along the $z-axis$ for inclined dislocation loop lying in a (111) plane and randomly distributed. The displacement field is computed using the classic Green third order operator $\mathbf{B}$ 114

3.14 Plot of the periodic displacement field u_1^* (normalized by a) along the $z-axis$ for inclined dislocation loop lying in a (111) plane and randomly distributed. The displacement field is computed using the consistent discrete third order Green operator $\mathbf{B}^D$ and corrected with the sub-voxelization method 115
3.15 Plot of the displacement field u_1 (normalized by a) along the $z-axis$ for inclined dislocation loop lying in a (111) plane and randomly distributed. The periodic displacement $\mathbf{u}_1^*$ and the total displacement field $\mathbf{u}_1$ are compared 116
3.16 2D representation of the periodic displacement field u_1^* (normalized by a) in a centered plane perpendicular to $z-axis$ for inclined dislocation loop lying in a (111) plane and randomly distributed. The displacement field is computed using the classic Green third order operator $\mathbf{B}$ 117
3.17 2D representation of the periodic displacement field u_1^* (normalized by a) in a centered plane perpendicular to $z-axis$ for inclined dislocation loop lying in a (111) plane and randomly distributed. The displacement field is computed using the consistent discrete third order Green operator $\mathbf{B}^D$ and corrected with the sub-voxelization method 118
3.18 2D representation of the displacement field u_1 (normalized by a) in a centered plane perpendicular to $z-axis$ for inclined dislocation loop lying in a (111) plane and randomly distributed. $\mathbf{u}_1$ are compared . . 119

4.1 Displacement field resulting from a single dislocation loop in each VER. (a) Full field and (b) periodic part 123
4.2 Computation of a 1D profile. The intensity at voxels (represented here in 2D) are added if their scalar product with the diffraction vector $\mathbf{g}$ are equal. The sums are then split on the two nearest points of the grid. 125
4.3 (a)Hexagonal loop (i.e. transformed platelet) lying in a (111) plane of a FCC crystal used for diffraction peaks simulation. (b) Dislocation dipole in a 111 plane 126
4.4 2D section plots of the diffracted intensity for a single hexagonal dislocation loop deduced from the displacement field computed with the classical operator (a) and (b), the discrete operator (c) and (d), and after sub-voxelization correction (e) and (f). Representation in (111) plane at left and in $(01\bar{1})$ plane at right 127
4.5 1 D plot of the corrected displacement field of a faulted dislocation loop. This displacement field (at left) is compared to the displacement field due to a perfect loop at right. 129
4.6 2D section plots of the diffracted intensity : comparison between a faulted dislocation loop (at right) and a perfect loop (at left). (a) and (b) are representation in (111) plane, (c) and (d) are representation in $(01\bar{1})$ plane 130

4.7 2D section plots of the diffracted intensity : comparison between a rectangular (at right) and a hexagonal dislocation loop (at left). (a) and (b) : (111) plane, (c) and (d) : $(01\bar{1})$ plane . . . 131
4.8 2D plots of the diffracted intensity : comparison between a single(at left) and random distributed dislocation loop (at right).(a) and (b) are representation in (111) plane, (c) and (d) are representation in $(01\bar{1})$ plane . . . 132
4.9 1D peak profiles computed for one dislocation loop using the different methods described in the previous chapter . . . 133
4.10 1D peak profiles computed for one dislocation loop using corrected displacement field : comparison between single and randomly distributed dislocation loops . . . 134
4.11 1D peak profiles computed for one dislocation loop using the corrected displacement field : comparison between a faulted and perfect dislocation loop . . . 135
4.12 1D peak profiles computed for 64 random distributed hexagonal loop for 32 and 128 voxels side of loops. . . . 136
4.13 Plot of the real and imaginary parts of the 1D (200) diffraction peak simulated for 64 loops. . . . 137
4.14 Linear fit of the real and imaginary part of the FFT of peaks for 64 randomly distributed hexagonal loops of size 32 voxels. The slope and the intersection with the $xaxis$ of the linear function are used to determine characteristic parameters. . . . 139
4.15 Second (a) and third (d) order variance and their fit for 64 randomly distributed hexagonal loops (size 32 voxels). . . . 141
4.16 (a) Different steps in the fit of v_4. (b) Fourth-order variance and it fit for 64 randomly distributed hexagonal loops (size 32). . . . 142
4.17 1D diffraction peaks respectively for the (200), (020), and (002)**g** vectors, for a random distribution of 64 hexagonal loops with the same 128 voxels side . . . 143
4.18 1D diffraction peaks simulated respectively for the (200), (400), and (600) **g** vectors, for a random distribution of 64 hexagonal loops with the same 128 voxels side . . . 143
4.19 The normalized real part $ln(A_L/A_0)/L^2$ of the FFT of the peaks for the (200), (020), and (002) **g** vectors (a) and for the (200), (400), and (600)**g** vectors (b). . . . 144
4.20 The normalized imaginary part $(B_L/A_0/L^3)$ of the FFT of the peaks for the (200), (020), and (002) **g** vectors (a) and for the (200), (400), and (600) **g** vectors (b). . . . 144
4.21 Normalized real part $ln(A_L/A_0)/L^2$ of the FFT of the peaks for the (200) **g** vector for 64 random distribution of hexagonal loops with the same voxels side : 32, 64,128, 196, 256 voxels configurations are represented. . . . 145

4.22 Normalized imaginary part $B_L/A_0/L^3$ of the FFT of the peaks for the (200) **g** vector for 64 random distribution of hexagonal loops with the same voxels side : 32, 64,128, 196, 256 voxels configurations are represented. 145
4.23 Different variance orders for the (200)**g** vector for a 64 random distribution of hexagonal loops with the same voxels side. Second order (a) and (b), third order (c) and (d), fourth order (e) and (f), for the 32 and 128 loops side configuration respectively. 148
4.24 The normalized real part $ln(A_L/A_0)/L^2$ of the FFT of the peaks for the (200)**g** vector for a random distribution of hexagonal loops with the same 64 voxels side. Five configurations are represented : (a) 64, 128, 256 and 512 loops. (b) 4096 loops 149
4.25 The normalized imaginary part $B_L/A_0/L^3$ of the FFT of the peaks for the (200)**g** vector for a random distribution of hexagonal loops with the same 64 voxels side. Five configurations are represented : (a) 64, 128, 256 and 512 loops. (b) 4096 loops 149
4.26 Different variance orders for the (200)**g** vector for a random distribution of hexagonal loops with the same 64 voxels side : 64 (left) and 128 (right) loops. 150
4.27 The normalized real part $ln(A_L/A_0)/L^2$ (a) and imaginary part $B_L/A_0/L^3$ (b) of the FFT of the peaks for the (200)**g** vector for a single dislocation dipole with different size : 32, 64 and 128 voxels 152
4.28 Different variance orders for a single dislocation dipole with 32 voxels side : Second order (a) second order (b), third order c) 153
4.29 The normalized real part $ln(A_L/A_0)/L^2$ (a) and imaginary part $B_L/A_0/L^3$ (b) of the FFT of the peaks for the (200)**g** vector for random distribution of 64 or 256 dislocation dipoles with 64 voxels side 154
4.30 Different variance orders for the (200)**g** vector for a random distribution of dipole dislocation with 64 (left) and 256 (right) voxels side . . 155
4.31 Comparison between the theoretical and the computed dislocation densities for a randomly distributed dislocation loops.(a) Variation of the number of dislocation loops. (b) Variation of the dislocation loop size 156
4.32 Comparison between the theoretical and the computed dislocation density for a single dislocation dipole 157
4.33 The cut off radius R_e^* for a random distribution of dislocation loop. (a) Variation of the dislocation size. (b) Variation of the number of dislocation loop 158
4.34 $\langle s^2 \rangle$ for a random distribution of dislocation loop of dislocation. (a) Variation of the dislocation size. (b) Variation of the number of dislocation loop 158
4.35 $\langle s^2 \rangle$ for a single dislocation dipole with different size (a) and for a random distribution of dislocation dipoles (b) 159

A.1 (a)Definition of the unit cell. (b) The infinite repetition by translation of the unit cell gives the crystal lattice. 182
A.2 Schematic view of the diffraction showing the incident wave vector $\mathbf{k}$, the diffraction wave vector $\mathbf{k}'$ and the diffraction vector $\mathbf{g}_{hkl}$ 184
A.3 Ewlad's construction. The atoms located on the Ewald sphere can diffract the incident beam 185
A.4 The function $\frac{sin^2(Nx)}{sin^2(x)}$ plotted close to its first maximum for different values of N. As N tends to infinity, the curve becomes a delta function 189
A.5 The effect of a uniform deformation on the intensity line profile. This uniform deformation does not change the maximum intensity but it position is shifted 190
A.6 2D representation of the crystal divided in columns along the direction of the direction vector 191
A.7 The logarithmic plot of $lnA_n(l)$ [150]. The plot is used to separate size and distortion effect 192

D.1 Different variance order for the (200)$\mathbf{g}$ vector for a 64 random distribution of hexagonal loops with the same voxels side. Second order (a) and (b), third order (c) and (d), fourth order (e) and (f), for the 64 and 196 loops side configuration respectively. 200
D.2 Different variance order for the (200)$\mathbf{g}$ vector for a 64 random distribution of hexagonal loops with the same voxels side. Second order (a), third order (b), fourth order (c) for the 256 loops side. 201
D.3 Different variance order for the (200)$\mathbf{g}$ vector for a random distribution of hexagonal loops with the same 64 voxels side : 256 (left) and 512 (right) loops. 202
D.4 Different variance order for the (200)$\mathbf{g}$ vector for4096 distribution of hexagonal loops with the same 64 voxels side 203
D.5 Different variance orders for a single dislocation dipole with 64 (left) or 128 (right) or voxels side 204

Liste des tableaux

4.1 Characteristics parameters computed with the analysis methods for different size of 64 random distributed hexagonal loops. 147
4.2 Characteristics parameters computed with the analysis methods for 64, 128, 256, 512 or 4096 random distribution of hexagonal loops with the same 64 voxels side 151
4.3 Characteristics parameters computed with the analysis methods for a single dislocation dipole with different sizes 151
4.4 Characteristics parameters computed with the analysis methods for random distribution of 64 or 256 dislocation dipoles with 64 voxels side 152

General introduction

X-ray Diffraction is one of the most common and effective physicochemical characterization methods for crystalline materials and for studying their mechanical behavior. It is a nondestructive method based on the interaction between an X-ray beam and a studied material. The incident X-ray beam with a given wavelength is projected on the sample. A crystal or an atom contained in this sample and satisfying the so-called "Bragg conditions", diffracts the incident beam. The rotation of the sample or the X ray beam tube allows to have different directions of the incident beam. The diffracted beam propagates in a specific direction which varies according to the parameters of the experiment. It is recorded by a detector. In the case of a unit diffracted beam, this detector is placed in a specific direction and in the opposite case, the detector rotates around the sample. All the recorded beams are called diffractogram. With this diffractogram, it is possible to collect several information on the studied material specially if it is a crystalline material (ordered structure).

The analysis of the diffractogram obtained with a crystalline material provided several information : the nature and the position of the atoms, the displacement of atoms, the characteristics of the crystalline cell (dimensions, symmetry, electronic density etc...). For a crystalline material, it allows to determine with high accuracy, the shape and the different orientations of the crystals, the lattice etc. It is the most efficient and most used method for computing residual stresses. Microstructural defects such as dislocations, cracks, their nature, density and distribution can be determined with X-ray diffraction. The use of X-ray beam provided by a synchrotron radiation source and the evolution of this technique have resulted in a reduction of the acquisition time of a diffractogram. Thus, the microstructural evolution of a material during a fast variation of temperature or stresses, can be followed and modeled using XRD technique. These in situ tests also allow to determine plastic deformation and dislocation motion. 2D or 3D mapping of the distribution of the deformation field during a loading can also be obtained.

For its efficiency, this technique is used for the study of nickel-based single crystalline superalloys which are extensively used in aeronautical turbines. In fact, these superalloys have good thermomechanical properties during high creep temperature. These mechanical properties are mainly due to their microstructure with a matrix (denoted γ) with a cubic face-centered structure and which is reinforced by pre-

cipitates (denoted γ') which are ordered and coherent. The mechanical behavior and especially the plasticity of these materials used in extreme conditions must be known in order to guarantee safety or to propose improvements during aeronautical turbines design. Synchrotron radiation diffraction allowed to study these superalloys during creep tests carried out in situ and at high temperatures [27, 26, 25, 130, 129]. Several 2D images are obtained during this diffraction test and their post-analysis allows to study the influence of several parameters such as the initial microstructure but also to study the evolution of plastic deformation during loading.

The post processing of these images is not an easy task. Indeed, the recent evolution especially the Double Crystals Diffraction (DCD) [130, 129], allows to increase considerably the acquisition frequency. Thus several 2D images are obtained after an in situ test. It follows some difficulties related to the processing of these images for a good understanding of internal evolution of the material during the test : the time required for the analysis of these images and the appropriate processing software for these 2D images. The existing analysis programs and softwares : MWP (Multiple Whole Profil) CMWP (Conventionnal Multiple Whole Profil) are more suitable for 1D diagrams [110]. Very little information is therefore extracted from these 2D images. Moreover, it not easy to be allowed to perform an in situ test in major synchrotron centers or it take several time. To be independent of these centers and to use less time for the post-processing of the results, a numerical method for modeling X-ray diffraction patterns based on the mechanical behavior of materials was proposed. This numerical method also allows to complete the experimental method.

Numerical modeling of X-ray diffraction patterns is developed to compare experimental and numerical results. It is based on a complete modeling of the mechanical behavior of material for the computation of strain[4, 135] or displacement [141, 60] field which will allow to evaluate the intensity of a diffracted beam. In order to have efficient numerical models for simulate X-ray diffraction patterns, it is important to use efficient methods to evaluate efficiently and with high accuracy the strain or displacement fields in a material. The analytic solutions are available only for simple mechanical problems. Finite element methods are widely used to compute the mechanical fields. These methods, based on the mesh of the material allow to evaluate the mechanical fields for complex problems in various domain : elasticity, plasticity, elasto-plasticity , elastoviscoplasticity [93, 24, 116, 19] etc ...However, due to computation time, Fast Fourier Transform (FFT) based calculation methods are the most interesting alternative to other mechanical field calculation methods.

FFT-based methods are used to solve equilibrium and compatibility equations in continuum mechanics for homogeneous and heterogeneous materials. They are used to determine : the effective properties of a composite, for the computation of the local fields in the heterogeneous materials and polyscrystals [98, 99, 92, 75, 74, 3, 6, 7]. They are based on the resolution of the Lippmann-Schwinger equation, which is obtained by combining the fields equations in a heterogeneous material.

It involves Green functions computed for a given reference homogeneous medium [72]. The material is discretized in pixels (for 2D problems) or in voxels (for 3D problems). The mechanical fields are calculated at any point of this grid in the Fourier space and using inverse Fourier transform, these fields are obtained in the real space. In addition to simplicity, these methods can reduce the calculation time and are generally more accurate than other computational methods. These algorithms were modified to compute mechanical fields in the case of infinite contrast or to improved convergence rate [92, 163, 120]. For these advantages, FFT algorithms are very efficient for modeling the mechanical behavior of homogeneous/heterogeneous materials for the simulation of diffraction patterns.

Due to the ability of FFT algorithms to compute accurately the mechanical fields in a heterogeneous material under loading, we will make some necessary improvements in this thesis to suppress numerical oscillations occurring at material discontinuities [37]. The improved algorithm will be used to compute the displacement field in a heterogeneous material containing dislocation loops lying in different slip systems. The dislocation loops will be modeled by stress-free strain field called "eigenstrains". The calculated displacement field will be corrected using a numerical method to suppress artifacts due to voxelization [38]. The corrected displacement field will be used to evaluate the value of a diffracted intensity in the vicinity of a diffraction vector using virtual peaks generation method [141]. The numerical peaks obtained will be analyzed with statistical methods in order to determine the characteristic parameters of the deformed microstructure.

This manuscript will be organized in four chapters

The first chapter will be divided in two part : the first part will be a state of the art on X-ray diffraction theory. The technique and its evolution will be described. We will present some different applications of X-ray diffraction. The available X-ray diffraction profile analysis programs will be presented in these part. We will also discussed the X-ray diffraction simulations methods proposed by some authors. In the second part, we will present a state of the art on FFT algorithms for computing mechanical fields in a periodic representative elementary volume. All improvements made after the classic Moulinec and Suquet "basic" scheme [98, 99] to solve convergence problems or to solve problems related to "Aliasing" or Gibbs phenomena will be reported.

In the second chapter, we will determine the expression of a fourth order periodic and discrete consistent Green operator for FFT algorithms. The method is based on the resolution of the Lippmann-Schwinger equation in the Fourier space and an adapted discretization of the spatial domain. This fourth order Green operator allows to compute accurately the mechanical strain/stress fields with precision and without oscillation. Several numerical examples on a homogeneous or heterogeneous material show the suppression of numerical oscillations at material discontinuity. The comparison with the analytic results shows the efficiency of the proposed Green

operator. The convergence rate of the initial algorithm is also slightly improved by the application of this new operator considering for the moment small mechanical contrasts.

In this third chapter, we determine an expression of a third order Green operator which allows to calculate the field of displacement with the FFT algorithms. The oscillations occurring on the displacement field with the classic Green operator are removed with this new operator. We develop in this chapter a subvoxelization method to suppress the artifacts in the case of slip systems having an angle with the FFT grid ((111) type plane). This method is based on the use of the translational invariance property of the Green operator and a finer grid. With several examples, we will show that this "subvoxelization" allows to remove the artifacts.

In the last chapter, we will present and use a X-ray diffraction simulation method to generate virtual diffraction peaks. We obtain for the reference studied case, a 3D mapping of the intensity in the vicinity of a diffraction vector. These 3D data are processed to obtain 2D and 1D profiles. This virtual peaks will be analyzed in order to determine dislocations parameter such as density or spatial distribution factors. A discussion of these results allow to relate the microstructure parameters to the diffraction profile shape.

Chapitre 1

Bibliographic study on X-ray diffraction and FFT-based calculation methods

1.1 Introduction

In this first chapter, we shall present a state of the art for X-ray diffraction theory and for the computation of mechanical fields in periodic materials using Fast Fourier Transform (FFT) algorithm. When an incident X-ray beam is projected on a material (solid or powder), an atom of this material satisfying the so-called "Bragg" conditions, diffracts the X-ray beam. A camera located at a specific distance records the diffracted beam. The principle of the X-ray diffraction technique is to study the diffracted beam recorded for different positions of the material. The analysis of these diffracted beams gives various information on the diffracting material. In the case of in-situ experiments, the analysis of diffracted beam allows to study the mechanical behavior of materials. The evolution of the method has resulted in numerical modeling of diffraction patterns. This numerical modeling allows to complete the experimental modeling and in some cases, it is an interesting alternative. However this numerical approach needs an accurate and efficient method to compute the mechanical fields in the material. In this thesis, we will focus on numerical modeling of diffraction patterns using recently developed Fourier transform method because FFT-based methods have shown efficiency in computing mechanical fields.

In the first part of this chapter, we will first present the experimental technique. The X-ray diffraction theory will be briefly presented. Numerical modeling of diffraction patterns by various methods will also be summarized. The second part will be a literature review on FFT type numerical algorithms for calculating mechanical fields in periodic materials subjected to different types of loading.

1.2 X-ray diffraction

The diffraction of a X-ray beam is an elastic diffusion of an atom contained in the diffracting material. Thus, the wavelengths of the incident and diffracted beam are equal. The propagation direction of the diffracted X-ray beam depends on its wavelength and the parameters intrinsic to the diffracting material. Consequently, the analysis of the diffracted beam allows to study these intrinsic parameters and determine the nature or the internal evolution of the material. The corresponding technique is simply called X-Ray Diffraction (XRD) or X-ray crystallography. This technique is suitable for the study of crystalline materials. Such materials have atoms arranged in an ordered way. Most reported studied concerns the diffraction of a monochromatic X-ray beam (advanced experimental technique allows to obtain a beam with a given wavelength) by a crystalline material containing defects such as dislocations, cracks...

In the next section, we will present some experimental techniques. We will focus on the recent techniques based on synchrotron radiation developed for the study of a single crystal superalloys. Thus, the X-ray diffraction theory will be developed and relevant contributions in peaks broadening or analysis will be reported. The X-ray diffraction simulation methods will be developed and the connection between these methods will be established.

1.2.1 In situ XRD on Ni-based superalloy single crystals

The experimental setup is built around three elements : the sample, an X-ray generator tube and a beam detector. In most cases, turning the sample or the X-ray generator allows to record various diffracted beams corresponding to different configurations in the studied material. The high intensity of the synchrotron radiation, combined with faster higher resolution detectors allows to record a diffraction peak in a few hundredths of seconds. The construction of high-energy lines on synchrotrons such as the ESRF (Grenoble, France), DeSy (Hamburg, Germany), APS (Chicago, USA) or sPring-8 (Hyogo, Japan), allows to provide a beam of short wavelength, little absorbed by the material, which allows transmission measurements on depths suitable for massive sample study. Through the development of appropriate test devices, it is now possible to track the response of a material during in situ experiments [86]. Triple-crystal synchrotron X-ray diffractometry (TCD) or double-crystal synchrotron X-ray diffractometry (DCD) are two recent advanced experimental techniques which allow to study materials in real time.

1.2.1.1 Triple-crystal synchrotron X-ray diffractometry (TCD)

Three-crystal diffraction (TCD) is a well known high resolution diffraction technique [87, 129]. The device has three crystals [121, 129] : the first is the monochromator, the second the sample and the last the analyzer. The polychromatic beam is first diffracted by the monochromator, which selects a single wavelength for the incident ray. Then this monochromatic beam is diffracted by the sample according to Bragg conditions. Different areas of the specimen with slightly different lattice parameters and orientation diffract the incident beam into slightly different orientations. The analyzer (identical to the monochromator) selects one of these directions and diffracts the corresponding beam into a detector as shown in Fig1.1 [129]

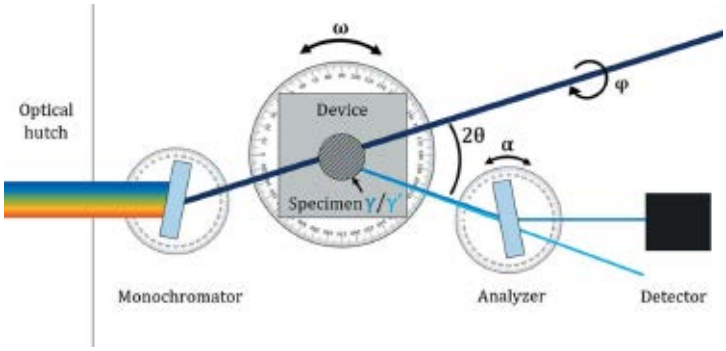


FIGURE 1.1 – Setup of a triple-crystal diffractometer.

The angular rotation ω allow to bring a desired family of planes in diffraction position and then gives access to the local orientation of the diffracting zone. A complete diffractogram is recorded during a scan by performing a simultaneous rotation of ω and α as $\delta\alpha = 2\delta\omega$. The rotation ω in fig.1.2 corresponds to transverse scans almost perpendicular to the diffraction vector. In this case the intensity measurements are sensitive to the mosaicity (geometry) of the sample. The rotation α in fig.1.2 [61] corresponds to longitudinal scans along the diffracted vector. The measurements are sensitive to the distribution of the lattice parameters along the diffraction vector.

This efficient experimental technique was used in references [25, 27, 26] to study high temperature creep behavior of a γ/γ' Nickel-based Superalloy (AM1). The aim of this study was to compute, the mismatch $\delta_\perp$ between the γ and γ' phases, introduce by interface dislocations. This parameter can be deduced with a good precision from the profile of the diffraction peak Fig.1.3. $\delta_\perp$ is proportional to the distance between the obtained peak for γ and γ'. However, With the TCD, a record of the γ/γ' diffractogram takes about 5 minutes. This important recording time does not allow some in-situ experiments. To obtain real-time measurements and study fast transitions, it was necessary to improve the acquisition frequency.

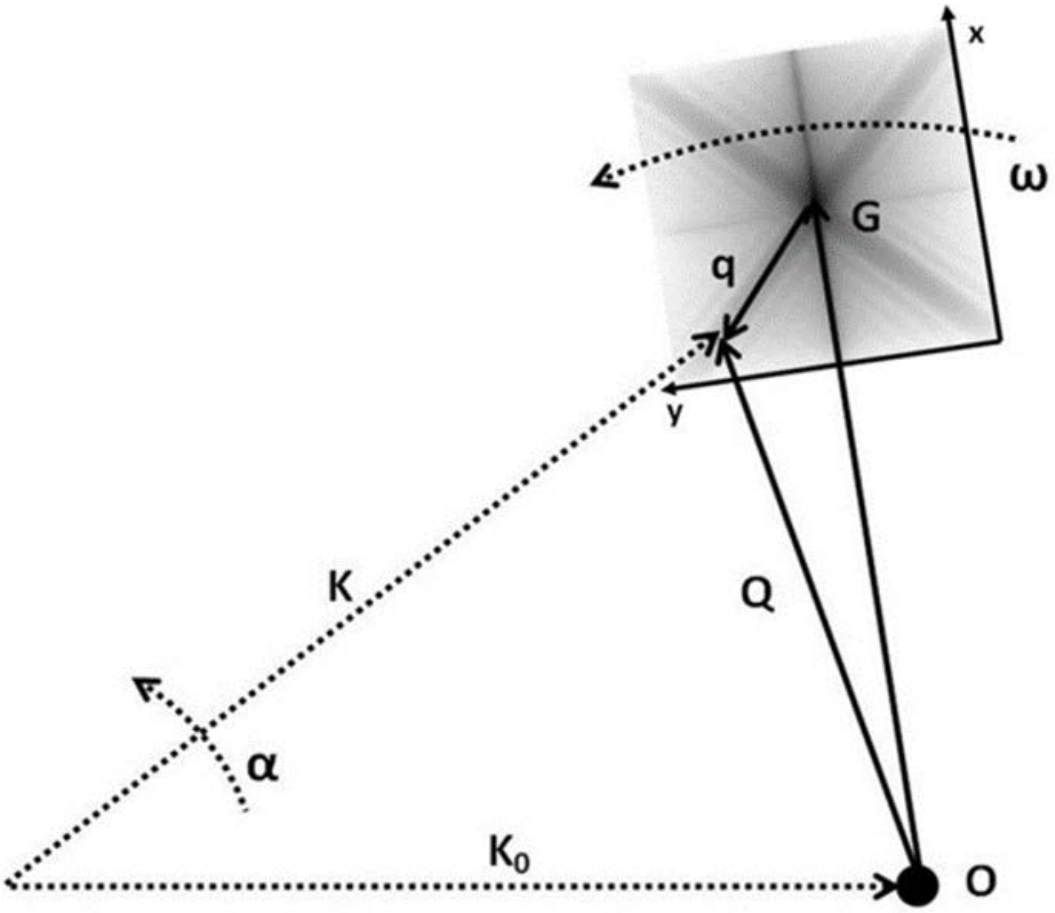


FIGURE 1.2 – Reciprocal-space mapping using the ω (specimen) and α (analyser) rotations. A ω rotation scans the mosaicity, and an α scan gives the distribution of lattice parameters [61]. K, K_0 represent the incident and the diffracted beam respectively. G is the reciprocal lattice vector and Q correspond to the exact Bragg position

1.2.1.2 Far field 2D X-ray diffractometry (DCD)

A Double-crystal synchrotron X-ray diffractometry (DCD) was developed. The analyzer is removed as shown in fig. 1.4. There are two configurations : the near-field and the far-field. In the near-field DCD technique , the detector is located in the diffraction cone of the sample. In the case of the γ/γ' Nickel-based Superalloy (AM1) for example, the near-field camera does not allow to separate the contributions of each phase. In the far-field DCD technique [130, 129], the diffracted beam is recorded by a far field camera as shown in fig1.5. The far-field DCD allows to study in real

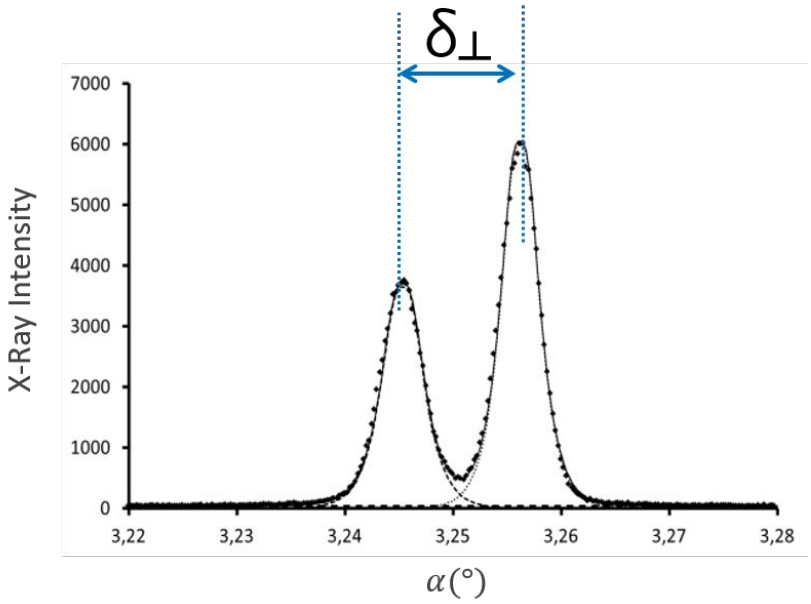


FIGURE 1.3 – TCD $\theta/2\theta$ scan diffraction peak for an Ni-base single-crystal superalloy [25]

time the γ/γ' Nickel-based Superalloy and compute $\delta_\perp$, to estimate the interfacial dislocation density (or to determine the parameter influencing it) etc. In some other cases, another experimental technique can be used to study various material. Once the diffraction peak is recorded, it must be analyzed to retrieve the information it contains. This analysis is based on the X-ray diffraction theory and equations.

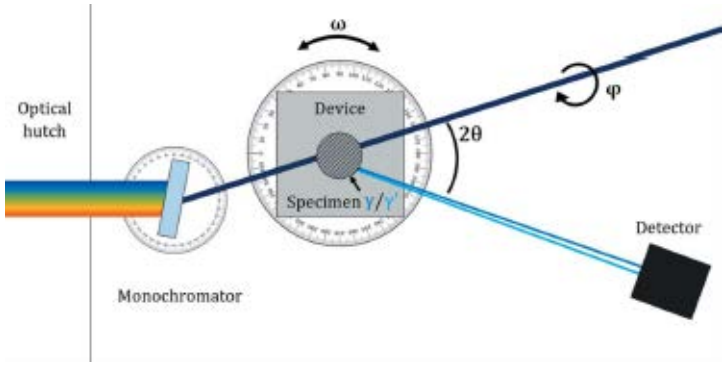


FIGURE 1.4 – Setup of a double crystal diffractometer.

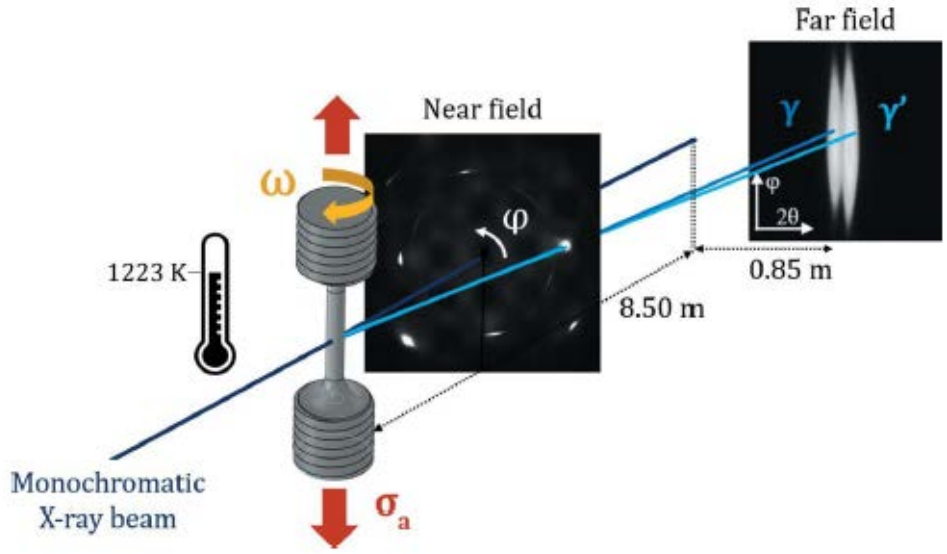


FIGURE 1.5 – Far-field DCD technique [130, 129]. The diffracted beam is recorded by a far field camera and the γ and γ phases are separated.

1.2.2 Basics of X-ray diffraction theory

A non specialized reader will find in Appendix A a brief summary of basic XRD theory, and an introduction to the ideas discussed below. In the following, we shall assume that diffraction of a well collimated and monochromatic X-ray beam by a perfect single crystal with a macroscopic size should occur only at points of the reciprocal lattice. The real shape of the peaks results from deviation from the above hypothesis, i.e : imperfections in the beam, a finite size of the crystal, and a non-uniform strain in the crystal.

1.2.2.1 Instrumental width of the setup and coherence length

Coherence is the property of light responsible for interference effects. Two different coherences are described : spatial coherence describes the relationship between waves at different points in space and the temporal coherence describes the correlation between waves observed at different times [162].

Spatial coherence

The spatial effect is also called the transverse coherence. It results from to the fact that the light source is not ideally point-wise but has some lateral extension.

The transverse effect is explained in the fig. 1.6 [62, 63]. The distance S_1S_2 represents the light source (or slits limiting the beam) and D_1D_2 the detector. Let's study the amplitude at point O_D and D_1 coming from S_1 and S_2. At O_D, the waves coming from S_1 and S_2 have followed an equal path and interfere constructively. At point D_1, the difference between the path length is : (we note $S = S_1S_2$, $R = O_SO_D$ and $W = D_1O$)

$$L_1 - L_2 \approx \frac{1}{2R}\left(\left(\frac{W+S}{2}\right)^2 - \left(\frac{W-S}{2}\right)^2\right) = \frac{WS}{2R}$$

If this shift is equal to $\frac{\lambda}{2}$ (λ is the wavelength of the beams), the beams cancel at point D_1. The beams are added only if the shift is less than $\frac{\lambda}{2}$:

$$\begin{aligned} \frac{WS}{2R} &< \frac{\lambda}{2} \\ W &< \frac{\lambda R}{S} \end{aligned} \tag{1.1}$$

This last condition is the transverse coherence condition and $\frac{\lambda R}{S}$ is called the transverse coherence length of the beam [89, 141, 109]. If the crystal size is less than $\frac{\lambda R}{S}$, the beam is taken as coherent and the amplitude scattered by all atoms add. Conversely, for areas separated by more than $\frac{\lambda R}{S}$, the scattered intensities will add. Typically values of $\frac{\lambda R}{S}$ varie from : $20\mu m$ to $120\mu m$ for a 3^{rd} generation synchrotron sources.

Temporal coherence

The temporal coherence is also called the longitudinal coherence. It defines the degree of coherence of the light source along its propagation direction and refers to the monochromaticity of the beam. The longitudinal coherent length is defined as the propagation distance over which two wavefronts, one of wavelength λ and the other of wavelength slightly different $\lambda + \delta\lambda$, simultaneously coming from a point source are in phase opposition. The longitudinal coherent length is defined as $\frac{1}{2}\frac{\lambda^2}{\delta\lambda}$ [162]. The bandwidth $\frac{\delta\lambda}{\lambda}$ is given by the monochromator. The lower the bandwidth value, the better the monochromator is and lower the intensity.

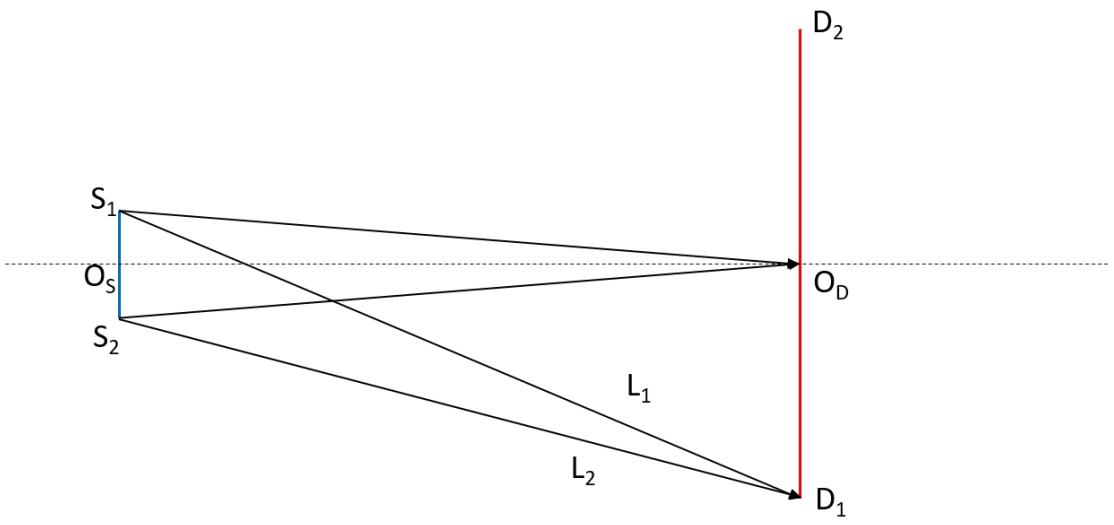


FIGURE 1.6 – Schematic representation of the diffraction by two Young's holes

1.2.2.2 A non uniform deformation

In Appendix A, we derived the expression of the diffracted intensity. We also study the effect of the crystal size and the effect on a uniform deformation in the crystal. We derived an expression of the intensity in the case of point defects whose distribution in crystal is the source of non-uniform deformation. In this section, we will discuss X-ray diffraction analysis model which allow to determine the micro-structure parameters from peak profile.
The expression of the intensity is given by the double summation [150] (see Appendix A) :

$$I(\mathbf{g}) = I_0 F^2 \sum_m \sum_{m'} e^{(i2\pi/\lambda)\mathbf{g}(\mathbf{r}_m - \mathbf{r}_{m'})} \tag{1.2}$$

where λ is the wavelength and $\mathbf{g}$ is the diffraction vector. I_0 is proportional to the initial X-ray beam intensity, F is the complex structure factor and $\mathbf{r}_m$ is the position of unit cells assimilated to one of its origin. In presence of a local deformation, the atoms deviate from their initial position such as in a strained crystal, $\mathbf{r}_m$ is given by :

$$\mathbf{r}_m = m_1\mathbf{a}_1 + m_2\mathbf{a}_2 + m_3\mathbf{a}_3 + \mathbf{u}(m_1, m_2, m_3) \tag{1.3}$$

where $\mathbf{u}$ is the displacement field [150]. The total intensity is written as Fourier series (see Appendix A).The Fourier coefficients are denoted A_n and B_n which are

the cosine and sine parts respectively. The logarithm of the cosine coefficient can be written as :

$$lnA_L = lnA_L^S - 2\pi^2 L^2 g^2 \langle \varepsilon_L^2 \rangle \tag{1.4}$$

where : L is the distance between pair of atoms in the direction of the diffraction vector $\mathbf{g}$. $\langle \varepsilon_L^2 \rangle$ is the means square values of average strain computed in the direction of $\mathbf{g}$. It is defined as a function of the displacement field in eq. 1.5. This last equation shows that the means square values of average strain can be determined by the measured peak profile. Once the means square values of average strain is determined, the challenge is to relate these values to the defects in the crystal. In the case of dislocations, the density and the distribution parameters will be searched from these values. Several authors searched for an analytic expression for $\langle \varepsilon_L^2 \rangle$ by assuming different distributions of dislocations.

$$\boldsymbol{\varepsilon}_{\mathbf{g}}(L, \mathbf{r}) = \frac{\frac{\mathbf{g}}{|\mathbf{g}|}\mathbf{u}\ (\mathbf{r} + \frac{L}{2}\frac{\mathbf{g}}{|\mathbf{g}|}) - \frac{\mathbf{g}}{|\mathbf{g}|}\mathbf{u}\ (\mathbf{r} - \frac{L}{2}\frac{\mathbf{g}}{|\mathbf{g}|})}{L} \tag{1.5}$$

Calculation of the means square strain

A logarithmic behavior is proposed for the mean square strain $\langle \boldsymbol{\varepsilon}_{\mathbf{g},\mathbf{L}}^2 \rangle$. This behavior is recovered by Ribarik in [110]. He computed and plot in fig. 1.7 the value of the mean square strain $\langle \boldsymbol{\varepsilon}_{\mathbf{g},\mathbf{L}}^2 \rangle$ in a $50 \times nm$ crystal box containing 10 randomly distributed edge dislocations.

The expression of the mean square strain proposed by several authors is based on this logarithmic behavior. Krivoglaz and Ryaboshapka [71] assumed a totally random distribution of infinite straight parallel dislocations in the crystal and proposed the following expression for $\langle \varepsilon_L^2 \rangle$ at small values of L :

$$\langle \boldsymbol{\varepsilon}_{\mathbf{g},\mathbf{L}}^2 \rangle = \left(\frac{\mathbf{b}}{2\pi} \right)^2 \pi \rho C log \left(\frac{D}{L} \right) \tag{1.6}$$

where D is the crystal size, $\mathbf{b}$ is the Burgers vector, ρ is the dislocation density and C is the contrast factor of dislocation (this contrast factor will be discussed in next sections). This model is valid when dislocation Burgers vector of sign $(-)$ and $(+)$ have same presence probability. The Warren-Averbach procedure for analyzing peak profiles is based on this model [151, 110]. This model presents an important shortcoming : when the crystal D size tends to infinity, the model diverges.

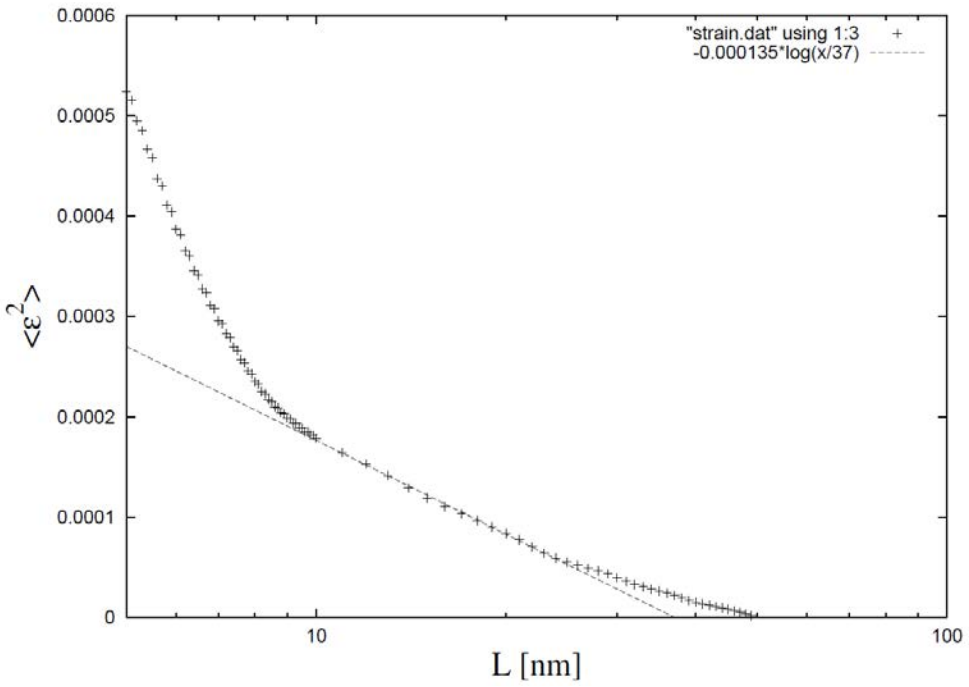


FIGURE 1.7 – The mean square strain computed in a $50nm \times 50nm$ crystal box containing 10 randomly distributed edge dislocations. Logarithmic scale in x-axis. The dashed line shows that the computed mean square strain is well described by a logarithmic dependence for small values of L

In order to improve the previous model, Wilkens [154] proposed another model. Wilkens [154] considers parallel and infinite dislocations. He divided a normal section of the crystal in small subsection with equal size R_e^*. Each subsection contains equal number of screw (the result is also valid for edge or curved dislocations) dislocation Burgers vector of sign $(-)$ and $(+)$ randomly distributed. Wilkens called this configuration : as a restrictedly random distribution. The length parameter R_e^* replaces the crystal size, thus the logarithmic singularity in eq. 1.6 is eliminated. R_e^* is called the effective outer cut off radius of dislocations. The expression of the mean square strain value proposed with this configuration is [154] :

$$\langle \boldsymbol{\varepsilon}^2_{\mathbf{g},\mathbf{L}} \rangle = \left(\frac{\mathbf{b}}{2\pi} \right)^2 \pi \rho C f \left(\frac{L}{R_e^*} \right) \tag{1.7}$$

The strain function f in the so-called Wilkens function. The explicit expression of the Wilkens function is given in Eq.1.8. In this equation, $f\left(\frac{L}{R_e^*}\right) = f^*(\eta)$ and $\eta = \frac{1}{2} exp\left(-\frac{1}{4}\right) \frac{L}{R_e^*}$. The derivation of this expression of the strain function allows to compute the mean square strain in the entire L range and does diverge when the crystal increases. Note that the logarithmic behavior described in [71] model is recovered with this model for small values of L. In practice an approximation of

this function can be used for small or large values of L as shown in fig. 1.8 [110] : $f^*(\eta) = -log(\eta) + \left(\frac{7}{4} - log2\right)$ for small values and $f^*(\eta) = \frac{512}{90\pi}\frac{1}{\eta}$ for large values.

$$
\begin{aligned}
& f^*(\eta) = -log(\eta) + \left(\frac{7}{4} - log2\right) + \frac{512}{90\pi}\frac{1}{\eta} + \\
& \frac{2}{\pi}\left[1 - \frac{1}{4\eta^2}\right]\int_0^\eta \frac{arcsinV}{V}\mathrm{d}V - \frac{1}{\pi}\left[\frac{769}{180}\frac{1}{\eta} + \frac{41}{90}\eta + \frac{2}{90}\eta^3\right]\sqrt{1-\eta^2} - \\
& \frac{1}{\pi}\left[\frac{11}{12}\frac{1}{\eta^2} + \frac{7}{2} + \frac{1}{3}\eta^2\right] arcsin\eta + \frac{1}{6}\eta^2, \qquad if\eta \quad \leq 1, \\
& f^*(\eta) = \frac{512}{90\pi}\frac{1}{\eta} - \left[\frac{11}{24} + \frac{1}{4}log2\eta\right]\frac{1}{\eta^2}, \qquad if\eta \quad \geq 1
\end{aligned}
\tag{1.8}
$$

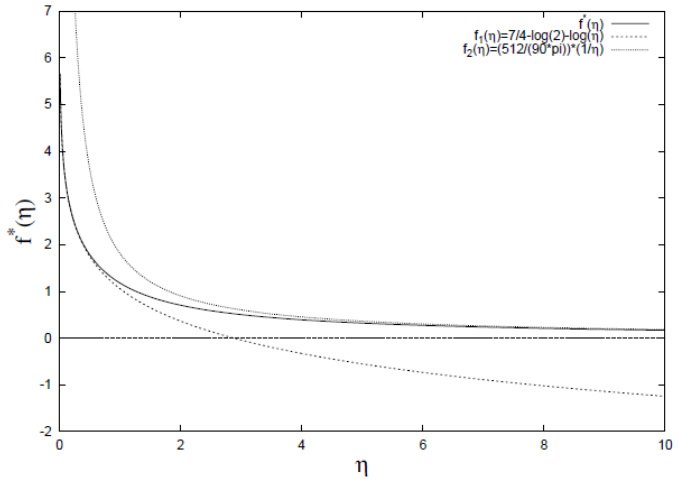


FIGURE 1.8 – The function $f^*(\eta)$ and two of its approximations : for small and large values of L

Wilkens also introduced a parameter $M^* = R_e^* \times \sqrt{\rho}$ (ρ being the dislocation density). This parameter is used to characterize the dislocation distribution : if M^* is small, the dislocation are strongly correlated but if the value of M^* is large, the dislocation are randomly distributed. It is noted that the Fourier transform given by the Wilkens model is real, this means that its inverse Fourier transform, the strain intensity profile is symmetric, which is not always fulfilled in case of real measurements. Some other authors proposed different models to take into account asymmetric broadening of profiles [134, 100, 45, 46]

Another model was proposed by Groma and Csikor [52, 22]. The aim of these authors was to propose a simple interpolation function which can connect the strain function proposed by several authors [71, 70, 154, 51, 53]. The expression of the

mean square strain values proposed by Groma and Csikor is [52, 22] :

$$\langle \boldsymbol{\varepsilon}^2_{\mathbf{g},\mathbf{L}} \rangle = \left(\frac{\mathbf{b}}{2\pi} \right)^2 \pi C f^{GR-CS}(L) \tag{1.9}$$

where :

$$f^{GR-CS}(L) = W log\left(1 + \frac{X}{\mid L \mid}\right) + \frac{Y}{1 + ZL^2}$$

W, X, Y and Z are the function parameters. The computation method used to determine these parameters is not detailed here. Note that the physical parameters such as dislocation density or the effective outer cut off radius of dislocations are determined with these constants (using $L \to 0$ and $L \to \infty$, see eq. 1.10). The parameters ρ^{dip} and ρ^{dis} are the dislocation dipole density and the dislocation density respectively. C^{dip}_{h00} and C^{dis}_{h00} are the dipole and dislocation contrast factors respectively. This strain function is efficient in peak profile analyzing and successfully implemented in an analyzing program [112]

$$\begin{aligned} \rho^{dis} &= \frac{W}{C^{dis}_{h00}} \\ Re &= X exp(\frac{Y}{W}) \\ \rho^{dip} &= \frac{W}{2C^{dip}_{h00}} \end{aligned} \tag{1.10}$$

About the strain contrast factor

The strain contrast factor also called the contrast factor of dislocations, usually denoted C, is introduced to handle the anisotropic broadening of X-ray line. The most suitable model to characterize this dependence is the dislocation model $\langle \varepsilon^2_{\mathbf{g},L} \rangle$, which is based on C whatever the author. This factor depends on the elastic constant of the material, the dislocation line vector ($\mathbf{l}$), the Burgers vector ($\mathbf{b}$) and the normal direction to the slip system. For example, $C \approx 0$ when $\mathbf{b}.\mathbf{g} = 0$ and this means that this dislocation has no, or almost no broadening effect on X-ray line. For any dislocation, the value of the contrast factor (depending on the reflection hkl), can be determined experimentally for a single crystal. An average value of C is observed

in the case of a polyscrystal [131]. In the case of cubic crystals (untextured material and random distribution of all possible slip systems) for example, the average contrast factor $\bar{C}$ [132] is (similar expressions are used for hexagonal and orthorhombic crystals) :

$$\bar{C} = C_{h00}(1 - qH^2) \tag{1.11}$$

The values of C_{h00} is given in [132] and H^2 is :

$$H^2 = \frac{h^2k^2 + h^2l^2 + k^2l^2}{(k^2 + h^2 + l^2)^2} \tag{1.12}$$

1.2.3 Analysis method based on the profiles moment

Different methods of X-ray line profile analysis are developed to extract microstructural information from diffraction profiles. In previous sections and in Appendix A, we noted that the position, shape and the width of the profile provided information about the microstructure. X-ray line profile analysis method is based on the analysis of the width (breadth methods) or on the analysis of the entire profiles (pattern fitting or whole profile methods). The most important analysis methods are : the Williamson-Hall procedure [155] (breadth methods), the Warren-Averbach procedure [151](breadth methods), the Multiple Whole Profile (MWP) [82, 91, 110, 113, 133] (whole profile method), methods analyzing the moments of the profiles [51, 13].
In this manuscript, we will discuss the methods analyzing the moments of the profiles because they will be used in next chapters. The aim of this model is to provide a general model valid near or far from dislocations lines. This efficient method was proposed by Groma [51] and is based on the asymptotic behavior of the different order moments of the intensity distribution. Groma considered a system of dislocation parallel to a crystal axis. The analytic expression of the cosine coefficient $A(n)$ is derived and its logarithmic expression is :

$$lnA = \Lambda\langle\rho\rangle n^2 ln\left(\frac{n}{\bar{R}_1}\right) + i\langle s^2\rangle n^3 ln\left(\frac{n}{\bar{R}_2}\right) + \frac{1}{2}\Lambda^2\left[\langle\rho^2\rangle - \langle\rho\rangle^2\right] n^4 ln\left(\frac{n}{\bar{R}_3}\right) ln\left(\frac{n}{\bar{R}_4}\right) \tag{1.13}$$

$\bar{R}_1, \bar{R}_2, \bar{R}_3, \bar{R}_4$ are constants with length dimension. $\langle ... \rangle$ indicates the spatial average, $\langle\rho\rangle$ is the average dislocation density, $\langle\rho^2\rangle$ is the average two particle total

density with $\rho^2(\mathbf{r})$ defined as :

$$\rho^2(\mathbf{r}) = w^2_{+,+}(\mathbf{r},\mathbf{r}') + w^2_{-,-}(\mathbf{r},\mathbf{r}') + w^2_{+,-}(\mathbf{r},\mathbf{r}') + w^2_{-,+}(\mathbf{r},\mathbf{r}') \tag{1.14}$$

where $w^2_{+,+}(\mathbf{r},\mathbf{r}'), w^2_{-,-}(\mathbf{r},\mathbf{r}'), w^2_{+,-}(\mathbf{r},\mathbf{r}'), w^2_{-,+}(\mathbf{r},\mathbf{r}')$ are two-particle dislocation density functions with positive and negative signs of the Burgers vector indicated by the subscripts. Groma [51] used the expression in eq. 1.13 to derive an expression of the $k-th$ order statistical moment of the scattered intensity which is recalled in eq. 1.15.

$$M_k(q) = \frac{\int_{-\infty}^{\infty} s^k I(q)\mathrm{d}s}{\int_{-\infty}^{\infty} I(q)\mathrm{d}s} \tag{1.15}$$

$q = \frac{2}{\lambda}\left(sin(\theta) - sin(\theta_0)\right)$, where θ_0 is the Bragg angle and θ is the diffraction angle. In [51, 13], the author derived an analytic expression of the second and the fourth order moments :

$$M_2(q) = \frac{1}{\pi^2\varepsilon_F} - \frac{L}{4\pi^2K^2\varepsilon_F} + \frac{\Lambda\langle\rho\rangle}{2\pi^2} log\left(\frac{q}{q_0}\right) \tag{1.16}$$

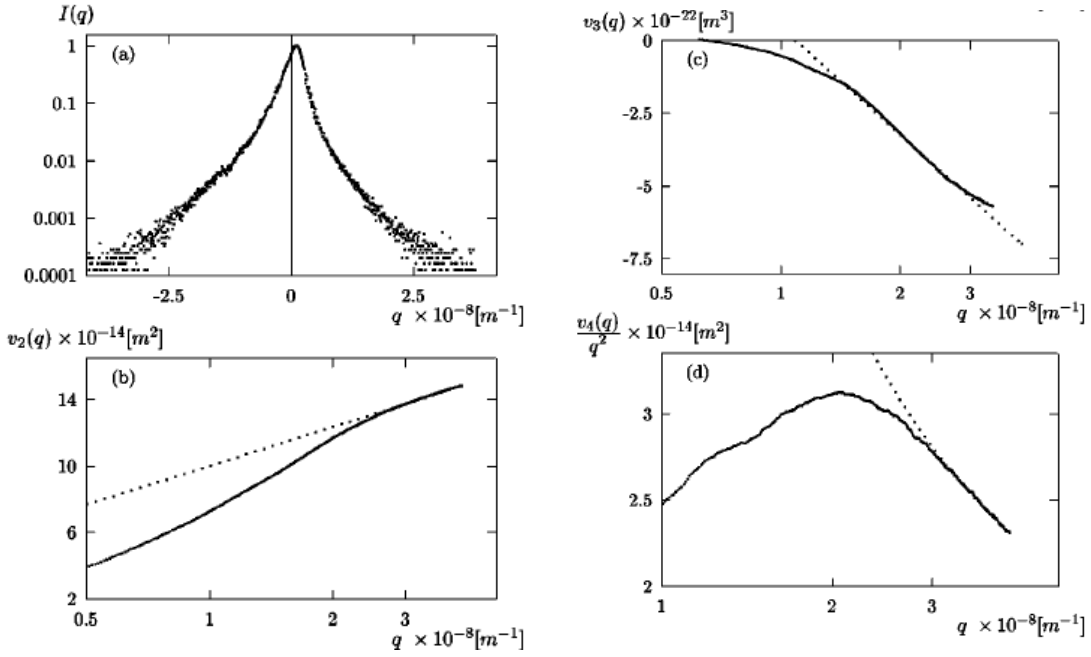
$$\frac{M_4(q)}{q^2} = \frac{1}{3\pi^2\varepsilon_F}q + \frac{\Lambda\langle\rho\rangle}{4\pi^2} + \frac{3\Lambda^2\langle\rho^2\rangle}{4\pi^2}\frac{log^2\left(\frac{q}{q_1}\right)}{q^2} \tag{1.17}$$

$\Lambda = \frac{\pi}{2}g^2b^2C$, $\varepsilon_F = \frac{3}{2}L_0$ (L_0 being the crystal size parameter). Another similar value which may be investigated is the $k-th$ order variance. It defined as :

$$v_k = \frac{\int_{-q'}^{q'} q^k I(q)\mathrm{d}q}{\int_{-\infty}^{\infty} I(q)\mathrm{d}q} \tag{1.18}$$

The general form of the second, third and fourth order variance is [51] :

$$\begin{aligned} v_2(q') &= 2\Lambda\langle\rho\rangle ln\left(\frac{q'}{q_0}\right) \\ v_3(q') &= -6\langle s^{'(2)}\rangle ln\left(\frac{q'}{q_1}\right) \\ v_4(q') &= \Lambda\langle\rho\rangle q'^2 + 12\Lambda^2\langle\rho^{'(2)}\rangle ln\left(\frac{q'}{q_2}\right) ln\left(\frac{q'}{q_3}\right) \end{aligned} \tag{1.19}$$



(a) (b)

FIGURE 1.9 – (a) Line profile measured on a tensile deformed Cu single crystal. (b) Fitted second-order variance. (c) Fitted third-order variance divided by q^2. (d) Fitted Fourth-order variance [51].

where q_1, q_2, q_3 are constant values. Using the variance or the moment it is possible to determine the characteristic parameters of the dislocation configuration : $\langle\rho\rangle$ or $\langle\rho^2\rangle$. The method corresponds in fitting the used expression to the order variance or moment of the measured profile for large q values. The method is applied by Groma on a line profile measured on tensile deformed Cu single crystal in fig. 1.10. This figure shows that the linear behavior of the different order variance for large value of s. The linear behavior of the moment is shown by Borbely and Groma in [13].

1.2.4 X-ray diffraction simulations

During last years, the numerical simulation of X-ray diffraction patterns received a surge of interest. Sometimes, this simulation is an interesting alternative to experimental study because the purpose of the study can not be achieved by experimental tests. This evolution is strongly related to the increasing capability of computers. This simulation has multiple goals. First, to save time in studied materials because an experimental test takes much more time from the sample preparation up to the profile analysis. Another goal of this simulation is to complete the experimental study in order to validate hypotheses [135, 141]. It is based on the numerical com-

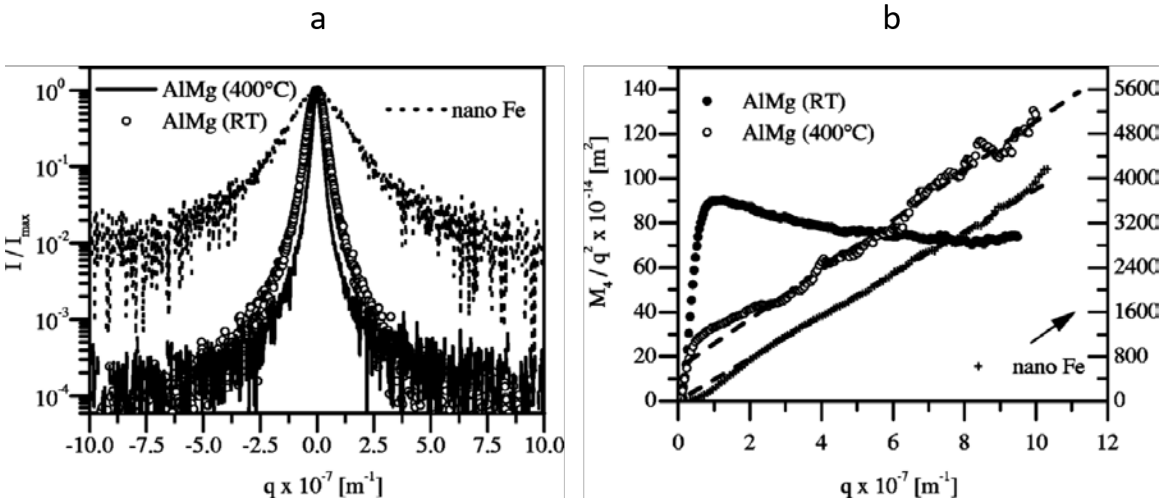


FIGURE 1.10 – (a) High-resolution X-ray Bragg peaks. (b) Characteristic behavior of the fourth order moment divided by q^2. [13].

putation of the mechanical fields in a material. As discussed in previous sections, the line profiles are sensitive to the strain field in the material and in most of the cases it is the single cause of the line broadening. It is straightforward to show that the line profile are also sensitive to the displacement field. In the following, we discussed a numerical method tool to generate virtual line profiles based on displacement or strain field [135, 148, 150, 126]

1.2.4.1 Numerical method based on displacement field

The most powerful technique to generate diffraction peaks using displacement field is the one proposed by Warren [150] called the Fourier method. It is based on the kinematical theory of diffraction. Let us consider a distorted single crystal, we already reported the expression of the diffracted intensity I [150, 135]

$$I(\mathbf{g}) = I_0 F^2 \sum_m \sum_{m'} exp\left(\pi i \mathbf{g}(\mathbf{r}_m - \mathbf{r}_{m'})\right) \tag{1.20}$$

Applying the powder pattern theorem which derives from the general procedure of wilson [150, 159], we derived in AppendixA an expression of the diffracted intensity in the case of a diffracted vector parallel to one of the unit cell vector eq. A.20. This expression can be written as a function of the distance $L = \mid \mathbf{L} \mid$ between a pair of

unit cell :

$$I(\mathbf{q}) = \sum_{|\mathbf{L}|=-\infty}^{\infty} [A(\mathbf{L})cos(2\pi\mathbf{Lq}) + B(\mathbf{L})sin(2\pi\mathbf{Lq})] \tag{1.21}$$

where $\mathbf{q}$ is the deviation from the exact Bragg position $\mathbf{g}$. $A(\mathbf{L})$ and $B(\mathbf{L})$ are the Fourier coefficients. This expression is called the "Fourier method of Warren" in reference to his author [150]. $A(\mathbf{L})$ and $B(\mathbf{L})$ have a definition similar to A_n and B_n (see Appendix A). $A(\mathbf{L})$ (respectively $B(\mathbf{L})$) is also product of distortion Fourier coefficients $A^D(\mathbf{L})$ and size Fourier coefficients $A^S(\mathbf{L})$ (respectively $B^D(\mathbf{L})$ and $B^S(\mathbf{L})$) such as :

$$A^D(\mathbf{L}) = \langle cos\,[2\pi\mathbf{gu}\ (\mathbf{L})]\rangle, \qquad B^D(\mathbf{L}) = \langle sin\,[2\pi\mathbf{gu}\ (\mathbf{L})]\rangle \tag{1.22}$$

$\langle ...\rangle$ indicate the spatial average and $\mathbf{u}$ is the displacement between the pair of unit cell separated by L. The simulation method proposed by Warren [150] is to compute the distribution of the displacement field $\mathbf{u}$ in the crystal. This distribution allows to compute $A^D(\mathbf{L})$ and $B^D(\mathbf{L})$ and thus evaluate the intensity distributions function given in eq. 1.21. The shortcoming of this method is the computational time which is intensive since the Fourier length $\mid \mathbf{L} \mid$ varies in all the diffracting domain. A strain based method was proposed by Stokes [126].

1.2.4.2 Numerical method based on strain field

This method derives from the Fourier method of Warren. It was proposed by Stokes and Wilson [126], thus it known as the Stokes-Wilson approximation and is based on the apparent strain (local strain computed along the diffraction vector). Since $\Delta\mathbf{u}\ (\mathbf{L})$ is along $\mathbf{L}$ and the direction of the diffraction vector $\mathbf{g}$, a difference in displacement denoted $\varepsilon^{\mathbf{L}}$ is defined :

$$\varepsilon^L = \frac{\mathbf{g}.\Delta\mathbf{u}(\mathbf{L})}{\mid \mathbf{g} \mid\mid \mathbf{L} \mid} \tag{1.23}$$

Thus, the Fourier coefficients written in eq. 1.22 can be rewritten using a proba-

bility distribution function (PDF) of ε^L $p_{\varepsilon^L}(\varepsilon^L)$ [148, 35, 140, 80]

$$\begin{aligned} A^D(\mathbf{L}) &= \int_{-\infty}^{+\infty} p_{\varepsilon^L}(\varepsilon^L) cos\left(2\pi \mid \mathbf{g} \mid \varepsilon^L \mid \mathbf{L} \mid\right) \mathrm{d}\varepsilon^L, \\ B^D(\mathbf{L}) &= \int_{-\infty}^{+\infty} p_{\varepsilon^L}(\varepsilon^L) sin\left(2\pi \mid \mathbf{g} \mid \varepsilon^L \mid \mathbf{L} \mid\right) \mathrm{d}\varepsilon^L \end{aligned} \tag{1.24}$$

This is the first step of their derivation. Now an apparent strain ε was defined as :

$$\varepsilon = \frac{\mathbf{g}. \bigtriangledown \mathbf{u} \ .\mathbf{g}}{\mid \mathbf{g}^2 \mid} \tag{1.25}$$

Then, the authors made an assumption. They assumed that for large values of $\mid \mathbf{L} \mid$, the relative displacement is randomly distributed between unit cells and then cancel each other out. This assumption leads to the fact that $p_{\varepsilon^L}(\varepsilon^L) = p_\varepsilon(\varepsilon)$. The expression of the intensity is :

$$I(\mathbf{q}) = \int_{-\infty}^{+\infty} \int_{-\infty}^{+\infty} p_\varepsilon(\varepsilon) exp\left(2\pi i \mid \mathbf{L} \mid \varepsilon \mid \mathbf{g} \mid\right) exp\left(2\pi \mid \mathbf{q} \mid\mid \mathbf{L} \mid\right) \mathrm{d}\varepsilon \mathrm{d} \mid \mathbf{L} \mid \tag{1.26}$$

This corresponds to the Stokes-Wilson's result that was also retrieved and used in [80, 4]. The authors in reference [80, 4] also show that the intensity in eq. 1.26 can also be computed using eq. 1.27. This means that the intensity profile can be simulated just by computing the probability distribution function (PDF) of the apparent strain.

$$I(\mathbf{q}) = p_{\mathbf{q}}(\mathbf{q}) \frac{1}{\mid \mathbf{g} \mid} p_\varepsilon(\varepsilon) \tag{1.27}$$

1.2.4.3 A new numerical method based on strain field

The aim of this numerical method proposed by Upadhyay et. al in [135], is to derive a numerical method based on the strain field to simulate the intensity. They assumed that only the out-of-core compatible elastic strains contributes to the diffraction. The core contributions (including compatible elastic and incompatible elastic and plastic strains) are neglected . The total volume occupied by the dislocation core is very small and would not have a significant effect on the peaks

broadening [1, 43, 136]. Starting from this assumption, they wrote the power series of the differences in displacement $\Delta\mathbf{u}(\mathbf{L})$ and separated this expansion into symmetric components and the anti-symmetric components. Only the symmetric components corresponding to elastic strain gradients are considered. We present below, some successive equations leading to the expression of the intensity. The power series expansion of $\Delta\mathbf{u}(\mathbf{L})$ is :

$$\Delta\mathbf{u}(\mathbf{L}) = \mathbf{u}(\mathbf{x}) + \mathbf{L}.\bigtriangledown\mathbf{u} + \mathbf{L}^2 : \bigtriangledown\bigtriangledown\mathbf{u} + ... - \mathbf{u}(\mathbf{x})$$

The derivation leads to the computation of another expression of the Fourier coefficients, $A^D(\mathbf{L})$ and the intensity as follow :

$$A^D(\mathbf{L}) = \langle cos\left[\frac{2\pi t}{\mid \mathbf{g} \mid}\left(\mathbf{g}_i\mathbf{g}_j\mathbf{u}_{i,j} + \frac{t}{\mid \mathbf{g} \mid}\mathbf{g}_i\mathbf{g}_j\mathbf{g}_k\mathbf{u}_{i,jk}\right)\right]\rangle \tag{1.28}$$

$$I(\mathbf{q}) = \int_{-\infty}^{+\infty}\int_{-\infty}^{+\infty} p_{\varepsilon^L}(\varepsilon^L) exp\left(2\pi i \mid \mathbf{g} \mid \varepsilon^L \mid \mathbf{L} \mid\right) exp\left(2\pi\mathbf{L}.\Delta\mathbf{q}\right) \mathrm{d}\varepsilon^L \mathrm{d} \mid \mathbf{L} \mid . \tag{1.29}$$

To summarize, three different methods for the simulation of the peaks in the vicinity of the diffraction vector are described above.

1.2.4.4 Comparison of previous simulation methods

The accuracy of the simulation methods described above were compared by Upadhyay et. al in [135]. The authors applied the methods in the case of restrictedly random distribution (RRD) of dislocations introduced by Wilkens [154]. To perform this, they considered an infinitely long rectangular cuboid with two square faces subdivided in subdomains. They considered in this domain a set of 32 infinitely long straight screw dislocations with Burgers vector $\mathbf{b} = \pm\frac{1}{2}[110]$ perpendicular to a square face. Dislocations with such a Burgers vector are typically found in f.c.c. materials. Five diffraction vectors were studied and the results of $\mathbf{g} = [11\bar{3}]$ and $\mathbf{g} = [31\bar{3}]$ are reported. Fig1.11, is a comparison between the intensity obtained with the Fourier method using the displacement [150] (Fourier $\Delta\mathbf{u}$), the Fourier based method using the strain field [135] (Fourier ε^L) and the PDF of strain from the Stokes Wilson's approximation [126]. Note that a Gaussian filter was applied to the Fourier coefficients by convoluting the Fourier transform of that Gaussian with the peak shape. This correction could be explained by taking into account the instrumental broadening. It allows to compare the Fourier based method and the Stokes Wilson method.

The plots show that there is an excellent match between the diffraction peaks generated using the Fourier-based methods [150, 135]. These profiles overlap with filtering. According to the authors, this similarity is due to the fact that in this example the product $2\pi\mathbf{g}.n\mathbf{b}$ becomes $2\pi n$ such as the exponential term $exp(2\pi\mathbf{g}.n\mathbf{b})$ does not contributes to the diffraction peaks. More generally, the effect of the scalar product $\mathbf{g}.\mathbf{b}$ on the diffraction peaks is reported and discussed in the literature. This effect is also explained by the contrast factor C. Another important discussion provided in [135] is the effect of the microstructure or in other words the arrangement and the nature of dislocations. In the RRD microstructure used in fig. 1.11, the net Burgers vectors in each subdomain is zero. To study the effect of microstructure, the authors performed other simulations with nonzero net Burgers vector in the subdomains. According to the authors, no effect of the nonzero net Burgers vector could be extrapolated. However, the authors reported differences between the effects of geometrically necessary dislocations and statistically stored dislocation (for RRD) on the simulated diffraction peaks. The conclusion of such simulations is that the analysis of diffraction peaks allows to understand material microstructure.

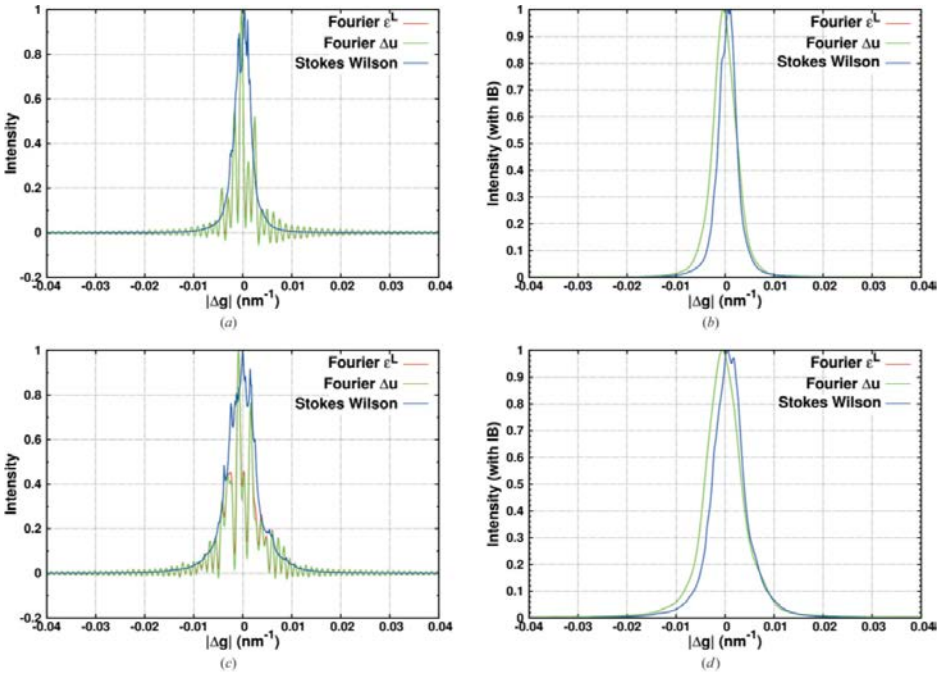


FIGURE 1.11 – Comparison of normalized unfiltered and filtered, i.e. with instrumental broadening (IB), intensity from the Fourier average-strain (Fourier ε^L) and Fourier displacement (Fourier $\mathbf{\Delta u}$) methods, and the PDF of strain from the Stokes Wilson approximation for an RRD of 32 screw dislocations for diffraction vectors (a), (b) $\mathbf{g} = [11\bar{3}]$ and (c), (d) $\mathbf{g} = [31\bar{3}]$

1.2.4.5 Simulation method based on the digital pixel

This approach is proposed in [160]. Their technique allows to generate virtual synthetic diffraction image under *in situ* loading using a pixelization of the detector. The main steps of the method is detailed now :

- Material configuration : the crystal is meshed with finite elements. Material information such as crystal structure, stress, strain are defined for each element. The elements are populated by grid points which have the same material parameters as the element. This grid points define the positions in the crystal.

- Theoretical part : the aim of this part is to use the X-ray diffraction theory to determine the direction of the diffracted beam for a given X-ray wavelength and a lattice plan (hkl). The derivation is not entirely detailed here. Coordinate systems are defined for the crystal, the sample and the laboratory . A vector of the reciprocal lattice in the crystal is connected to the laboratory coordinate system via rotation matrix. For a given X-ray wavelength, the position at which the diffraction occurs for a (hkl) plan is computed in the crystal coordinate system and obtained in the laboratory coordinate system. Then the direction of the diffraction beam is computed in the laboratory coordinate for this X-ray wavelength. Note that a range of X-ray wavelengths is considered to account for the X-ray energy bandwidth. This range is discretized in sufficiently small wavelength step. The position at which the diffraction occurs is computed for each small wavelength step for any (hkl) plane within each element. At the end of this step, all the computed positions are grouped into intervals. Each interval corresponds to a small wavelength step.

-Simulation part : The grid points belonging to an interval are projected on the virtual detector as shown in fig. 1.12a. Each point is projected on the direction of the diffraction beam vector of his element. The diffracted intensity contribution from each element is weighted by the volume of the element. The weighted diffracted intensity contributions from each element are binned into each pixel on the virtual detector and summed up to obtain an intensity value for each pixel, as shown in fig. 1.12b. The final result is presented in fig. 1.12c after application of a detector point spread function.

1.2.4.6 A numerical method to simulate Laue diffraction patterns

This method was proposed in [125, 58]. The aim of this simulation was to record on the detector the position of the different reflection. The map of these reflection will be compared to the experimental results. The principle of the method is illustrated in fig. 1.13. The vector $\mathbf{P}$ on the detector determines the position of the reflection and might be computed. To compute this vector, the authors defined crystal, sample and a laboratory coordinate systems as in the previous section. The sample and the

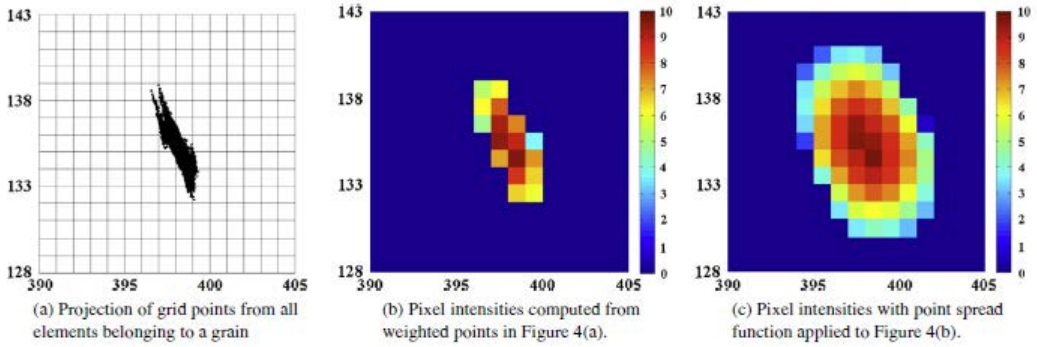


FIGURE 1.12 – Example : computing the diffracted intensity of a synthetic diffraction spot on the virtual detector [160]

laboratory coordinate system are represented in fig. 1.13, (x, y, z) and (d_1, d_2, d_3) respectively. The unit vector $\mathbf{n}_q$ of the diffraction vector is computed in the crystal coordinate system and converted in the sample system using an orientation matrix. Then the diffraction vector $\mathbf{S}$ is computed in lab coordinate using the detector normal vector $\mathbf{n}_D$. The knowledge of $\mathbf{S}$ and $\mathbf{D}$ (which does not change) allow to compute the position vector $\mathbf{P}$. Fig. 1.14 is a comparison between experiments and simulation results obtain for a deformed Nickel. Bertin and Cai [11] applied this method to generate virtual micro Laue X-ray diffraction patterns from discrete dislocation dynamics.

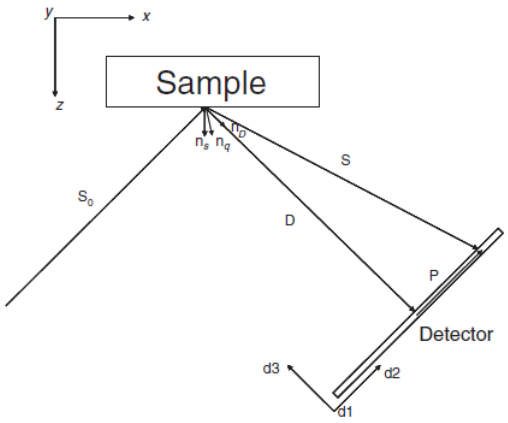


FIGURE 1.13 – Illustration of the setup for 90° reflection Laue experiment [125]

1.2.4.7 Another displacement field method

In reference [141], Vaxelaire et al. proposed another method based on the displacement field. We present here the derivation of this method. They started from

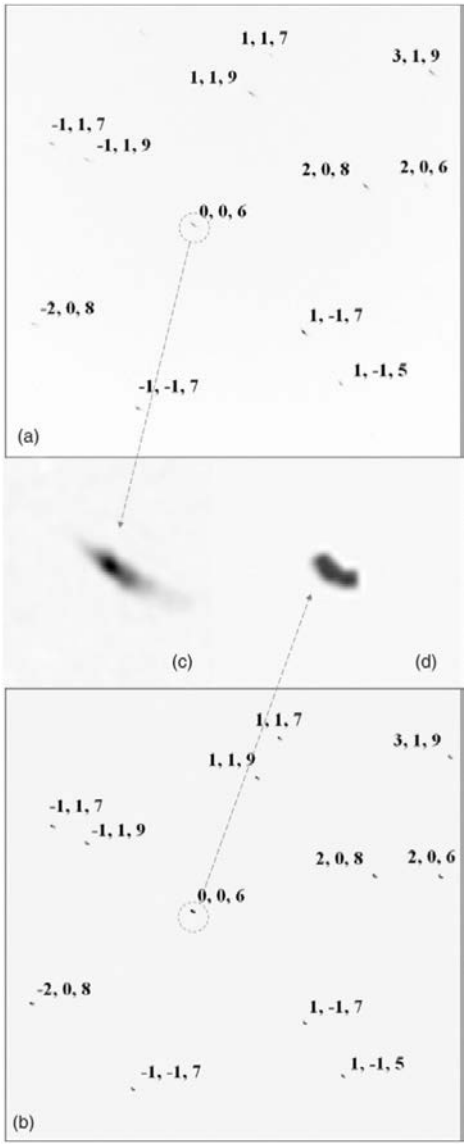


FIGURE 1.14 – (a) Experimental Laue diffraction pattern from 2% plastically deformed Ni. (b) Simulated Laue pattern. (c) *Streaking* of the Laue spot (006) in the experiment. (d) *Streaking* of the Laue spot (006) in the simulation [125]

the expression of the diffracted intensity (see Appendix A, eq. A.11) :

$$I(\mathbf{g}) = \mid \sum f(\mathbf{g}) exp(i2\pi/\lambda)\mathbf{g}\mathbf{r}_m) \mid^2 \tag{1.30}$$

The diffraction vector $\mathbf{g}$ is the reciprocal space's vector so that :

$$\frac{\mathbf{g}}{\lambda} = h\mathbf{b}_1 + k\mathbf{b}_2 + l\mathbf{b}_3$$

where $\mathbf{b}_1$, $\mathbf{b}_2$, $\mathbf{b}_3$ are the reciprocal space unit vectors. Using the same notation as the previous sections, the intensity in the vicinity of the diffraction vector $\mathbf{g}$, defined by the vector $\mathbf{q} = \mathbf{g} + \mathbf{g}_B$ (where $\mathbf{g}_B$ is the exact Bragg's position), is given by [141] :

$$I(\mathbf{q}) = \mid \sum_{xyz} f(\mathbf{g}) exp(i\mathbf{u}(x,y,z).\mathbf{g}) exp(i2\pi(hx + ky + lz)) \mid^2 \tag{1.31}$$

$$I(\mathbf{q}) = \mid FT(f(\mathbf{g}).exp(i\mathbf{g}.\mathbf{u}(\mathbf{x})) \mid^2 \tag{1.32}$$

The displacement field $\mathbf{u}$ is computed by Vaxelaire et al. [141] with the Finite Element Method (FEM). Same method was used by Dupraz et al. [34] to study the signature of dislocations and stacking faults of FCC nanocrystals [34]. However, Dupraz et al. computed the displacement field with atomistic calculations. In next chapter we will use this method with displacement field computed with Fast Fourier Transform (FFT) and eigenstrain method. After the discussion of these methods, we conclude that these implementations need the computation of the displacement field or the strain field.

1.2.5 Conclusions

In this section, we have first summarized X-ray diffraction technique and we described the Three Crystal Diffraction (TCD) and the Double Crystal Diffraction (DCD) set ups. Then, we have reported the X-ray diffraction theory with some basic ingredients given in Appendix A). The analysis of the diffraction peaks to understand the material behavior have been presented and some analysis program used by several authors have been discussed : the Fourier transform method or the moment method. In order to complete the experimental technique, the X-ray diffraction peak profiles were simulated and we present in this first chapter some methods to generate such virtual peaks. It appears that these simulation methods need the computation of the mechanical fields such as the strain or the displacement. In the next section, we will focus on the computation of mechanical fields using the FFT-based method with a non extensive literature review algorithms.

1.3 FFT-based method for computed mechanical fields

1.3.1 Introduction and advantage of the numerical method

Numerical modeling of in-situ X-ray diffraction diagrams requires the computation of mechanical fields (displacements or strains) with high accuracy and less computational times. The displacement or the strain field will be the input data for the diffraction pattern simulation [141, 135]. These mechanical fields are obtained by solving the fields equations for heterogeneous composite materials undergoing macroscopic loading and containing different distributions of defects (such as dislocations, cracks ...) or containing stress free strain fields (usually called eigenstrains). This numerical resolution was essentially performed using the finite element method. The Finite element method is based on the meshing of a representative volume element of the solid. These methods are widely used by scientists because they allow to compute numerically the behavior of even very complex microstructure and boundary value problems provided that they are continuous and described by linear or non linear partial differential equations. They are used to solve homogeneous and heterogeneous problems in linear or non linear elasticity, for polycrystals [93, 24, 116, 19]. In the case of polycrystals, the large number of degrees of freedom could reduce the size of the microstructure simulated with the Finite element method. In general, the implementation of the finite element method can be complex (difficulty of making a suitable mesh for some microstructures containing discontinuities like dislocations...), and expensive in computing time (for fine meshes) and memory.

In most cases, it is possible to transform the micromechanical models equations written in time domain into the frequency domain and try to solve them explicitly. With this transformation, one introduces a frequency variable instead of the temporal variable and equations resolution is simpler : for example a partial derivative becomes a simple product of function in the frequency domain. The solutions in the time domain are obtained by making an inverse transformation. Different transformations can be used but the most known transformations are : the Fourier transform and the Laplace transform. Among these computational methods, the Fourier transform is the most adapted and the most used for the resolution of several problems of mechanics because the inverse of Laplace transform is more difficult to compute. Fourier transforms based methods received a surge of interest these last decades in mechanics of materials thanks to the development and availability of FFT (Fast Fourier Transform) packages [44] (FFTW,...).

During the last decades, these numerical algorithms based on the Fast Fourier

Transform (FFT) have been developed since the pioneering work of Moulinec and Suquet [98, 99] because this spectral approach has many advantages : first, the computation time is low compared to the FEM method, the CPU time for as FFT varies a $N.logN$ [99, 107] whereas it is N^2 for FEM (N is the resolution). Second it is possible to evaluate the local and overall responses of complex microstuctures (composite materials, polycrystals) directly from pixelized/voxelized digitalized microstructures in contrast with the FEM method which needs a more or less complicated meshing procedure of the microstructure [74, 76, 73]. Another positive aspect is that the implementation of the FFT to solve linear elastic heterogeneous problems with eigenstrains is straightforward [60, 3, 101, 33]. Fig1.15 [107], shows the distribution of the accumulated plastic deformation fields and the stress fields obtained by FFT (Fig1.15 (a) and (c)) and by FE (Fig1.15 (b) and (d)) in a aluminum polycrystal submitted to rolling and containing 100 grains [107]. The polycrystal unit cell is discretized in $32 \times 32 \times 32$ voxels. The same precision is noted in both approaches, but the calculation times are 3 hours for the FFT simulation and 5 days for the FEM. These comparisons were performed on an Intel® Xeon® machine equipped with 8 processors and 16 GB of shared memory. Another advantage of this method is that it discretization allows to use directly images of microstructure obtained by scanning electron microscopy (SEM), X-ray tomography...

1.3.1.1 Linear heterogeneous problems

In mechanics of materials, FFT-based methods were initially introduced in heterogeneous linear elasticity for the numerical resolution of the so called Lippmann-Schwinger equation that couples the stress equilibrium equation, strain compatibility and the linear elastic constitutive laws. The solutions are obtained from the spatial convolution of the Green operator with a polarization stress field which contains the information on the heterogeneity and / or the non-linearity of the material. The stress, strain and displacement fields are denoted $\boldsymbol{\sigma}$, $\boldsymbol{\varepsilon}$ and $\mathbf{u}$ respectively. The elastic stiffness tensor at each position vector $\mathbf{x}$ in the unit cell is denoted $\mathbf{C}(\mathbf{x})$.

In the unit cell, the stress equilibrium is written in indicial form :

$$\sigma_{ij,j}(\mathbf{x}) = 0 \tag{1.33}$$

The strain compatibility equation involved is written in indicial form using the strain/displacement relationship :

$$\varepsilon_{ij}(\mathbf{x}) = \frac{1}{2}(u_{i,j}(\mathbf{x}) + u_{j,i}(\mathbf{x})) \tag{1.34}$$

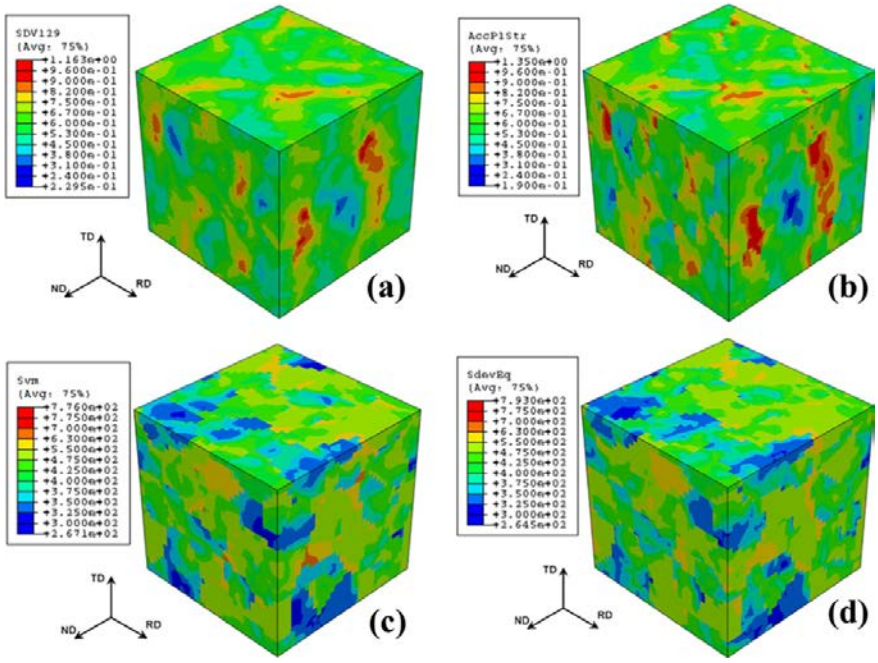


FIGURE 1.15 – Results of simulations of the rolling of an aluminum polycrystal containing 100 grains and discretized in 32×32×32 elements (voxels in the case of the FFT). Left : distributions of accumulated plastic deformations (a) and stresses (c) obtained by FFT. On the right : distributions of accumulated plastic deformations (b) and stresses (d) obtained by FE. Comparisons were made on the same scale, only the maximum and minimum values differ. Calculation times are 3 hours for the FFT and 5 days for the FE method [107].

The linear Hooke's law is rewritten in indicial form :

$$\sigma_{ij}(\mathbf{x}) = C^o_{ijkl}\varepsilon_{kl}(\mathbf{x}) + \tau_{ij}(\mathbf{x}) \tag{1.35}$$

τ_{ij} is the stress polarization tensor defined as :

$$\tau_{ij}(\mathbf{x}) = \delta C_{ijkl}(\mathbf{x})\varepsilon_{kl}(\mathbf{x}) \tag{1.36}$$

where δC_{ijkl} is the fluctuation of the elastic stiffness tensor with respect to a linear homogeneous elastic medium with elastic stiffness $\mathbf{C}^o$: $\delta\mathbf{C}(\mathbf{x}) = \mathbf{C}(\mathbf{x}) - \mathbf{C}^o$. By assuming periodic boundary conditions, the local strain field is defined as a sum of its average value $\mathbf{E}$ and a fluctuation term (see Moulinec and Suquet [99]) :

$$\begin{aligned} \boldsymbol{\varepsilon}(\mathbf{u}(\mathbf{x})) &= \mathbf{E} + \boldsymbol{\varepsilon}(\mathbf{u}^*(\mathbf{x})) \\ \mathbf{u}(\mathbf{x}) &= \mathbf{u}^*(\mathbf{x}) + \ \mathbf{E}.\mathbf{x} \end{aligned} \tag{1.37}$$

The fluctuation field $\mathbf{u}^*(\mathbf{x})$ is assumed to be periodic and the traction vector $\boldsymbol{\sigma}.\ \mathbf{n}$ is assumed to be anti-periodic. With this periodic boundary conditions, the fields equations can be written in the Fourier space. The Fourier vector is denoted $\boldsymbol{\xi}$ and the Fourier transform of a function f in the Fourier space is written $\hat{f}$. i is the complex imaginary unit : $\mathrm{i} = \sqrt{-1}$. Eq. 1.33 and eq. 1.35 are written respectively in the Fourier space :

$$\mathrm{i}\xi_j \widehat{\sigma}_{ij}(\widehat{\boldsymbol{\xi}}) = 0 \tag{1.38}$$

$$\widehat{\sigma}_{ij}(\boldsymbol{\xi}) = C^o_{ijkl}\widehat{\varepsilon}_{kl}(\boldsymbol{\xi}) + \widehat{\tau}_{ij}(\boldsymbol{\xi}) \tag{1.39}$$

Using the Fourier transform of eq. 1.34 and the symmetry of $\widehat{\varepsilon}_{kl}$ and C^o_{ijkl} eq. 1.38 becomes :

$$\xi_j\xi_l C^o_{ijkl}\widehat{u}^*_k(\boldsymbol{\xi}) = \mathrm{i}\xi_j\widehat{\tau}_{ij}(\boldsymbol{\xi}) \qquad for \qquad \boldsymbol{\xi} \neq 0 \tag{1.40}$$

Following Mura [104], we can introduce the Christoffel (also called acoustic tensor) matrix $K_{ik} = C^o_{ijkl}\xi_j\xi_l$. Then, introducing this matrix and making inversion, one gets :

$$K_{ik}(\boldsymbol{\xi})\widehat{u}^*_k(\boldsymbol{\xi}) = \mathrm{i}\xi_j\widehat{\tau}_{ij}(\boldsymbol{\xi}) \tag{1.41}$$

$$\widehat{u}^*_i(\boldsymbol{\xi}) = \frac{N_{ij}(\boldsymbol{\xi})}{D(\boldsymbol{\xi})}X_j(\boldsymbol{\xi}) \tag{1.42}$$

where $N_{ij}(\boldsymbol{\xi}) = N_{ji}(\boldsymbol{\xi})$ and $D(\boldsymbol{\xi})$ are respectively the cofactor matrix and the determinant of $K_{ij}(\boldsymbol{\xi})$, and $X_j(\boldsymbol{\xi}) = \mathrm{i}\xi_k\widehat{\tau}_{jk}(\boldsymbol{\xi})$

For anisotropic homogeneous media, it is shown that [104] :

$$\begin{aligned} N_{ij}(\boldsymbol{\xi}) &= \frac{1}{2}\epsilon_{ikl}\epsilon_{jmn}K_{km}K_{ln} \\ D(\boldsymbol{\xi}) &= \epsilon_{mnl}K_{m1}K_{n2}K_{l3} \end{aligned} \tag{1.43}$$

where ϵ_{ikl} is the permutation tensor. For isotropic solids defined by the Lamé modulus λ^o and the shear modulus μ^o , the expression of $N_{ij}(\boldsymbol{\xi})$ and $D(\boldsymbol{\xi})$: are

simplified as ($\xi^2 = \xi_i\xi_i$) :

$$\begin{aligned} N_{ij}(\boldsymbol{\xi}) &= \mu^o\xi^2\left((\lambda^o + 2\mu^o)\delta_{ij}\xi^2 - (\lambda^o + \mu^o)\xi_i\xi_j\right) \\ D(\boldsymbol{\xi}) &= \mu^{o2}(\lambda^o + 2\mu^o)\xi^6 \end{aligned} \tag{1.44}$$

Note that the $N_{ij}(\boldsymbol{\xi})$ is homogeneous function of degree 4, and $D(\boldsymbol{\xi})$ is homogeneous function of degree 6, therefore the Green function defines as $G_{ij}(\boldsymbol{\xi}) = \frac{N_{ij}(\boldsymbol{\xi})}{D(\boldsymbol{\xi})}$ is a homogeneous function of degree -2.

Using now eq. 1.34, and transform it in the Fourier space leads to :

$$\begin{aligned} \widehat{\epsilon}_{ij} &= \mathrm{i}\frac{1}{2}(\xi_j\widehat{\mathbf{u}}_i^*(\boldsymbol{\xi}) + \xi_j\widehat{\mathbf{u}}_j^*(\boldsymbol{\xi})) && \boldsymbol{\xi} \neq 0 \\ \widehat{\varepsilon}_{ij} &= E_{ij} && \boldsymbol{\xi} = 0 \end{aligned} \tag{1.45}$$

Introducing eq. 1.41 into eq. 1.45 yields :

$$\begin{aligned} \widehat{\varepsilon}_{ij}(\boldsymbol{\xi}) &= -\widehat{\Gamma}_{ijkl}\widehat{\tau}_{kl}(\boldsymbol{\xi}) && \boldsymbol{\xi} \neq 0 \\ \widehat{\varepsilon}_{ij} &= E_{ij} && \boldsymbol{\xi} = 0 \end{aligned} \tag{1.46}$$

where $\widehat{\boldsymbol{\Gamma}}$ is the Fourier transform of the modified Green operator $\boldsymbol{\Gamma}$ and is defined as :

$$\widehat{\Gamma}_{ijkl}(\boldsymbol{\xi}) = \frac{1}{4}\left(\frac{N_{ik}(\boldsymbol{\xi})}{D(\boldsymbol{\xi})}\xi_j\xi_l + \frac{N_{jk}(\boldsymbol{\xi})}{D(\boldsymbol{\xi})}\xi_i\xi_l + \frac{N_{il}(\boldsymbol{\xi})}{D(\boldsymbol{\xi})}\xi_j\xi_k + \frac{N_{jl}(\boldsymbol{\xi})}{D(\boldsymbol{\xi})}\xi_i\xi_k\right) \tag{1.47}$$

In the case of isotropic homogeneous medium, $\widehat{\boldsymbol{\Gamma}}$ reads :

$$\widehat{\Gamma}_{ijkl}(\boldsymbol{\xi}) = \frac{1}{4\mu^o\xi^2}\left(\delta_{ik}\xi_j\xi_l + \delta_{il}\xi_j\xi_k + \delta_{jk}\xi_i\xi_l + \delta_{jl}\xi_i\xi_k\right) - \frac{(\lambda^o + \mu^o)}{\mu^o(\lambda^o + \mu^o)}\frac{\xi_i\xi_j\xi_k\xi_l}{\xi^4} \tag{1.48}$$

Note that the equation obtained in eq. 1.46 is the co-called Lippmann-Schwinger equation [72]. The previous development were is made in the Fourier space. Note

that this equation leads to an integral equation in the real space because the stress polarization field is function of the strain field, therefore it resolved using numerical algorithm. The advantage of using the Fourier method is that the spatial (non local) convolution becomes a local product in the Fourier space which is easy to solve using iterative algorithm and FFT.

1.3.1.2 Spatial and Fourier discretization

In order to solve Eq. 1.46, a spectral method based on the voxelization of the miscrostrucutre is used. The unit cell is then defined by 2D or 3D images and independent mechanical properties are assigned to each image. Thus each image can define individually one phase of the composite material but in most applications, a limited number of phases is used. The different local mechanical fields are computed along each image.
The Discrete Fourier Transform (DFT) method is used. The unit cell with volume Ω is discretized into a regular grid of $N_1 \times N_2$ pixels in 2D problems or $N_1 \times N_2 \times N_3$ voxels in 3D problems. For 3D applications, the voxel coordinates are [99] :

$$\mathbf{x}_d(i_1, i_2, i_3) = \left((i_1 - 1)\frac{T_1}{N_1}, (i_2 - 1)\frac{T_2}{N_2}, (i_3 - 1)\frac{T_3}{N_3}\right),$$

with

$$i_1 = 1, ...N_1 \quad i_2 = 1, ...N_2 \quad i_3 = 1, ...N_3$$

and T_i denotes the period of the unit cell in the i^{th} direction.

The discrete frequencies in Fourier space are given by :

$$\xi_i = (-\frac{N_i}{2} + 1)\frac{1}{T_i}, (-\frac{N_i}{2} + 2)\frac{1}{T_i}, ..., -\frac{1}{T_i}, 0, \frac{1}{T_i}, ..., (\frac{N_i}{2} - 1)\frac{1}{T_i}, (\frac{N_i}{2})\frac{1}{T_i}$$

if N_i is even and

$$\xi_i = -\frac{N_i - 1}{2}\frac{1}{T_i}, ..., -\frac{1}{T_i}, 0, \frac{1}{T_i}, ..., \frac{N_i - 1}{2}\frac{1}{T_i}$$

if N_i is odd.

1.3.1.3 Numerical resolution

The iterative algorithm to resolve the Lippmann-Shwinger equation was first proposed by Moulinec and Suquet [98, 99] for a given macroscopic strain field $\mathbf{E}$. In the initialization part, the strain field is equal to $\mathbf{E}$ at all point ($\mathbf{x}_d$) of the real space and an initial stress field is computed at theses points. In the iteration part,

the Lippmann-Schwinger equation is resolved at each point with direct and inverse Fourier transform to switch between real and Fourier space. This basic algorithm is completely described in Algorithm 1 for linear elastic and heterogeneous materials.

Algorithm 1 Classic algorithm proposed by Moulinec and Suquet for a periodic material submitted to a prescribed strain $\mathbf{E}$

Initialization : (given $\mathbf{E}$)

1: $\boldsymbol{\varepsilon}^o(\mathbf{x}_d) = \mathbf{E}$

2: $\boldsymbol{\sigma}^o(\mathbf{x}_d) = \mathbf{C}(\mathbf{x}_d) : \boldsymbol{\varepsilon}^o(\mathbf{x}_d), \quad \forall \mathbf{x}_d \in \Omega$

Iteration : $i+1$ ($\boldsymbol{\varepsilon}^i(\mathbf{x}_d)$ and $\boldsymbol{\sigma}^i(\mathbf{x}_d)$ known)

3: $\widehat{\boldsymbol{\sigma}}^i$ =FFT($\boldsymbol{\sigma}^i$),

4: Convergence test,

5: $\widehat{\boldsymbol{\varepsilon}}^{i+1}(\boldsymbol{\xi}) = \widehat{\boldsymbol{\varepsilon}}^i(\boldsymbol{\xi}) - \widehat{\boldsymbol{\Gamma}}(\boldsymbol{\xi}) : \widehat{\boldsymbol{\sigma}}^i(\boldsymbol{\xi}) \quad \forall (\boldsymbol{\xi}) \neq 0, \qquad \widehat{\boldsymbol{\varepsilon}}^{i+1}(0) = \mathbf{E}$

6: $\boldsymbol{\varepsilon}^{i+1}$ =FFT$^{-1}(\widehat{\boldsymbol{\varepsilon}}^{i+1})$

7: $\boldsymbol{\sigma}^{i+1}(\mathbf{x}_d) = \mathbf{C}(\mathbf{x}_d) : \boldsymbol{\varepsilon}^{i+1}(\mathbf{x}_d), \forall \mathbf{x}_d \in \Omega$

Note that at step 5 in this algorithm, the following property of the modified Green operator is used (due to the strain compatibility) :

$$\boldsymbol{\Gamma} * (\mathbf{C}^o : \boldsymbol{\varepsilon}) = \boldsymbol{\varepsilon}$$

This iterative algorithm stops when a defined convergence criterion is achieved (step 4) : a discrete error is computed at this step and is compared to the fixed precision and the algorithm stops when the discrete error is smaller than this precision. In the classical algorithm, the convergence criterion is based on the Fourier transform of the stress field computed at step (3) and the discrete error reads (the symbol $||\ .\ ||$ denotes the Euclidian norm of a second-order tensor) :

$$e_{stress} = \frac{\left(\frac{1}{N}\sum || \ (\boldsymbol{\xi}).\widehat{\boldsymbol{\sigma}}^i(\boldsymbol{\xi}) \ ||^2\right)^{\frac{1}{2}}}{|| \ \widehat{\boldsymbol{\sigma}}^i(\mathbf{0}) \ ||}$$

Many mechanical problems were resolved using this basic algorithm including non linear problems [99].

1.3.1.4 Extension to non linear elastic plastic behavior

The basic algorithm described in the previous section was extended to non linear behavior. In order to integrate non linearity, the step 7 of algo. 1 must be modified.

An incremental elastic-plastic behavior at small strain governed by a J_2-flow theory with isotropic hardening was considered in [99, 127, 96, 23]

$$\dot{\boldsymbol{\sigma}} = \mathbf{C} : (\dot{\boldsymbol{\varepsilon}} - \dot{\boldsymbol{\varepsilon}}^p) \tag{1.49}$$

$\boldsymbol{\varepsilon}^p$ denoted the plastic strain. The constitutive law in eq. 1.49 is integrated using discretization of the time interval into $[t_n, t_{n+1}]$. The field equation are solved for $(\boldsymbol{\varepsilon}_n, \boldsymbol{\sigma}_n, p_n)$ at time t_n. At step $n+1$, the input date is $\boldsymbol{\varepsilon}^o(\mathbf{x}_d)$ compute with eq. 1.50 . At this step the unknown $\boldsymbol{\varepsilon}_{n+1}$ is computed. The numerical algorithm described in algo. 2 is run in the step $n+1$ to determine $\boldsymbol{\varepsilon}_{n+1}$.

$$\boldsymbol{\varepsilon}^o(\mathbf{x}_d) = \boldsymbol{\varepsilon}_n(\mathbf{x}_d) + \frac{t_{n+1} - t_n}{t_n - t_{n-1}}(\boldsymbol{\varepsilon}_n - \boldsymbol{\varepsilon}_{n-1}) \tag{1.50}$$

Algorithm 2 Extension of the basic algorithm proposed by Moulinec and Suquet to non linear behavior [99]

Initialization : (given $\mathbf{E}$)

1: $\boldsymbol{\varepsilon}^o(\mathbf{x}_d)$ given by eq.
2: *compute* $\boldsymbol{\sigma}^o(\mathbf{x}_d)$ and $p^o$from$(\boldsymbol{\varepsilon}^o, \boldsymbol{\sigma}_n, \boldsymbol{\varepsilon}_n, p_n)$

Iteration : $i+1$ ($\boldsymbol{\varepsilon}^i(\mathbf{x}_d)$ and $\boldsymbol{\sigma}^i(\mathbf{x}_d)$ known)

3: $\widehat{\boldsymbol{\sigma}}^i$ =FFT$(\boldsymbol{\sigma}^i)$,
4: Convergence test,
5: $\widehat{\boldsymbol{\varepsilon}}^{i+1}(\boldsymbol{\xi}) = \widehat{\boldsymbol{\varepsilon}}^i(\boldsymbol{\xi}) - \widehat{\boldsymbol{\Gamma}}(\boldsymbol{\xi}) : \widehat{\boldsymbol{\sigma}}^i(\boldsymbol{\xi}) \quad \forall(\boldsymbol{\xi}) \neq 0, \qquad \widehat{\boldsymbol{\varepsilon}}^{i+1}(0) = \mathbf{E}^{i+1}$
6: $\boldsymbol{\varepsilon}^{i+1}$ =FFT$^{-1}(\widehat{\boldsymbol{\varepsilon}}^{i+1})$
7: compute $\boldsymbol{\sigma}^{i+1}$ and p^{i+1} from $(\boldsymbol{\varepsilon}^{i+1}, \boldsymbol{\sigma}_n, \boldsymbol{\varepsilon}_n, p_n)$

1.3.1.5 Applications

Application to thermo-elastic (eigenstrain) problems

For all these advantages, FFT-based methods have been used to solve different problems. First these algorithms were used to compute mechanical fields and properties for linear elastic composites [99, 128, 67]. Usually the defects present in materials are modeled by a stress-free strain (called eigenstrain), which can be computed using discrete Fourier transform [102]. The stresses and strains due to this eigenstrain were computed using formal solutions based on continuous or discrete Fourier transforms [103, 33, 59, 147, 88]. FFT algorithms allow also to compute mechanical fields due to eigenstrains. In [3], the authors studied the mechanical behavior of a heterogeneous

material subjected to a thermal strain tensor. This eigenstrain is given by :

$$\varepsilon^*_{ij}(\mathbf{x}) = \alpha_{ij}(\mathbf{x})(T - T_0)$$

where the second-rank tensor α_{ij} denotes the thermal expansion coefficients and $(T - T_0)$ is the temperature change. Taking into account the eigenstrain field in the material modifies, the derivations of section 1.3.1.1, especially the expression of the stress polarization tensor, which becomes :

$$\tau_{ij}(\mathbf{x}) = \delta C_{ijkl}(\mathbf{x})\varepsilon_{kl}(\mathbf{x}) - C_{ijkl}(\mathbf{x})\varepsilon^*_{kl}(\mathbf{x}) \tag{1.51}$$

In order to take into account this eigenstrain, the authors modified the classic algorithm proposed by Moulinec and Suquet [98, 99] (see algo.1). The value of the eigenstrain defined in a part of the material is assigned to voxels of this region at the beginning of the algorithm. Their iterative fixed-point algorithm for heterogeneous elastic materials with eigenstrains and for macroscopic stress-free states is described below (Algorithm 3) following the "thermoelastic FFT"-based method [3] :

Algorithm 3 Classic algorithm proposed by [3] for heterogeneous elastic materials with eigenstrains (or thermal strains)

Initialization : ($\boldsymbol{\varepsilon}^*(\mathbf{x}_d)$ known)

1: $\mathbf{E}^{(0)} = \langle \boldsymbol{\varepsilon}^*(\mathbf{x}_d) \rangle$
2: $\boldsymbol{\varepsilon}^o(\mathbf{x}_d) = \mathbf{E}^{(0)} \quad \forall \mathbf{x}_d \in \Omega$
3: *Compute* $\widehat{\mathbf{\Gamma}}(\xi_j) \quad \forall \xi_j$

Iteration : $i+1$ ($\boldsymbol{\varepsilon}^i(\mathbf{x}_d)$ *and* $\mathbf{E}^i$ known)

4: $\boldsymbol{\tau}^{i+1}(\mathbf{x}_d) = \delta\mathbf{C}(\mathbf{x}_d) : \boldsymbol{\varepsilon}^i(\mathbf{x}_d) - \mathbf{C}(\mathbf{x}_d) : \boldsymbol{\varepsilon}^*(\mathbf{x}_d)$
5: $\widehat{\boldsymbol{\tau}}^{i+1}(\xi_j) = FFT(\boldsymbol{\tau}^{i+1}(\mathbf{x}_d))$
6: $\boldsymbol{\varepsilon}^{i+1}(\mathbf{x}_d) = \mathbf{E}^i - FFT^{-1}(\widehat{\mathbf{\Gamma}}(\xi_j) : \widehat{\boldsymbol{\tau}}^{i+1}(\xi_j))(\mathbf{x}_d))$
7: $\boldsymbol{\sigma}^{i+1}(\mathbf{x}_d) = \mathbf{C}(\mathbf{x}_d) : (\boldsymbol{\varepsilon}^{i+1}(\mathbf{x}_d) - \boldsymbol{\varepsilon}^*(\mathbf{x}_d))$,
8: $\mathbf{E}^{i+1} = \langle \boldsymbol{\varepsilon}^{i+1}(\mathbf{x}_d) \rangle - \mathbf{C}^{o^{-1}}(\mathbf{x}_d) : \langle \boldsymbol{\sigma}^{i+1}(\mathbf{x}_d) \rangle$
9: Convergence test

The symbol $\langle . \rangle$ indicates a volume average over the unit cell. At step (e), the macroscopic strain field is iteratively adjusted [92, 3]. Unlike the basic algorithm, the convergence criterion to stop the iterative procedure is defined on the strain field (step (f)). In that case, the numerical error reads :

$$e_{strain} = \frac{\langle || \boldsymbol{\varepsilon}^{i+1}(\mathbf{x}_d) - \boldsymbol{\varepsilon}^i(\mathbf{x}_d) || \rangle}{|| \mathbf{E}^{i+1} ||} \tag{1.52}$$

Using this modified algorithm, the authors computed the stress field in a unit cell containing a heterogeneous inclusion and made comparisons with Eshelby's analytical result. The mechanical contrast is defined by $R = K_m/K_i = 2$. The stress field along a center line parallel to x-axis is shown on fig. 1.16.

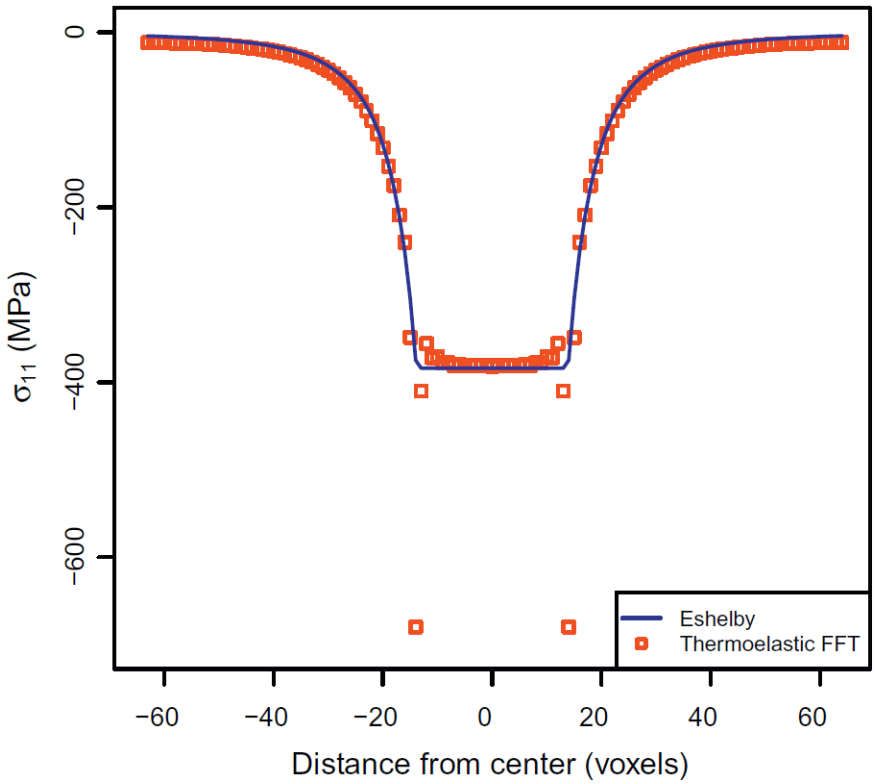


FIGURE 1.16 – Stress field along a center line parallel to x-axis due to a dilatational eigenstrain contained in a spherical inclusion. The resolution is $128 \times 128 \times 128$ with 14 voxel radius. The dangling voxels leads to a large deviations at the interface between inclusion and matrix [3]

The value of the stress field in the inclusion is compared to the Eshelby theoretical result. The FFT method gives a value equal to $-375MPa$ while the Eshelby solution gives $-375.4MPa$. This corresponds to an error of about 0.1%. Thus the shape of stress fields given by both methods are similar. This allowed authors to conclude that FFT algorithms are efficient methods to compute mechanical fields ie interior and exterior Eshelby tensors. Another aspect of this method discussed in this paper is the effect of dangling voxels. In the case of a spherical inclusion, one defines dangling voxels as voxels located at the pole of the inclusion and having only one nearest-neighbor voxel belonging to the inclusion. This singularity appears when the used resolution is not important. The consequence is a large error due to the voxelization in the predictions of the mechanical fields using FFT algorithm as shown in figure 1.17. One note a local error about 50% near the interface where the dangling voxels are located. This effect can be avoided using a more important

resolution as in Fig1.17.

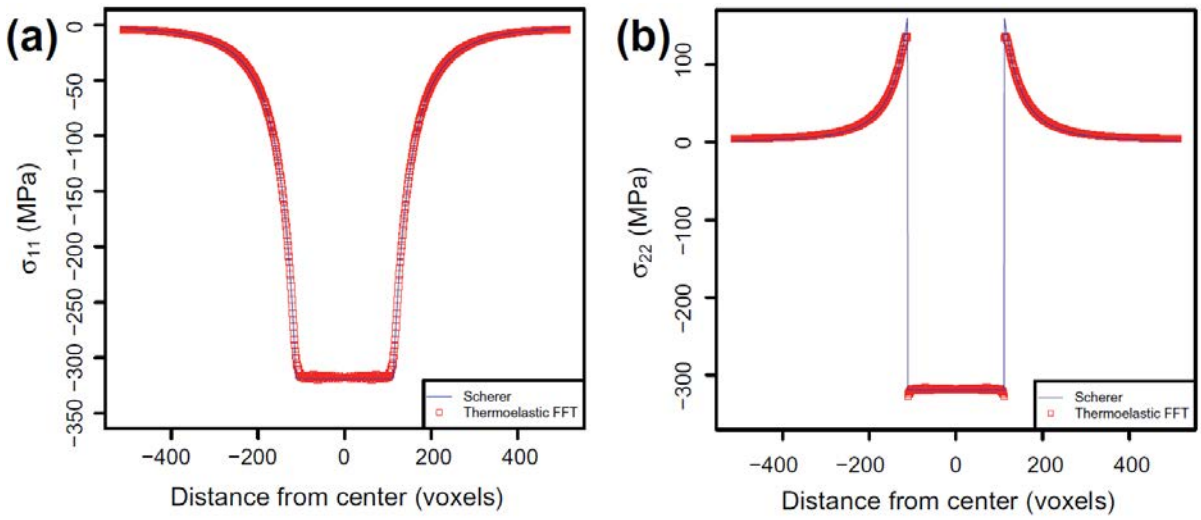


FIGURE 1.17 – Stress field along a center line parallel to x-axis due to a dilatational eigenstrain contained in a spherical inclusion. (a) the component σ_{11} and (b)σ_{33}. The resolution is $1024 \times 1024 \times 1024$ with 14 voxel radius [3].

In thermoelasticity, Donegan et al [32] used the FFT-based method and algo. 3 to develop a numerical method to resolve thermoelastic problems and compute residual stresses and strains in heterogeneous polycrystals.

Application to Discrete Dislocation Dynamics (DDD)

The eigenstrain formalism was also used in Discrete Dislocation Dynamics (DDD) which describes discrete dislocation motion using the Peach Koehler force[81]. Based on this work and taking advantage from FFT-based algorithms, Bertin et al [12] proposed a full-field stress-strain computational approach denoted DDD-FFT. In this paper, the authors showed that the DDD-FFT is very efficient for simulating plasticity of homogeneous isotropic and anisotropic materials. One of the most advantages of this approach is the gain in computational time with respect to regular DDD approach. Fig. 1.18 [12] is a comparison between the DDD-FFT and the regular DDD regarding computational cost. The computational time is reduced with the proposed approach. The FFT-based approach proposed in reference [11] is an extension of the DDD-FFT.

In reference [49], the authors proposed a formalism of dislocation dynamics in

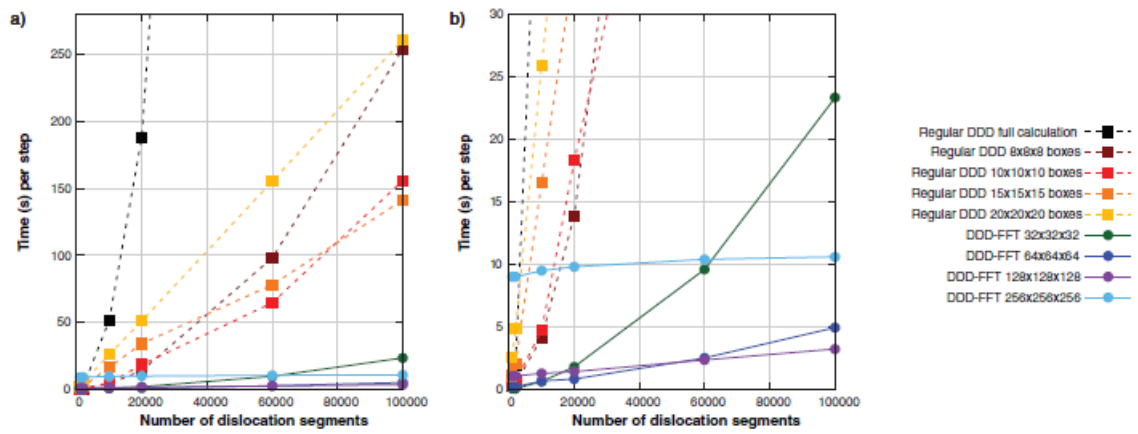


FIGURE 1.18 – Comparison of the computational cost between regular DDD method and the DDD-FFT approach [12].

which discrete dislocations are represented by eigenstrain for the computation of the stress field. Their method includes effects on anisotropy on dislocation iterations. They also modeled inclined discrete dislocations. The modeling of such dislocations often leads to aliasing effects (spurious oscillations appear on the computed mechanical fields near discontinuities like dislocations). In order to avoid this effect, the authors proposed a suitable algorithm to represent the dislocations pairs on the FFT grid. The entire details of this algorithm is not presented here but fig. 1.19 is a schematic view of the principle of this algorithm. Fig. 1.19a represents a pair of dislocation on FFT grid. Fig. 1.19b is a possible corresponding representation with uniform eigenstrain value at each adjacent voxel (pixel in the figure). Fig. 1.19c described the representation proposed by the authors to avoid aliasing effect. The value of the eigenstrain at the adjacent voxels are determined using the anti-aliasing algorithm described in [49, 161].

Application to Field Dislocation Mechanics (FDM)

Field dislocation mechanics (FDM) and field disclination mechanics are among micromechanical domains in which FFT-based received a surge of interest specially in LEM3. Using a spatial distribution of Nye's dislocation density tensor [105] in a periodic medium, many authors developed a numerical scheme to resolve different problems with dislocations, disclinations or defects. In [6], the authors proposed a spectral approach to solve the elasto-static equations. They used a continuous representation of crystal defects (dislocations or disclinations) in contrast with Volterra [145] discrete representation. With this description, the Burgers vector $\mathbf{b}$ of the dislocation representing it strength, is equal to the integral of the Nye's tensor field $\boldsymbol{\alpha}$

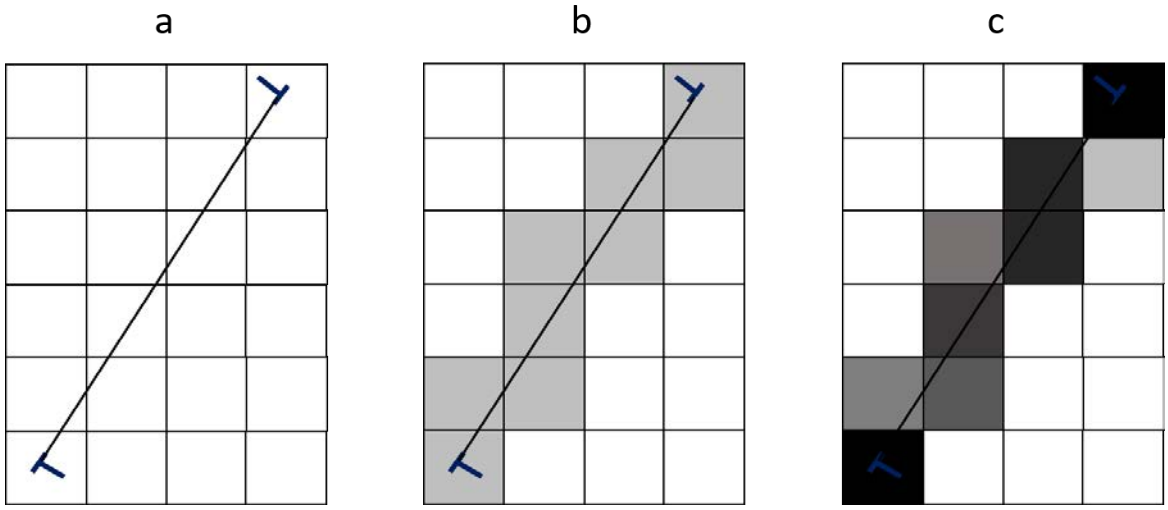


FIGURE 1.19 – Schematic view of the representation of a pair of dislocations on a FFT grid [49]

over appropriate surface patches S with unit normal $\mathbf{n}$:

$$\begin{aligned} \boldsymbol{\alpha} &= \mathbf{curl}\mathbf{U}_e \\ \mathbf{b} &= \int_S \boldsymbol{\alpha}.\mathbf{n}\mathrm{d}S \end{aligned} \tag{1.53}$$

where $\mathbf{U}_e$ is the elastic distortion field. Field equations with FDM contains both Poisson equation or Navier equation (or Lippmann Schwinger equation). The resolution of these equations with spectral methods based on FFT and on Stokes Helmholtz classic decomposition allows to compute compatible and incompatible fields. The spectral method was tested through some examples. Fig1.20 [6, 31] is a 2D map of shear stresses due to a single screw dislocation density. The FFT results were compared to the FE results using linear elements. It is observed, from this example and other applications in this paper, that both FFT FDM theory and FEM solutions are very efficient in computing the elastic fields of dislocations. However, the FFT method is rather attractive in terms of computation time. For the previous application, the CPU time with the FFT method is 6.3 s. It reaches 20 min with the FE method. The same authors developed in[7] a FFT-based method to compute stress and couple stress fields in a homogeneous linear higher order elastic media for a given a spatial distribution of generalized disclination density tensors. Another similar contribution is the spectral approach proposed in [29] to solve the hyperbolic dislocation density transport equation governing the spatio-temporal evolution of the dislocation density tensor with the use of low-pass exponential filter. Compa-

rison of numerical results with analytic solutions or finite element solutions showed the accuracy and stability of the FFT solutions.

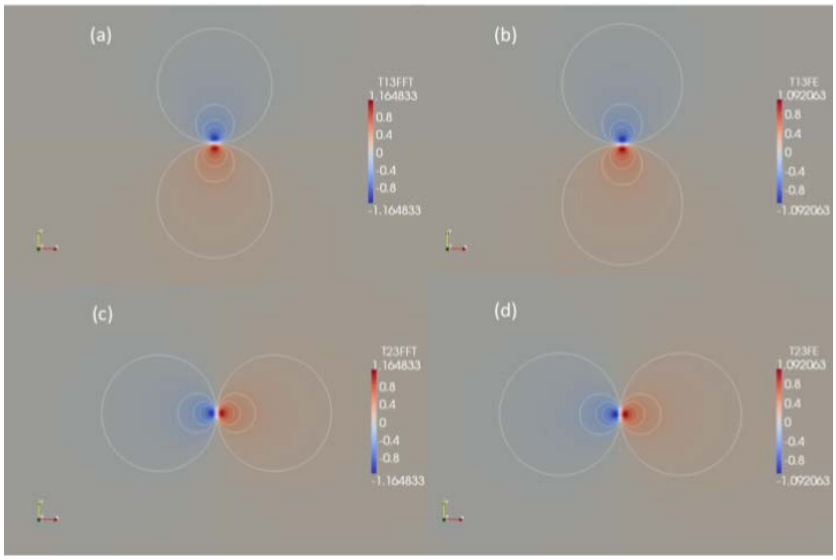


FIGURE 1.20 – Comparisons of the shear stress contours for a screw dislocation calculated with static FFT FDM and with static FEM FDM

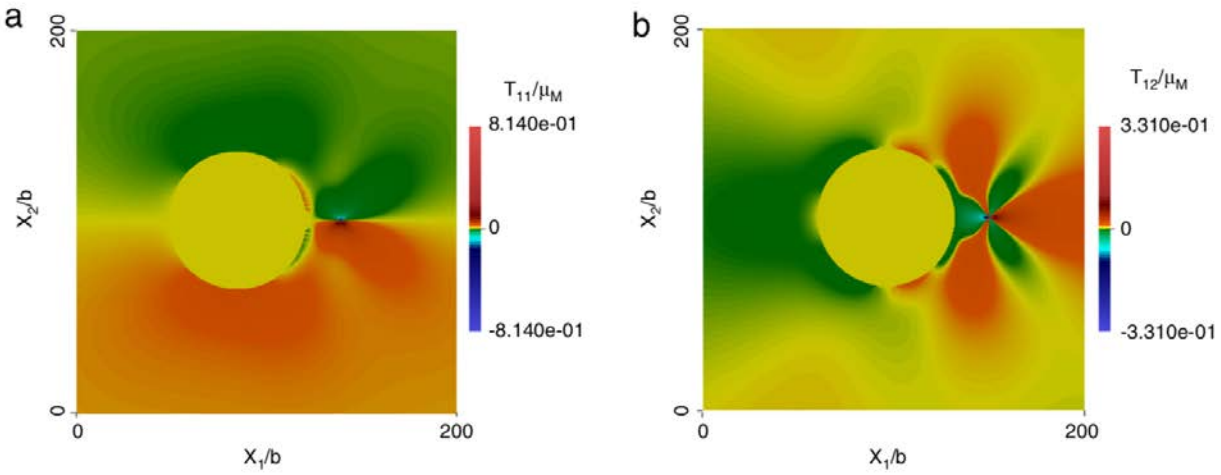


FIGURE 1.21 – 2D maps of normalized stress components σ_{11} (a) and σ_{22} (b) obtained with edge dislocation interacting with a circular hole [30]

Application to polycrystalline viscoplasticity (VP-FFT formulation) and polycrystalline elasticiy

Since 2001, many subsequent numerical implementations of the FFT-based method have been proposed by different authors in order to describe various constitutive laws for the behavior of single crystal within polycrystals. Lebensohn [75] was the first to apply the FFT approach developed by Moulinec and Suquet [98, 99] to viscoplastic polycrystal plasticity.

The author developed a n-site viscoplastic FFT formulation to predict the viscoplastic responses of anisotropic polycrystals. He studied the influence of mechanical contrast, the choice of reference medium, the effect of rate sensitivity on the convergence of the viscoplastic FFT formulation. Fig. 1.22 shows the error in equilibrium as function of the number of iterations in the simulation of a single-phase FCC polycrystal. One can note that when the FFT resolution is better, then the convergence is more rapid.

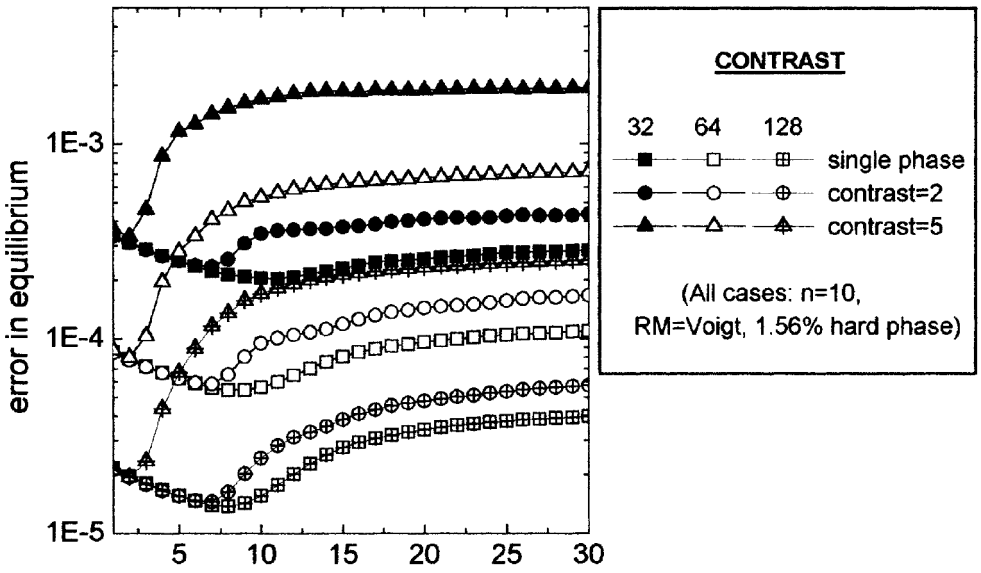


FIGURE 1.22 – Numerical error on the stress equilibrium for different resolution and different contrast with a viscoplastic FFT polycrystalline formulation [75]

The authors in [15] associated FFT-based method and a self-consistent homogenization scheme to describe elastic behavior of a polycrystal taking into account local anisotropy. In linear viscosity, 2-D behavior of polycrystals were studied and the distribution of mechanical fields in the polycrstal was evaluated in [77]. The numerical results obtained in this paper were compared to analytic results and the authors discussed the accuracy of the solutions when the phase contrast between single crystals increases. In rigid-viscoplasticity, the evolution of the structure in a copper aggregate undergoing plastic deformation is studied in [76]. In this paper, the

authors showed that FFT-method allows to study grains orientations, misorientations and orientation dependence of intragranular misorientations. The comparison between obtained results (average value of orientations and misorientations and experimental data obtained with orientation imaging microscopy (OIM) showed good agreement. Still in rigid-viscoplasticity, Rollett at al [115], computed viscoplastic strain in a polycrystal submitted to uniaxial loading and effect of microstructure defects on formation of hot stress hot spots. They showed that these ones are more located near GBs.

Elastoviscoplastic FFT scheme (EVP-FFT formulation)

In small strain crystalline elasto-viscoplasticity, FFT-based methods were also used (crystal plasticity EVPFFT). Lebensohn et al [73] formulated numerical model to predict mechanical fields within a polycrystal in elasto-viscoplastic polycrystal. This formulation was used to predict the mechanical fields in anisotropic copper and the results were compared to the mechanical fields in an artificial FCC polycrystal as shown in fig. 1.23.

CP-EVPFFT was also applied to study the behavior of a ice under transient creep [127], to evaluate heterogeneous strain and stress field that grow in grains with comparison to experimental data [50]. Fig. 1.24 is a comparison between simulated and experimental results.

Other recent applications : Non local plasticity, damage, large deformation ...

Djaka et al. [28] extended the CP-EVPFFT from Lebensohn et al [73] to non local mesoscale field dislocation mechanics to describe size effects in channel-type microstructures. Their approach is denoted MFDM-EVPFFT and corresponds to an application of the spectral approach developed in [29] and described in previous paragraphs. MFDM-EVPFFT allows to compute the dislocation density in a polycrystal under loading. In reference [8], the authors proposed a MFDM-EVPFFT formulation which accounts for the evolution of GNDs (geometrically necessary dislocations) solving a hyperbolic-type partial differential equation, and GND effects on both plastic flow and hardening. Fig. 1.25 is the study of Hall-Petch scaling law for the macroscopic flow stress as a function of the mean grain. Fig. 1.26 represents the spatial distribution of equivalent cumulated plastic strain at 0.2% overall plastic strain for two grain sizes.

The constitutive regimes of polycrystals studied with FFT-based methods also

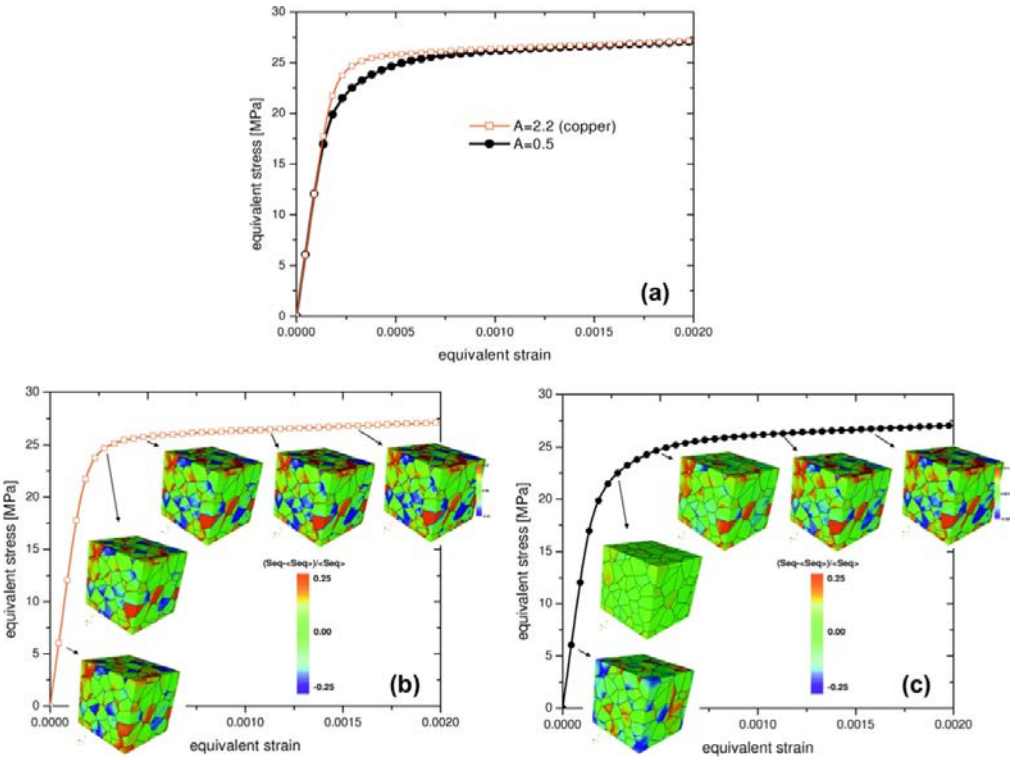


FIGURE 1.23 – (a) Effective response predicted with the EVP-FFT model for the copper polycrystal ($A = 2.2$) and the artificial FCC random polycrystal ($A = 0.5$) deformed in uni axial tension up to 0.2% . (b) and (c) Predicted fields of normalized fluctuations of the von Mises stress, for the copper polycrystal (b) and the artificial FCC polycrystal (c), in different stages of the loading. [73]

include : lower-order [55] and higher-order strain-gradient plasticity [79] ,transformation plasticity [106, 114] , dilatational plasticity [74, 78], curvature-driven plasticity [137], quasi-brittle damage [83, 123] and fatigue [117, 118].

References [65] is an application of FFT-based algorithms for large deformations. In this paper, Kabel et al. first recalled the limit of the fixed point solver of Moulinec and Suquet [98, 99] in terms of convergence specially for large deformation. They also recalled the efficiency of the Newton-Krylov method (which is the combination of Newton Raphson method and the Krylov solvers [47, 144]) to handle large deformations problems. The authors proposed a modification of the Newton-Krylov method in order to keep their fast convergence capability and reduce the memory requirements. Fig. 1.27 [65] shows the contour plot for the energy density of the deformation for a 10% compression. The number of iterations with the Moulinec and Suquet (MS) is very important in comparison with the NewtonKrylov type method. Some other authors applied FFT-based method in large-strain elasto-viscoplasticity [36, 122, 66, 143, 90].

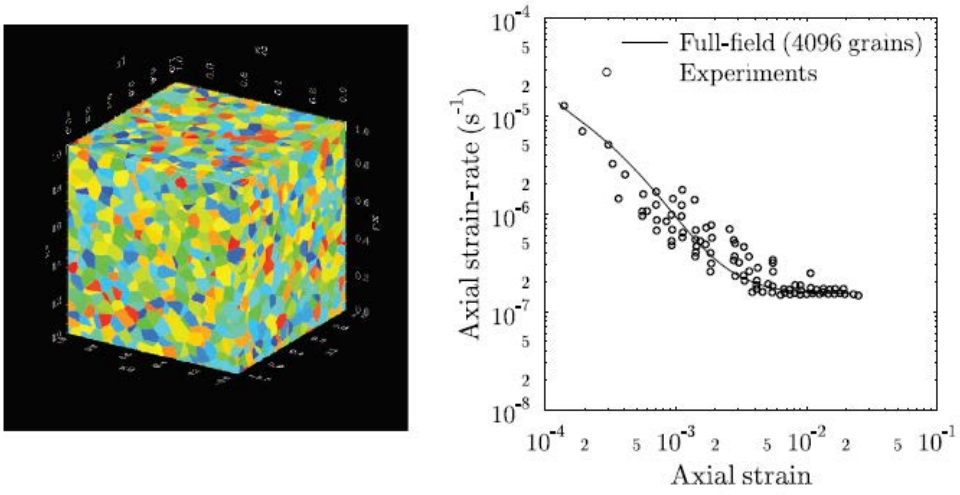


FIGURE 1.24 – Transient creep experiments. Comparison between the experimental results and the full-field simulations performed on the configuration on the left with the CP-EVP-FFT solver [127]

However these algorithms present numerical difficulties that several authors have attempted to solve concerning convergence and accuracy.

1.3.1.6 Convergence of the FFT-based algorithms

One of the main problem of these algorithms is the rate of convergence. In fact the formal strain solution of the Lippmann-Schwinger equation in heterogeneous elasticity with eigenstrains can be expanded in a Neumann series which reads [144] :

$$\boldsymbol{\varepsilon}(\mathbf{x}) = \sum_{n=0}^{+\infty} \left[-(\boldsymbol{\Gamma} * \delta\mathbf{C})(\mathbf{x})\right]^n : \left(\mathbf{E} + (\boldsymbol{\Gamma} * \mathbf{C} : \boldsymbol{\varepsilon}^*)(\mathbf{x})\right) \tag{1.54}$$

The rate of convergence of this power series expansion is related to the spectral radius of the operator : $\boldsymbol{\Gamma} * \delta\mathbf{C}$ [92]. Therefore, the convergence of the FFT-based algorithm depends strongly on the Green operator and the contrast between phases [69]. It was noticed that when the fixed-point algorithm [99, 3] known as " the basic algorithm" is implemented, the convergence is achieved only if two conditions are simultaneously satisfied : the mechanical contrast between phases is small and the reference medium is well chosen as prescribed in [92]. Therefore, it is difficult to study composite with pores or rigid inclusions with the initial basic algorithm of Moulinec and Suquet.

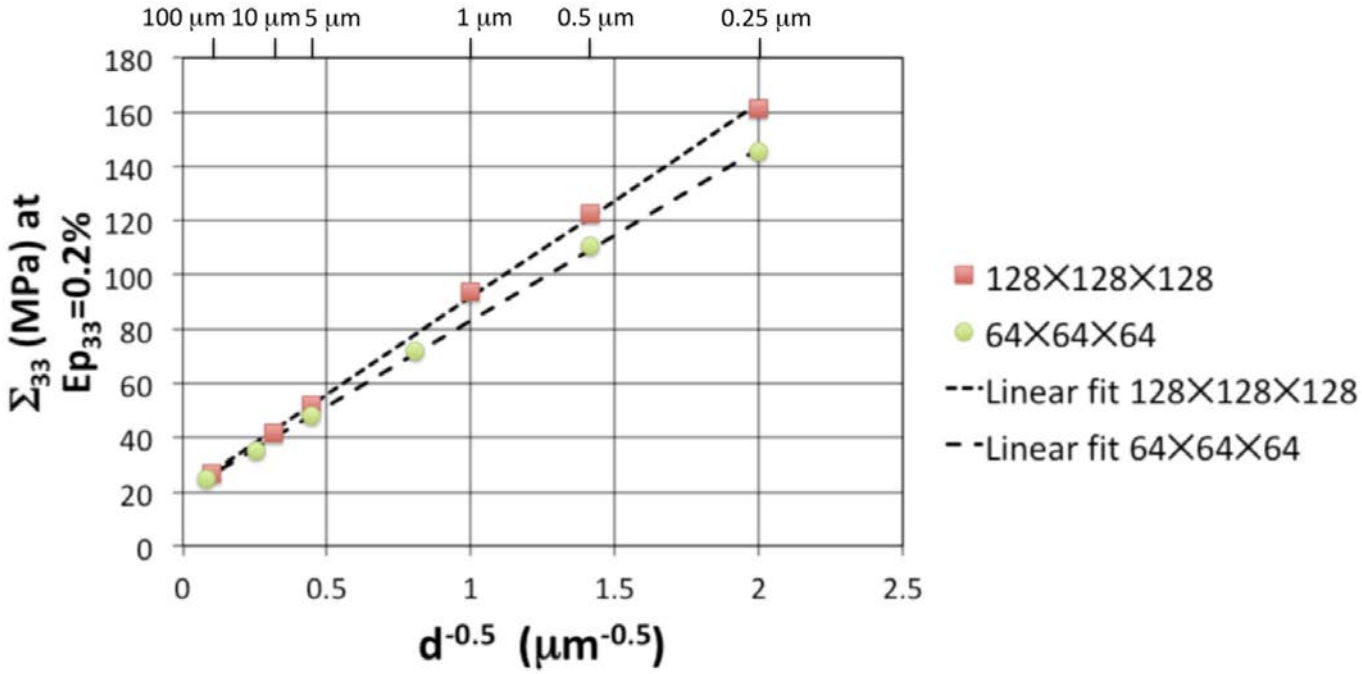


FIGURE 1.25 – Grain size effect reported on the overall flow stress at 0.2% overall plastic strain ($E^p = 0.2\%$) and comparison with a Hall-Petch type scaling law (linear fits : dotted lines). The numerical simulations were performed with the MFDM EVPFFT formulation with a RVE of 100 grains and$128 \times 128 \times 128$ voxels and with a RVE of 27 grains and $64 \times 64 \times 64$ voxels

A first problematic associated to this numerical difficulty is how to accelerate the basic algorithm for a given contrast [98, 99]. Eyre and Milton [42], developed a method to accelerate the basic algorithm called the "accelerated scheme". They used low and high resolutions in their computations. Using the low resolution, they computed an initial solution with another expression of the stress polarization field $\boldsymbol{\tau}$ [94]. This first solution is accurate and computed with little computational resources. Using an appropriate interpolation, they computed the final solution on a fine grid. The accuracy of the initial solution allows a quick convergence on the fine grid. This improvement is efficient for material with high mechanical contrast.

Another interesting accelerated scheme is proposed by Zeman et al. using conjugate gradient [163]. To summarize, this consists in linearizing the Newton method Lippmann schwinger [139] and then solving it using conjugate gradient method. The authors compared their method to the basic scheme [98]. Fig 1.28 [163], is a comparison between the number of iterations with the classic FFT-based method [98, 99] (FFTH) and the accelerated method proposed in [163] (CG). This figure shows that for a given phase contrast, the total number of iterations of their algo-

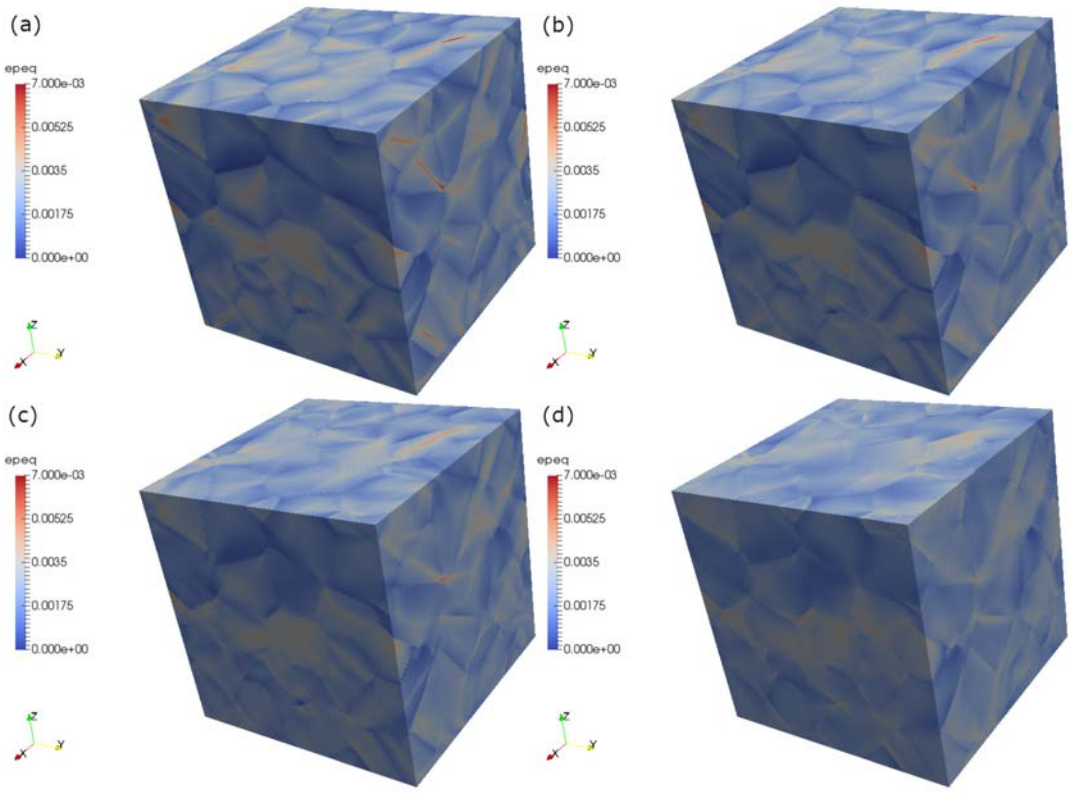


FIGURE 1.26 – Spatial distribution of equivalent cumulated plastic strain ε_p^{eq} recorded at $E^p = 0.2\%$ for three average grain sizes (MFDM-EVPFFT) with same scale range : $0.25\mu m$ (a), $1\mu m$ (b),$10\mu m$ (c). Simulation results with conventional CP-EVPFFT (d) with same scale range.

rithm to achieve an error is less than one given by the basic algorithm. The results clearly show that the number of iterations grows as square root of the contrast with the conjugate gradient method while it increases linearly with contrast using basic classic FFT algorithms [98, 99].

Gelebart et al. [47] extended this method to non-linear behaviors. Their approach is based on a Newton-Raphson algorithm and is fundamentally different from the basic FFT based approaches which rely on a fixed-point algorithm. The Lippmann Schwinger equation obtained in the case of non linear behavior is resolved as a non-linear system by a Newton-Raphson method. The approach is applied to study soft and stiff inclusion for a macroscopic or mixed loadings. The approach shows some advantages like a low sensitivity to the reference material and efficiency in computational time. Fig 1.29 is a comparison about the number of iterations at convergence of the basic scheme [99] (BS), the conjugate gradient method [163] (CG) and the proposed method [47](NR). The number of iterations at convergence is plotted as

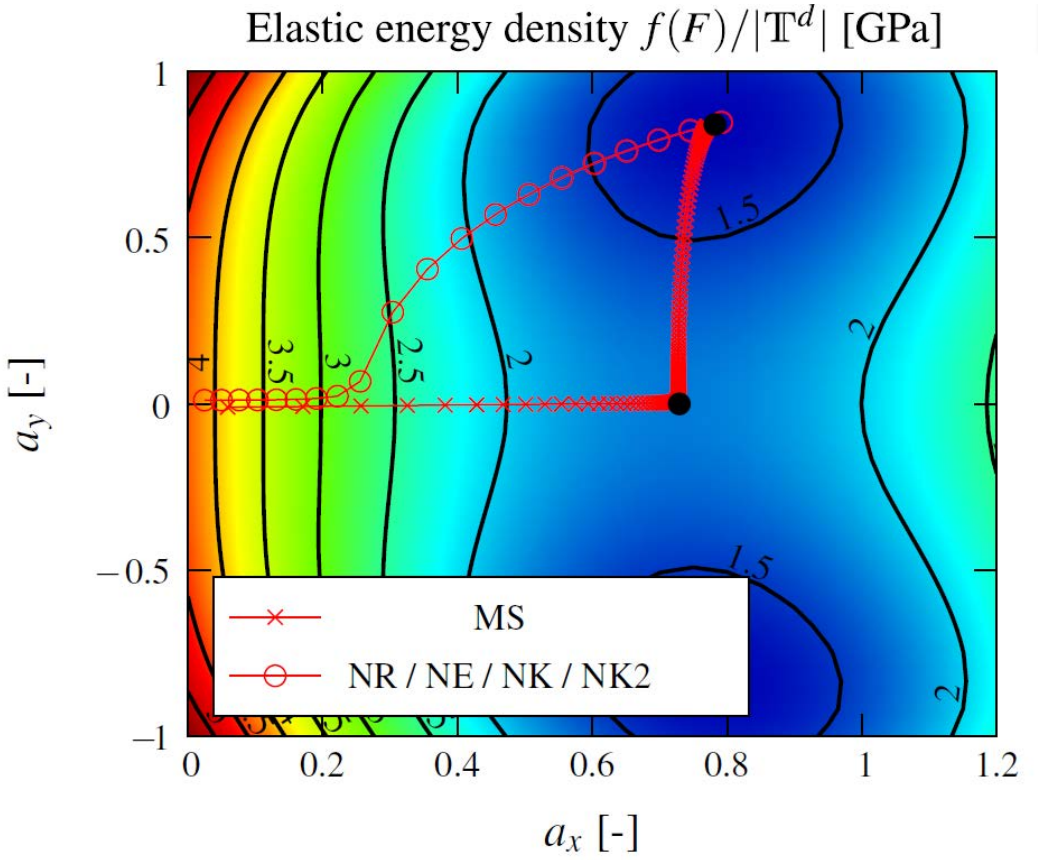


FIGURE 1.27 – Iterations of the FFT-based schemes for 10% compression. MS is the Moulinec Suquet basic algorithm and NE,NR,NK and NK2 are other FFT methods based on the Newton-Krylov algorithm [65]

function of the mechanical contrast.

Another problematic associated to this numerical difficulty is how to make FFT-based algorithm converge for infinite contrast. The previous improved method allows to accelerate the basic algorithm but do not converge for composite materials with very high or infinite contrast (material containing void or rigid inclusions). To study these composite materials, other schemes were developed. In [92], the authors proposed an iterative scheme based on the augmented Lagrangian method. They used an energetic variational principle and introduce a Lagrange multiplier. Besides, the iterative algorithm used is the one proposed by Uzawa [48, 85]. The method was applied to different situations : linear porous materials, rigid plastic porous materials, linear and nonlinear rigid composite, polycrystalline material with power law behavior[73].

Monchiet and Bonnet [95] also developed a numerical approach based on the

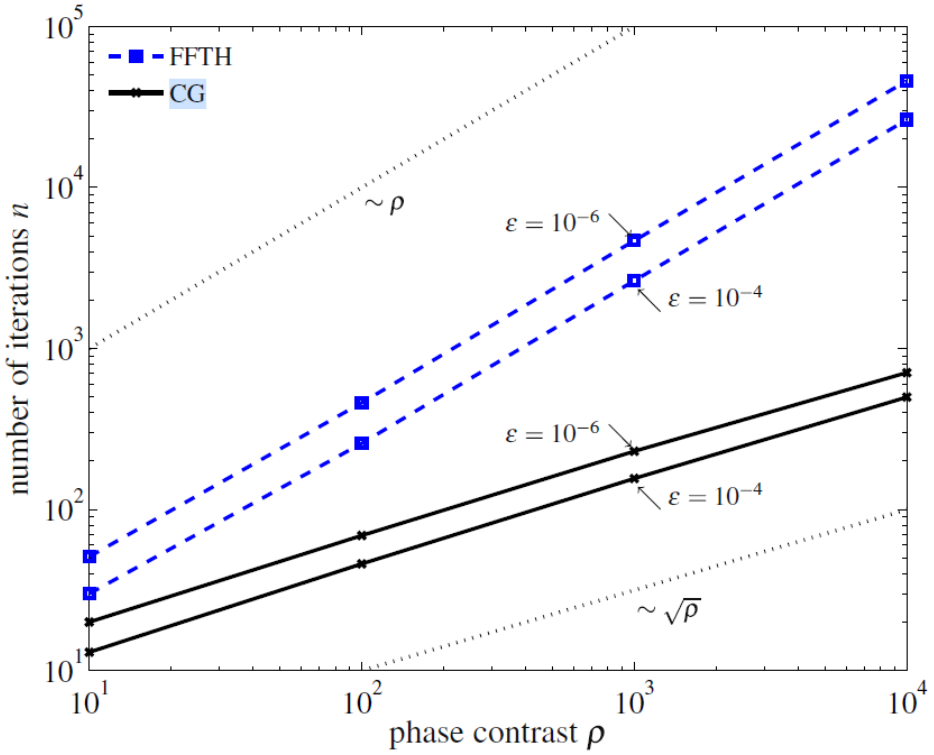


FIGURE 1.28 – Comparisons of the number of iteration with the classic FFT-based method [98, 99] (FFTH) and the accelerated method proposed in [163] (CG)

accelerated scheme proposed Eyre and Milton [42]. They first proposed a numerical algorithm algo. 4, based on the stress field [95] (for a given macroscopic stress $\boldsymbol{\Sigma}$). While the basic numerical algorithm based on strain field [99] algo. 1 allows to study composites containing soft inclusions, the proposed algorithm algo. 4 is better suited for composites made up of stiff inclusions. In algo. 4, the fourth order operator $\boldsymbol{\Delta}$ is the "stress Green's tensor" and $\mathbf{S}$ denotes the elastic compliance tensor. Fig 1.30 [95] shows the comparison between the number of iterations at convergence for the strain-based and the stress-based algorithm and confirms the assumption of Monchiet and Bonnet [95]. When the composite contains both rigid inclusions and voids, previous methods cannot be used.

For these materials, the authors [95] developed a new algorithm. It is based on the polarization field $\boldsymbol{\tau}$ eq. 1.36. Their algorithm for a given macroscopic average polarization $\mathbf{T}$ reads (algo 5) :

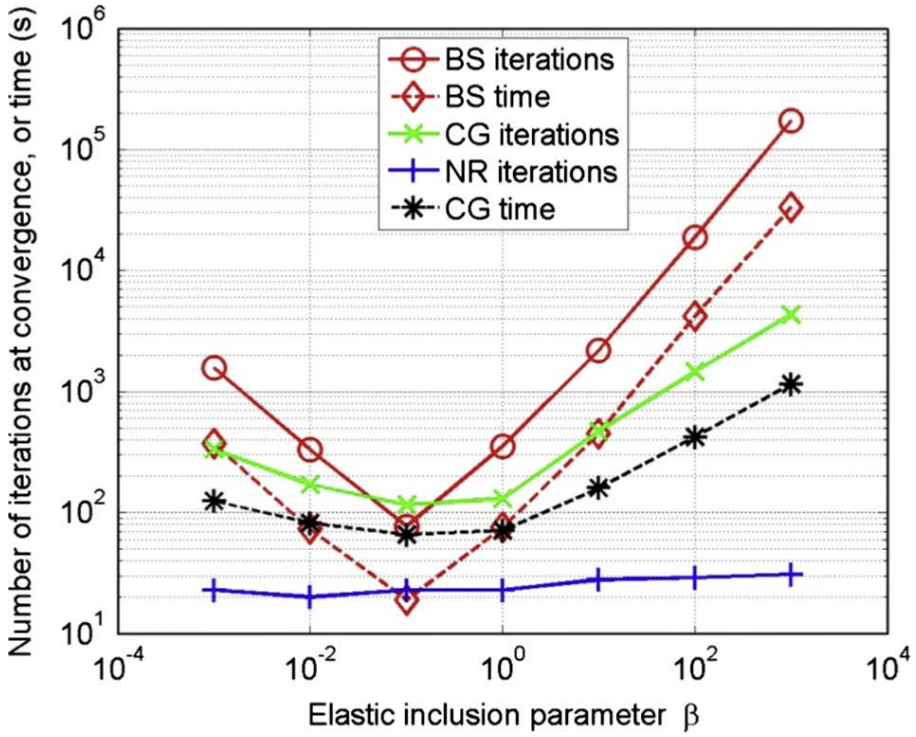


FIGURE 1.29 – Convergence properties as a function of the inclusion behavior [47]. The parameter β stands as the mechanical contrast between matrix and inclusion.

Algorithm 4 Basic algorithm : stress formulation [95]

Initialization : (given $\boldsymbol{\Sigma}$)

1: $\boldsymbol{\sigma}^o(\mathbf{x}_d) = \boldsymbol{\Sigma}$

2: $\boldsymbol{\varepsilon}^o(\mathbf{x}_d) = \mathbf{S}(\mathbf{x}_d) : \boldsymbol{\sigma}^o(\mathbf{x}_d), \quad \forall \mathbf{x}_d \in \Omega$

Iteration : $i+1$ ($\boldsymbol{\varepsilon}^i(\mathbf{x}_d)$ and $\boldsymbol{\sigma}^i(\mathbf{x}_d)$ known)

3: $\widehat{\boldsymbol{\varepsilon}}^i = \text{FFT}(\boldsymbol{\varepsilon}^i)$,

4: Convergence test,

5: $\widehat{\boldsymbol{\sigma}}^{i+1}(\boldsymbol{\xi}) = \widehat{\boldsymbol{\sigma}}^i(\boldsymbol{\xi}) - \widehat{\boldsymbol{\Delta}}(\boldsymbol{\xi}) : \widehat{\boldsymbol{\varepsilon}}^i(\boldsymbol{\xi}) \quad \forall(\boldsymbol{\xi}) \neq 0, \quad \widehat{\boldsymbol{\sigma}}^{i+1}(0) = \boldsymbol{\Sigma}$

6: $\boldsymbol{\sigma}^{i+1} = \text{FFT}^{-1}(\widehat{\boldsymbol{\sigma}}^{i+1})$

7: $\boldsymbol{\varepsilon}^{i+1}(\mathbf{x}_d) = \mathbf{S}(\mathbf{x}_d) : \boldsymbol{\sigma}^{i+1}(\mathbf{x}_d), \forall \mathbf{x}_d \in \Omega$

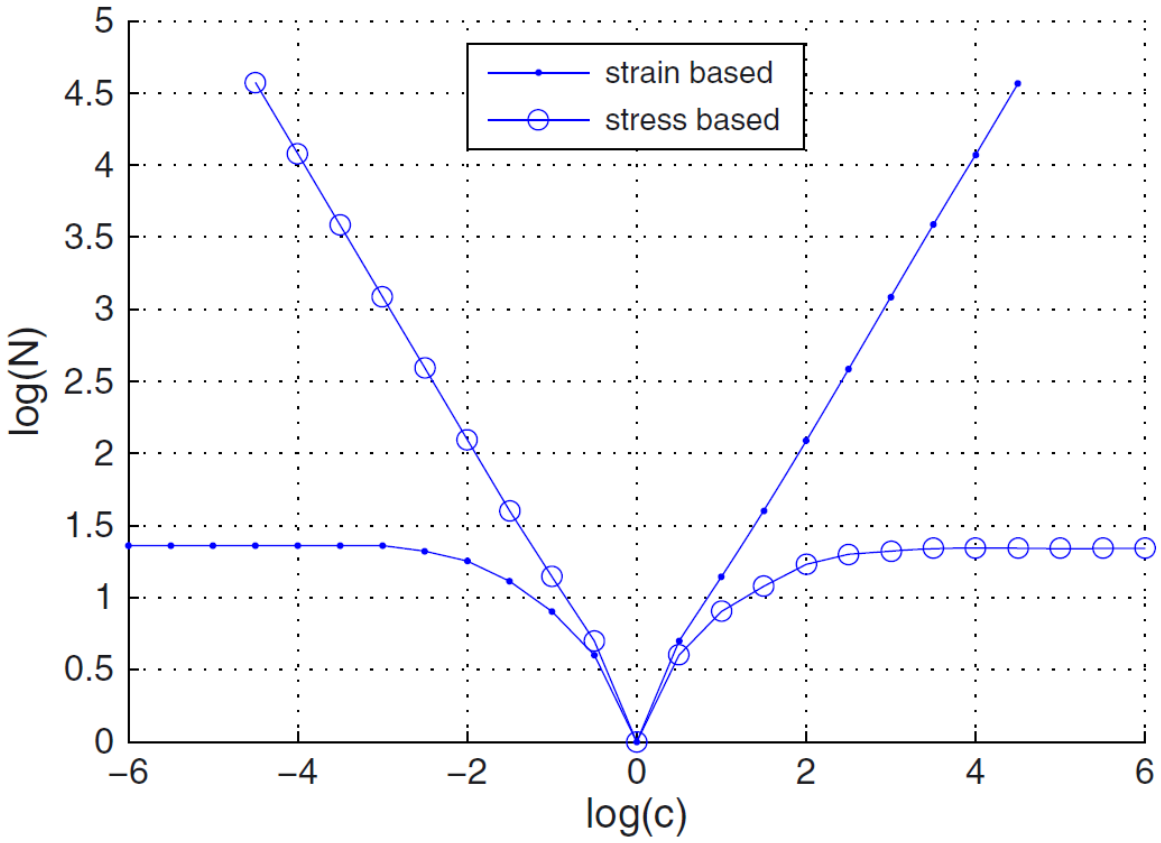


FIGURE 1.30 – Comparison between the number of iterations at convergence for the strain-based and the stress-based algorithms [95]

Algorithm 5 Monchiet-Bonnet's Numerical algorithm based strain/stress fields [95]

Initialization : (given $\mathbf{T}$)

1: $\boldsymbol{\tau}^o(\mathbf{x}_d) = \mathbf{T}$

Iteration : i ($\boldsymbol{\tau}^i(\mathbf{x}_d)$ known)

2: $\boldsymbol{\varepsilon}^i(\mathbf{x}_d) = \delta\mathbf{S}(\mathbf{x}_d) : \boldsymbol{\tau}^i(\mathbf{x}_d)$

3: $\widehat{\boldsymbol{\varepsilon}}^i$ =FFT$(\boldsymbol{\varepsilon}^i)$,

4: $\boldsymbol{\sigma}^o(\boldsymbol{\xi}) = \mathbf{C}^o : \boldsymbol{\varepsilon}^i(\boldsymbol{\xi}) + \boldsymbol{\tau}^i(\boldsymbol{\xi})$

Iteration : $i+1$ ($\boldsymbol{\varepsilon}^i(\boldsymbol{\xi})$ and $\boldsymbol{\sigma}^i(\boldsymbol{\xi})$ known)

5: Convergence test,

6: $\widehat{\boldsymbol{\tau}}^{i+1}(\boldsymbol{\xi}) = \widehat{\boldsymbol{\tau}}^i(\boldsymbol{\xi}) - \alpha\mathbf{C}^o : \widehat{\boldsymbol{\Gamma}}(\boldsymbol{\xi}) : \widehat{\boldsymbol{\sigma}}^i(\boldsymbol{\xi}) - \beta\widehat{\boldsymbol{\Delta}}(\boldsymbol{\xi}) : \widehat{\boldsymbol{\varepsilon}}^i(\boldsymbol{\xi}) \quad \forall(\boldsymbol{\xi}) \neq 0, \quad \widehat{\boldsymbol{\tau}}^{i+1}(0) = \mathbf{T}$

7: $\boldsymbol{\tau}^{i+1}$ =FFT$^{-1}(\widehat{\boldsymbol{\tau}}^{i+1})$

The convergence criterion is not based on the strain nor the stress field. It is based on both mechanical fields. The algorithm stops when :

$$\alpha \mathbf{C}^o : \widehat{\boldsymbol{\Gamma}}(\boldsymbol{\xi}) : \widehat{\boldsymbol{\sigma}}^i(\boldsymbol{\xi}) + \beta \widehat{\boldsymbol{\Delta}}(\boldsymbol{\xi}) : \widehat{\boldsymbol{\varepsilon}}^i(\boldsymbol{\xi}) = 0$$

In the algorithm, they introduced coefficients α and β. An appropriate choice of these coefficients allows to obtain the best rate of convergence whatever the mechanical contrast. This approach coincides with the accelerated scheme when $\alpha = 2$ and $\mathbf{T} = \langle \mathbf{C}(\mathbf{x}) \rangle - \mathbf{C}^o$. The capability of this approach to handle the composites containing rigid inclusions and voids is shown in fig.1.31. The polarization approach appears to be more efficient for very high contrast.

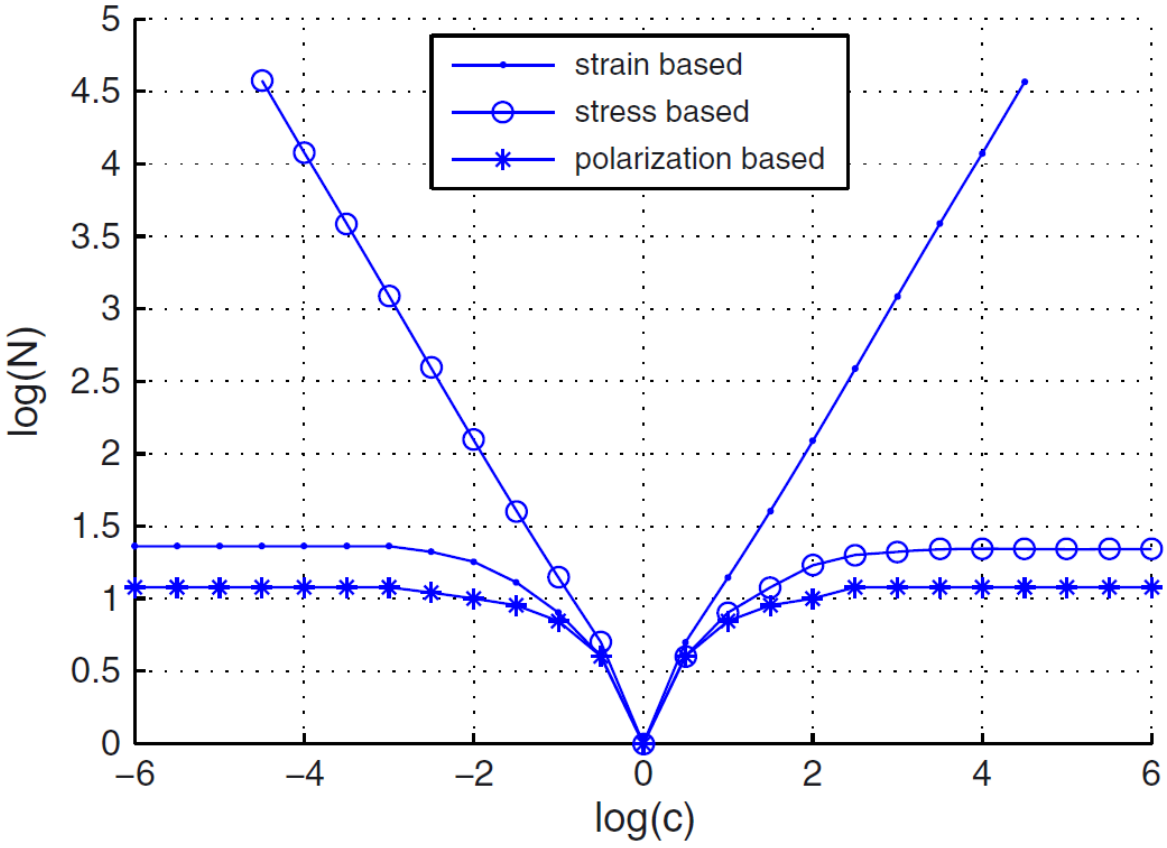


FIGURE 1.31 – Comparison between the number of iterations at convergence of the strain-based, the stress-based, and the polarization based [95]

An interesting comparison of FFT-based method is reported in Moulinec and Silva [97]. The authors compared four methods already exposed here : the "basic algorithm" [99], the "accelerated scheme" [42], the "augmented Lagrangian scheme" [92] and the "polarization-based method" [95]. In Fig1.32, the authors compared the number of iterations obtained with these methods for a mechanical problem. The

"accelerated scheme" [42] and the "polarization-based method" [95] appears to be the more efficient schemes for infinite contrasts.

References [65, 146, 122, 17, 16, 47, 120, 18] are among examples of improved schemes, or comparison of the improved schemes. Theses improvements allow now to use FFT-based methods for composite materials with infinite contrasts with a good convergence rate. The better rate of convergence may be counterbalanced by the easy implementation of the FFT-based algorithm which is even lost in some cases. For example when K denotes the contrast between the composite's phases, the number of iterations N_i necessary to have a given precision is proportional to K for the basic scheme and for the accelerated scheme, N_i is proportional to $\sqrt{K}$. However, it is noteworthy that one iteration for the basic scheme is less time consuming than one for the accelerated scheme [92].

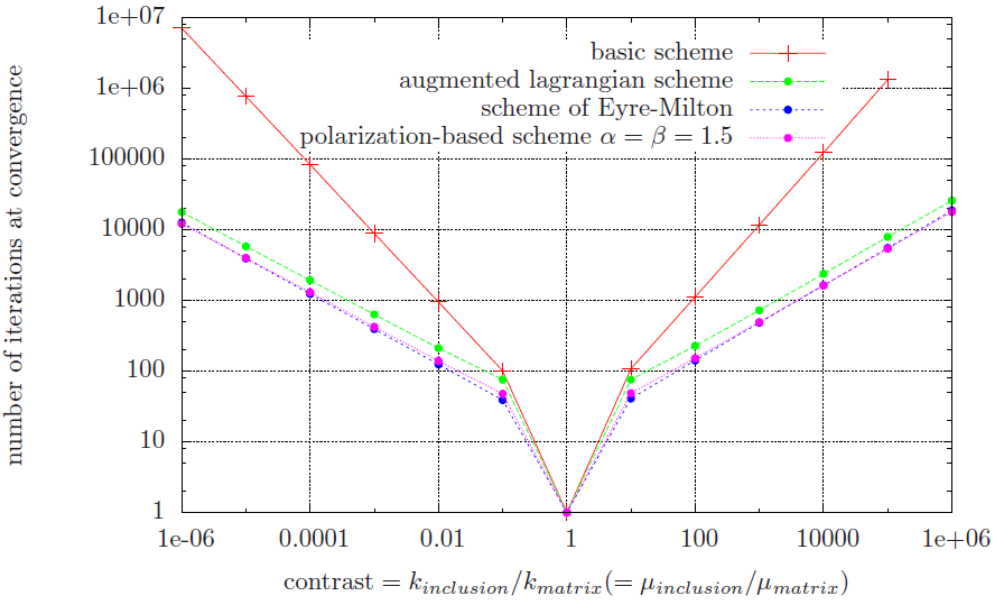


FIGURE 1.32 – Comparison of the number of iterations at convergence for different schemes. The studied material is a periodic microstructure with one spherical inclusion [92]

The rate of convergence of the FFT-based methods is also highly sensitive to the choice of the stiffness for the reference medium. Although the stiffness of the reference medium does not influence the results, its choice determines the number of total iterations. Therefore, it is important to choose an optimum value. Theoretical procedures yielding the optimum value reference medium are often missing, so authors developed numerical methods independent of this choice or perform numerical tests to determine this "optimum" value. In general, the elastic constants of the reference medium are assumed isotropic : k^o (bulk modulus) and μ^o (shear modulus),

are given as functions of the elastic constants $k(\mathbf{x})$ and $\mu(\mathbf{x})$ in the composite. The elastic constants of the reference medium are chosen as follows for the basic scheme [99] :

$$\begin{aligned} k^o &= \frac{1}{2}\left(\inf_{x\in V} k(\mathbf{x}) + \sup_{x\in V} k(\mathbf{x})\right) \\ \mu^o &= \frac{1}{2}\left(\inf_{x\in V} \mu(\mathbf{x}) + \sup_{x\in V} \mu(\mathbf{x})\right) \end{aligned} \tag{1.55}$$

Note that other authors showed that this is not the optimum choice. In [156], the authors demonstrated that instead of $\frac{1}{2}$ in eq. 1.55, the optimum value is between 0.5003 and 0.509 and this result is confirmed in [31]. For the accelerated schemes the elastic constants of the reference medium are chosen as follows :

$$\begin{aligned} k^o &= \sqrt{\inf_{x\in V} k(\mathbf{x}) \sup_{x\in V} k(\mathbf{x})} \\ \mu^o &= \sqrt{\inf_{x\in V} \mu(\mathbf{x}) \sup_{x\in V} \mu(\mathbf{x})} \end{aligned} \tag{1.56}$$

In the polarization-based iterative scheme, the optimal reference medium can only be determined numerically because it is related to α and β. The authors suggested that it depends on the elastic properties of constituents and their spatial distribution. In the case of augmented Lagrangian, the elastic constants of the reference medium must be determined numerically. Michel et al. [92] showed that the elastic constants of the reference medium does not depend very strongly on the spatial resolution. Therefore, it is suggested to determine the optimum value at low resolution and used it in the computations at higher resolutions. In [163], the authors showed that the conjugated gradient methods do not depend on the choice of the reference medium.

1.3.1.7 Numerical oscillations

Another problem encountered with classical algorithms is the occurence of spurious oscillations on mechanical fields. Unlike the difficulties related to convergence, this question is less treated in the literature even though recent advances tried to tackle this problem in discrete spectral approaches. It is related to the use of the Discrete Fourier Transform (DFT) [14]. This well known phenomenon can be linked to "Gibbs" phenomenon or to "Aliasing". The Gibbs phenomenon appears during approximation of piecewise continuous function while "aliasing" appears during sampling of a spatial function.

Gibbs phenomenom

A continuous piecewise function is often approximated using Fourier series. J.Willard Gibbs and Henry Wilbraham [56] discovered a peculiar manner of these Fourier series at jump discontinuities of the approximated function. In fact, the Nth partial sum of the Fourier series is a continuous function, therefore it is impossible to approximate uniformly the piecewise function. Fig1.33 shows an example of a functional approximation of square wave using harmonics.
Due to discretization, all the functions involved in the FFT-based algorithm are piewece functions which are approximated by power series expansion (see for example the strain solution in Eq. 1.54) and this could lead to Gibbs phenomenon.

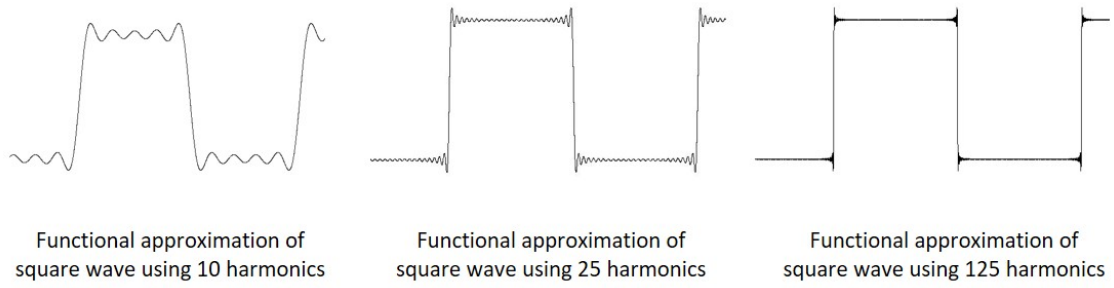


FIGURE 1.33 – Illustration of the Gibbs phenomenon with a square wave approximated by harmonics. The Gibbs phenomenon is more important when the order of the partial sum of the Fourier series increases.

Aliasing

The discretization of the real part in the FFT-method involves in sampling of functions. "Aliasing" can occur if some sufficient condition for perfect reconstruction are not hold. It has been shown that for any sampling interval $\triangle$, a frequency called Nyquist critical frequency f_c is defined :

$$f_c = \frac{1}{2\triangle}$$

If the continuous sampled function is not bandwidth limited to less than the Nyquist critical frequency, each frequency component outside of the range $(-f_c, f_c)$ is falsely translated into that range. The obtained function in this range is different from the original one. Fig1.34 shows an example on computing the Fourier transform of a sampled function, see [108].

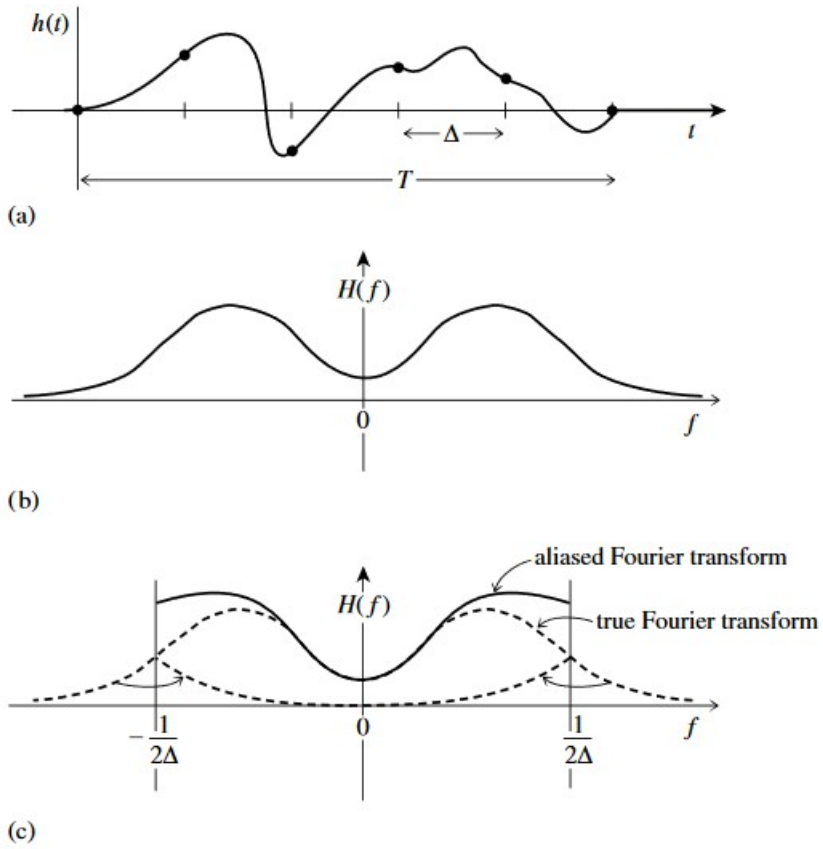


FIGURE 1.34 – The continuous function shown in (a) is nonzero only for a finite interval of the period T. It follows that its Fourier transform, whose modulus is shown schematically in (b), is not bandwidth limited but has finite amplitude for all frequencies. If the original function is sampled with a sampling interval $\triangle$, as in (a), then the Fourier transform (c) is defined only between plus and minus the Nyquist critical frequency. Power outside that range is folded over or "aliased" into the range. The effect can be eliminated only by low-pass filtering the original function before sampling

Effect of Discrete Fourier Transform (DFT)

In the FFT-based algorithm (algo.3), the applicability of the DFT is based on the assumption that the relevant functions are periodic. If it is not the case and these functions are not bandwidth limited to less than the Nyquist critical frequency, the "aliasing" and/or "Gibbs" effects tend to appear. In the previous described algorithms, algo1 and algo3, a particular attention is given to the modified Green operator $\mathbf{\Gamma}$, involved in the Lippmann-Schwinger equation. This modified operator is, by definition, computed for an infinite medium. In the described algorithm, this operator is used but was not periodized. We associated (as others authors in the literature) the numerical oscillations appearing on some component fields in next

chapter to this operator. To suppress oscillations, some authors either improved the basic algorithm or proposed another expression of the modified Green operator.

Removal of numerical oscillations

The pioneering works [98, 99] related this problem to the number N of voxels. For them, the problem occurs only if the number of voxels is small. Moulinec and Suquet proposed a method which consists in using another expression of the Green operator $\widehat{\mathbf{\Gamma}}$ at the highest frequencies :$\boldsymbol{\xi}_j = \pm(\frac{N_j}{2}-1)\frac{1}{T_j}$ (where T_j denotes the period of the unit cell) :

$$\widehat{\mathbf{\Gamma}} = \mathbf{C}^{o-1}$$

At theses high-frequencies, the stress is forced to be zero when the convergence is reached. For these authors, this choice allowed to avoid most of oscillations on the mechanical fields. In the next chapter, a numerical example shows that this method is efficient to remove a part of numerical oscillations but not all the oscillations are not completely removed. In order to avoid the artifacts related to highest frequencies, a second strategy used "attenuation factors" based on the discrete Fourier transform (DFT) of linear spline functions [68] or low-pass filtering to dampen high frequency terms in the solutions, i.e a raised cosine filter[122]. A third strategy first reported by [102], [33] and [158] was to compute discrete Green operators based on Finite Difference approximations. This research direction was followed by many authors in the last few years who showed it efficiency for many physical problems. [157, 6, 156, 7, 120, 79, 119, 30, 142, 143]. While [102] and [33] considered a centered-finite difference-based scheme, [158] reported forward and backward finite difference-based schemes. Among the different efficient recent schemes, a discrete Green operator based on a centered finite difference-based scheme on a rotated grid (i.e. a "rotated scheme") was recently proposed by [156]. This method was discussed in the previous section and consists in using a partial differentiation $i\xi_j^R$ instead of the classic partial differentiation $i\xi_j$. The efficiency of this method to suppress oscillations and find the effective properties of a material with a limited number of iterations is shown. Fig.1.35 [156] shows the effect of the different partial differentiation on the accuracy of the solution for three different resolutions.

It was successfully applied to Field Dislocation Mechanics equations for heterogeneous materials in [30]. Higher-order centered difference-based schemes were also reported to be very efficient for different applications [142, 143]. Another recent finite difference discretization scheme performed on a staggered grid was developed by [120]. This refined scheme combined with DFT was seen to be efficient for three dimensional porous materials to give numerical solutions devoid of oscillations. Furthermore, a new discretization method based on linear hexahedral finite elements adapted for the basic scheme and the conjugate gradient method [119] was reported and an equivalence has been demonstrated between the "rotated scheme" and hexahedral finite elements with reduced integration. In their Galerkin discretization

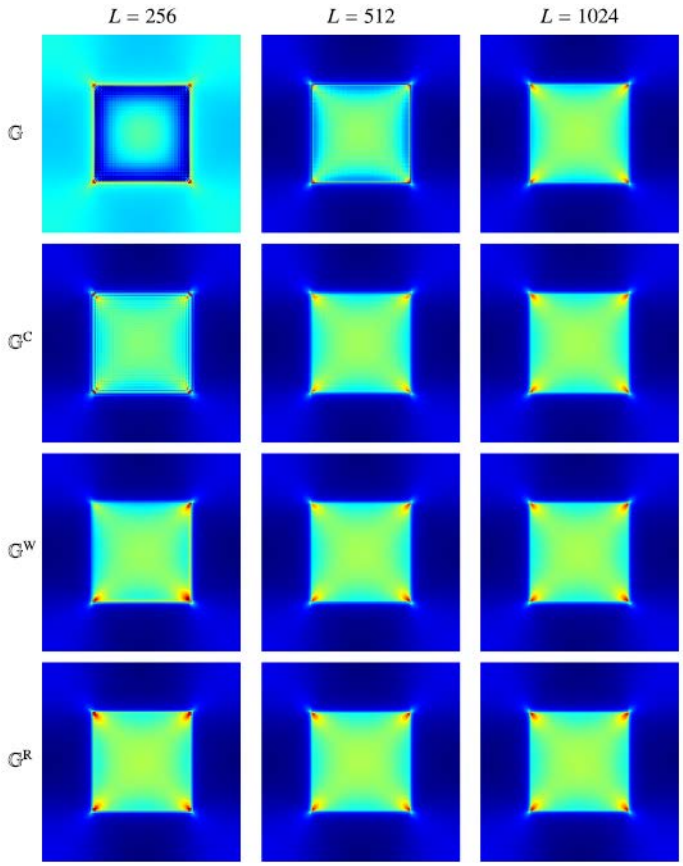


FIGURE 1.35 – Stress component σ_{12} predicted by the various FFT schemes at three resolutions. G (using partial derivative $i\xi_j$), G^C (using $i\xi_j^C$), G^W(using $i\xi_j^w = exp^{i\frac{2\pi m_j}{T_j}} - 1$), G^R (using ξ_j^R) [156]

of the Lippmann-Schwinger equation, [16] proposed a fourth strategy based on a "consistent discrete Green operator" which was adapted to a general variational framework based on the Hashin-Shtrikman's energy principle. Later, it was however considered by [16] as too costly for three-dimensional computations and a filtering approach was finally used by these authors.

1.4 Conclusions

This state of art review allowed to describe X-ray diffraction technique. The evolution of the experimental method and the emergence of the numerical method have been described. This numerical method of diffraction pattern simulation would in the long run be an alternative to the experimental method. It nevertheless requires the numerical calculation of the strain or displacement fields in a heterogeneous com-

posite material containing dislocations or stress-free strain fields. Spectral methods based on FFT algorithms are efficient for calculating mechanical fields accurately. The efficiency of these methods and their applications in various fields of mechanics has been recalled in this literature review. Numerical difficulties in the application of these methods are essentially convergence problems for high mechanical contrasts and occurrence of spurious oscillations at material discontinuities. In this state of the art report, we showed that these difficulties have been reported by several authors with more or less effective numerical solutions.

In the next chapter, we will focus on the development of a discrete consistent Green operator for the removal of spurious oscillations previously reported namely due to "aliasing". This operator allows to compute the strain and stress fields in a material containing eigenstrains and is applied to cubic and spherical (Eshelby) inclusions problems.

Chapitre 2

Development of a new consistent discrete Green operator for FFT-based methods to solve heterogeneous problems with eigenstrains

2.1 Introduction

In this chapter, we showed that the easy use of the conventional continuous Fourier transform of the modified Green operator (which will be denoted CGO in the whole manuscript) in the Lippmann-Schwinger equation for heterogeneous materials with eigenstrains leads to spurious oscillations when computing the local responses of composite materials close to materials discontinuities like interfaces, dislocations. This spurious oscillations are very important when the spatial resolution is low and result from aliasing and/or Gibbs phenomenon. Unfortunately, the spatial resolution can not be increased indefinitely because it is proportional to the computational method cost. We proposed a new expression of a periodized discrete Green operator. This new operator is derived using the Discrete Fourier Transform method and a consistent Fourier grid to resolve the Lippmann-Schwinger equation. This expression is given as a function of the classic "Continuous Green Operator" (CGO) and it takes into account, explicitly, the discreteness of the Discrete Fourier Transform methods. We show that the development of this new consistent discrete Green operator in the Fourier space named "Discrete Green Operators" (DGO) allows to eliminate oscillations while retaining similar convergence capability using low spatial resolution. Numerical examples are used to demonstrate the convergence of the infinite sum involved in the expression of this new operator and to show efficiency

of this new operator. The chapter is organized as follows : in the next section, the Lippmann-Schwinger equation for heterogeneous elastic materials with eigenstrains is recalled, its resolution in the Fourier space using an iterative numerical scheme and the convergence criterion are reported. In section 2 the *DGO* for stress/strain is developed starting from a one-dimensional representation. The properties of these *DGO* are highlighted and are discussed in comparison with classic *CGO*. In Section 3, numerical stress solutions obtained with the *DGO* are calculated for cubic-shaped inclusions, spherical Eshelby and inhomogeneity problems. The results are discussed and compared with analytical solutions and the classic discretization method using the *CGO*.

2.2 The Lippmann-Schwinger equation and its numerical spectral resolution

2.2.1 The Lippmann-Schwinger equation for eigenstrained heterogeneous materials

In this section, we present the field equations for a linear elastic problem with eigenstrains used to compute the response of a composite medium with periodic boundary conditions.
The periodic unit cell with volume Ω is subjected to a uniform overall strain tensor denoted $\mathbf{E}$. This overall strain corresponds to the spatial average of the strain field on the unit cell. In this chapter (and in the whole manuscript), we describe materials and physics defects in the unit cell (such as dislocations, misfit strain, thermal expansion...) using a stress free strain (eigenstrain) field denoted $\boldsymbol{\varepsilon}^*$. In the case of dislocation loops, the eigestrain field is given by :

$$\varepsilon^*_{ij} = \frac{A_s}{2V}(n_i b_j + n_j b_i)$$

where A_s is the area on which planes with normal $\mathbf{n}(n_1, n_2, n_3)$ has slipped due to a disloation loop, by a relative amount $\mathbf{b}(b_1, b_2, b_3)$ and V is the volume occupied by the loops [84, 2]. When the material contains two phases (for example γ and γ' in a Nickel-based superalloy), the eigenstrain, here "misfit strain" is generated by the difference between the lattices parameters and is given by(for the Nickel based superalloy) :

$$\varepsilon^*_{ij} = 2\frac{a_{\gamma'} - a_\gamma}{a_{\gamma'} + a_\gamma}\delta_{ij}$$

where $a_{\gamma'}$ and a_γ are the lattice parameters of phases γ' and γ respectively [130, 129] and δ_{ij} denotes the Kronecker delta symbol. Let us denote $\mathbf{u}$, $\boldsymbol{\varepsilon}$, $\boldsymbol{\sigma}$, the displacement, strain, Cauchy stress and eigenstrain fields, respectively.

Let us now define a homogeneous linear elastic reference material with elastic stiffness $\mathbf{C}^o$ such as at every position vector $\mathbf{x} \in \Omega$, the elastic stiffness tensor reads :

$$\mathbf{C}(\mathbf{x}) = \mathbf{C}^o + \delta\mathbf{C}(\mathbf{x}) \tag{2.1}$$

where $\mathbf{C}$ is the fourth order tensor of spatially heterogeneous elastic moduli with classic minor and major symmetries for components : $C_{ijkl} = C_{jikl} = C_{ijlk} = C_{klij}$. The tensor $\delta\mathbf{C}(\mathbf{x})$ denotes the spatial fluctuations of $\mathbf{C}(\mathbf{x})$ with respect to $\mathbf{C}^o$.
For this problem, the balance of linear momentum without body force yields :

$$\mathbf{div}\boldsymbol{\sigma}(\mathbf{x}) = 0 \qquad \forall \mathbf{x} \in \Omega \tag{2.2}$$

where $\mathbf{div}$ is the divergence operator. Furthermore, from strain compatibility, the local total strain tensor $\boldsymbol{\varepsilon}(\mathbf{x})$ reads :

$$\boldsymbol{\varepsilon}(\mathbf{x}) = \nabla^s \mathbf{u}(\mathbf{x}) \tag{2.3}$$

where the symbol ∇^s denotes the symmetric part of the gradient operator ∇. In the present small strain setting, $\boldsymbol{\varepsilon}(\mathbf{x})$ additively decomposes as a sum of elastic strain $\boldsymbol{\varepsilon}^e$ and eigenstrain $\boldsymbol{\varepsilon}^*$ tensors as follows :

$$\boldsymbol{\varepsilon}(\mathbf{x}) = \boldsymbol{\varepsilon}^e(\mathbf{x}) + \boldsymbol{\varepsilon}^*(\mathbf{x}) = \mathbf{S}(\mathbf{x}) : \boldsymbol{\sigma}(\mathbf{x}) + \boldsymbol{\varepsilon}^*(\mathbf{x}) \tag{2.4}$$

where $\mathbf{S} = \mathbf{C}^{-1}$ is the elastic compliance tensor. $\mathbf{C}$ and $\mathbf{S}$ have same minor major symmetries for components. The combination of Eq. 2.2, Eq. 2.3, Eq. 2.4 together with Eq. 2.1 and the introduction the Green's function method leads to an integral equation usually called "Lippmann-Schwinger equation" [98, 99, 72] in the mechanics community, which reads :

$$\boldsymbol{\varepsilon}(\mathbf{x}) = \mathbf{E} - (\boldsymbol{\Gamma} * \boldsymbol{\tau})(\mathbf{x}) \qquad \forall \mathbf{x} \in \Omega \tag{2.5}$$

In Eq. 2.5, the symbol $*$ denotes the spatial convolution product between two functions (in this case $\boldsymbol{\Gamma}$ and $\boldsymbol{\tau}$). In this equation, $\boldsymbol{\Gamma}$ is the modified Green operator associated with $\mathbf{C}^o$ and $\boldsymbol{\tau}$ is the stress polarization field defined as :

$$\boldsymbol{\tau}(\mathbf{x}) = \delta\mathbf{C}(\mathbf{x}) : \boldsymbol{\varepsilon}(\mathbf{x}) - \mathbf{C}(\mathbf{x}) : \boldsymbol{\varepsilon}^*(\mathbf{x}) \tag{2.6}$$

The numerical resolution of Eq. 2.5 is not an easy task for two main reasons. First, it contains a spatial convolution of two functions in real space, and the numerical full field computation of a convolution in the real space is complicated. Second, it is an implicit equation : the strain solution $\boldsymbol{\varepsilon}(\mathbf{x})$ is defined as function of the stress polarization field $\boldsymbol{\tau}(\mathbf{x})$ in Eq.2.5 and Eq.2.6, the stress polarization field contains the strain solution. This implicit equation needs specific resolution methods. To overcome these difficulties, Eq. 2.5 can be written in the Fourier space so that the spatial convolution is transformed to a simple product. For periodic media, the numerical Fast Fourier Transform (FFT)-based resolution initially proposed by [98, 99] is an efficient way to iteratively solve the implicit equation in order to obtain the strain solution.

2.2.2 Fourier space resolution

From the convolution theorem in the Fourier space [14], the Lippmann-Schwinger equation (Eq. 2.5) can be transformed in the Fourier space as follows :

$$\widehat{\boldsymbol{\varepsilon}}(\boldsymbol{\xi}) = -\widehat{\boldsymbol{\Gamma}}(\boldsymbol{\xi}) : \widehat{\boldsymbol{\tau}}(\boldsymbol{\xi}) \qquad \forall \boldsymbol{\xi} \neq 0, \qquad \widehat{\boldsymbol{\varepsilon}}(0) = \mathbf{E} \tag{2.7}$$

where $\widehat{\boldsymbol{\Gamma}}$ and $\widehat{\boldsymbol{\tau}}$ are the Fourier transforms of $\boldsymbol{\Gamma}$ and $\boldsymbol{\tau}$, respectively. $\boldsymbol{\xi}$ represents the Fourier vector. In Eq. 2.7, $\widehat{\boldsymbol{\Gamma}}$ writes in index notations :

$$\widehat{\Gamma}_{ijql}(\boldsymbol{\xi}) = \frac{1}{4}(\widehat{G}_{iq}\xi_j\xi_l + \widehat{G}_{il}\xi_j\xi_q + \widehat{G}_{jq}\xi_i\xi_l + \widehat{G}_{jl}\xi_i\xi_q) \tag{2.8}$$

where $\widehat{\mathbf{G}}$ is the Fourier transform of the elastic Green tensor defined as [104] :

$$\begin{cases} \widehat{G}_{ij}(\boldsymbol{\xi}) = \dfrac{N_{ij}(\boldsymbol{\xi})}{D(\boldsymbol{\xi})} & \forall \boldsymbol{\xi} \neq 0 \\ \widehat{G}_{ij}(0) = 0 \end{cases} \tag{2.9}$$

where $N_{ij}(\boldsymbol{\xi})$ denotes the rectangular components of the cofactor matrix related to the acoustic tensor $F_{ij} = C^o_{ijql}\xi_q\xi_l$ and $D(\boldsymbol{\xi})$ is the determinant of F_{ij}. Due to the symmetry properties of C^o_{ijql}, $N_{ij}(\boldsymbol{\xi})$ satisfies : $N_{ij}(\boldsymbol{\xi}) = N_{ji}(\boldsymbol{\xi})$, therefore $\widehat{G}_{ij} = \widehat{G}_{ji}$ and $\widehat{\Gamma}_{ijql} = \widehat{\Gamma}_{jiql} = \widehat{\Gamma}_{ijlq} = \widehat{\Gamma}_{qlij}$.

For isotropic elasticity using the two Lamé constants, λ and μ,($C^0_{ijkl} = \lambda\delta_{ij}\delta_{kl} + \mu\left(\delta_{ik}\delta_{jl} + \delta_{il}\delta_{jk}\right)$), N_{ij} and $D(\boldsymbol{\xi})$ read :

$$N_{ij}(\boldsymbol{\xi}) = \mu\xi^2\{(\lambda + 2\mu)\delta_{ij}\xi^2 - (\lambda + \mu)\xi_i\xi_j\}$$
$$D(\boldsymbol{\xi}) = \mu^2(\lambda + 2\mu)\xi^6$$

where $\xi^2 = \xi_k\xi_k$. Using these formulas, the expression of $\widehat{\Gamma}_{ijql}$ was given for example in [99] for isotropic material :

$$\widehat{\Gamma}_{ijql}(\boldsymbol{\xi}) = \frac{1}{4\mu|\ \boldsymbol{\xi}\ |^2}(\delta_{qi}\xi_l\xi_j + \delta_{li}\xi_q\xi_j + \delta_{qj}\xi_l\xi_i + \delta_{lj}\xi_q\xi_i) - \frac{\lambda + \mu}{\mu(\lambda + 2\mu)}\frac{\xi_i\xi_j\xi_q\xi_l}{|\ \boldsymbol{\xi}\ |^4}$$

Writing the Lippmann-Schwinger in the Fourier space allows to transform the spatial convolution to simple product. Now this equation can be solved more easly in the Fourier space due to this simple product but it is still an implicit equation. Recently, [3] proposed an iterative scheme for eigenstrain problems of the augmented Lagrangian (AL) type [92] to solve Eq. 2.5 using Eq. 2.7. The FFT-based numerical algorithm used for heterogeneous elastic materials with eigenstrains is presented in the next section.

2.2.3 Numerical Algorithm

In order to solve Eq.2.7, we use the numerical algorithm algo.3 proposed by [3] and described in section1.3.1.5. This algorithm is used in all mechanical problems presented in this manuscript. It allows to take into account the eigenstrain in the material and is therefore appropriate for the study of a Nickel based superalloy which contains eigenstrain field due to the misfist between the γ/γ' phases or due to dislocations

2.2.4 Some numerical examples

In the forthcoming applications, the unit cell with volume Ω is discretized in $128 \times 128 \times 128$ voxels. The material is only subjected to an eigenstrain field (which is a stress-free strain). As only eigenstrains are imposed, the overall applied stress is set to zero. The overall strain is unknown and updated at each step following the algorithm described in algorithm3. The detailed eigenstrain fields will be specified for each application.

2.2.4.1 Homogeneous cubic inclusion

We study the mechanical fields generated by an uniform eigestrain field localized in a cubic inclusion. This inclusion shape is centered in the unit cell and his dimensions are $32 \times 32 \times 32$ voxels . For this case, the isotropic elastic constants of both matrix and inclusion are the following : The Young's modulus is $E_m = E_i = 333.4GPa$ and the Poisson ratio is $\nu_m = \nu_i = 0.26$. This approximately corresponds to the room temperature elastic constants for a single crystalline Ni-based superalloy. The eigenstrain ε^*_{ij} is assumed to be present in the inclusion and uniform in it defined as : $\varepsilon^*_{ij} = 0$ for all i, j except $\varepsilon^*_{33} = 1$. This value of the eigenstrain field allows to compute analytical solutions for the homogeneous cubic inclusion for comparison with numerical results. The analytical results is presented in Appendix C following [84]

The algorithm described in algorithm3 is used to compute the stress field at every voxel of the unit cell. The precision is fixed at 10^{-6}. The algorithm converges in one iteration as excepted for this homogeneous case. Fig. 2.1 shows a diagonal component (σ_{33}) and Fig. 2.2 shows a non-diagonal component (σ_{12}) of the stress field for both numerical and analytical method.

The results of fig.2.1 shows that FFT-method are efficent techniques for com-

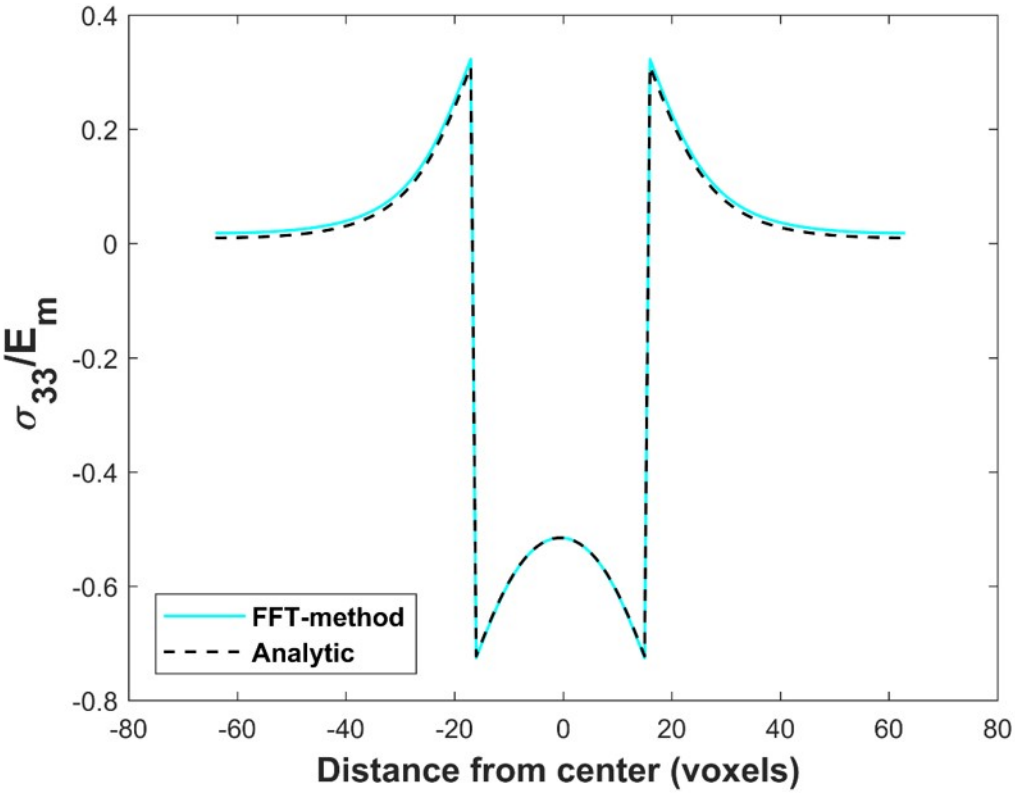


FIGURE 2.1 – The normalized stress component σ_{33} along the z-axis through the center of the unit cell for the cubic-shaped inclusion configuration with eigenstrain, given by FFT-method and analytical solution (see Appendix C).

puting the local stress field. The shape of the stress fields given by FFT-method and analytical method are almost similar. The stress fields are identical in the center of the unit cell and the small discrepancy at the border of the unit cell is due to periodicity effect, see Appendix C.For the non-diagonal component showed on 2.2, the stress field computed with FFT-method shows some spurious oscillations which are also present on all other non-diagonal component of the stress field (not presented here) . Although these oscillations are impressive on the non-diagonal component, their effect on a macroscopic stress or an homogenized stress field is not important. However for some applications such as X-ray diffraction simulations, these oscillations are harmful and need to be removed.

2.2.4.2 Homogeneous spherical inclusion

In this section, we evaluate the accuracy of the FFT-solution by comparing the numerical results to the reference Eshelby theoretical solutions for a spherical inclu-

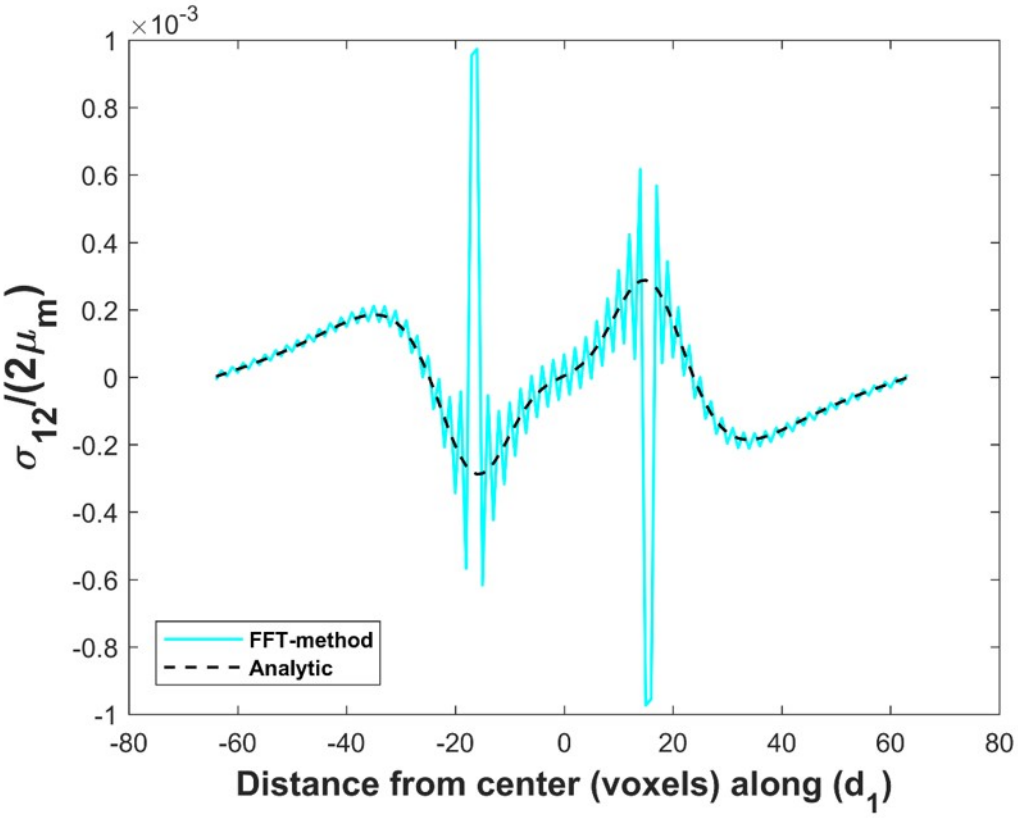


FIGURE 2.2 – The normalized stress component σ_{12} along the z-axis through the center of the unit cell for the cubic-shaped inclusion configuration with eigenstrain, given by FFT-method and analytical solution (see Appendix C).

sion problem with eigenstrain in a homogeneous isotropic elastic periodic medium. According to the Eshelby's theoretical result, the stress is uniform inside an ellipsoidal inclusion [39] whereas it is non uniform outside an ellipsoidal inclusion [40, 104]. The inclusion is centered in the unit cell and his radius is $R = 14\ voxels$. Let us note that for the Eshelby's inclusion solution, the ellipsoidal inclusion (here spherical) is embedded in an infinite matrix. In order to verify that an inclusion radius of 14 voxels for a unit cell of $128 \times 128 \times 128$ voxels is a good approximation, an interesting study was reported by [3]. This study showed that this choice is reasonable and leads to a good match between the numerical FFT-based solution for periodic medium and Eshelby analytical solutions for infinite medium. Whatever the used resolution, a volume fraction of 0.55% for the inclusion is good a approximation. Here, we use the same isotropic elastic constants and eigenstrain tensor as [3] in order to make comparisons with their reported results. The homogeneous Young's modulus is $65.4GPa$ and the homogeneous Poisson ratio is 0.42. The eigenstrain field contained in the inclusion is defined as a pure dilatational eigenstrain : $\varepsilon^*_{ij} = 0.005$ if $i = j$ and $\varepsilon^*_{ij} = 0$ if $i \neq j$.

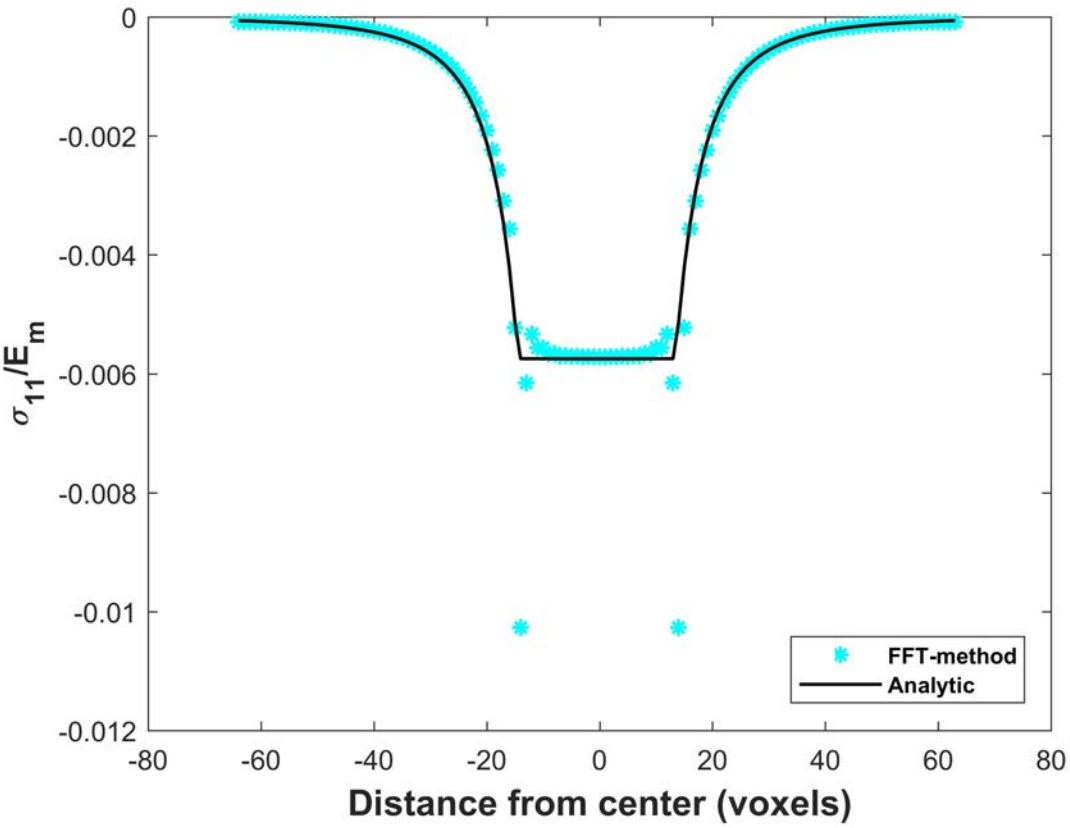


FIGURE 2.3 – Normalized stress field component σ_{11}/E_m along a centered line parallel to the x-axis for the spherical inclusion with eigenstrain, given by the Eshelby's analytical solution and computed with FFT-method. Here, the classic spatial discretization is used : $x_i = i\frac{d}{N}$.

The stress field along a centerline parallel to the x-axis is represented in Fig.2.3. Two interesting discussions can be made by analyzing this figure :First, the constant value of the stress component σ_{11} for the interior points predicted by Eshelby's analytical result is $-375.9MPa$. FFT-methods based gives approximately : $-374MPa$. Thus, the corresponding error is about 0.5% which shows a good accuracy. The shape of the stress field in the matrix is also similar for both FFT-method and analytical result.

Secondly, this figure also shows a special effect at the interface between inclusion and matrix where a large deviation from the Eshelby's solution is observed. This error is not due to oscillations as observed before for the cubic-shaped inclusion near discontinuities but is due to so-called "dangling voxels" which are isolated voxels located at the poles of the spherical inclusion. This discretization problem was explained by [3] who suppressed the problem by increasing the total number of voxels of the unit cell up to $1024 \times 1024 \times 1024$ voxels. Another method to solve this problem is to change the spatial definition of the spherical inclusion with regard to the spatial discretization : a voxel should be assigned to the inclusion if its distance from the center is *less than* the given radius of the inclusion instead of *less than or equal* as frequently used corresponding to the spatial discretization : $x_i = i\frac{d}{N}$. The corresponding real space discretization would be : $x_i = i\frac{d}{N} + \frac{d}{2N}$. Fig 2.12 is an application of such discretization. This figure shows the stress components σ_{11} and σ_{33} obtained with the new spatial discretization. It is shown that the "dangling voxels" effect is eliminated and the FFT-method for σ_{11} and σ_{33} give similar and accurate results as analytical result for these stress components.

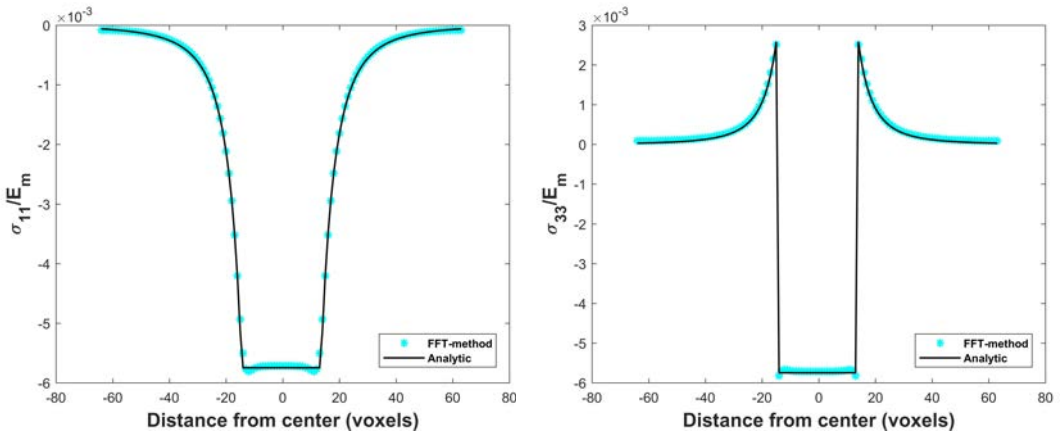


FIGURE 2.4 – Normalized stress field components σ_{11}/E_m (figure (a)) and σ_{33}/E_m (figure (b)) along a centered line parallel to the x-axis for the spherical inclusion with eigenstrain, given by the Eshelby's analytical solution and computed with CGO and DGO_{81}. Here, the following spatial discretization is used : $x_i = i\frac{d}{N} + \frac{d}{2N}$

Now, we represent on fig 2.5, the normalized shear stress field component $\sigma_{12}/(2\nu)$

along a centered line parallel to the x-axis for both FFT-method and analytical method. The stress field computed by FFT-method shows strong oscillations as observed before for the cubic-shaped inclusion.

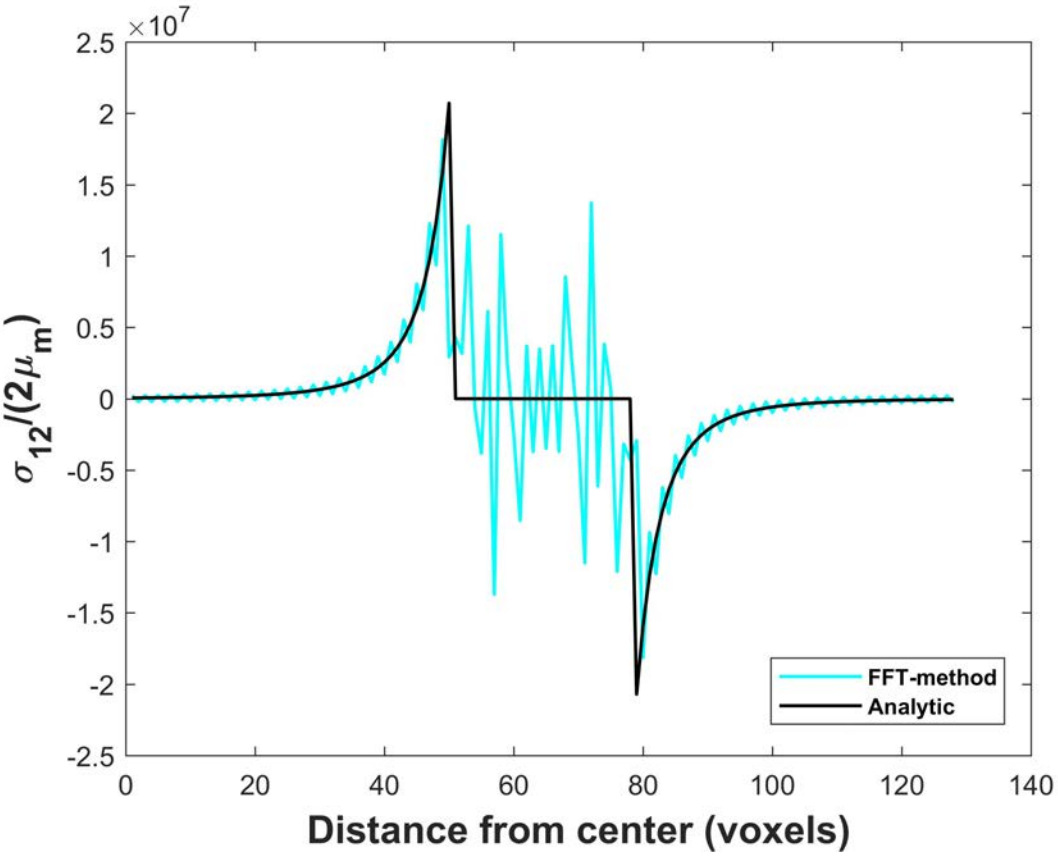


FIGURE 2.5 – Normalized stress field component $\sigma_{12}/(2\nu)$ along a centered line parallel to the x-axis for the spherical inclusion with eigenstrain, given by the Eshelby's analytical solution and computed with FFT-method.

2.3 Suppression of numerical oscillations

In the last section, we showed spurious oscillations on some component of the stress field computed using FFT-method. This oscillations are due to the aliasing or the Gibbs phenomenon as describe in section1.3.1.7. in this section we developed the previous solutions proposed to suppress these numerical oscillations. Most of this solutions are based on the Green operator but they all lead to the modification of the initial algorithm or to the use of another discretization. For example, the use of low-pass filtering proposed in [122] involve to include new functions in the numerical

resolution. The simplicity of the basic algorithm [98, 99] is lost when using "rotated scheme" [156] or staggered grid [120] . To our knowledge, a consistent periodized discrete Green operator (DGO) for the Lippmann-Schwinger equation has not been developed yet. The objective of the next section is to give some mathematical details on the development of such consistent DGO that will be applied to the thermoelastic FFT-based algorithm introduced in Eq. 3.

2.4 Development of consistent periodized discrete Green operators (DGO)

This developement hab been publisehd in International Journal of Plasticity in 2019 [37]

2.4.1 One-dimensional case

First, let us consider a one-dimensional problem for the sake of clarity. We denote $e(x)$ a periodic function of a real variable x that can be identified as the strain field or the displacement field. This function is defined as a spatial convolution of two functions : $t(x)$ a periodic function, which is similar to the stress polarization field and $g(x)$ which is similar to a Green operator. By denoting d the spatial period of $e(x)$ and $t(x)$, $\widehat{T}(\xi)$ the Fourier transform of $t(x)$, we can write (here the notation $j = \sqrt{-1}$ is adopted for the imaginary unit) :

$$t(x) = \sum_{k=-\infty}^{\infty} \widehat{T}(\xi) exp(j2\pi\xi_h x) \tag{2.10}$$

with $\xi_h = \frac{h}{d}$ and :

$$\widehat{T}(\xi) = \frac{1}{d}\int_{-d/2}^{+d/2} t(x) exp(-j2\pi\xi_h x)\mathrm{d}x \tag{2.11}$$

The function $t(x)$ is periodic, then :

$$\widehat{T}(\xi) = \frac{1}{d}\int_{0}^{d} t(x) exp(-j2\pi\xi_h x)\mathrm{d}x$$

For N points along the x-axis, let us now suppose the following spatial discretization for their x position : $x_i = i\frac{d}{N} + \frac{d}{2N}$ where $i \in [0, N-1]$ (see Fig. 2.6).
Let us assume that $t(x)$ is approximated with the discrete stepwise uniform function $t^d(x_i)$ derived in a consistent way with the introduced spatial discretization as shown in Fig. 2.6.

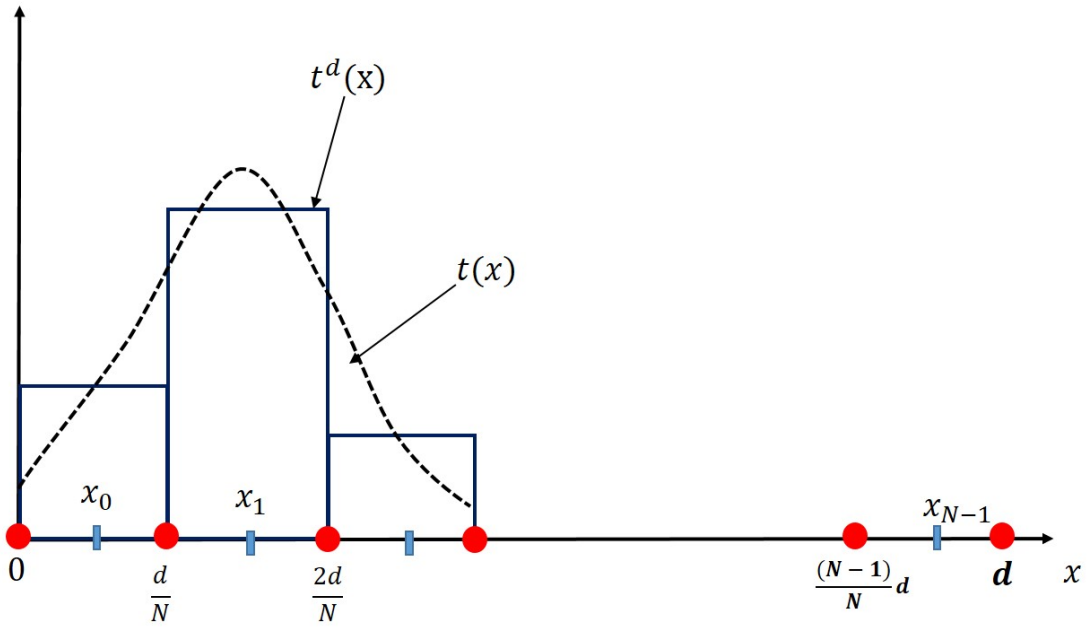


FIGURE 2.6 – Definition of $t^d(x_i)$ with respect to $t(x)$. This configuration is consistent with the spatial discretization explained in the text.

The Fourier transform of $t^d(x_i)$ is denoted $\widehat{T^d}(\xi_h)$. Using the discrete piece-wise approximation of $t(x)$ by $t^d(x_i)$ and the fact that :

$$\int_0^d \approx \sum_{i=0}^{N-1} \int_{x_i-\frac{d}{2N}}^{x_i+\frac{d}{2N}}$$

the Fourier transform of $t^d(x_i)$ reads :

$$\widehat{T^d}(\xi_h) = \frac{1}{d} \sum_{i=0}^{N-1} t^d(x_i) \int_{x_i-d/2N}^{x_i+d/2N} exp(-j2\pi\xi_h x')\mathrm{d}x' \tag{2.12}$$

Using the change of variables $X = x' - x_i$ yields :

$$\widehat{T^d}(\xi_h) = FT[t^d(x_i)](\xi) = \frac{1}{d} \sum_{i=0}^{N-1} t^d(x_i) exp(-j2\pi\xi_h x_i) \int_{-d/2N}^{d/2N} exp(-j2\pi\xi_h X)\mathrm{d}X \tag{2.13}$$

From the formula :

$$\int_{-d/2N}^{+d/2N} exp(-j2\pi\xi_h X)\mathrm{d}X = \frac{d}{N} sinc\left(\pi\xi_h \frac{d}{N}\right)$$

we obtain :

$$\widehat{T^d}(\xi_h) = \frac{1}{N} sinc\left(\pi\xi_h \frac{d}{N}\right) \sum_{i=0}^{N-1} t^d(x_i) exp(-j2\pi\xi_h x_i) \tag{2.14}$$

In Eq. 2.14, the Discrete Fourier Transform (DFT) of $t^d(x_i)$ can be identified :

$$\widehat{T^D}(\xi_h) = \sum_{i=0}^{N-1} t^d(x_i) exp(-j2\pi\xi_h x_i) \tag{2.15}$$

Therefore, Eq. 2.14 becomes :

$$\widehat{T^d}(\xi_h) = \frac{1}{N}\widehat{T^D}(\xi_h) sinc\left(\pi\frac{k}{N}\right) \tag{2.16}$$

where k varies from $-\infty$ to $+\infty$. Using a change of variables : $k = mN + l$, where $l \in [0, N-1]$ and m varies from $-\infty$ to $+\infty$, the last equation writes :

$$\widehat{T^d}(\xi_h) = \frac{(-1)^m}{\pi(mN+l)}\widehat{T^D}(\xi_h) sin\left(\pi\frac{l}{N}\right) \tag{2.17}$$

Eq. 2.17 defines the Fourier transform of a continuous periodic function as a function of the Fourier transform of the discrete stepwise function $t^d(x_i)$.

With the previous definitions, the Fourier transform of the function $g(x)$ (Green operator) is denoted $\widehat{G}(\xi)$. It is defined through the relationship between $\widehat{T}(\xi)$ the Fourier transform of $t(x)$ and $\widehat{E}(\xi)$ the Fourier transform of $e(x)$:

$$\widehat{E}(\xi) = \widehat{G}(\xi)\widehat{T}(\xi) \tag{2.18}$$

with :

$$e(x) = \sum_{k=-\infty}^{\infty} \widehat{E}(\xi_h) exp(j2\pi\xi_h x) \tag{2.19}$$

where $\xi_h = \frac{k}{d}$ denotes the discrete frequencies. Using the variable $k = mN + l$ as introduced before, $e(x)$ writes :

$$e(x) = \sum_{l=0}^{N-1}\sum_{m=-\infty}^{\infty} \widehat{E}(\xi_{mN+l}) exp(j2\pi\xi_{mN}x) exp(j2\pi\xi_l x) \tag{2.20}$$

Here, $e(x)$ is approximated by $e^d(x_i)$:

$$e^d(x_i) = \sum_{l=0}^{N-1}\sum_{m=-\infty}^{\infty} \widehat{E}(\xi_{mN+l}) exp(j2\pi\xi_{mN}x_i) exp(j2\pi\xi_l x_i) \tag{2.21}$$

Using $x_i = i\frac{d}{N} + \frac{d}{2N}$ (where i=0,1,.....N-1) leads to :

$$e^d(x_i) = \sum_{l=0}^{N-1} exp(j2\pi\xi_l x_i) \sum_{m=-\infty}^{\infty} (-1)^m \widehat{E}(\xi_{mN+l}) \tag{2.22}$$

Here, we can remark that if $e^d(x_i)$ has a finite value at all points x_j in the periodic domain, then the infinite sum $\sum_{m=-\infty}^{\infty} (-1)^m \widehat{E}(\xi_{mN+l})$ is also finite at all Fourier points

ξ_l with $l \in [0, N-1]$. Now, we can use the definition of the inverse DFT to calculate $e^d(x_i)$:

$$e^d(x_i) = \frac{1}{N} \sum_{l=0}^{N-1} \widehat{E^D}(\xi_l) exp(j2\pi\xi_l x_i) \tag{2.23}$$

By comparing Eq. 2.22 and Eq. 2.23, the DFT of $e(x)$ can be identified as :

$$\widehat{E^D}(\xi_l) = N \sum_{m=-\infty}^{\infty} (-1)^m \widehat{E}(\xi_{mN+l}) \tag{2.24}$$

where $\widehat{E^D}(\xi_l)$ is finite at all Fourier points ξ_l. For each discrete $k = mN + l$, we directly obtain from Eq. 2.18 :

$$\widehat{E}(\xi_{mN+l}) = \widehat{G}(\xi_{mN+l})\widehat{T}(\xi_{mN+l}) \tag{2.25}$$

The expression of $\widehat{T}(\xi_{mN+l})$ is obtained from Eq. 2.17 :

$$\widehat{T^d}(\xi_{mN+l}) = \frac{(-1)^m}{\pi(mN+l)} \widehat{T^D}(\xi_{mN+l}) sin\left(\pi \frac{l}{N}\right) \tag{2.26}$$

Then, we have from the DFT :

$$\widehat{T^D}(\xi_{mN+l}) = \sum_{l=0}^{N-1} t^d(x_i) exp(-j2\pi\xi_{mN+l}x_i) = (-1)^m \widehat{T^D}(\xi_l) \tag{2.27}$$

Finally, Eq. 2.26 reads :

$$\widehat{T^d}(\xi_{mN+l}) = \frac{1}{\pi(mN+l)} \widehat{T^D}(\xi_l) sin\left(\pi \frac{l}{N}\right) \tag{2.28}$$

By using Eq. 2.24, Eq. 2.25 and Eq. 2.28 :

$$\widehat{E^D}(\xi_l) = N \sum_{m=-\infty}^{\infty} \widehat{G}(\xi_{mN+l})(-1)^m \frac{sin\left(\frac{\pi l}{N}\right)}{\pi(mN+l)} \widehat{T^D}(\xi_l) \tag{2.29}$$

From this last equation, we deduce the final expression of the periodized discrete Fourier transform of $g(x)$ denoted $\widehat{G^D}(\xi_l)$:

$$\widehat{G^D}(\xi_l) = \frac{N}{\pi} sin\left(\frac{\pi l}{N}\right) \sum_{m=-\infty}^{\infty} \frac{(-1)^m}{mN+l} \widehat{G}(\xi_{mN+l}) \tag{2.30}$$

$\widehat{G^D}(\xi_l)$ represents a discrete Green operator (DGO) for this one-dimensional problem which converges to a finite value at all Fourier points ξ_l with $l \in [0, N-1]$ due to the definition $\widehat{E^D}(\xi_l) = \widehat{G^D}(\xi_l)\widehat{T^D}(\xi_l)$ and the convergence of $\widehat{E^D}(\xi_l)$ to a finite value (see above). In the next sub-section, we will define the consistent periodized DGO for the three-dimensional problem to solve the Lippmann-Schwinger equation (i.e. the strain solution).

2.4.2 Consistent periodized discrete Green operators $\widehat{\boldsymbol{\Gamma}^D}(\boldsymbol{\xi}_{ijq})$

The theoretical result given by Eq. 2.30 for the one-dimensional discrete configuration can be easily extended to obtain consistent three-dimensional periodized discrete Green operators (DGO) related to tensors $\widehat{\boldsymbol{\Gamma}}(\boldsymbol{\xi})$ defined in section 2.2.2 through Eq. 2.8. With previous notations, the single index l in Eq. 2.30 can be replaced by three indices i, j, k to obtain DGO expression with triple infinite sums from the definitions :

$$\widehat{\boldsymbol{\varepsilon}^D}(\boldsymbol{\xi}_{ijq}) = -\widehat{\boldsymbol{\Gamma}^D}(\boldsymbol{\xi}_{ijq}) : \widehat{\boldsymbol{\tau}^D}(\boldsymbol{\xi}_{ijq}) \qquad \forall \boldsymbol{\xi}_{ijq} \neq 0 \tag{2.31}$$

such that :

$$\widehat{\boldsymbol{\Gamma}^D}(\boldsymbol{\xi}_{ijq}) = A_{ijq} \sum_{m,n,p=-\infty}^{\infty} \frac{(-1)^{m+n+p}}{mN+i} \frac{1}{nN+j} \frac{1}{pN+q} \widehat{\boldsymbol{\Gamma}}(\boldsymbol{\xi}_{mN+i,nN+j,pN+q}) \tag{2.32}$$

where :

$$A_{ijq} = \left(\frac{N}{\pi}\right)^3 sin\left(\frac{\pi i}{N}\right) sin\left(\frac{\pi j}{N}\right) sin\left(\frac{\pi q}{N}\right) \tag{2.33}$$

and $\boldsymbol{\xi}_{ijq}$ are three-dimensional discrete frequencies with $i \in [0, N-1], j \in [0, N-1], q \in [0, N-1]$.

2.4.3 Symetries and convergence of $\widehat{\boldsymbol{\Gamma}^D}(\boldsymbol{\xi}_{ijq})$

Due to the symmetry properties of $\widehat{\Gamma}, \widehat{\Gamma^D}$ has these symmetries :

$$\widehat{\Gamma^D_{ijql}} = \widehat{\Gamma^D_{jiql}} = \widehat{\Gamma^D_{ijlq}} = \widehat{\Gamma^D_{qlij}}$$

;

$$\widehat{\Gamma^D_{ijql}}(-\boldsymbol{\xi}) = \widehat{\Gamma^D_{ijql}}(\boldsymbol{\xi})$$

The last symmetry property allows to compute $\widehat{\boldsymbol{\Gamma}^D}$ only for positive frequencies and deduce the value of negative frequencies. Only some component of $\widehat{\boldsymbol{\Gamma}^D}$. All these properties allows to reduce computaional time and the numerical computations of $\widehat{\boldsymbol{\Gamma}^D}$ is performed only once before performing the iterative algorithm.

Using the same arguments as for the one-dimensional case, it is straightforward to show that the infinite serie $\widehat{\boldsymbol{\Gamma}^D}(\boldsymbol{\xi}_{ijq})$ converges to finite values at all three-dimensional Fourier points ξ_{ijq}. However this not easy to establish analytically the convergence of this infinite serie. Numerical experiments (see section 2.5) will show that this series converges but slowly. This is explained using using Eq. 3.8 and the fact that N_{ij} is a polynomial homogeneous function of degree 4 and D is a polynomial homogeneous function of degree 6, so according to Eq. 3.8 together with Eq. 2.8 or Eq. 3.7, the $\widehat{\Gamma_{ijql}}$ components are homogeneous functions of degree 0.
A parametric study and examples will be proposed on three-dimensional computational grids to evaluate the convergence of the developed discrete consistent Green operator $\widehat{\boldsymbol{\Gamma}^D}(\boldsymbol{\xi}_{ijq})$ that has the form of infinite series by choosing a satisfactory truncation order to obtain accurate numerical results in comparisons with analytical solutions. Truncated discrete Green operators at the k-order will be denoted DGO_k and the infinite sums on m, n, p will be replaced by finite sums on m, n, p in the interval $[-k, k-1]$ where k is an integer.
As shown in Appendix B, the values of the stepwise strain fields computed with DGO_k at the center of the N^3 voxels are equal to those computed at the same points with the CGO (i.e. $\widehat{\boldsymbol{\Gamma}}$) on a subdivided $(2kN)^3$ grid. As the stress and strain fields have discontinuities at the boundaries of each of the N^3 voxels, a full computation with $\widehat{\boldsymbol{\Gamma}}$ on the $(2kN)^3$ computational grid exhibits the usual Gibbs oscillations at the voxel edges. However, as the mechanical fields are actually computed at the centers of the N^3 voxels, i.e. far from the discontinuities, no oscillation occurs when using the DGO_k.

2.4.4 Comparison with the consistent periodized discrete Green operator introduced by Brisard and Dormieux [16, 17]

The discrete Green operator proposed in Eq. 2.32 is very similar in spirit to the consistent discrete Green operator developed by [16, 17]. However, their operator has some major difference with Eq. 2.32. To compare both discrete Green operators, let us consider a two-dimensional computational grid as in [16, 17]. Therefore, Eq. 2.32 reduces to :

$$\widehat{\boldsymbol{\Gamma}^D}(\boldsymbol{\xi}_{ij}) = \left(\frac{N}{\pi}\right)^2 sin\left(\frac{\pi i}{N}\right) sin\left(\frac{\pi j}{N}\right) \sum_{m,n=-\infty}^{\infty} \frac{(-1)^{m+n}}{mN+i} \frac{1}{nN+j} \widehat{\boldsymbol{\Gamma}}(\boldsymbol{\xi}_{mN+i,nN+j}) \tag{2.34}$$

Using the definition of the *sinc* function, we have :

$$\begin{aligned} sinc\left(\frac{\pi(mN+i)}{N}\right) &= (-1)^m \left(\frac{N}{\pi}\right) sin\left(\frac{\pi i}{N}\right) \frac{1}{mN+i} \\ &= (-1)^m i \, (mN+i)^{-1} \, sinc\left(\frac{\pi i}{N}\right) \end{aligned} \tag{2.35}$$

Then, Eq. 2.34 can be rewritten as follows :

$$\widehat{\boldsymbol{\Gamma}^D}(\boldsymbol{\xi}_{ij}) = (ij)sinc\left(\frac{\pi i}{N}\right)sinc\left(\frac{\pi j}{N}\right)\sum_{m,n=-\infty}^{\infty}\frac{(-1)^{m+n}}{mN+i}\frac{1}{nN+j}\widehat{\boldsymbol{\Gamma}}(\boldsymbol{\xi}_{mN+i,nN+j}) \quad (2.36)$$

which is different from the expression given by [16] (p. 667) :

$$\widehat{\boldsymbol{\Gamma}^D}(\boldsymbol{\xi}_{ij}) = (i^2j^2)sinc^2\left(\frac{\pi i}{N}\right)sinc^2\left(\frac{\pi j}{N}\right)\sum_{m,n=-\infty}^{\infty}\frac{1}{(mN+i)^2}\frac{1}{(nN+j)^2}\widehat{\boldsymbol{\Gamma}}(\boldsymbol{\xi}_{mN+i,nN+j}) \quad (2.37)$$

By comparing Eq. 2.36 with Eq. 2.37, it is remarkable to see that both expressions are different in the sense that the discrete Green operator of [16, 17] contains the same terms as for the present discrete Green operator but these ones are raised to the power squared. A fine comparison with the paper of [16](see the exact DFT expression of the stress polarization on top right p. 666 in [16]) shows that our derivations in section 2.4.1 is the same as their derivation up to Eq. 2.17 but is different from Eqs. 2.17 to 2.30. This difference results from the use the Lippmann-Schwinger equation which is a convolution as in Eq. 2.18 while in [16] an energy formulation based on the Hashin-Shtrikman variational principle was derived with the help of the Plancherel theorem, see their equations (7) and (12). Let us note that both discrete operators satisfy : $\widehat{\boldsymbol{\Gamma}^D}(\boldsymbol{\xi}_{00}) = \mathbf{0}$. In this paper, the discrete Green operator derived by [16, 17] will not be discussed anymore in the numerical examples since it is designed for a Galerkin based algorithm, i.e. starting from the weak form of the Lippmann-Schwinger equation instead of its strong form as in section 2.2.3.

2.5 Applications to references cases

In the forthcoming applications, the unit cell with volume Ω is discretized in $128 \times 128 \times 128$ voxels. The heterogeneous material is only subjected to an eigenstrain field (which is a stress-free strain). As only eigenstrains are imposed, the overall applied stress is set to zero. The overall strain is unknown and updated at each step following the algorithm described in section 2.2. The detailed eigenstrain fields will be specified for each application. In this section, the FFT-based method using the classical continuous Green operator will be denoted *CGO* (Continuous Green Operator) [99] and the FFT-based method with the proposed discrete Green operator (computed with a given truncation order k) will be denoted DGO_k (Discrete Green Operator).
First, in section 2.5.1, a cubic-shaped inclusion with eigenstrain field is studied, in homogeneous isotropic elasticity and the obtained stress fields are calculated using the *DGO* with different orders k as well as the *CGO* approximation, like in section 2.2.4. The numerical results will be compared to analytical solutions considered as

periodic solutions started from the solution given by [84] (see Appendix C). In section 2.5.2, a spherical Eshelby-type problem is reconsidered to assess the present numerical method based on DGO_k. In section 2.5.3, a spherical inhomogeneity solution with eigenstrain is considered and discussed using low contrasted elastic moduli between phases as in [3].

2.5.1 Cubic-shaped eigenstrained inclusion in a homogeneous isotropic elastic periodic medium

For this case, the isotropic elastic constants of both matrix and inclusion are the following : The Young's modulus is $E_m = E_i = 333.4GPa$ and the Poisson ratio is $\nu_m = \nu_i = 0.26$, as in section2.2.4.1. The eigenstrain ε^*_{ij} is assumed to be present in the inclusion and uniform in it defined as : $\varepsilon^*_{ij} = 0$ for all i, j except $\varepsilon^*_{33} = 1$.
The inclusion shape is cubic and is centered in the unit cell. The dimensions of the cubic-shaped inclusion are $32 \times 32 \times 32$ voxels. This inclusion is schematically represented in Fig. 2.7 with the Cartesian basis. Some specific material points are considered to examine the spatial stress variations at different locations away or near materials discontinuities. These points are denoted O, A, B, C in Fig. 2.7 and their positions are given in terms of voxel numbers from the center O of the unit cell (or the cube). Therefore, the voxel coordinates of these points are $O(0,0,0), A(16,0,0), B(16,16,16), C(0,16,16)$. Three different specific lines denoted d_1, d_2, d_3 are also reported on Fig. 2.7. These lines are specifically designed to study stress profiles along their path as a function of the distance from materials discontinuities (inclusion/matrix interfaces, junctions between two sides of the cube, edge lines, cube corners, etc.)

The presence of the eigenstrain field is at the origin of the development of inelastic incompatibilities and therefore non uniform (internal) stress field σ_{ij} inside both the inclusion and the matrix are obtained. Three stress components, namely σ_{33}, σ_{11}, σ_{12}, resulting from the different CGO, DGO_k with different values of k are reported on Fig. 2.8 and Fig. 2.9. Fig. 2.8 displays the profile of σ_{33} normalized by E_m along the line d_1 (Fig. 2.8(a)(b)) and along the line d_2 (Fig. 2.8(c)(d)). Fig. 2.9 displays the profile of σ_{11} normalized by E_m along the line d_1 (Fig. 2.9(a)(b)) and the profile of σ_{12} normalized by $2\mu_m$ (where μ_m is the elastic shear modulus) along the line d_1 (Fig. 2.9(c)(d)). In both figures, the stress field solutions are zoomed up to well observe the differences between the numerical approximations and the analytical solution in Fig. 2.8(b)(d) and in Fig. 2.9(b)(d). To study the convergence of the DGO_k, k varies from 1 to 101 and the analytical result (see Appendix C) is also reported on Fig. 2.8 and Fig. 2.9 for comparison.

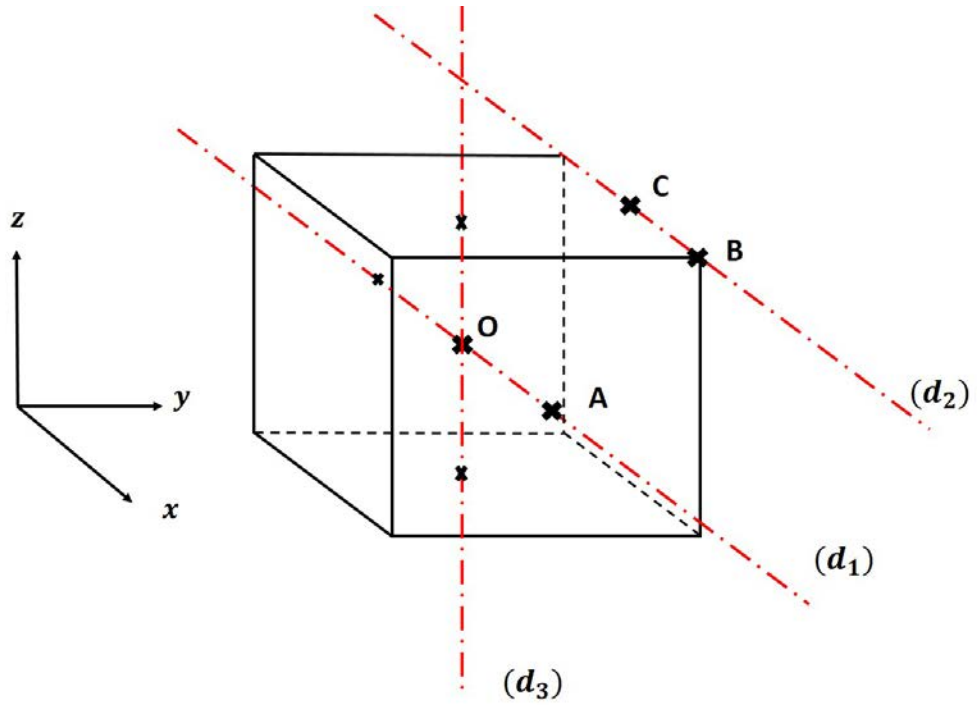


FIGURE 2.7 – Representation of the cubic-shaped inclusion. The line d_1 is defined as parallel to the x-axis through the center of the unit cell, the line d_2 is defined as parallel to the x-axis through an edge line, the line d_3 is defined as paralle to the z-axis through the center of the unit cell. Materials points O, A, B, C are some specific points used in analysis of numerical results.

The first comment concerns the convergence rate and the accuracy given by the periodized DGO_k as a function of k. From $k = 81$, it is observed from all stress components that the numerical stress values tend to the same values along the lines d_1 and d_2. This means that the proposed DGO_k tends to converge but slowly, which was expected from section 2.4. Furthermore, looking at the zoomed pictures, it is observed that the DGO_{81} leads to very accurate results compared to the analytical result. At first glance, the CGO gives relatively good results regarding σ_{33} as well along the two paths d_1 and d_2 and regarding σ_{11} along d_1. However, Fig. 2.9(c) shows inaccurate results due to spurious oscillations on the σ_{12} component with the CGO along the line d_1.

In order to quantify the convergence of periodized DGO_k, the relative difference ϵ is calculated between the analytical solution and the numerical solutions for σ_{33} obtained at different locations from DGO_k or CGO. This relative difference is defined as :

$$\epsilon = \left| \frac{\sigma_{33}^{num} - \sigma_{33}^{anal}}{\sigma_{33}^{anal}} \right|$$

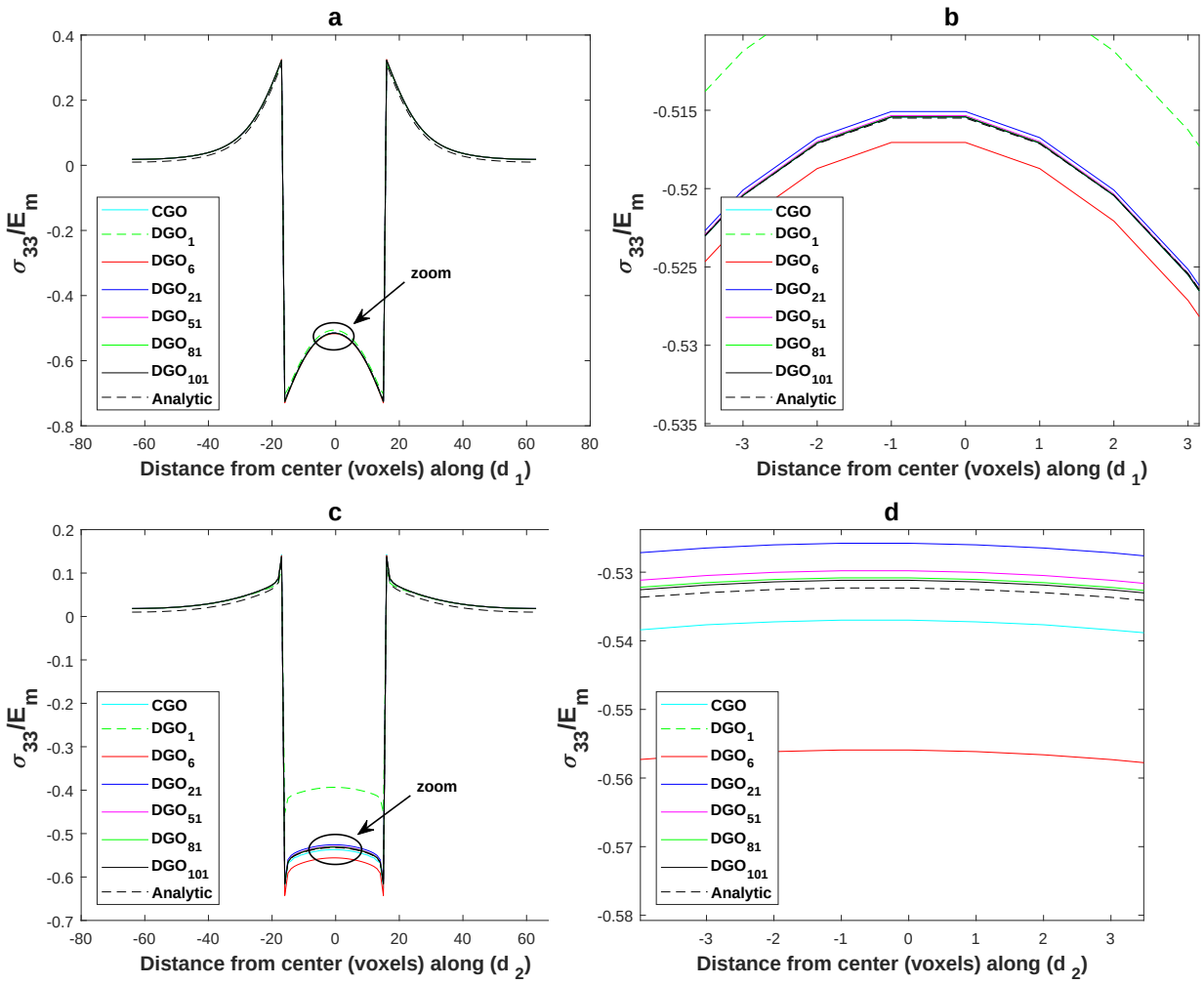


FIGURE 2.8 – The normalized stress component σ_{33} along d_1 (figures (a) and (b)) and along d_2 (figures (c) and (d)) for he cubic-shaped inclusion configuration with eigenstrain, given by analytical solution ((see Appendix C)), and computed with CGO and DGO_k for different k (DGO_1, DGO_6, DGO_{21}, DGO_{51}, DGO_{81}, DGO_{101}).

The values of ϵ are computed at the specific points O, A, B, C of the inclusion. Fig. 2.10 shows the relative difference ϵ plotted as a function of k using logarithmic scales. It is observed that ϵ decreases as k increases. Besides, the value of ϵ calculated with the DGO_k approximation reaches an admissible value (i.e. $\epsilon < 5 \times 10^{-3}$) for a truncation of the DGO corresponding to $k = 81$.

Fig. 2.10 also shows the relative difference ϵ computed with the CGO. At the center of the inclusion (i.e. where there is no materials discontinuity) (Fig. 2.10(a)), ϵ is close to 10^{-4} with the CGO which is similar to the result given by the DGO_k with $k = 101$. However, the prediction given by the CGO is not as good as point O for the other points where materials discontinuities are present such as points B, A, C as observed on Figs. 2.10(b)(c)(d) respectively. For all these points, the

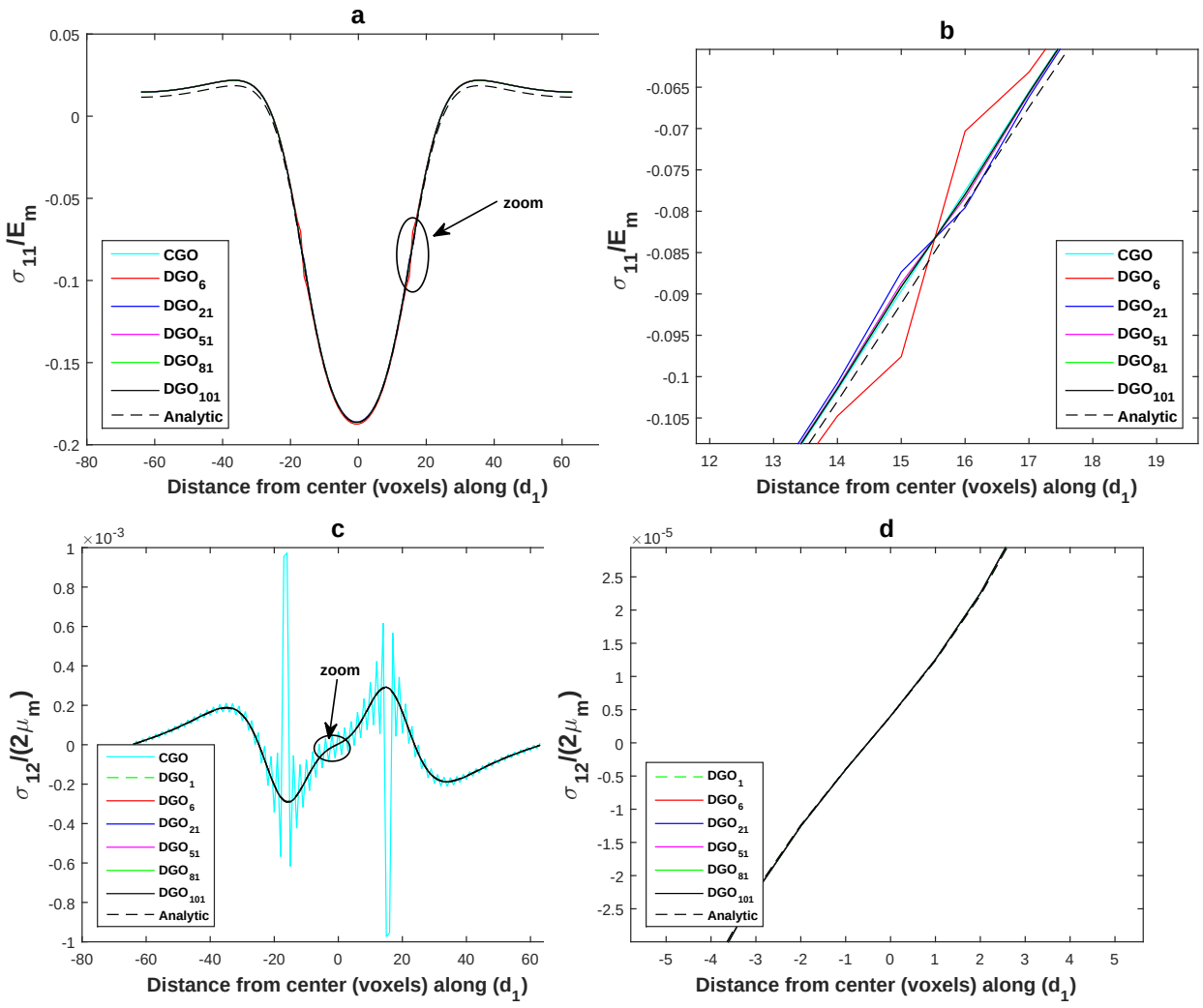


FIGURE 2.9 – The normalized stress components σ_{11} (figures (a) and (b)) and σ_{12} (figures (c) and (d)) along the line d_1 for the cubic-shaped inclusion configuration with eigenstrain, given by the analytical solution (see Appendix C), and computed with CGO and DGO_k for different k (DGO_1, DGO_6, DGO_{21}, DGO_{51}, DGO_{81}, DGO_{101}).

relative difference with the analytical solution obtained with DGO_{81} is much smaller than the one with CGO. It means that the proposed periodized discrete Green operator $\widehat{\mathbf{\Gamma}}^D$ (Eq. 2.32) improves the accuracy of the classical FFT-based method algorithm based on the CGO in the vicinity of materials discontinuities and $k = 81$ reflects a good compromise to have enough accuracy for this example. However, the computational time is more important with DGO_k : it is multiplied by $(2k)^3$ (due to $3D$ infinite sum containing in Eq. 2.32) but in practice, this multiplicative factor is less important. For example, the computational time for computed CGO on our cluster (Intel Xeon X5550 2.66GHz CPU 46 nodes, 48Go per node) is 7 seconds and the computational time for DGO_{81} is 116913 seconds. The numerical burden is

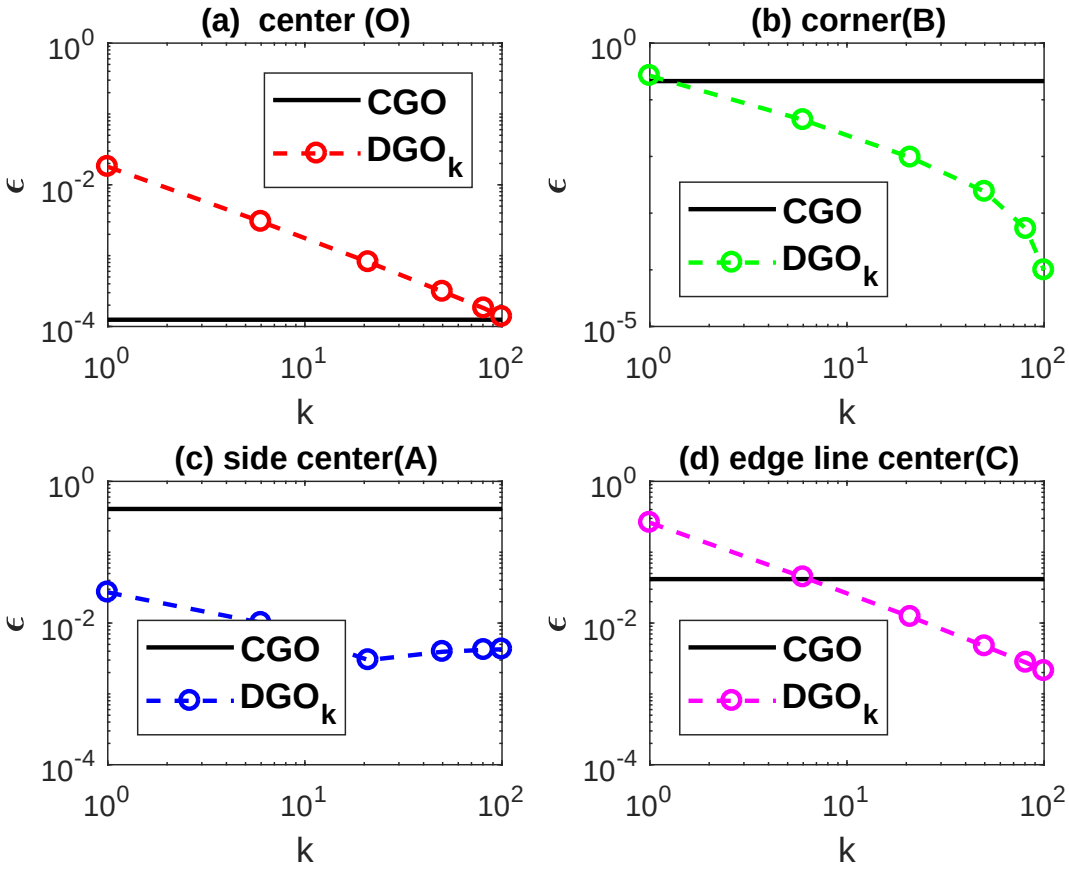


FIGURE 2.10 – Relative difference ϵ computed at some specific points O (figure (a)), B (figure (b)), A (figure (c)), C (figure (d)). The specific points were defined in Fig. 2.7 of the cubic-shaped inclusion with CGO and DGO_k (for different values of k). Solid lines represent the CGO solution and dotted lines represent the DGO_k solutions.

thus very important but DGO_{81} is computed only one time and can be stored for later use. In addition, it is not always necessary to set $k = 81$. In Fig. 2.10, it is shown that it is possible to have also acceptable results for lower k, except at the cubic-shaped center.

In addition to accuracy, the most important advantage of DGO_k is its beneficial effect on the oscillations that appear on some components of the stress field (e.g. σ_{12}) with spectral methods based on the CGO. The numerical oscillations are completely removed by DGO_{81}. [99] already observed and commented these numerical oscillations on the mechanical fields. To fix the problem, these authors used a different expression of the classical modified Green operator at the highest frequencies as recalled in section 2.2.3. This procedure means that the classical Green operator is "truncated" at such frequencies. As an example of comparison with the DGO, Fig.

2.13 shows the effect of the Moulinec-Suquet's "truncation" method and the effect of DGO_{81} on the normalized shear stress (σ_{12} normalized with $2\mu_m$). This figure clearly shows that the procedure proposed by [99] is not sufficient to completely suppress the oscillations observed on this stress component along d_1 whereas the periodized discrete Green operator DGO_{81} completely removes them.

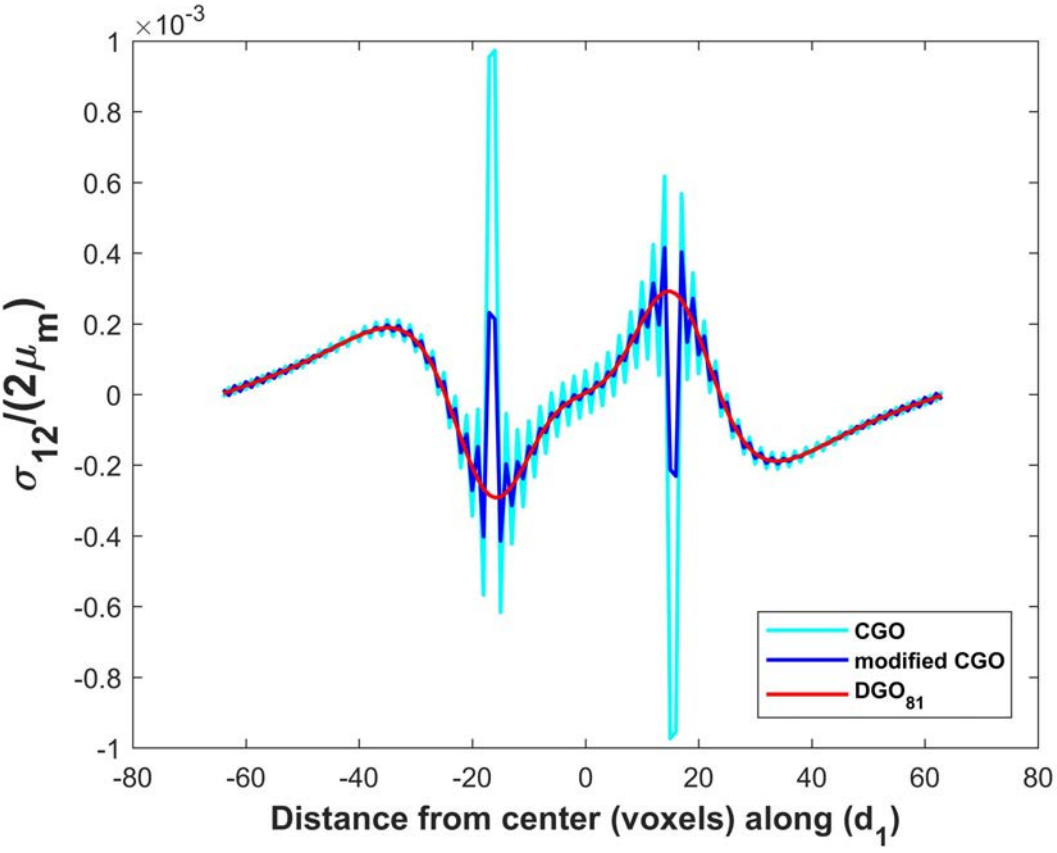


FIGURE 2.11 – The shear stress component σ_{12} normalized with $2\mu_m$ (where μ_m is the elastic shear modulus) for the cubic-shaped inclusion configuration with homogeneous isotropic elasticity computed with CGO, DGO_{81} and FFT-solution with CGO "truncated" at the highest frequencies [99] (named "modified CGO" in the figure).

2.5.2 Spherical inclusion problem with eigenstrains in a homogeneous isotropic elastic periodic medium

In this section, we evaluate the accuracy of the proposed DGO solution by comparing the numerical results to the reference Eshelby solution for a spherical inclusion problem with eigenstrain in a homogeneous isotropic elastic periodic medium. This study and the example performed in section2.2.4.2 but here, the stress field is computed also using DGO. The spherical inclusion is defined using the real space discretization : $x_i = i\frac{d}{N} + \frac{d}{2N}$ to avoid "dangling voxels effect" described above.

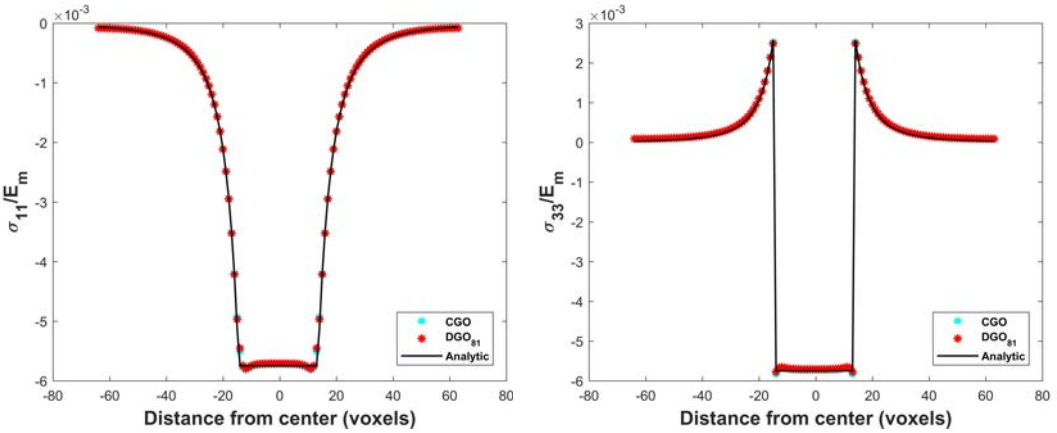


FIGURE 2.12 – Normalized stress field components σ_{11}/E_m (figure (a)) and σ_{33}/E_m (figure (b)) along a centered line parallel to the x-axis for the spherical inclusion with eigenstrain, given by the Eshelby's analytical solution and computed with CGO and DGO_{81}. Here, the following spatial discretization is used : $x_i = i\frac{d}{N} + \frac{d}{2N}$

The stress field components σ_{11} and σ_{33} along a centerline parallel to the x-axis is represented for three cases in Fig. 2.12 : CGO, DGO_{81} and Eshelby's solution. The constant value of the stress component σ_{11} for the interior points predicted by Eshelby's analytical result is $-375.9MPa$. Both FFT-methods based on CGO and DGO_{81} give approximately the same value : $-374MPa$. Thus, the corresponding error is about 0.5% which shows a good accuracy without oscillation. We conclude that for components which don't shows numerical oscillations, the classic Green opertor provide an interesting precision and the proposed discrete operator also provide a identical accuracy.

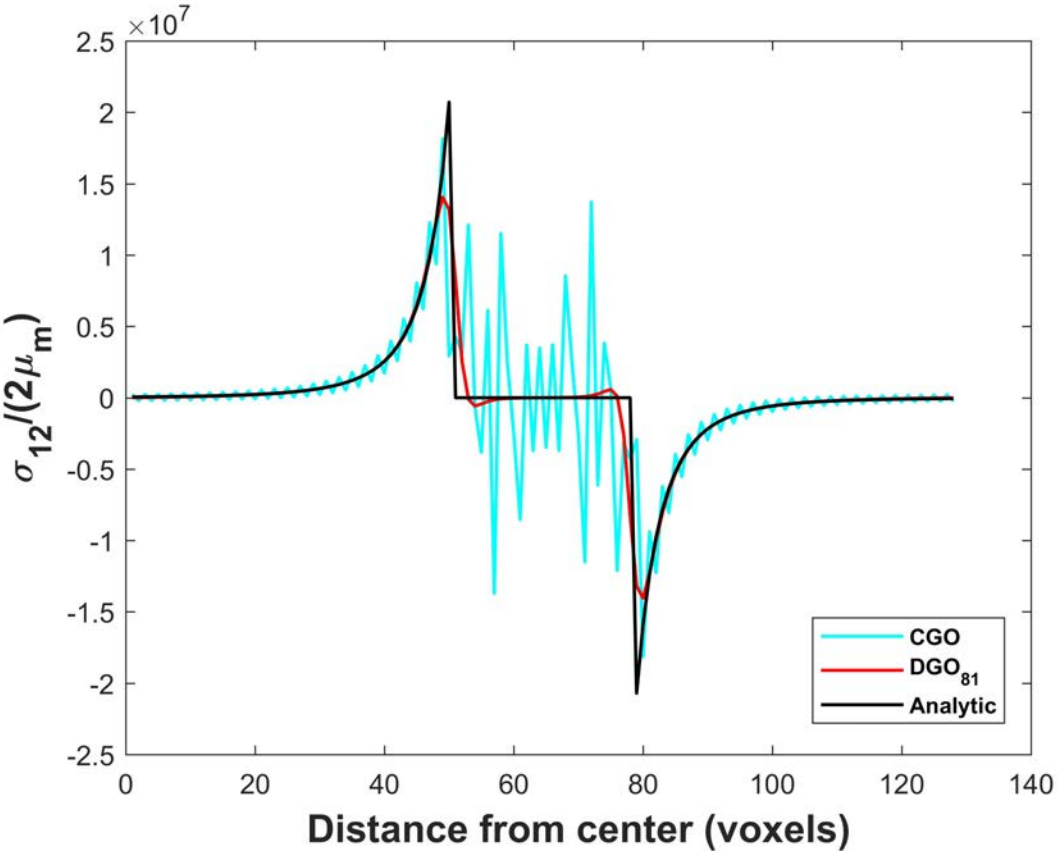


FIGURE 2.13 – Normalized stress field component $\sigma_{12}/(2\mu_m)$ along a centered line parallel to x-axis for the spherical inhomogeneity problem with eigenstrain, given by analytical solutions and numerically computed with CGO and DGO_{81}.

2.5.3 Spherical inhomogeneity problem with eigenstrains

Here, the same spherical configuration as in section 2.5.2 is considered but with elastic inhomogeneity in addition to eigenstrain. An inhomogeneity radius of 14 voxels is still used for a unit cell of $128 \times 128 \times 128$ voxels. The isotropic elastic stiffness tensor of the inhomogeneity is different from the one of the matrix phase. Like in [3], the bulk modulus of the matrix phase is fixed and the bulk modulus of the inhomogeneity phase is defined by the ratio $R = K_m/K_i = 2$, which means that the inhomogeneity i is more compliant than the matrix m. Here, the case $R = 0.5$, i.e. an inhomogeneity stiffer than the matrix, is also investigated to test the numerical convergence for both inverse contrasts, see Fig. 2.15. The isotropic Young's modulus of the matrix phase is $E_m = 65.4$GPa and the Poisson ratio for matrix and inhomogeneity phases is $\nu_m = \nu_i = 0.42$. This corresponds to a small mechanical contrast that can be treated with the fixed-point algorithm described in algorithm. 3. The elastic constants of the reference medium are chosen as : $K_0 = \beta(K_m + K_i)$, $\nu_0 = \nu_m = \nu_i = 0.42$ with $\beta = 0.5$. A special attention is given to the number of iterations needed for convergence and to the stress solution accuracy using the CGO or the DGO. At each iteration, the error for testing convergence is reported using the strain field criterion as defined in eq. 1.52. The iterative algorithm stops when the error is less than or equal to $e = 1 \times 10^{-6}$ to have enough accuracy on stress fields. The obtained mechanical fields are compared to available analytical solutions. Analytical solutions for spherical inhomogeneity problems in infinite medium were derived by [104] and [64].

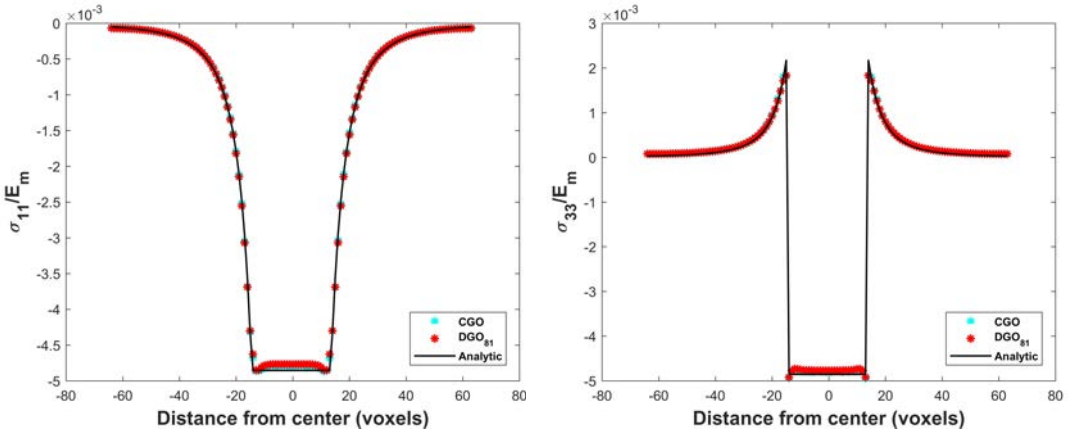


FIGURE 2.14 – Normalized stress field components σ_{11}/E_m (figure (a)) and σ_{33}/E_m (figure (b)) along a centered line parallel to the x-axis for the spherical inhomogeneity problem with eigenstrain, given by analytical solutions [104, 64] and numerically computed with CGO and DGO_{81}. Here, $R = K_m/K_i = 2$.

In Fig. 2.14, both FFT-based results given by the CGO and the DGO_{81} are compared with the analytical solutions for normalized stress field components σ_{11}/E_m

and σ_{33}/E_m along a centered line parallel to the x-axis. The analytical uniform value of the stress field in the inhomogeneity is $-317MPa$ for both components. Both CGO and DGO_{81} give approximately same numerical uniform values inside the inhomogeneity for these components, which is $-313.5MPa$. This corresponds to a relative error of 1% which is acceptable.
The number of iterations before reaching convergence is 15 iterations regardless of the used Green operator. Furthermore, Fig. 2.15 describes the error as a function of iteration number up to 50 iterations. For this mechanical contrast, it is observed that the errors calculated at each iteration with CGO and DGO_{81} are very close to each other. However, beyond 20 iterations at same iteration number, the error obtained with DGO_{81} is a little bit smaller than the one with CGO. This observation means that in the heterogeneous case, the accuracy with DGO_{81} is better than with CGO.

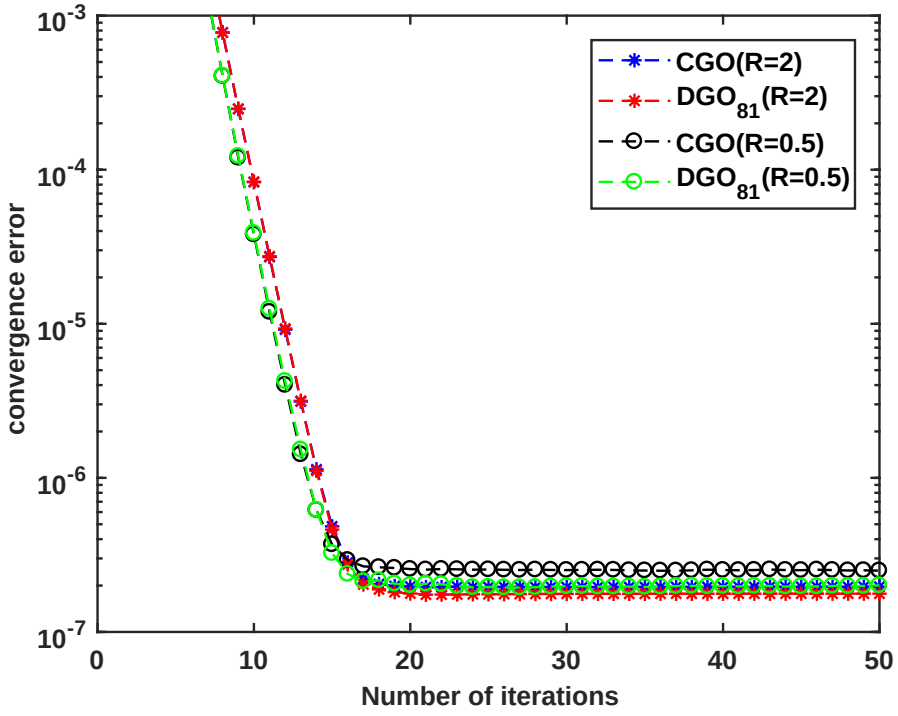


FIGURE 2.15 – The convergence error computed with the strain field criterion for both CGO and DGO_{81} methods as a function of iteration number up to 50 iterations for two mechanical contrasts : $R = K_m/K_i = 2$ and $R = K_m/K_i = 0.5$.

Fig. 2.16 represents the shear component σ_{12} normalized by $2\mu_m$ computed with CGO and DGO_{81}. The figure shows strong oscillations along the x-axis with the CGO. These oscillations are completely removed by the application of the proposed DGO_{81} which also well matches the analytical solution especially at materials discontinuities. As a conclusion of this inhomogeneous case, the substitution of the classical continuous Green operator (CGO) by the proposed discrete Green opera-

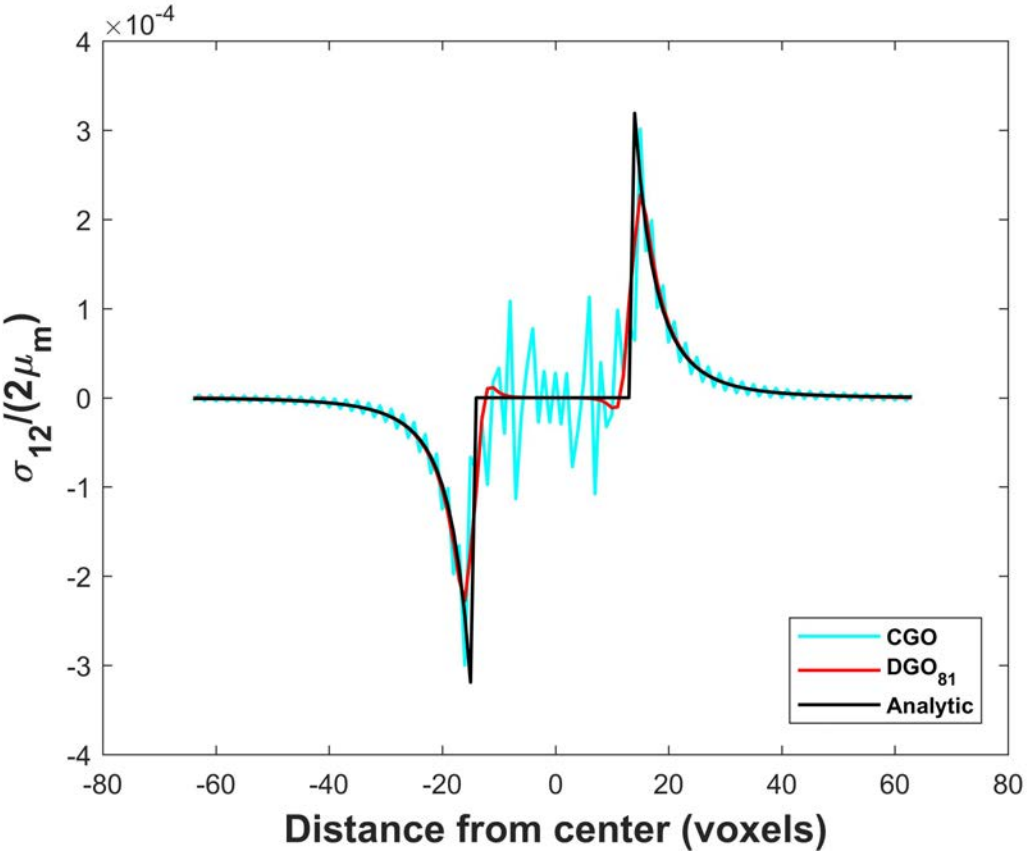


FIGURE 2.16 – Normalized stress field component $\sigma_{12}/(2\mu_m)$ along a centered line parallel to x-axis for the spherical inhomogeneity problem with eigenstrain, given by analytical solutions [104, 64] and numerically computed with CGO and DGO_{81}.

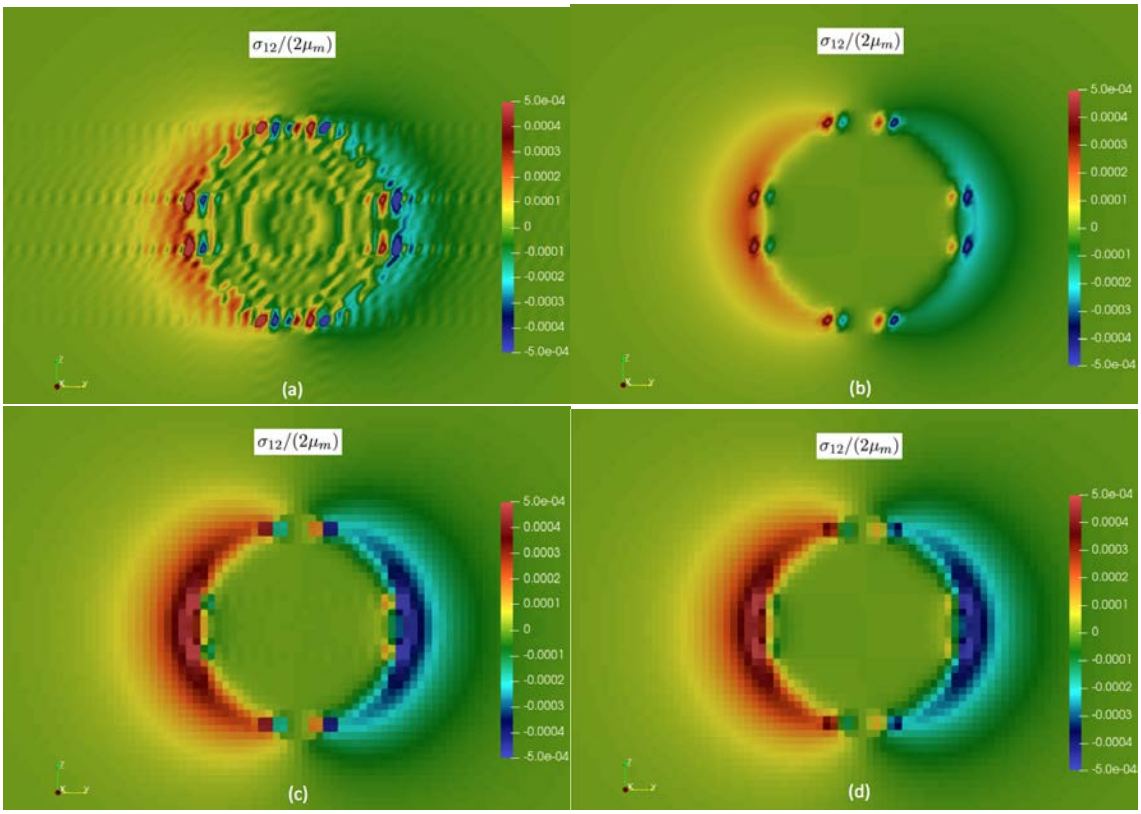


FIGURE 2.17 – 2D sections of the stress component σ_{12} normalized by $2\mu_m$ computed with CGO and DGO_{81}. Using the visualization software ParaView [138], *Point Data* are used to represent the result of CGO on figure (a) and DGO_{81} on figure (b) ; *Cell Data* are used to represent the result of CGO on figure (c) and DGO_{81} on figure (d).

tor (DGO_{81}) allows to remove spurious oscillations on mechanical fields and does not modify the convergence rate of the iterative scheme for the chosen mechanical contrast. In this work, the study of more important varying stiffness contrasts were not investigated as well as the optimized choice of the elastic stiffness reference medium. The two main reasons are that : (i) the present FFT-based algorithm is applied to Ni-based superalloys which exhibit a low mechanical contrast between phases, (ii) the truncation order k should be increased for higher contrasts.

In addition, 2D sections of the stress component σ_{12} normalized by $2\mu_m$ computed with CGO and DGO_{81} are reported on Fig. 2.17 to study stress patterns close to the interface between the matrix and the inhomogeneity. The section is a cut parallel to (y, z) plane intersecting the center of the inhomogeneity along the x-axis. Following Fig. 2.17(a) using *Point Data* or Fig. 2.17(c) using *Cell Data* with the visualization software ParaView [138], it is seen that the CGO produces artificial 2D wavy patterns on this stress component which are more pronounced inside the inhomogeneity and near material discontinuities. Such kind of artefacts using the CGO was also reported by [156]. They are clearly due to numerical oscillations which spoil the stress solution as already observed in Fig. 2.16. In contrast, the application of DGO_{81} allows to completely remove these artificial patterns, see Fig. 2.17(b) using *Point Data* or Fig. 2.17(d) using *Cell Data*. The eight pairs of stress hot spots (see Fig. 2.17(b)) result from the discrete voxelization for this spherical inhomogeneity, which gives a different rendering using *Cell Data* instead of *Point Data* with the software ParaView [138].

2.6 Conclusions

In this chapter, a new consistent periodized discrete Green operator (abbreviated DGO_k) is proposed to replace the classic continuous modified Green operator (CGO) in Fast Fourier Transform-based methods to numerically solve the Lippmann-Schwinger equation for periodic heterogeneous media with eigenstrain fields. The advantage of this new consistent Green operator is that it is well adapted to iterative schemes based on the Lippmann-Schwinger equation as the one developed by [3]. Through the different three-dimensional configurations treated in this chapter considering different inclusion shapes, eigenstrains and elastic properties (cubic-shaped inclusion, spherical Eshelby inclusions and spherical inhomogeneity), we show that this periodized DGO is very effective to suppress numerical oscillations near materials discontinuities. In order to same time and to memory, this operator is computed only for some voxels and once at the beginning of the iterative algorithm by truncating the series in the expression of the DGO up to a given order k.
For the purpose of this thesis, the study of this periodized discrete Green operator is limited to reference case and in inhomogeneity cases, the mechanical contrast

between phases is relatively low (which is sufficient to study superalloys). However, further studies will be focused on the extension of the present DGO method for dislocation mechanics, for high mechanical contrasts and to other more refined FFT-based schemes than fixed-point algorithms, i.e. fast gradient methods. Optimal choices of the DGO truncation order k and homogeneous reference medium for heterogeneous materials containing rigid inclusions and voids will be investigated in future works. Furthermore, the numerical method based on DGO could be applied to simulate Synchrotron high-resolution diffraction peaks on real microstructures, as described in first promising results [60, 38]. To be well understood, such diffraction peaks need very accurate predictions of local displacement fields in the course of plastic deformation, which are only reachable with the new DGO_k. In the next chapter, we will study a new expression of a third order discrete Green operator to accurately compute the displacement field and some numerical correction of displacement profiles.

Chapitre 3

FFT-based Computation of the displacement field and applications to dislocations

3.1 Objectives

In the previous chapter, we derived a new consistent periodized discrete Green operator (abbreviated DGO_k) to compute the stress/strain field in a periodic microstructure by solving the so-called Lippmann-Schwinger equation. However our numerical method developed in the next chapter to simulate diffraction patterns is based on the displacement field. Therefore, we need to derive another discrete Green operator to compute the displacement field.
The displacement field results from the applied macroscopic field or from the eigenstrain in the material. In this chapter, we will focus on the displacement field due to the eigenstrain which represents dislocations lying in slip planes. To compute this mechanical field, we develop a discrete Green operator. This third order operator is compatible with Lippmann-Schwinger equation and the obtained displacement field does not show numerical oscillations. This numerical method replaces the analytic solutions [57, 37] which are not easy to compute for some configurations in isotropic or anisotropic elasticity. The method is applied for dislocation loop lying in any slip plane. In the case of inclined dislocation loops (on (111) plane), some artifacts appear on the displacement field due to voxelization. We develop a numerical method, denoted sub-voxelization method, to suppress these artifacts
This chapter is organized as follows. In the next section, we will present two third order Green operators to compute the displacement field and an application in the case of of a prismatic dislocation loops. In section 3, we will present a discrete Green operator to compute the displacement field without oscillation with some applications. In the last section, we will present the sub-voxelization method which allows

to delete artifacts in the case of inclined dislocation loops.

3.2 Green operator for the displacement field and application

3.2.1 Green operator for the displacement field

Let us reconsider the mechanical problem already presented in details in the previous chapiter : a periodic unit cell with volume Ω subjected to a uniform overall strain tensor denoted $\mathbf{E}$. As shown in this chapter, the combination of the elastic equations and the introduction of the Green operator leads to the so-called Lippmann-Schwinger equation whose solution in the Fourier space is recalled below :

$$\widehat{\boldsymbol{\varepsilon}}(\boldsymbol{\xi}) = -\widehat{\boldsymbol{\Gamma}}(\boldsymbol{\xi}) : \widehat{\boldsymbol{\tau}}(\boldsymbol{\xi}) \qquad \forall \boldsymbol{\xi} \neq 0, \qquad \widehat{\boldsymbol{\varepsilon}}(0) = \mathbf{E} \tag{3.1}$$

where $\widehat{\boldsymbol{\tau}}$ is the Fourier transform of the stress polarization field :

$$\boldsymbol{\tau}(\mathbf{x}) = \delta\mathbf{C}(\mathbf{x}) : \boldsymbol{\varepsilon}(\mathbf{x}) - \mathbf{C}(\mathbf{x}) : \boldsymbol{\varepsilon}^*(\mathbf{x}) \tag{3.2}$$

As shown in the previous chapter, the FFT-based "basic" algorithm proposed by Moulinec [98, 99] allows to compute the strain field $\boldsymbol{\varepsilon}(\boldsymbol{\xi})$ in the Fourier space or $\boldsymbol{\varepsilon}(\mathbf{x})$ in the real space. This local total strain tensor $\boldsymbol{\varepsilon}(\mathbf{x})$ reads from strain compatibility :

$$\boldsymbol{\varepsilon}(\mathbf{x}) = \nabla^s \mathbf{u}^*(\mathbf{x}) \tag{3.3}$$

Using Eq.3.1 and Eq.3.3, it is possible to compute the Fourier transform of the displacement field. It is given by :

$$\widehat{\mathbf{u}}^*(\boldsymbol{\xi}) = -\widehat{\mathbf{B}}(\boldsymbol{\xi}) : \widehat{\boldsymbol{\tau}}(\boldsymbol{\xi}) \tag{3.4}$$

Using the inverse Fourier transform, the displacement field $\widehat{\mathbf{u}}^*(\mathbf{x}_d)$ is obtained in the real space :

$$\widehat{\mathbf{u}}^*(\mathbf{x}) = FFT^{-1}(\widehat{\mathbf{u}}^*(\boldsymbol{\xi})) \tag{3.5}$$

The computed fluctuation term $\widehat{\mathbf{u}}^*(\mathbf{x})$ is assumed to be periodic due to periodic boundary conditions. The total displacement is obtained by adding a linear part :

$$\mathbf{u}(\mathbf{x}) = \mathbf{u}^*(\mathbf{x}) + \ \mathbf{E}.\mathbf{x}$$

The linear part $\mathbf{E}.\mathbf{x}$ is the sum of strain $\langle \frac{1}{2}(u_{i,j} + u_{j,i})\rangle x_j$ and rotation part $\langle \frac{1}{2}(u_{i,j} - u_{j,i})\rangle x_j$. In the case of a dislocation with burgers vector $\mathbf{b} = (b_1, b_2, b_3)$ lying in a slip plane of normal $\mathbf{n} = (n_1, n_2, n_3)$, we compute the $\langle u_{i,j}\rangle x_j$ as :

$$\langle u_{i,j}\rangle x_j = \frac{1}{h} b_i f n_j x_j \tag{3.6}$$

where f is the volume fraction of deformed voxels : $\frac{N_f}{N^3}$ (N_f is the number of deformed voxels and N^3 is the total number of voxels). When f is very small, the linear part $\mathbf{E}.\mathbf{x}$ can be neglected.

The expression of the third order tensor $\widehat{\mathbf{B}}$ is written in indicial form in Eq.3.7. This operator is also denoted CGO as specified in the introduction of this manuscript.

$$\widehat{B}_{ijq}(\boldsymbol{\xi}) = \frac{\mathrm{i}}{2}(\widehat{G}_{ij}\xi_q + \widehat{G}_{iq}\xi_j) \tag{3.7}$$

where i denotes the imaginary unit ($\sqrt{-1}$). The third order tensor $\widehat{\mathbf{B}}$ has the following symmetries : $\widehat{B_{ijq}} = \widehat{B_{iqj}}$ due to the symmetry of the stress polarization tensor ($\tau_{ij} = \tau_{ji}$). $\widehat{\mathbf{G}}$ is the Fourier transform of the elastic Green tensor defined as [104] :

$$\begin{cases} \widehat{G}_{ij}(\boldsymbol{\xi}) & = & \frac{N_{ij}(\boldsymbol{\xi})}{D(\boldsymbol{\xi})} & \forall \boldsymbol{\xi} \neq 0 \\ \widehat{G}_{ij}(0) & = 0 & & \end{cases} \tag{3.8}$$

where $N_{ij}(\boldsymbol{\xi}) = N_{ji}(\boldsymbol{\xi})$ and $D(\boldsymbol{\xi})$ are respectively the cofactor matrix and the determinant of the Christoffel (also called acoustic tensor) matrix $K_{ik} = C^o_{ijkl}\xi_j\xi_l$. Note that eq. 3.5 is not an explicit equation, therefore it does not require a specific iterative algorithm. However, the Fourier transform of the stress polarization field $\widehat{\boldsymbol{\tau}}$ comes from the iterative algorithm used to compute the strain field. It is computed at the last iteration of the algorithm. Then, it is used to compute the Fourier transform of the displacement field and using the inverse Fourier transform the displacement field is obtained in the real space. The iterative algorithm used in our numerical code is presented in Algorithm6.

Algorithm 6 Classic algorithm proposed by [3] heterogeneous elastic materials with eigenstrains and applied macroscopic stress Σ

Initialization : ($\boldsymbol{\varepsilon}^*(\mathbf{x}_d)$ known)

$\mathbf{E}^{(0)} = \langle \boldsymbol{\varepsilon}^*(\mathbf{x}_d) \rangle + \mathbf{C}^{o^{-1}} : \Sigma$

$\boldsymbol{\varepsilon}^o(\mathbf{x}_d) = \mathbf{E}^{(0)} \quad \forall \mathbf{x}_d \in \Omega$

Compute $\widehat{\mathbf{\Gamma}}(\xi_j)$ *and* $\widehat{B}(\xi_j) \forall \xi_j$

Itération : $i+1$ ($\boldsymbol{\varepsilon}^i(\mathbf{x}_d)$ *and* $\mathbf{E}^i$ known)

$\boldsymbol{\tau}^{i+1}(\mathbf{x}_d) = \delta\mathbf{C}(\mathbf{x}_d) : \boldsymbol{\varepsilon}^i(\mathbf{x}_d) - \mathbf{C}(\mathbf{x}_d) : \boldsymbol{\varepsilon}^*(\mathbf{x}_d)$

$\widehat{\boldsymbol{\tau}}^{i+1}(\boldsymbol{\xi}_j) = FFT(\boldsymbol{\tau}^{i+1}(\mathbf{x}_d))$

$\boldsymbol{\varepsilon}^{i+1}(\mathbf{x}_d) = \mathbf{E}^i - FFT^{-1}(\widehat{\mathbf{\Gamma}}(\xi_j) : \widehat{\boldsymbol{\tau}}^{i+1}(\xi_j))(\mathbf{x}_d))$

$\boldsymbol{\sigma}^{i+1}(\mathbf{x}_d) = \mathbf{C}(\mathbf{x}_d) : (\boldsymbol{\varepsilon}^{i+1}(\mathbf{x}_d) - \boldsymbol{\varepsilon}^*(\mathbf{x}_d)),$

$\mathbf{E}^{i+1} = \langle \boldsymbol{\varepsilon}^{i+1}(\mathbf{x}_d) \rangle - \mathbf{C}^{o^{-1}}(\mathbf{x}_d) : \langle \boldsymbol{\sigma}^{i+1}(\mathbf{x}_d) \rangle$

Convergence test

If convergence is achieved

$\widehat{\mathbf{u}}^*(\boldsymbol{\xi}_j) = -\widehat{\mathbf{B}}(\boldsymbol{\xi}_j) : \widehat{\boldsymbol{\tau}}^{i+1}(\boldsymbol{\xi}_j)$

$\widehat{\mathbf{u}}(\mathbf{x}_d) = FFT^{-1}(\widehat{\mathbf{u}}^*(\boldsymbol{\xi}_j)) + (\nabla^s \mathbf{u}(\mathbf{x}_d)).\mathbf{x}_d)$

As demonstrated in the previous chapter, the use of the classic Green operator for the computation of mechanical fields leads to spurious oscillations at material discontinuities. Therefore, to compute the displacement field without oscillations, we proposed a third order discrete Green operator associated to $\widehat{\mathbf{u}}^*(\boldsymbol{\xi})$.

3.2.2 Discrete Green operator to compute the displacement field

The derivation of a discrete Green operator to compute the displacement field which will be denoted $\mathbf{B}^D$, is straightforward and based on the derivations given in the previous chapter. In fact, this expression can be deduced from the expression of the discrete periodized Green operator to compute the strain/stress field : $\mathbf{\Gamma}^D$. Eq.3.1 and eq. 3.5 give the Fourier transforms of both the strain and displacement fields as function of two Green operators and the derivation of the expression of $\mathbf{\Gamma}^D$ is based on Eq.3.5 and as both equations have the same form, we conclude that the expression of $\mathbf{B}^D$, is similar to $\mathbf{\Gamma}^D$ [38, 37]. For a 3D problem, the discrete consistent operator $\mathbf{B}^D$ is obtained from the definition :

$$\widehat{\mathbf{u}}^D(\boldsymbol{\xi}_{ijq}) = -\widehat{\mathbf{B}}^D(\boldsymbol{\xi}_{ijq}) : \widehat{\boldsymbol{\tau}}^D(\boldsymbol{\xi}_{ijq}) \qquad \forall \boldsymbol{\xi}_{ijq} \neq 0 \tag{3.9}$$

such as :

$$\widehat{\mathbf{B}}^D(\boldsymbol{\xi}_{ijq}) = A_{ijq} \sum_{m,n,p=-\infty}^{\infty} \frac{(-1)^{m+n+p}}{mN+i} \frac{1}{nN+j} \frac{1}{pN+q} \widehat{\mathbf{B}}(\boldsymbol{\xi}_{mN+i,nN+j,pN+q}) \tag{3.10}$$

where :

$$A_{ijq} = \left(\frac{N}{\pi}\right)^3 sin\left(\frac{\pi i}{N}\right) sin\left(\frac{\pi j}{N}\right) sin\left(\frac{\pi q}{N}\right) \tag{3.11}$$

Due to the symmetry properties of $\mathbf{B}$, $\mathbf{B}^D$ has these symmetries : $\widehat{B^D_{ijq}} = \widehat{B^D_{iqj}}$; $\widehat{B^D_{ijq}}(-\boldsymbol{\xi}) = \widehat{B^D_{ijq}}(\boldsymbol{\xi})$. Memory and time optimization used in the calculation of $\widehat{\boldsymbol{\Gamma}^D}(\boldsymbol{\xi}_{ijq})$ are all valid for $\widehat{\mathbf{B}^D}(\boldsymbol{\xi}_{ijq})$ and $\widehat{\mathbf{B}^D}$ is performed only once before performing the iterative algorithm. The infinite series $\widehat{\mathbf{B}^D}(\boldsymbol{\xi}_{ijq})$ converges but it is not easy to theoretically and mathematically investigate the convergence of this infinite series. In the next sections, numerical examples will be used to study this convergence. However, it is observed that $\widehat{\mathbf{B}^D}$ has a better convergence rate than $\widehat{\boldsymbol{\Gamma}^D}$. This can be explained using eq.3.10 and the fact that N_{ij} is a polynomial homogeneous function of degree 4 and D is a polynomial homogeneous function of degree 6 so the $\widehat{\Gamma_{ijql}}$ components are homogeneous functions of degree 0 (see chapter 2) and the $\widehat{B_{ijq}}$ components are homogeneous functions of degree -1.

3.2.3 Discrete operator to compute displacement fields at voxels corners

The previous discrete Green operator allows to compute the displacement field at the center of the voxels. In some cases, it is convenient to compute the displacement field at the voxels corner. In the next section for example, the application of the subvoxelization method requires the displacement field at voxels corner. This computation is performed using the Fourier shift theorem and leads to this third order Green operator :

$$\widehat{\mathbf{B}}^D_S(\boldsymbol{\xi}_{ijq}) = A_{ijq} \sum_{m,n,p=-\infty}^{\infty} \frac{e^{\mathrm{i}\frac{\pi i}{N}}}{mN+i} \frac{e^{\mathrm{i}\frac{\pi j}{N}}}{nN+j} \frac{e^{\mathrm{i}\frac{\pi q}{N}}}{pN+q} \widehat{\mathbf{B}}(\boldsymbol{\xi}_{mN+i,nN+j,pN+q}) \tag{3.12}$$

where A_{ijq} is defined in the previous section.

3.2.4 Application to the computation of displacement field

The third order Green operator is used in the previous algorithm to compute the displacement field due to an Eshelby-like squared prismatic dislocation loop. Such a dislocation loop is modeled by a one voxel thick square-shaped $32 \times 32 \times 1$ inclusion in $128 \times 128 \times 128$ voxels unit cell. The volume fraction of deformed voxel in this case is 0.000488. The linear part $\mathbf{E}.\mathbf{x}$ will be neglected and the study will be held only on the fluctuation term $\mathbf{u}^*$.

The isotropic elastic constants of both matrix and inclusion are the following : The Young's modulus is $E_m = E_i = 333.4GPa$ and the Poisson ratio is $\nu_m = \nu_i = 0.26$. This approximately corresponds to the room temperature elastic constants for a single crystalline Ni-based superalloy. The eigenstrain field ($\varepsilon^*_{ij} = 0$ for all i, j except $\varepsilon^*_{33} = 1$) is responsible for an equivalent Burgers vector for this prismatic loop equal to $b = 2a_3\varepsilon^*_{33}$ where $2a_3$ is the thickness of the inclusion in the z-direction (i.e. the voxel size). The analytical solution corresponding to this Burgers vector is given in Appendix C. Fig. 3.1 shows the normalized components u_1/b and u_3/b, along the $z - axis$ obtained from the approximation of CGO, DGO_k and from the analytic solution.

The aim of this example is to study the convergence of the associated DGO_k when k increases, its accuracy on the displacement field and its capability to completely suppress oscillations on the displacement field at the materials discontinuity between the inclusion and the matrix along the z- axis. The analysis of the figure shows that far from the dislocation loop, the FFT-method solutions and the analytic solution are almost identical. Near the dislocation loop, the FFT-based method with CGO approximation shows some oscillations in both components. These oscillations are related to the Gibbs or aliasing phenomenon discussed in the previous chapter. These oscillations are suppressed with DGO_k.

3.2.4.1 Convergence and accuracy of $\widehat{\mathbf{B}^D}(\boldsymbol{\xi}_{ijq})$

From $k = 21$, the values of these normalized displacements are almost identical eq. 3.2, which shows a faster convergence of $\widehat{\mathbf{B}^D}$ in comparison with the results obtained with $\widehat{\mathbf{\Gamma}}^D$ in the previous chapter. This trend was expected as discussed in section 3.2.2.
In order to quantify the convergence of displacement-based periodized DGO_k, two relative differences ϵ_1 and ϵ_3 are calculated between the analytic solutions and the numerical solutions for u_1 and u_3, respectively obtained at different locations from

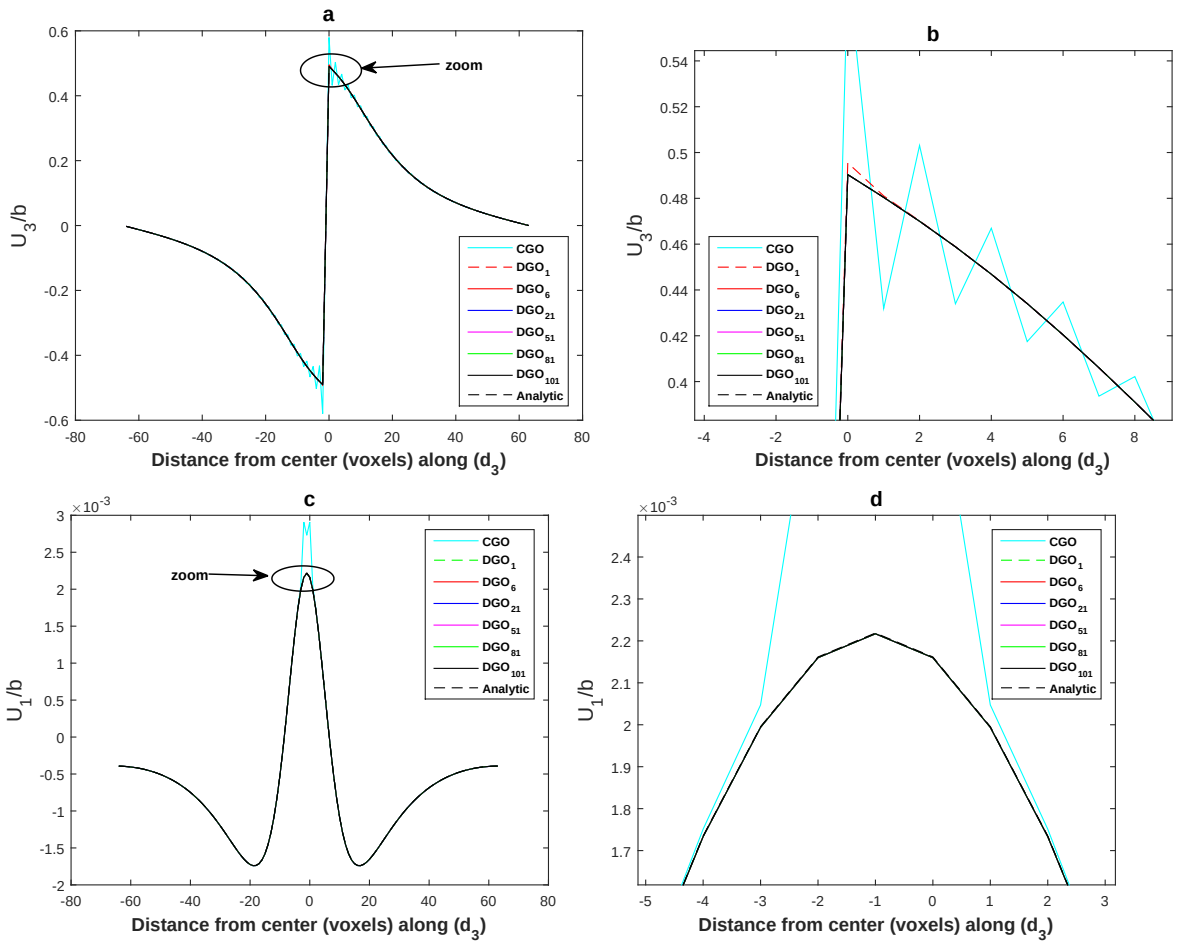


FIGURE 3.1 – The displacement field component u_3 (figures (a) et (b)) and u_1 (figures (c) et (d)) along a centered z-axis for a flat cubic-shaped inclusion (Eshelby-like squared prismatic dislocation loop), given by the analytical solution (see Appendix C) and computed with CGO, DGO_k for different k (DGO_1, DGO_6, DGO_{21}, DGO_{51}, DGO_{81}, DGO_{101}).

DGO_k or CGO. These relative differences are defined as :

$$\epsilon_1 = \left| \frac{u_1^{num} - u_1^{anal}}{u_1^{anal}} \right|$$

$$\epsilon_3 = \left| \frac{u_3^{num} - u_3^{anal}}{u_3^{anal}} \right|$$

Figs. 3.2(a)(b) shows the values of ϵ_1 and ϵ_3 for the DGO_k and the CGO methods. These values are computed at the center of the inclusion (point O) and plotted as a function of k using logarithmic scales. Regarding ϵ_1 (Fig. 3.2(a)), the solution given by the DGO_k is more accurate than the CGO from $k = 5$ where $\epsilon_1 < 10^{-3}$. Regarding ϵ_3 (Fig. 3.2(b)), the solution given by the DGO_k is more accurate than the CGO for all k values with $\epsilon_3 < 10^{-3}$.

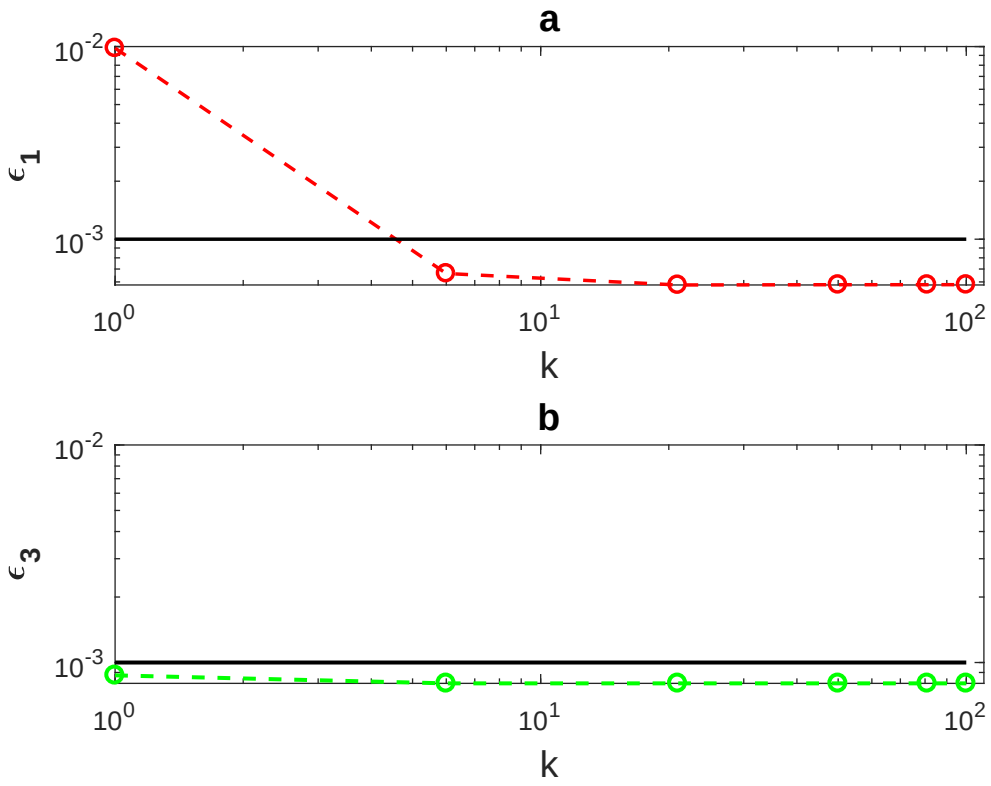


FIGURE 3.2 – Relative error ϵ_1 (figure (a)) and ϵ_3 (figure (b)) computed at the center of the inclusion (point O) for different values of k with displacement field components u_1 and u_3. Solid lines represent the CGO solution and dotted lines represent the DGO_k solutions.

Furthermore, on almost all components, the displacement field giving by the FFT-solution using the CGO based on $\widehat{\mathbf{B}}$ shows numerical oscillations due to the physical displacement discontinuity embodied by the Burgers vector describing strong plastic incompatibility at the interface between the inclusion and the matrix. These oscillations are completely removed by replacing $\widehat{\mathbf{B}}$ with the proposed periodized discrete operator $\widehat{\mathbf{B}^D}$ and the DGO_{21} (k=21) solution is a good compromise between accuracy as seen in Fig. 3.1 and computational cost (k remains low enough).

3.2.4.2 Displacement field at the voxels corner

The operator $\widehat{\mathbf{B}}_S^D(\boldsymbol{\xi}_{ijq})$ (see eq. 3.12) is used to compute the displacement field of the previous configuration. Fig 3.3 compares the displacement field obtained with $\widehat{\mathbf{B}}^D(\boldsymbol{\xi}_{ijq})$ (eq. 3.10) and $\widehat{\mathbf{B}}_S^D(\boldsymbol{\xi}_{ijq})$ (eq. 3.12).

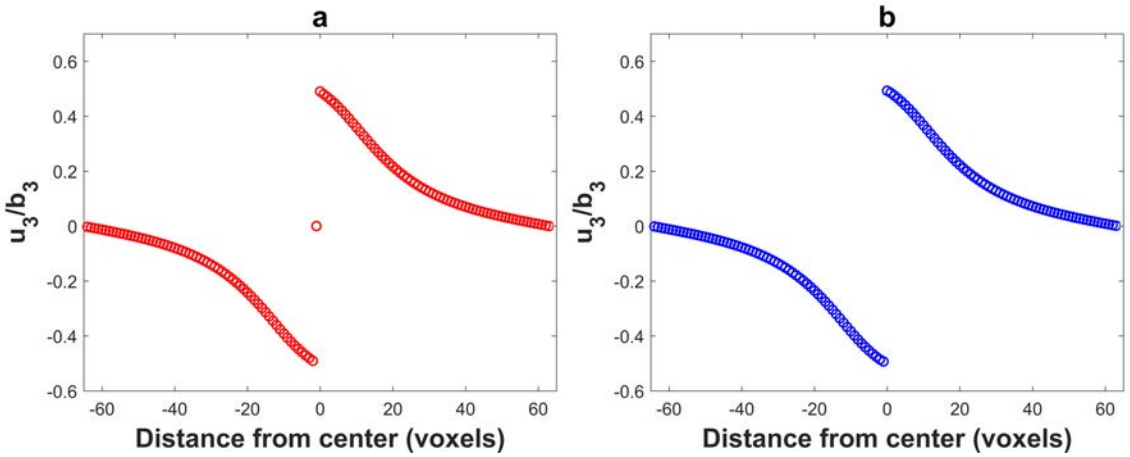


FIGURE 3.3 – The displacement field component u_3 along a centered z-axis for a flat cubic-shaped inclusion (Eshelby-like squared prismatic dislocation loop. (a) With discrete Green operator (eq. 3.10). (b) With shift discrete Green operator (eq. 3.12).

3.2.4.3 Effet of the Fourier grid resolution

In this section, we focus on the impact of the Fourier grid resolution on the numerical solutions. Moulinec and Suquet [99] first observed that the occurrence of oscillations on the mechanical fields is closely related to the number of voxels used in the discretization of the unit cell, i.e. the Fourier grid resolution. Fig. 3.4 compares the numerical results obtained with CGO and DGO_{21} for two different configurations : a unit cell constituted of $128 \times 128 \times 128$ voxels with a centered square inclusion of $32 \times 32 \times 1$ voxels and a unit cell constituted of $32 \times 32 \times 32$ voxels with a centered square inclusion of $8 \times 8 \times 1$ voxels. Fig. 3.4 shows the normalized

component u_3/b of the displacement field along the line d_3 for these two configurations. We first notice that the CGO exhibits numerical oscillations close to the discontinuity of u_3 which should theoretically be equal to b. The magnitude of these oscillations decreases as the number of voxels increases. However, these oscillations are not completely removed with the CGO and are always present even for a good resolution of $128 \times 128 \times 128$ voxels. The new periodized discrete operator $\widehat{\mathbf{B}^D}$ here embodied by the DGO_{21} allows to remove all oscillations for both resolutions. This result shows a non negligible advantage of the DGO over the CGO to give accurate results devoid of oscillations even for low Fourier grid resolutions to describe a given physical problem.

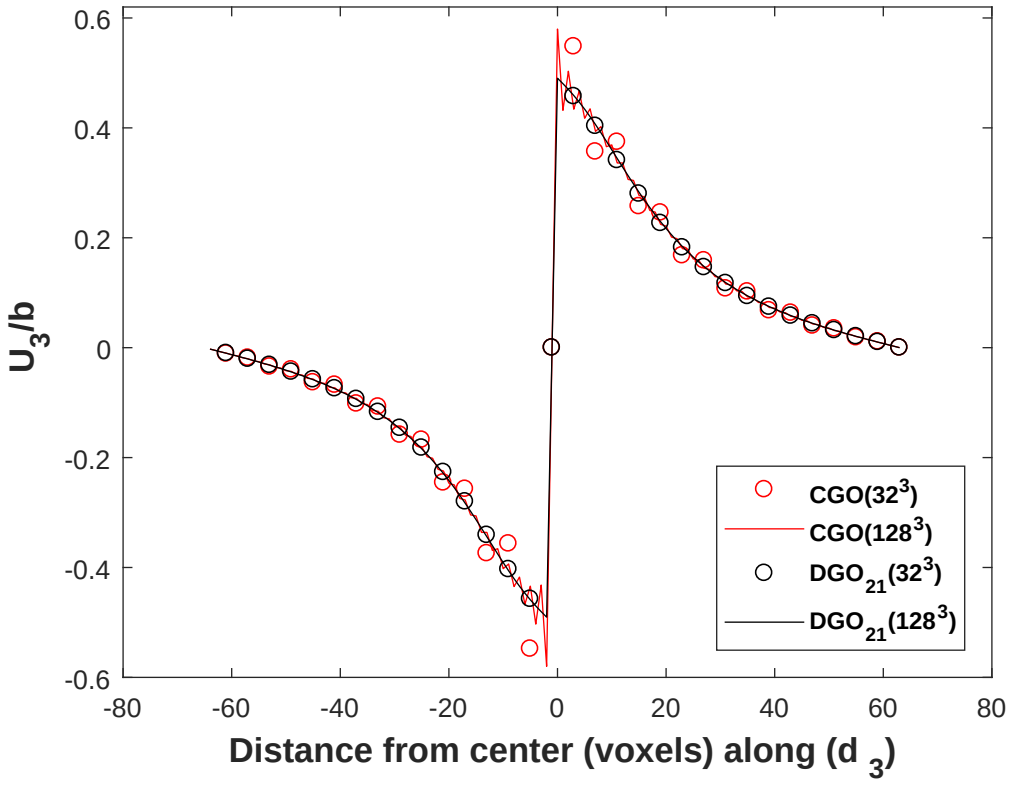


FIGURE 3.4 – Effect of the discretization level (Fourier grid resolution) on the accuracy of the displacement field component u_3/b along d_3 for a flat cubic-shaped inclusion (Eshelby-like squared prismatic dislocation loop) given by CGO, and DGO_{21} for two resolutions : $32 \times 32 \times 32$ voxels ($8 \times 8 \times 1$ voxels for the inclusion) and $128 \times 128 \times 128$ voxels ($32 \times 32 \times 1$ voxels for the inclusion).

3.3 Voxelization artifacts and proposition of sub-voxelization method

3.3.1 Displacement field due to an inclined dislocation loop

In the previous section, the computed displacement field is due to a square dislocation loop containing in a (001) plane. The modeling of such a plane is easy because they the loop is consistent with the FFT grid. In a face-centered cubic (FCC) crystal, (111) type slip systems are studied. Fig. 3.5 is a schematic representation of the two type planes described above. The numerical modeling of (111) type planes are also quite easy but they are not coherent with the FFT grid. This introduce others numerical effects on the computed mechanical fields [49, 38]. In order to understand this phenomenon, let us study a simple case.
The studied material is discretized in $N \times N \times N$ voxels ($N = 128$). We consider a square dislocation loop with a $\frac{1}{N}[01-1]$ Burgers vector ($\mathbf{b}(b_1, b_2, b_3)$)lying in a (111) slip plane of a FCC crystal. As in the previous sections, the dislocation loop is 32 voxels wide in the x and y directions, and 1 voxel thick but now with a z position such that $x+y+z = constant$. For example, in the case of a centered plane dislocation, we have : $x+y+z = 64+64+64$. The displacement has been computed with the periodized operator $\mathbf{\Gamma}^D$. Fig. 3.6 shows the normalized component u_3 of the displacement field along the $z-axis$.

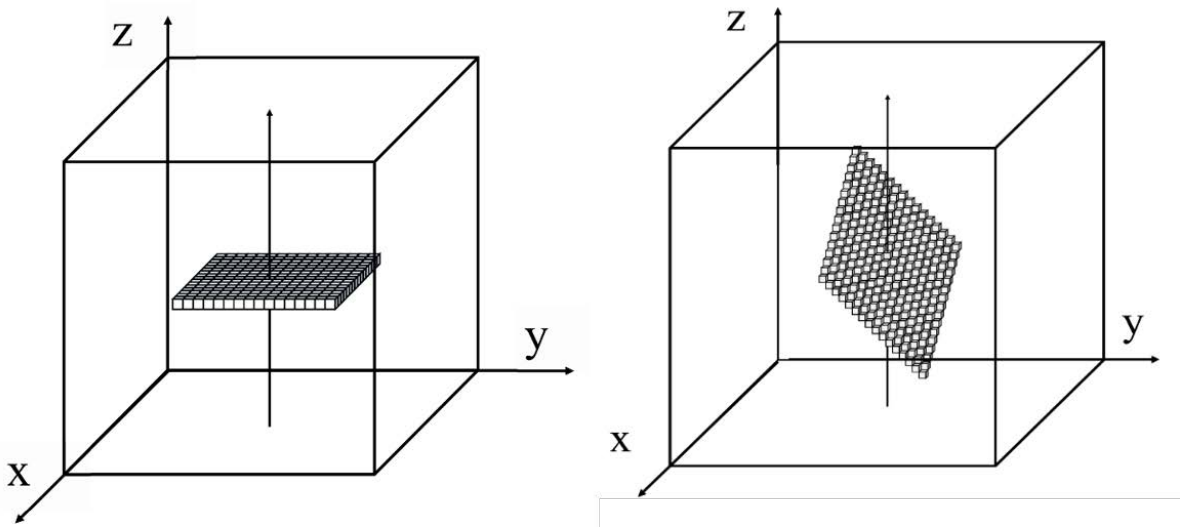


FIGURE 3.5 – Schematic reprsentation of slip planes and different square loops. On the left, a (001) plane consistent with the FFT grid and on the right (111) plane, not consistent with the FFT grid

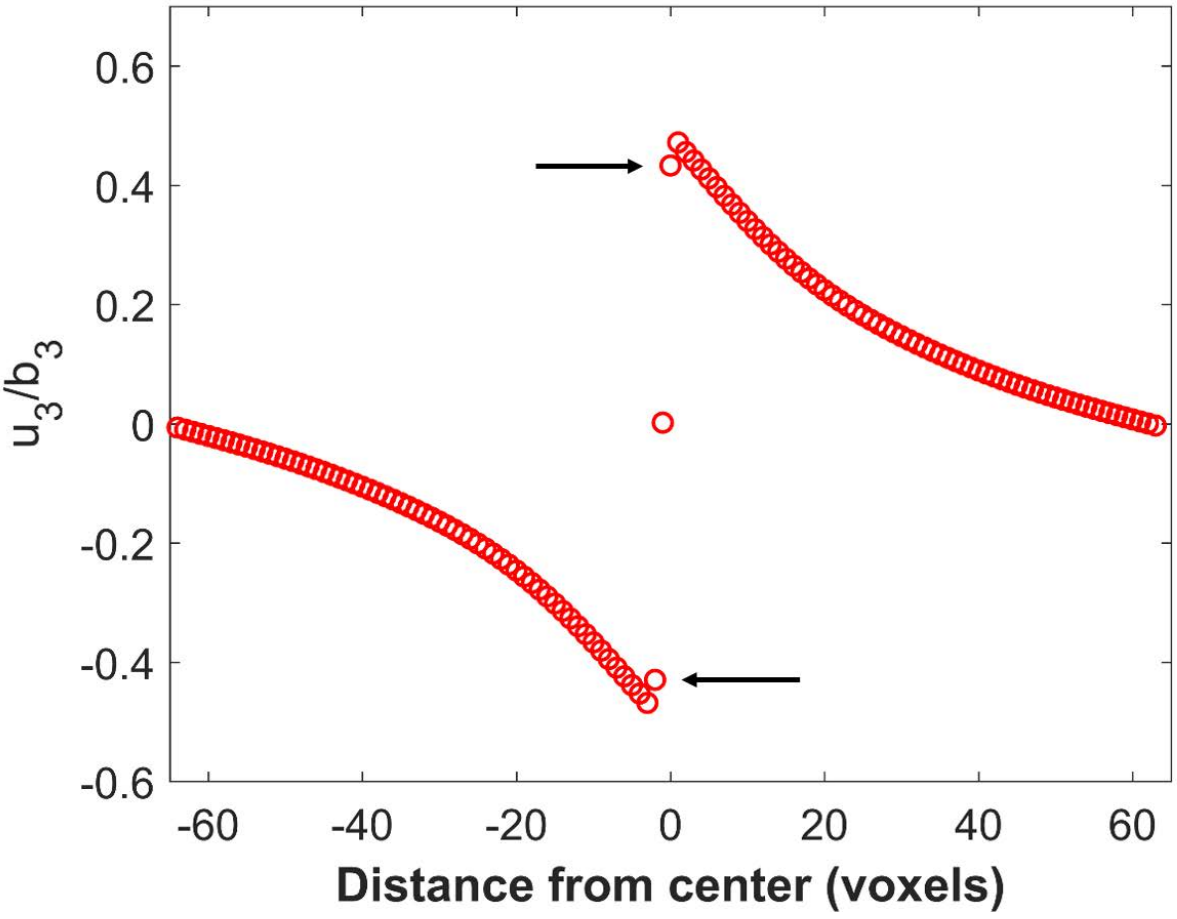


FIGURE 3.6 – Displacement field due to an inclined dislocation loop. The displacement field is represented along a centered line parallel to the $z - axis$

The displacement field represented on Fig 3.6 does not show numerical oscillations. Although the third order Green operator $\widehat{\mathbf{B}}^D$ is used, this result was not trivial because inclined dislocations are known to be difficult to study and usually lead to spurious numerical oscillations on the mechanical field [49]. In reference [49] for example, the authors develop a special algorithm to study this type of dislocations. Another phenomenon appears on the displacement field. This phenomenon is shown on the figure by black arrows. Our calculations showed that this effect appears only in the case of inclined dislocation loop. In the next subsection, all the possible causes of this phenomenon are described and after, a sub-voxelization method to suppress these artifacts is proposed.

3.3.2 Origin of the voxelization artifacts

Let us consider Fig 3.7 which is a schematic presentation of deformed voxels (voxels with eigenstrains) containing a (111) loop plane with black edges and voxels along which the displacement field on Fig3.6 is represented with red edges. The displacement in the center of the voxel belonging to the loop plane (numbered 0), is zero. A first neighbor voxel such as the one numbered 1, shares three faces and nine edges with the loop voxels. A second neighbor voxel such as the one numbered 2 shares no face and only three edges with the loop voxels. Further voxels have no contact with the platelet. Therefore, these voxels seem to be more influenced by the eigenstrain in the deformed voxels. As a consequence, the position at these voxels are shifted relative to the expected one, so that the displacement difference between these voxels is significantly lower than **b**, see Fig. 3.6 (points indicated by black arrows).

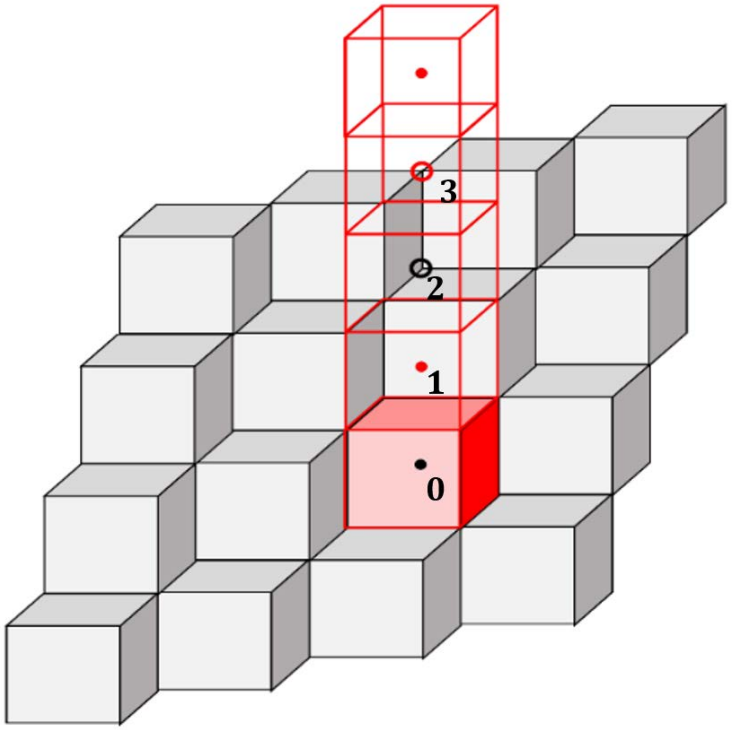


FIGURE 3.7 – Schematic representation of deformed voxels containing in (111) plane and voxels along which the displacement field is represented

Although the amplitude of this shift is small (less than 10% of the Burgers vector) it has unwanted consequences on the diffraction peak simulation. In fact, the diffraction peak profile are function of the displacement phase taken here as the displacement modulo Burgers vector. Due to these artifacts, a local oscillation of the displacement phase is observed. Fig. 3.8 represents the displacement phase : the

representation is made for 32 voxels centered in the unit cell along z direction. In the next chapter, numerical examples will confirm that this local oscillation on the displacement phase strongly affects the tails of the diffraction peaks.

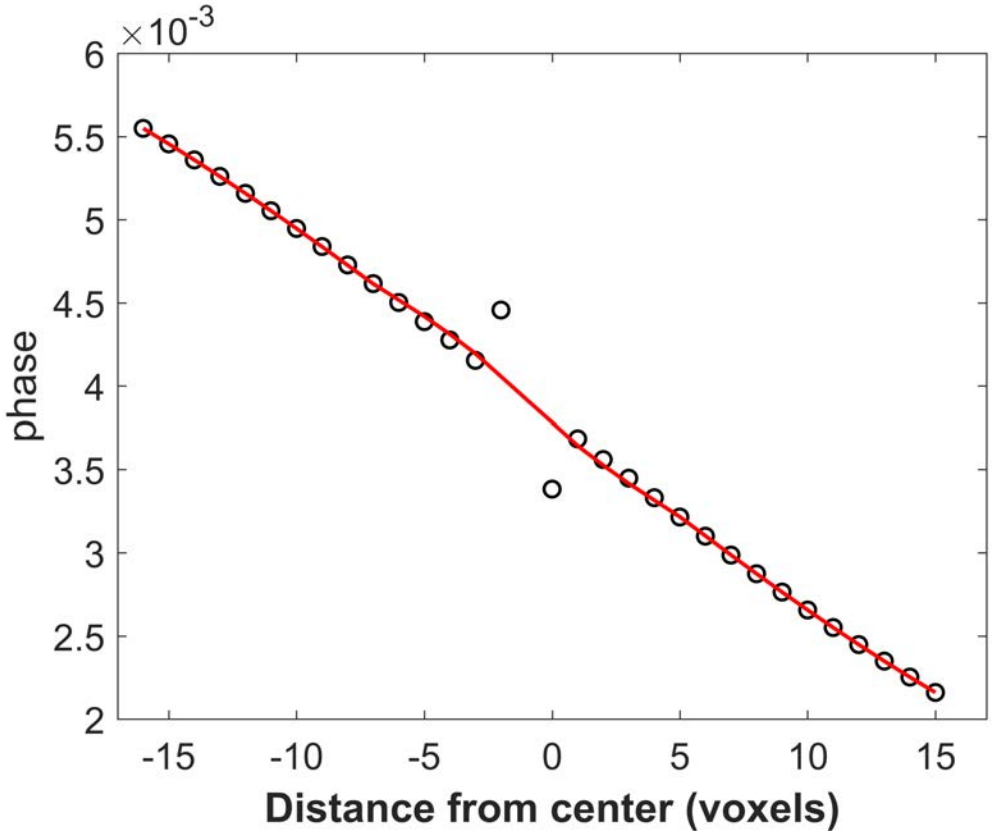


FIGURE 3.8 – Local oscillation of the phase due to artifacts (the representation is made for 32 voxels centered in the unit cell along z direction). The red line is approximately equal to the phase expected for this displacement field

3.3.3 Sub-voxelization method

The (conceptually) simplest way to remove this voxelization artifact would be to work on a multiple grid (to multiply the number of voxels along each direction by 2, 4, or more), then to down-sample the displacement field data. In that case, the FFT algorithms would lose much of their interest due to these more demanding computational efforts. We show below that this can be done in a more economical way by applying a patch to the FFT-computed displacement field.

Our technique is based on Fig. 3.9a below. This figure is a 2D representation (for the sake of clarity) of inclined dislocation loop modeled by voxels with eigenstrain

(red voxels). The usual FFT grid containing $N \times N \times N$ voxels is represented on Fig3.9a. The displacement field due to the inclined dislocation loop is computed on this grid and is denoted $\mathbf{u}^{hom}(\mathbf{x})$. On this grid the thickness of the dislocation loop seems to be larger than the physical thickness of the dislocation loop. There is only one way to reduce the thickness : to increase N. This is shown on Fig. 3.9b.

The principle of the method is to compute the displacement field denoted $\mathbf{u}^{sub}(\mathbf{x})$ (due to this more realistic dislocation loop) at some neighboring voxels using the usual grid of Fig. 3.9a. A *patch* $\mathbf{D}(\mathbf{x})$ is then computed for the neighboring voxels by subtracting $\mathbf{u}^{hom}(\mathbf{x})$ from $\mathbf{u}^{sub}(\mathbf{x})$:

$$\mathbf{D}(\mathbf{x}) = \mathbf{u}^{sub}(\mathbf{x}) - \mathbf{u}^{hom}(\mathbf{x}) \tag{3.13}$$

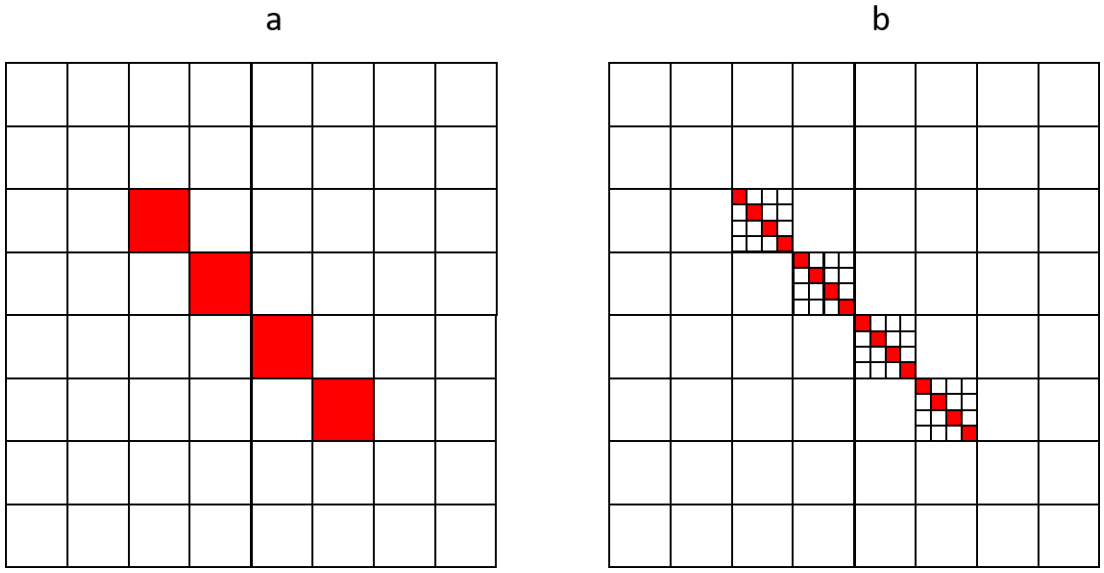


FIGURE 3.9 – 2D representation of a dislocation loop in a tilted plane on a (8×8 FFT grid. (a) With a homogeneous eigenstrain in the voxels occupied by the dislocation loop. (b) With each voxel subdivided into 4×4 sub-voxels, 4 of which have a non zero eigenstrain

This patch is stored and added to $\mathbf{u}^{hom}(\mathbf{x})$ for all neighbors of an isolated deformed voxel. The computation of $\mathbf{u}^{sub}(\mathbf{x})$ on the usual grid is based on the figure below. Fig. 3.10a representes a deformed voxel on a usual grid centered in O in gray. The displacement field $\mathbf{u}^{hom}$ due to this deformed voxel on another voxel of the usual grid centered at A is computed using Algorithm6. This voxel is now discretized in $n \times n$ sub-pixels for $2D$ applications or $n \times n \times n$ sub-voxels in $3D$ applications (4×4 sub-pixels in the example). $\mathbf{u}^{sub}$ is the displacement field at voxel centered at point A due to this sub-voxels centered at B_j.

The displacement $\mathbf{u}^{sub}$ is also equal to the sum of the displacement field $\mathbf{u}_i^j$ due to a single sub-voxel deformed centered at O on a row of sub-voxels centered at $A_j$such as $OA_j = B_jA$. This is shown in Fig. 3.10b. Now considering Fig. 3.11, this displacement field ($\mathbf{u}^{sub}$) is also equivalent to the sum of the displacements $\mathbf{u}_i^{'j}$ due to a deformed voxel centered at point O on the initial grid on points A'_j such as $OA'_j = nB_jA$. This is shown in Fig. 3.11b. The only difference between these last two sums is due to the long-range strain field, and approximately results in a linear drift of the displacement. As the end of the vectors OA'_j does not lie on the grid points (voxel centers) but on the corners of the voxels, the displacement field on Fig. 3.11b must be calculated with the shifted Green operator $\widehat{\mathbf{B}}_S^D$. A last point is the scaling of the $\mathbf{u}_i^j$ and $\mathbf{u}_i^{'j}$ sums during the operations of Fig. 3.10 and Fig. 3.11. To keep the one Burgers vector jump between both sides of the sub voxels plane in Fig. 3.10a, the eigenstrain in the sub voxels must be multiplied by n. The backwards change of scale requires a division by n, therefore there is no scaling factor between $\mathbf{u}^{hom}$ and $\mathbf{u}^{sub}$. In conclusion,$\mathbf{u}^{sub}$ is computed on the usual grid using the method described above

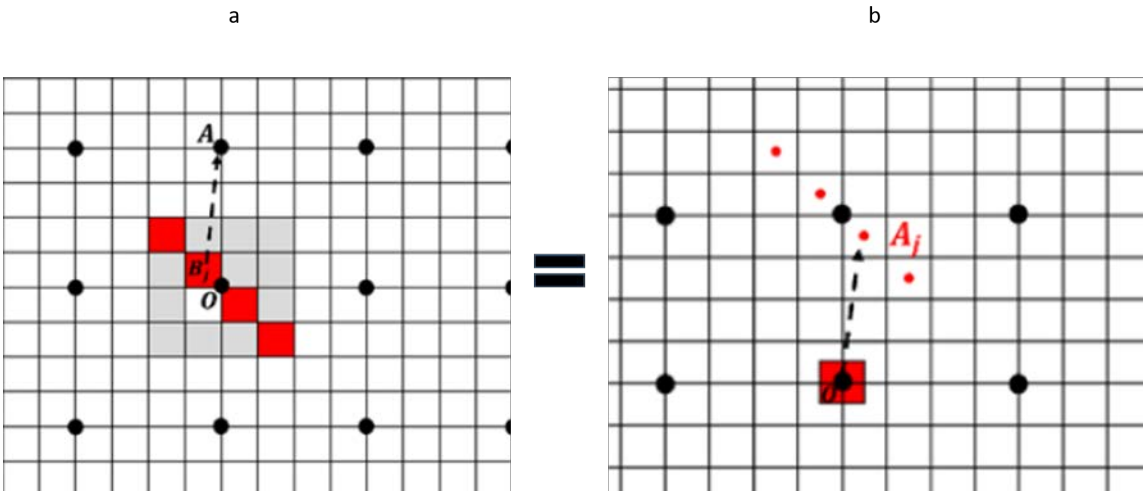


FIGURE 3.10 – 2D representation of the computational grid. Black dots correspond to the voxels center. (a) A voxel with center O is discretized in 4×4 in 2D ($4\times4\times4$) sub-voxels. Some sub-voxels contain an eigenstrain (red sub-voxels). We want to compute the displacement field at voxel centered at point A, due to these deformed sub-voxels centered at B_j. (b) Effect of one deformed sub-voxel centered at O on a row of sub-voxels centered at B_j such as $OA_j = B_j$ A. The sum of these effects is equal to the previous displacement field.

In our numerical code, the patch $\mathbf{D}(\mathbf{x})$ is stored as $D_{ij}^{pl}(\mathbf{x})$. $D_{ij}^{pl}(\mathbf{x})$ is the difference in displacement in direction i due to a voxel which belongs to the plane "pl" of a dislocation loop with a Burgers vector j at a position ($\mathbf{x}$) relative to the transformed voxel. For a for fcc "pl" is equal to (111),($\bar{1}$11),(1$\bar{1}$1),(11$\bar{1}$) .

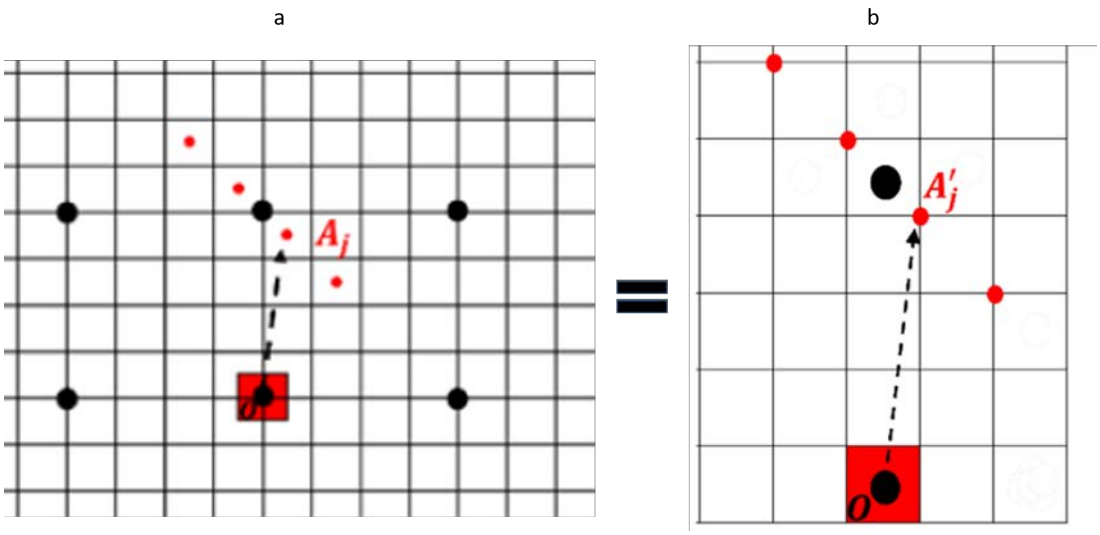


FIGURE 3.11 – Effect of deformed voxels of the usual grid centered at O on a row of voxels (computed at corners A'_j using a shifted Green operator) such as $OA'_j = nB_jA$. This sum is equal to previous wanted sum.

This means that 36 components of $\mathbf{D}^{pl}_{ij}(\mathbf{x})$ must be computed. In practice, in a material with cubic symmetry, it is sufficient to compute $D^{111}_{13}(\mathbf{x})$ and $D^{111}_{33}(\mathbf{x})$, and to use the symmetries of the cube (fourfold [001] axis, threefold [111] axis, and $(1\bar{1}0)$ symmetry plane) and suitable exchanges of the components of $(\mathbf{x})$ to obtain the required components. The final recipe to compute $\mathbf{D}^{pl}_{ij}(\mathbf{x})$ and use the patch is now summarized :

- First, define one centered voxel with the eigenstrain associated to a dislocation with a Burgers vector [001] in a (111) plane.

- Second, compute the displacement field in directions $\mathbf{u}^{hom}_1$ and $\mathbf{u}^{hom}_3$ at the voxels center around the transformed voxel with the discrete periodized operator $\mathbf{B}^D$.

- Third, compute the displacement field in directions $\mathbf{u}^{hom}_1$ and $\mathbf{u}^{hom}_3$ at the voxels corner around the transformed voxel with the shifted discrete periodized operator $\mathbf{B}^D_S$.

- Fourth, calculate the $u^{sub}_1 = \sum u^{'j}_1$ and $u^{sub}_3 = \sum u^{'j}_3$ sums ($n \times n$ terms for each

sum) as in fig. 3.11a, then the raw $D_{13}^{111}(\mathbf{x})$ and $D_{33}^{111}(\mathbf{x})$ for (x_1, x_2, x_3) going from -3 to 3 times the voxel size.

- Fifth and lastly, use the farthest voxels to correct the drift of the components by a linear approximation so that all terms for large $\mathbf{x}$ are zero, and keep only the terms for the first three neighbors to be non zero

3.3.4 Numerical applications

In this section, the sub-voxelization method, is applied to some mechanical problems of computing the displacement field.

3.3.4.1 A single centered inclined dislocation loop

Let us consider the same example as in section 3.3.1. The computed displacement due to the inclined loop is now computed and corrected using the sub-voxelization method. The result is presented in Fig. 3.12. The centered point which is zero is shifted by $\mathbf{b}/2$.

3.3.4.2 A random distribution of inclined dislocation loops

In this example, we consider a homogeneous anisotropic copper. The elastic constants of this cubic material are $C_{11} = 168.49GPa, C_{12} = 121.42GPa, C_{44} = 75.39GPa$. This material contains 64 hexagonal dislocation loops randomly distributed in the material and lying in a (111) plane. All the size of the loops are identical and equal to 128 voxels. The Burgers vector has the form $\mathbf{b} = \frac{a}{2}[-110]$ (a is the lattice parameter). In this example, the RVE is discretized in $512 \times 512 \times 512$ voxels. As in the previous examples, the displacement field is only due to the eigenstrain contained in deformed voxels. The volume fraction of the deformed voxels in this case is equal to 0.0233. So the linear part will be considered.

Fig. 3.13, shows the fluctuation displacement field computed with the classic Green operator $\mathbf{B}$. One denote the oscillations on the displacement field. Fig. 3.14, shows the fluctuation displacement field computed with the discrete and periodized Green operator $\mathbf{B}^D$ and corrected with the sub-voxelization method. The oscillations and the artifacts are now suppressed. Finally Fig. 3.15 is the comparison between the fluctuated displacement $\mathbf{u}^*$ and the displacement field $\mathbf{u}$. In the next chapter

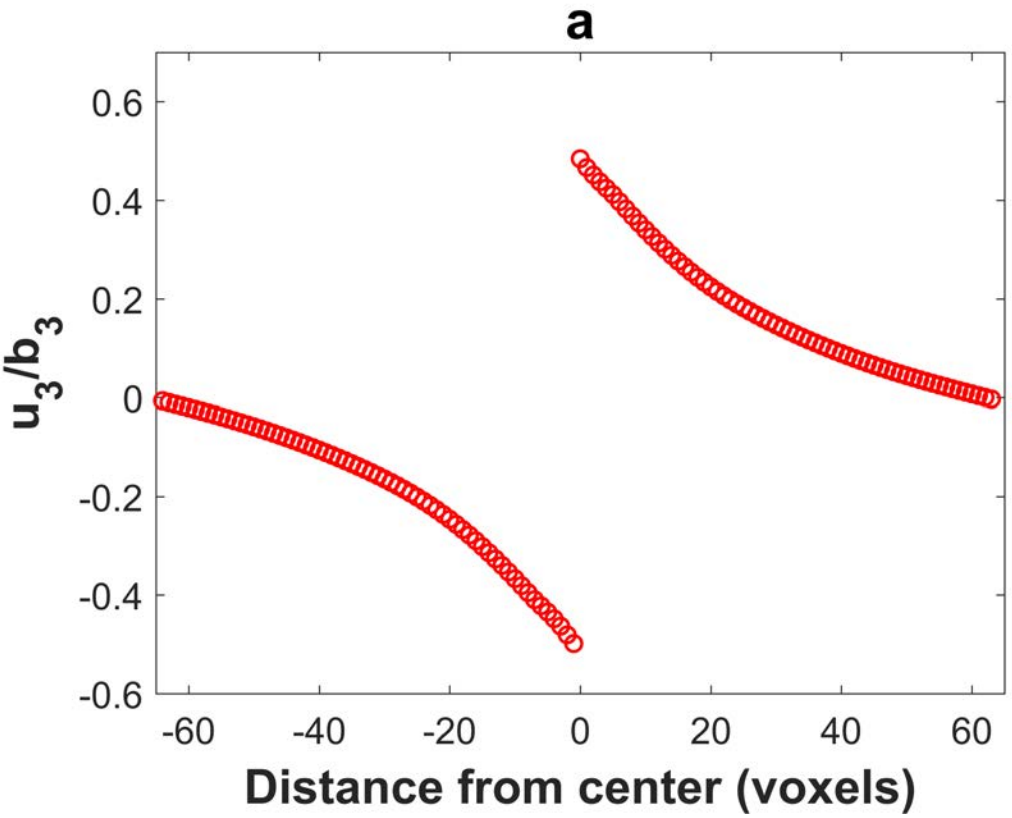


FIGURE 3.12 – (a) Plot of the displacement field u_3 (normalized by b_3) along the $z - axis$ for inclined dislocation loop. Artifacts are removed by sub-voxel method described above

we will show the effect of the periodic displacement field and the total displacement field on the peak profiles.

Fig 3.16, fig 3.17, fig 3.18 are 2D representations of previous displacement field : respectively the periodic one computed with classical Green operator or computed with the discrete periodized Green operator with the sub-voxelization method and the total term displacement. The representation is performed in the centered plane perpendicular to the $z - axis$.

3.4 Conclusion

In this chapter, In this paper, we showed that although the use of a periodized Green operator in the FFT-based method improves the final displacement field solution in a Representative Volume containing discontinuities (dislocation loops),

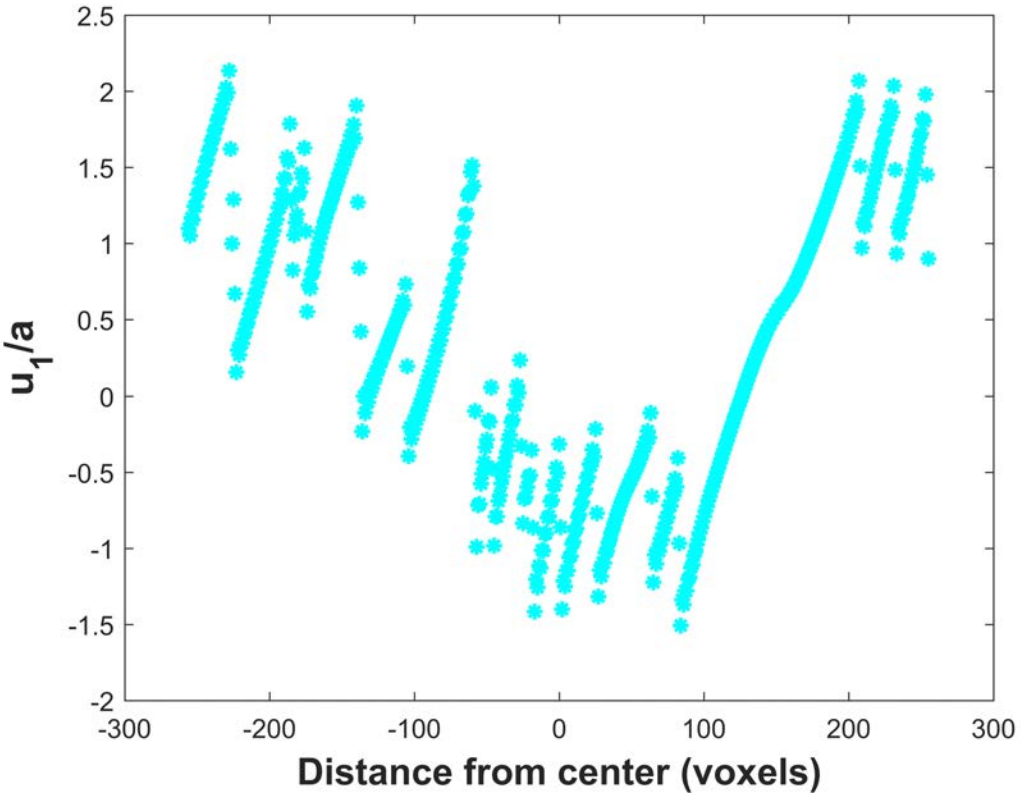


FIGURE 3.13 – Plot of the periodic displacement field u_1^* (normalized by a) along the $z-axis$ for inclined dislocation loop lying in a (111) plane and randomly distributed. The displacement field is computed using the classic Green third order operator $\mathbf{B}$

artifacts due to the voxelization of the dislocation loop planes are still present with respect to analytical solutions. These artifacts have unwanted consequences on the tails of diffraction peaks simulated by using this displacement field as input data. We have introduced a patch which corrects these artifacts by simulating the displacement field which would be obtained with a much finer voxelization without need to do the computations on a finer grid. A simple construction method for this patch has been given and the patch can be used in a single post-processing step to modify the initial FFT-based displacement field. The modified displacement field has been used to simulate one-dimensional diffraction peaks. The procedure strongly improves the shape of the peaks' tails, i.e. it gives a good description of the displacement field near the dislocation lines.

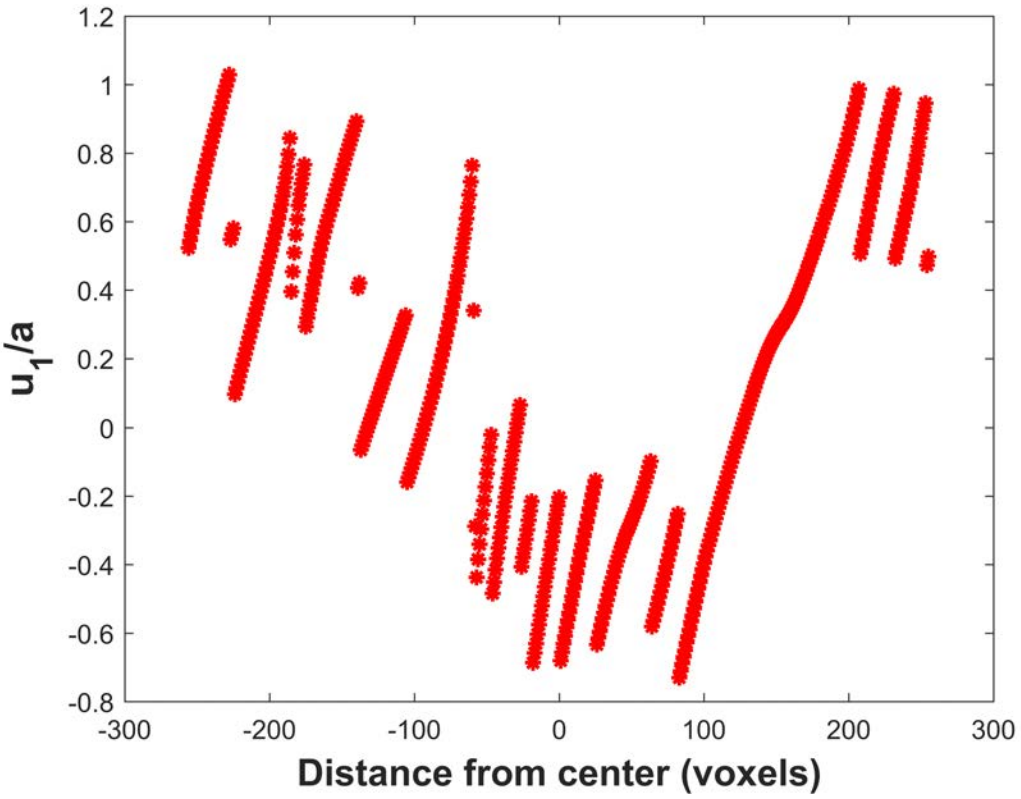


FIGURE 3.14 – Plot of the periodic displacement field u_1^* (normalized by a) along the $z-axis$ for inclined dislocation loop lying in a (111) plane and randomly distributed. The displacement field is computed using the consistent discrete third order Green operator $\mathbf{B}^D$ and corrected with the sub-voxelization method

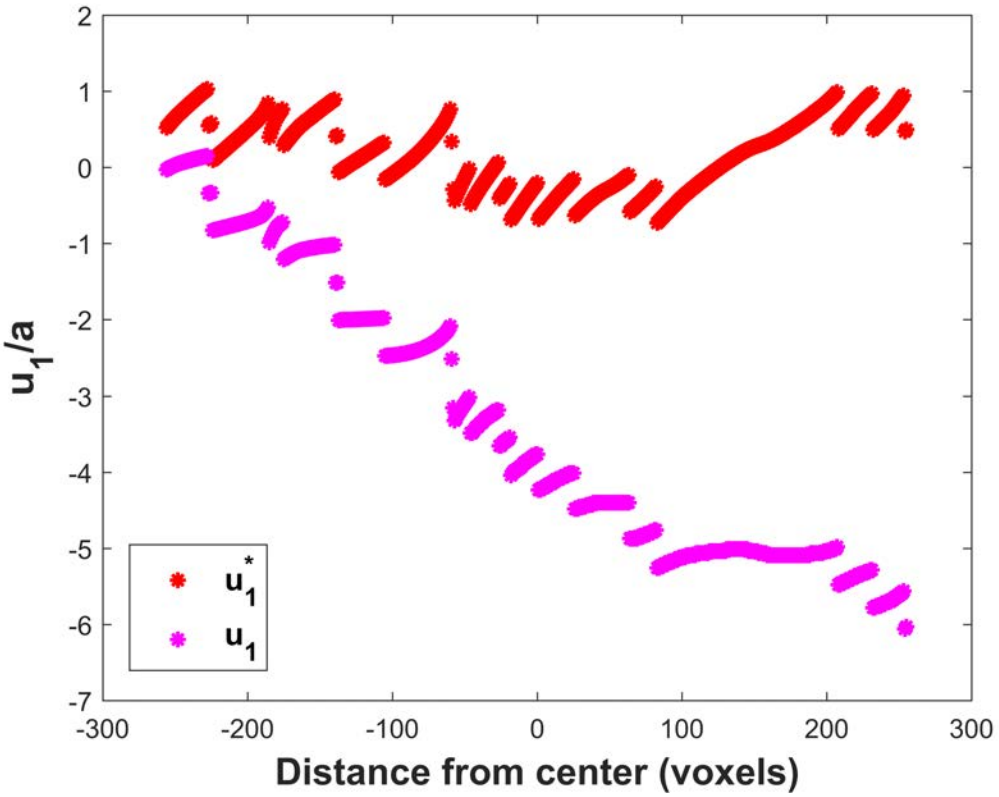


FIGURE 3.15 – Plot of the displacement field u_1 (normalized by a) along the $z-axis$ for inclined dislocation loop lying in a (111) plane and randomly distributed. The periodic displacement $\mathbf{u}_1^*$ and the total displacement field $\mathbf{u}_1$ are compared

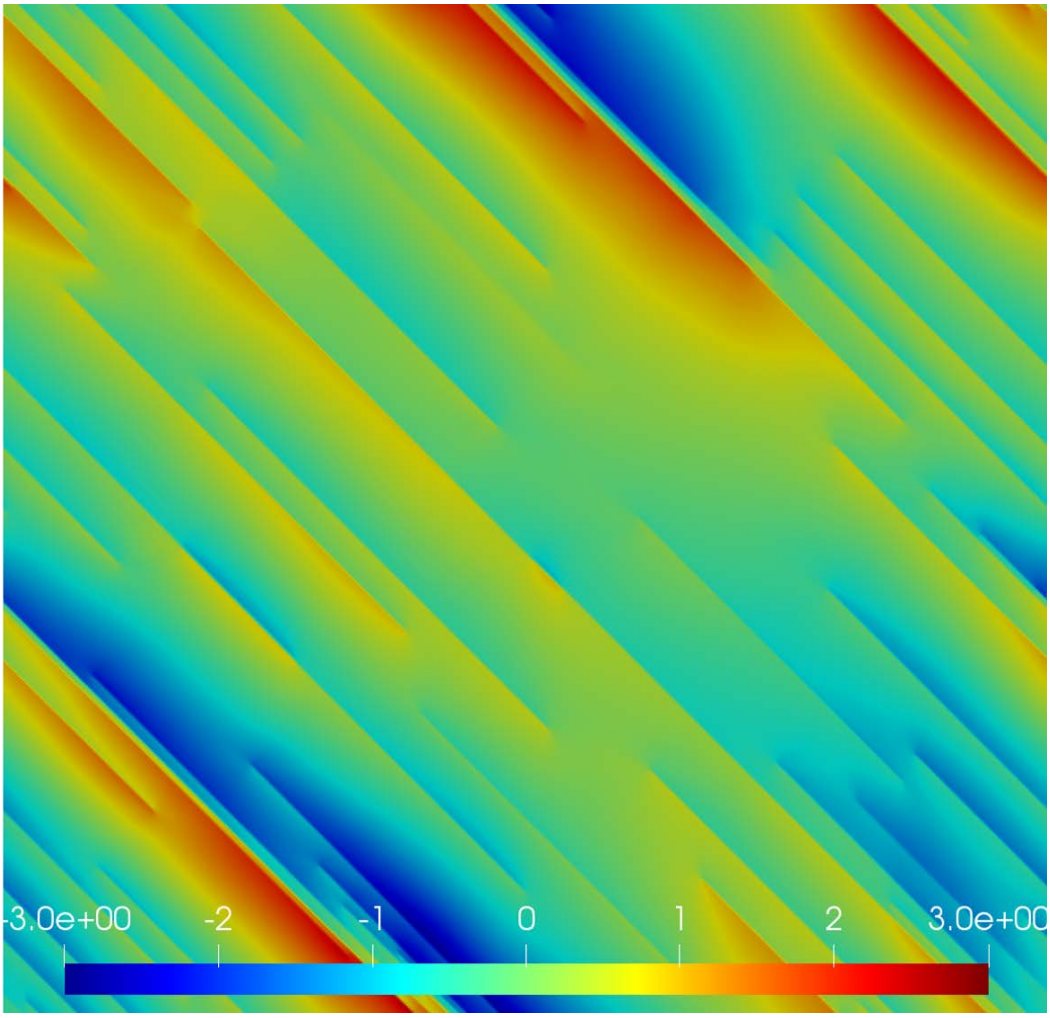


FIGURE 3.16 – 2D representation of the periodic displacement field u_1^* (normalized by a) in a centered plane perpendicular to $z - axis$ for inclined dislocation loop lying in a (111) plane and randomly distributed. The displacement field is computed using the classic Green third order operator $\mathbf{B}$

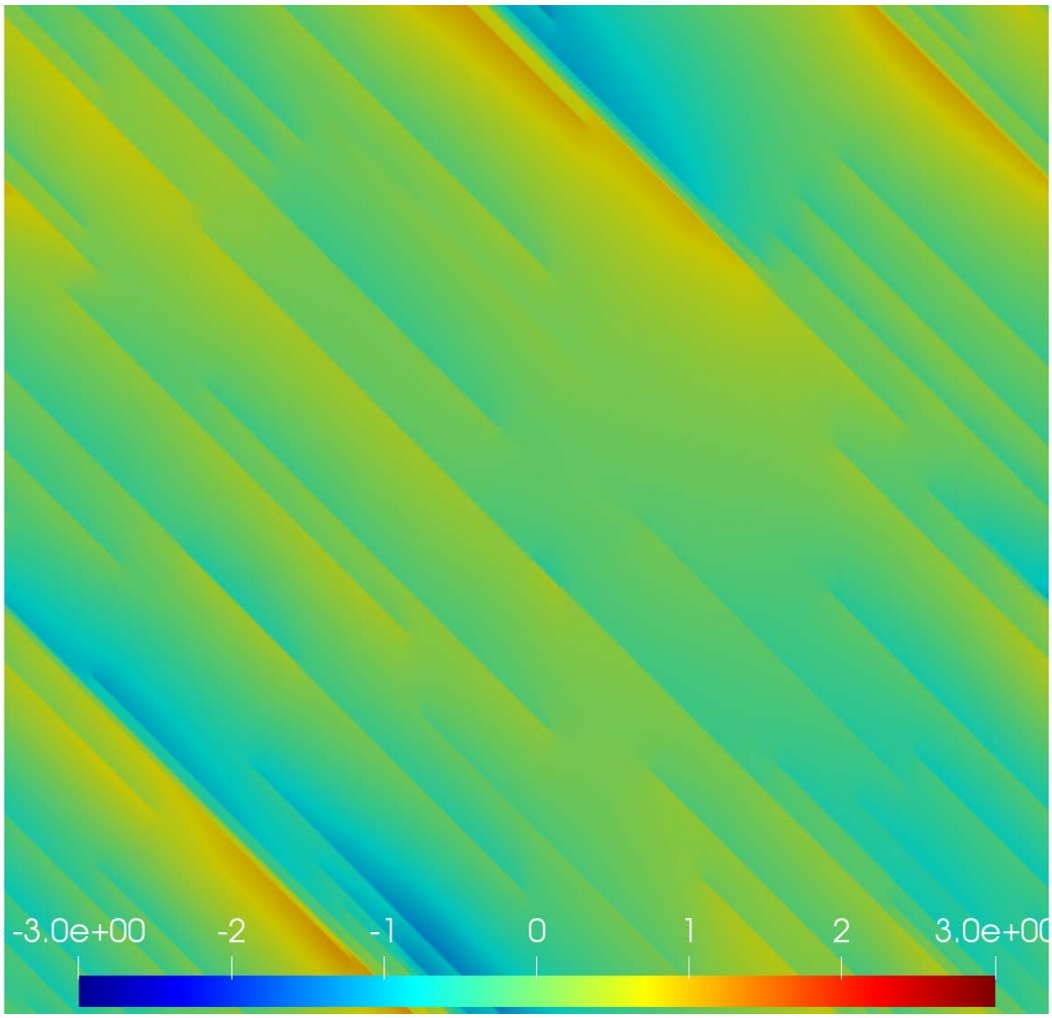


FIGURE 3.17 – 2D representation of the periodic displacement field u_1^* (normalized by a) in a centered plane perpendicular to $z-axis$ for inclined dislocation loop lying in a (111) plane and randomly distributed. The displacement field is computed using the consistent discrete third order Green operator $\mathbf{B}^D$ and corrected with the sub-voxelization method

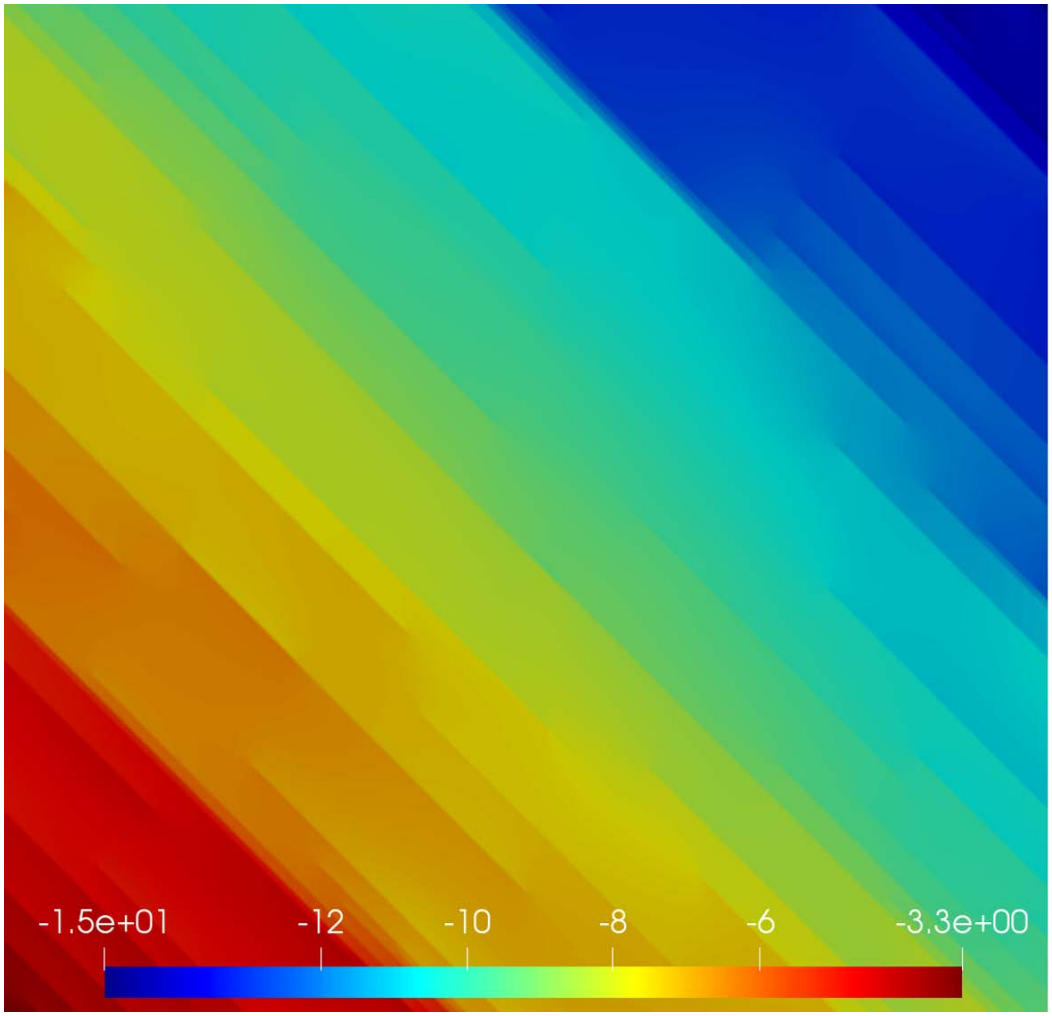


FIGURE 3.18 – 2D representation of the displacement field u_1 (normalized by a) in a centered plane perpendicular to $z - axis$ for inclined dislocation loop lying in a (111) plane and randomly distributed. $\mathbf{u}_1$ are compared

Chapitre 4

X-ray diffraction peaks modeling using the displacement field

4.1 Objectives

In the previous chapters, we developed a discrete and periodized Green operator to compute the displacement field in a periodic material. We proposed a sub-voxelisation method to correct the artifacts appearing in the case of inclined dislocations. The result is the distributed part of the displacement field. It can be used to compute the shape of the diffraction peak. The linear part of the displacement field can be deduced from the average strain computed in step 12 of algorithm 6. It results in a shift of the peak.

In order to compute the peaks, we follow the same method of Vaxelaire et al. [141], i.e. we compute the Fourier Transform of the $\mathbf{g}.\mathbf{u}$ field. Depending on the size of the simulated representative volume of matter and the experimental conditions such as the X-Ray beam coherence lengths, we can assume a coherent beam or a partially coherent beam where a full calculation is necessary [60].

The initial output of the FFT calculation is the A_{FFT} value of the scattered amplitude, which is squared to give the I_{FFT} intensity at each of the N^3 voxels of a RVE in reciprocal space representing the vicinity of the diffraction vector $\mathbf{g}$. From this, we obtain the I_{FFT} intensity profile on a $(2N)^3$ grid. It is then possible to visualize sections of the profiles or sum it on one or two directions to get 2D or 1D profiles which can be compared to experimental data and/or analyzed to evaluate the microstructural parameters such as the dislocation density and Burgers vectors.

The chapter is organized as follows. In the next section, we present the detailed

numerical method used to generate the diffraction profiles. Then, we present the 2D and 3D profiles obtained for single dislocation loops with different shapes, sizes, and Burgers vectors, and discuss the effect of the different corrections (periodized operator and subvoxelization) on the profiles. We then compute the peaks for various distributions of single dislocation loops. In the last two sections, we first analyze the 1D profiles by computing their Fourier Transforms or using restricted moments, then discuss the results.

4.2 Numerical model to simulate X-ray diffraction intensity peaks

4.2.1 Amplitude and intensity

The model developed to generate virtual X-ray diffraction peaks is similar to the model proposed by Vaxelaire et al. [141]. This method was already reported in the first chapter. It is used to compute the 3D diffracted amplitude produced in the vicinity of the diffraction vector in a Representative Volume of single crystal. This 3D amplitude is equal to the sum of complex amplitude scattered by each atom. It is given by the Fourier transform :

$$A_{FT}(\mathbf{q}) = FT\left(f(\mathbf{x}).exp(i\mathbf{g}.\mathbf{u}(\mathbf{x}))\right) \tag{4.1}$$

where $\mathbf{g}$ is the diffraction vector, $\mathbf{x}$ is the position of atoms and $f(\mathbf{x})$ is the scattering factor. $\mathbf{u}(\mathbf{x})$ is the displacement field. As in the case of the stress and strain fields, we use the Fast Fourier Transform :

$$A_{FFT}(\mathbf{q}') = FFT\left(f(\mathbf{x'}).exp(i\mathbf{g}.\mathbf{u}(\mathbf{x}'))\right) \tag{4.2}$$

where $\mathbf{x}'$ is the center of a voxel of the RVE and $\mathbf{q}'$ a grid point of the reciprocal space. In reference [141], the displacement field is computed using 3D finite element (FE) method. But here we use the displacement field computed with FFT algorithms as developed in the previous chapters. In order to perform the FFT calculation of eq. 4.2, $exp(i\mathbf{g}.\mathbf{u}(x'))$ needs to have the same periodicity as the RVE, i.e. $\mathbf{u}(x')$ to be the same, modulo a translation vector of the crystal lattice.

However, as shown in the 2D example of fig. 4.1a, this does not occur in a general case : as the RVE has been partly sheared by a dislocation loop in an horizontal

plane, the shift of the top of the RVE (red) vs. its bottom is only a fraction of a Burgers vector.

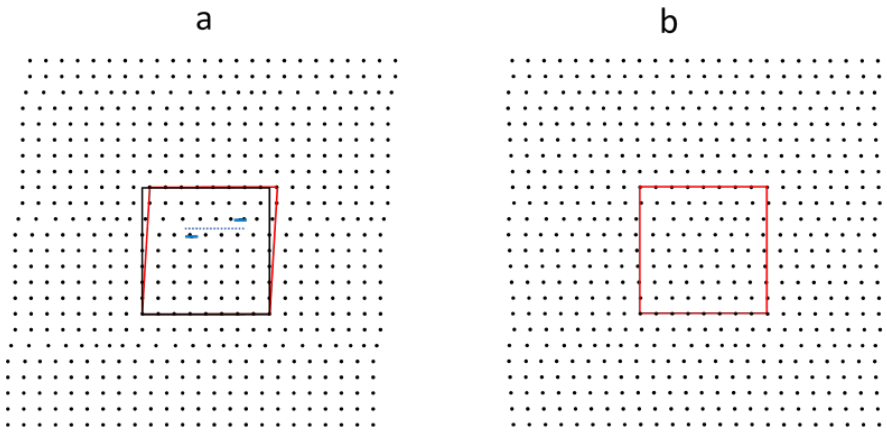


FIGURE 4.1 – Displacement field resulting from a single dislocation loop in each VER. (a) Full field and (b) periodic part

As shown in Chapter 3, the displacement field is computed as the sum of a linear part and a periodic part :

$$u_i(\mathbf{x}) = \langle u_{i,j} \rangle x_j + FFT^{-1}(\widehat{u*}_i(\boldsymbol{\xi}_j)) \tag{4.3}$$

where $\langle u_{i,j} \rangle$ is the non-symmetric displacement gradient tensor averaged on the unit cell which results both from external stresses (zero in the present computation) and from the average plastic strain due to dislocations. As seen in fig. 4.1b the second term in eq. 4.3, which results from the inverse FFT, is periodic but results in a rotation of the lattice planes, i.e. a rotation of the $\mathbf{g}$ vector. On the contrary, in fig. 4.1a, the orientation of the lattice planes remains constant. For a single dislocation loop, the rotation angle is smaller than $\frac{|b|}{|d|}$ and can be neglected. However, if a large number of dislocation loops with the same polarity are present within the RVE, the center of the diffraction peak (the extremity of the $\mathbf{g}$ vector) will be shifted. In order to keep the periodicity of $exp(i\mathbf{g}.\mathbf{u}(\mathbf{x}))$ we thus require the displacement δu along a basis vector V of the RVE to be a vector of the Bravais crystal lattice :

$$\langle u_{i,j} \rangle d = m\frac{a}{2}$$

The residual displacement :

$$\mid \langle u_{i,j} \rangle - \langle u*_{i,j} \rangle \mid d \leq \frac{a}{4}$$

is neglected.

The intensity is defined as the squared norm of the amplitude and is given by :

$$I_{FFT} = A_{FFT}(\mathbf{q}')\bar{A}_{FFT}(\mathbf{q}') \tag{4.4}$$

Using the periodicity of the FFT solution in reciprocal space and the relation between the Fourier transform and the FFT eq.2.16, we then obtain the I_{TF} intensity profile on a $(2N)^3$ grid :

$$I_{FT}(\mathbf{q}) = I_{FFT} sinc^2\left(\frac{\pi i}{N}\right) sinc^2\left(\frac{\pi j}{N}\right) sinc^2\left(\frac{\pi k}{N}\right) \tag{4.5}$$

Using this equation, it is possible to compute the 3D intensity in the vicinity of the diffracted vector $\mathbf{g}$.

4.2.2 1D projections

In order to obtain a 1D plot of the intensity vs. the magnitude of the $\mathbf{g}+\mathbf{q}$ vector, we need to sum the intensities of the voxels I_{TF} (i_1, i_2, i_3) having the same $\frac{\mathbf{g}}{|\mathbf{g}|}.\mathbf{q}$ dot product. The result is a two columns array, where the first column is a value of $\frac{\mathbf{g}}{|\mathbf{g}|}.\mathbf{q}$ and the second one the sum of corresponding intensities. As the h, k, l components are small integers, the distribution of $\frac{\mathbf{g}}{|\mathbf{g}|}.\mathbf{q}$ values is discrete and periodic, but the distances between successive points vary. For a $2N = 1024$ points grid (from -512 to 511), and a (200) $\mathbf{g}$ vector, 1024 lines are enough, while for a (311) vector, more lines are necessary. In order to plot all profiles on the same 1024 points grid $q = \frac{2\pi i}{d}$, the intensity of each line is distributed on the two neighboring integer points according to their distances.

Lastly, despite the extension of the grid from N^3 points to $(2N)^3$ points, we observe an unexpected decrease of the intensities at the tails where only a small number of voxels contribute to the sums. In order to obtain 2D images, on must project the intersection of the RVE and the Ewald's sphere on a detector parallel to the Ewlad's sphere tangent. This treatment is not used in this work but 2D section of the RVE are shown in the next section.

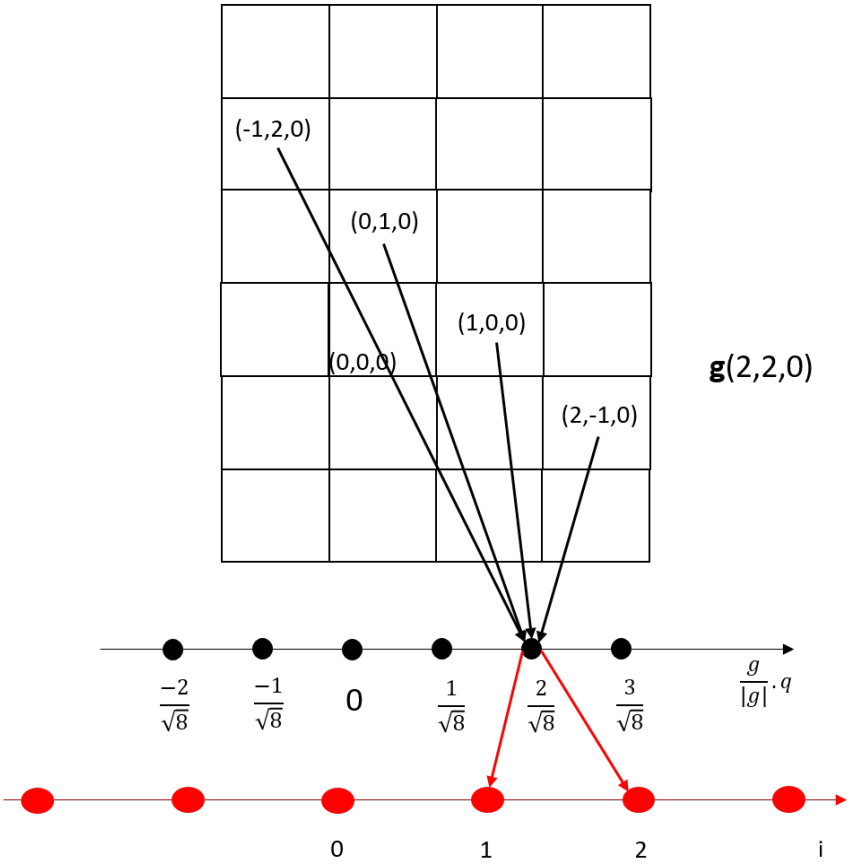
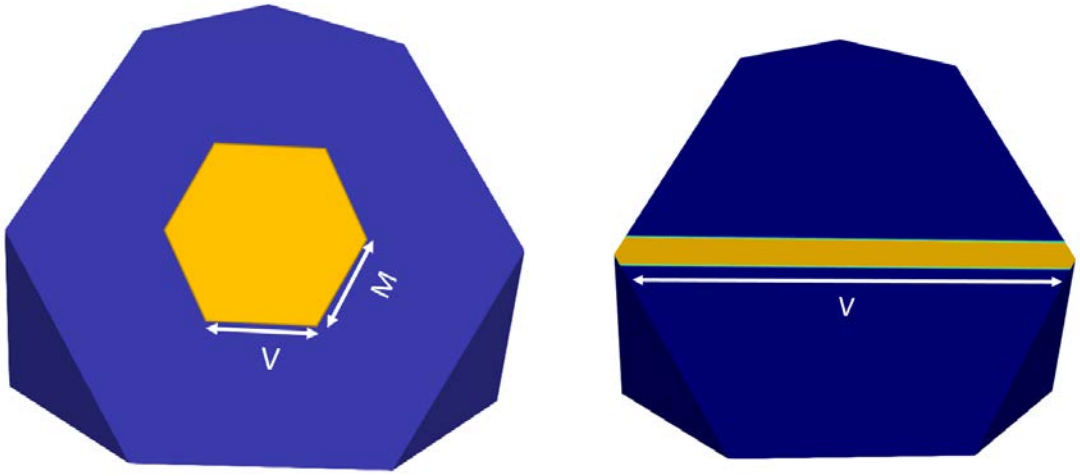


FIGURE 4.2 – Computation of a 1D profile. The intensity at voxels (represented here in 2D) are added if their scalar product with the diffraction vector **g** are equal. The sums are then split on the two nearest points of the grid.

4.2.3 Applications to reference cases

4.2.3.1 Simulation parameters

In the next numerical examples, we will assume a perfect coherent incident beam. Unless otherwise stated, the scattering factor $f(\mathbf{x})$ will be taken as constant. We will consider in the numerical examples a hexagonal dislocation loop lying in a (111) plane as shown in fig. 4.3(a). This loop has two screw dislocation segments (line V) and four mixed dislocation segments (line M). A screw dislocation dipole with a $[\bar{1}10]$ line direction as illustrated on fig 4.3(b) will also be considered.



(a) (b)

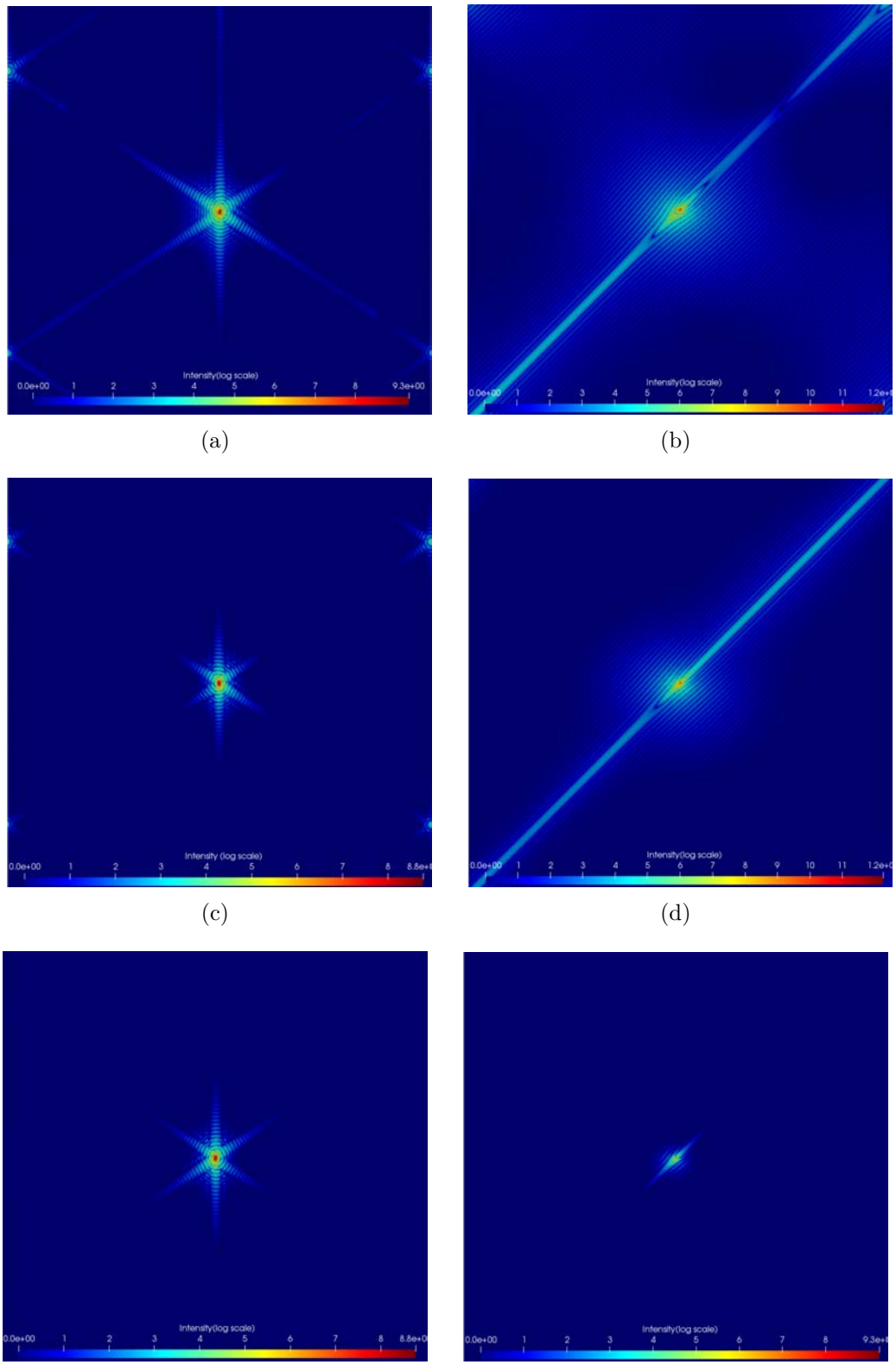
FIGURE 4.3 – (a)Hexagonal loop (i.e. transformed platelet) lying in a (111) plane of a FCC crystal used for diffraction peaks simulation. (b) Dislocation dipole in a 111 plane

4.2.3.2 Single dislocation loop

Let us consider a representative volume (size : $1\mu m^3$ divided into 512^3 voxels) containing a single dislocation loop a Burgers vector $\mathbf{b} = \frac{a}{2}[-110]$ lying in a (111) slip plane. Each segment is $36\sqrt{2}/512\mu m$ long. The corresponding dislocation density is $6 \times 10^{11} m^{-2}$. The displacement field due to this dislocation loop is computed using the discrete Green operator defined in the previous chapter. The artifacts appearing on this field are also suppressed using the subvoxelisation method. This displacement field is now used to simulate X-ray diffraction in the vicinity of a diffraction vector. The 3D distribution of the diffracted intensity is reported with an arbitrary logarithmic scale, in the (111) plane containing the dislocation loop, fig. 4.4 (left side) and in the (110) plane containing the Burgers vector fig. 4.4 (right side).

Perfect hexagonal dislocation loop

The aim of this example is to compare the simulated diffracted intensity with displacement fields computed respectively with the classical operator, the discrete operator, and the discrete operator corrected with the sub voxelisation method.



(a) (b)

(c) (d)

(e) (f)

FIGURE 4.4 – 2D section plots of the diffracted intensity for a single hexagonal dislocation loop deduced from the displacement field computed with the classical operator (a) and (b), the discrete operator (c) and (d), and after sub-voxelization correction (e) and (f). Representation in (111) plane at left and in $(01\bar{1})$ plane at right .

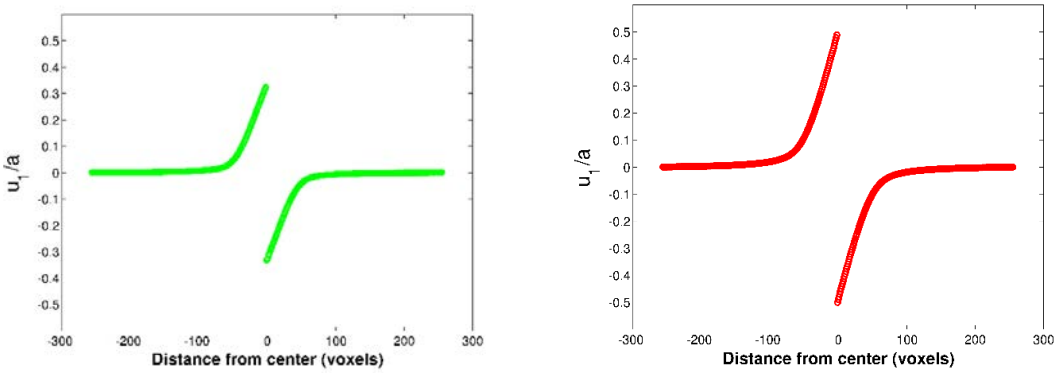
The centered voxel $(256, 256, 256)$, has the maximum intensity (about 10^{16}). All three peaks share common features : an asymmetric high intensity zone surrounding the central voxel. Note that each dislocation segment along a (110) direction in the loop plane generates a linear highly distorted zone, and the corresponding (Fourier transformed) scattered intensity is distributed in the orthogonal (110) plane. This (110) plane intersect the $(01\bar{1})$ plane along [111] and the (111) plane along a (211) direction. Therefore in the (111) plane, we denoted low intensity streaks along the $[2\bar{1}\bar{1}], [\bar{1}2\bar{1}]$, and $[\bar{1}\bar{1}2]$ directions on left side figures. On the right side figure , (-110) plane, we denoted a low intensity streaks along the [111] direction.

A salient feature of fig. 4.4(b) and fig. 4.4 (d) is a strong streak in direction [111] surrounded by oscillations. In fig. 4.4(b), its intensity is increasing with increasing distance from the center with a maximum in the vicinity of voxel $(512, 512, 512)$. The intensity is lower and slowly decreasing in fig. 4.4 (d). On the contrary, the streak intensity decreases strongly and is almost absent in fig. 4.4(f). Two phantom peaks are also visible in fig. 4.4(a) and 4.4(c) and are suppressed on fig. 4.4 (e). We relate the streak and the phantom peaks to a parasitic scattered amplitude resulting from a surface defect i.e. fast oscillations of the displacement field in the loop plane and its immediate vicinity : these are oscillations resulting from the classical Green operator and from the voxelization artifacts.

Faulted hexagonal dislocation loop

In this example, we consider dislocation loop having the same geometry as in the previous example but with $\mathbf{b} = \frac{a}{6}[-211]$. This corresponds to a stacking fault in the loop plane. All other parameters are unchanged. The displacement field due to this dislocation loop is reported on fig. 4.5(a). The displacement field is nearly the same as in fig. 4.5(b) (which is the displacement field obtained with a perfect dislocation studied in section. 4.2.3.2) with a 2/3 scale factor. Note that both displacement field are normalized by a.

As a result, the displacement shift in direction x at the loop plane is no longer a crystal lattice translation vector, the $\mathbf{g}.\mathbf{b}$ scalar product is 2/3, and there is a step in the phase : $2\pi\mathbf{g}.\mathbf{u}$. The Fourier transform of the faulted surface is a line along the [111] direction, and as the Fourier transform of a Heaviside step function is q^{-1}, we may expect a streak along [111] with an intensity varying as q^{-2}. Fig. 4.6(b) and fig.4.6(d) represent the 3D intensity, in (111) plane plane and $(01\bar{1})$ plane respectively, obtained with the displacement due to faulted dislocation loop and computed with the discrete Green operator. Fig. 4.6(d) shows a streak along [111] as expected and fig. 4.6(b) also shows phantom peaks which are related to the faulted dislocation. It is important to note the similarity between numerical oscillations or



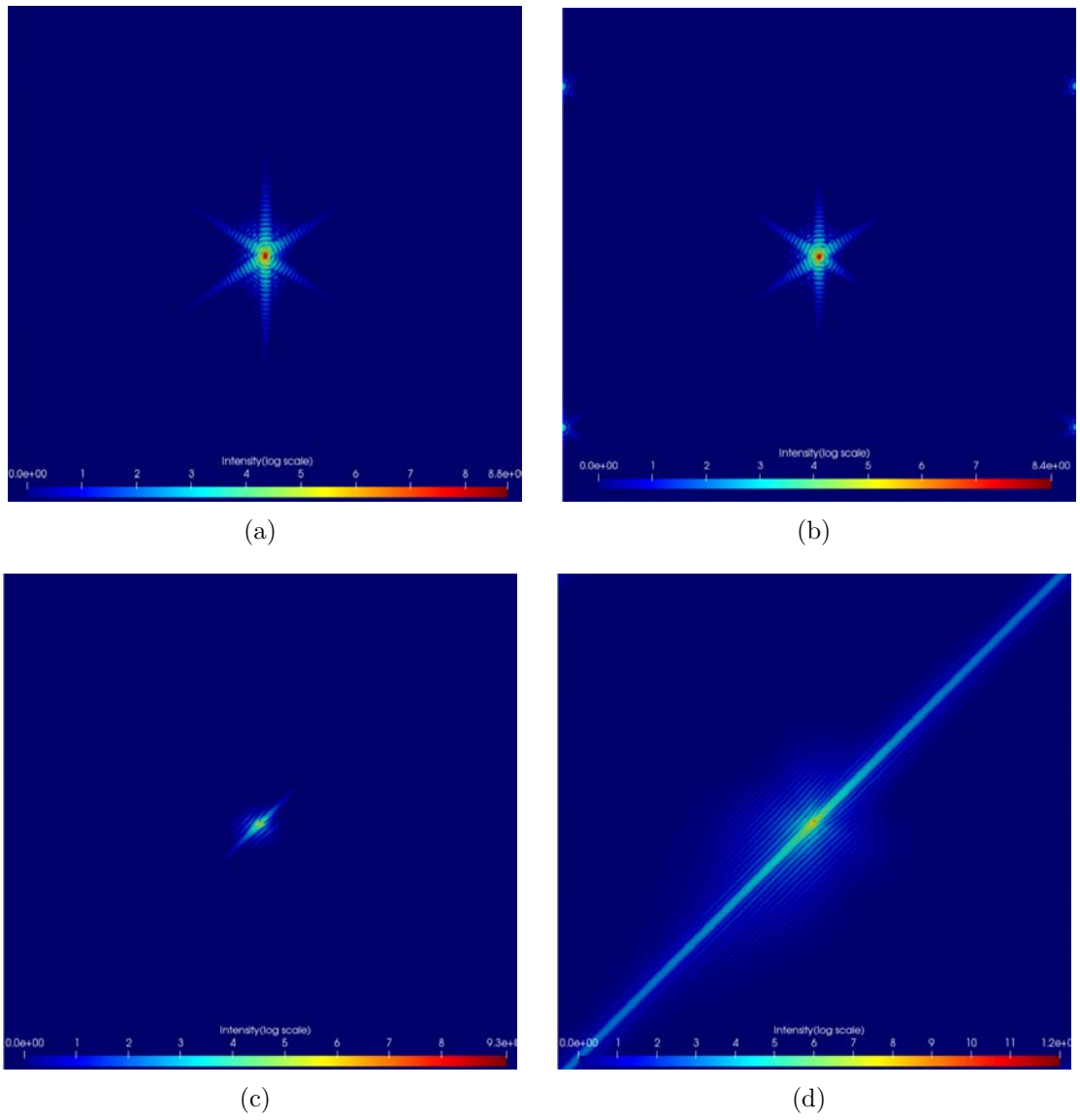
(a) (b)

FIGURE 4.5 – 1 D plot of the corrected displacement field of a faulted dislocation loop. This displacement field (at left) is compared to the displacement field due to a perfect loop at right.

artifacts effects (which are exclusively discretization effects) and faulted dislocation effects (which are physical effects) on the simulated intensity. When the numerical oscillations or the artifacts are not suppressed, a confusion is possible.

Comparison between a hexagonal and a rectangular dislocation loop

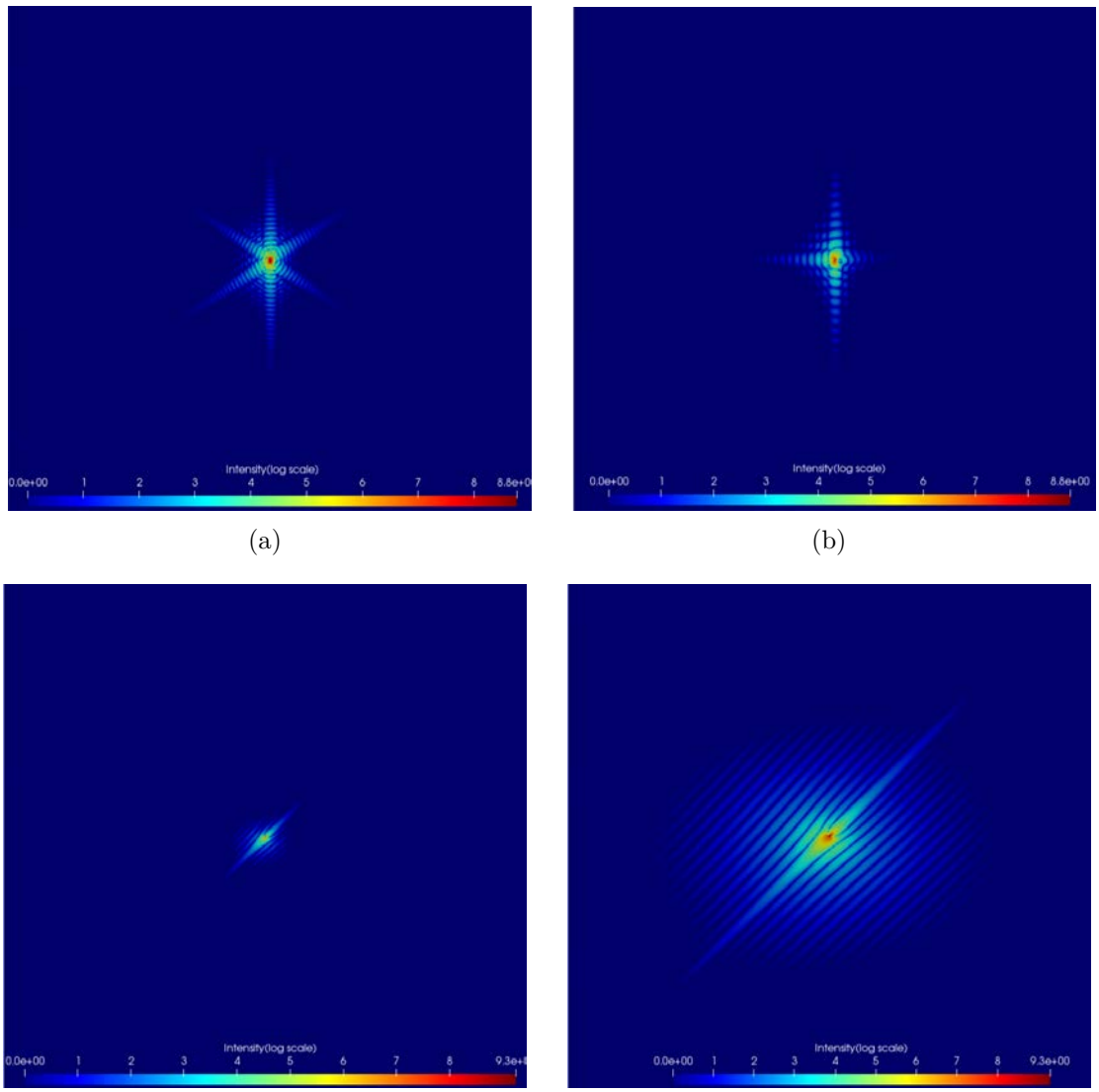
The aim of this section is to study the effect of the dislocation loop shape effect on the simulated intensity. In fig 4.7 the 3D intensity is represented with the same parameters as before for a rectangular fig.4.7 and for hexagonal (fig 4.7(a) and 4.7(c)) and rectangular dislocation loop (fig 4.7(b) and 4.7(d)).



(a) (b)

(c) (d)

FIGURE 4.6 – 2D section plots of the diffracted intensity : comparison between a faulted dislocation loop (at right) and a perfect loop (at left). (a) and (b) are representation in (111) plane, (c) and (d) are representation in $(01\bar{1})$ plane



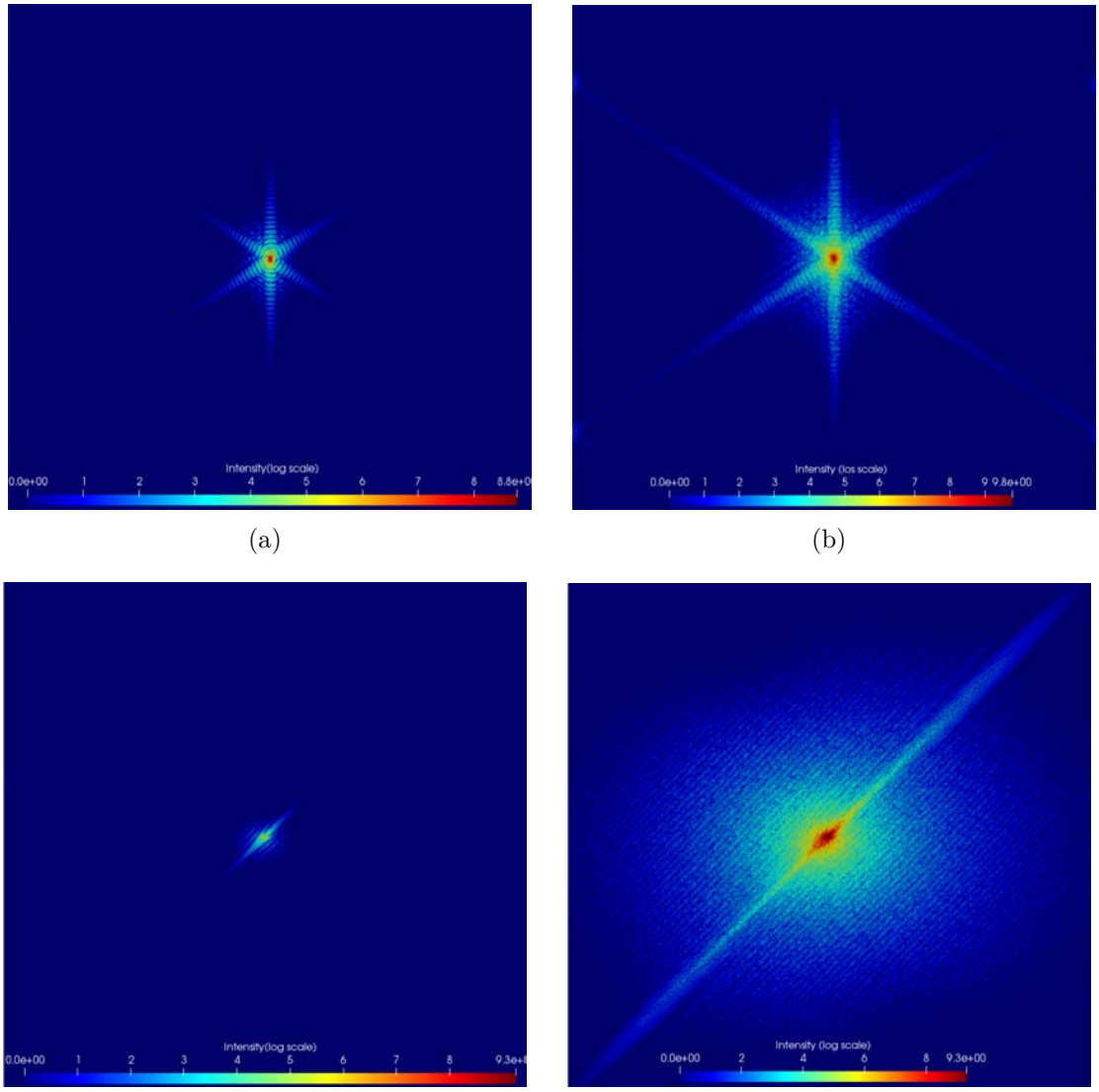
(a) (b)

(c) (d)

FIGURE 4.7 – 2D section plots of the diffracted intensity : comparison between a rectangular (at right) and a hexagonal dislocation loop (at left). (a) and (b) : (111) plane, (c) and (d) : $(01\bar{1})$ plane

4.2.3.3 Randomly distributed hexagonal dislocation loops

Now, we consider 64 hexagonal dislocation loops with the same (111) plane and Burgers vector distributed at random positions in the unit cell. The dislocation density is $3.8 \times 10^{13} m^{-2}$. All the other parameters are unchanged. The aim of this example is to study and confirm the effect of dislocation density on the simulated intensity. The 3D intensity is represented in the (111) plane and in the $(01\bar{1})$ plane and is compared to the single dislocation loop case in fig. 4.8.



(a) (b)

(c) (d)

FIGURE 4.8 – 2D plots of the diffracted intensity : comparison between a single(at left) and random distributed dislocation loop (at right).(a) and (b) are representation in (111) plane, (c) and (d) are representation in $(01\bar{1})$ plane

4.2.3.4 1D representation of the simulated intensity

Comparison of the displacement field and computation methods

Fig. 4.9 shows 1D profiles of the intensity in the case of single dislocation loop for which the displacement field is computed with the different methods discussed above. The peak shape near the top of the peaks is the same in all cases (except

a bump on the left side for the profile computed with the classical Green operator). Their long-range behavior is however quite different. When the displacement field has been calculated with the usual truncated operator (black line), a phantom peak is observed which is due to the short period oscillations near the displacement discontinuity (see fig. 3.1). The behavior of the peak calculated with the modified Green operator (blue curve) is only slightly better. When the intensity has been calculated with the sub voxel patch (red curve) the long-range intensity follows the expected intensity law $I(\mathbf{q}) = q^{-3}$ [70].

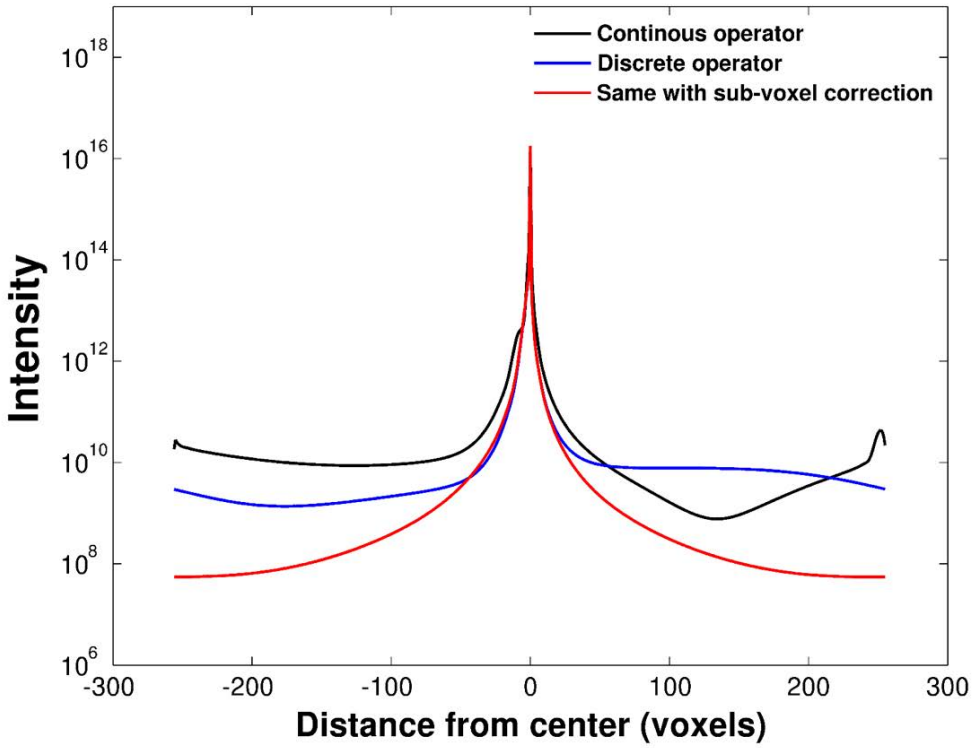


FIGURE 4.9 – 1D peak profiles computed for one dislocation loop using the different methods described in the previous chapter

Dislocation density effect on 1D intensity representation

We now consider 64 hexagonal dislocation loops with the same (111) plane and Burgers vector distributed at random positions in the unit cell. The dislocation density is $3.8 \times 10^{13} m^{-2}$. Fig. 4.10(b) compares the 1D profiles computed for both configurations (single dislocation loop and 64 randomly distributed dislocation loops). A decrease of the maximum intensity and a broadening of the top of the peak are observed in the second configuration. However, the tails of the peak still follow the

power law $I(q) = q^{-3}$ law and their intensity has been multiplied by 64 : the tail intensity is proportional to the dislocation density.

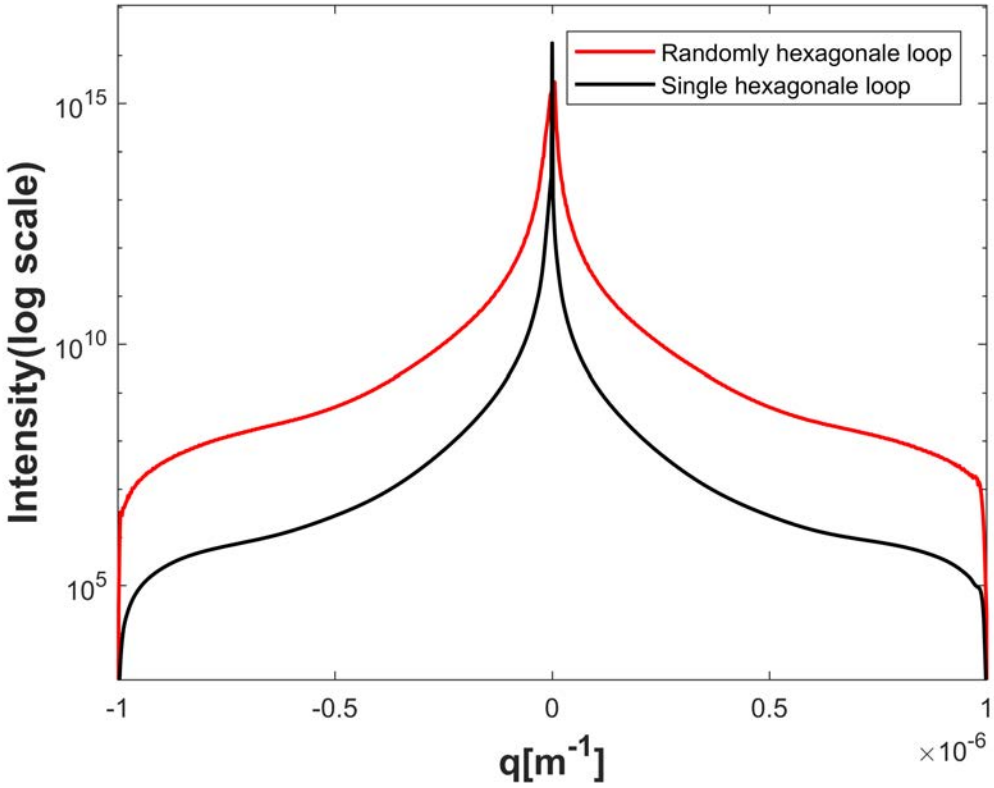


FIGURE 4.10 – 1D peak profiles computed for one dislocation loop using corrected displacement field : comparison between single and randomly distributed dislocation loops

Faulted vs perfect dislocation loop : Effect on 1D intensity representation

Fig. 4.11 compares the 1D profiles due to a perfect (black) and faulted (red) hexagonal dislocation loop. The top of the profile is thinner for the faulted loop (factor : 2/3), but the main difference is visible at the tail which follows a $I(q) = q^{-2}$ law. It may be remarked that, as in f.c.c. metals perfect dislocations are split into two partial dislocations (Shockley partials) linked by a stacking fault, this q^{-2} tail should also be visible, but with a very low intensity.

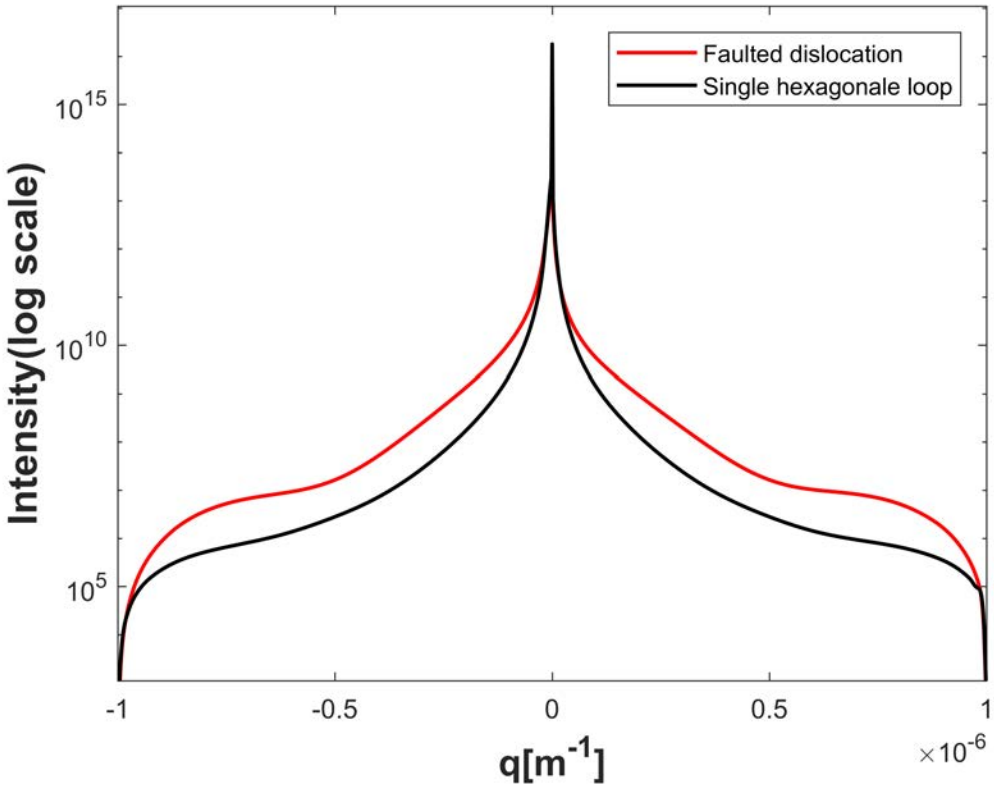


FIGURE 4.11 – 1D peak profiles computed for one dislocation loop using the corrected displacement field : comparison between a faulted and perfect dislocation loop

Faulted vs perfect dislocation loop : Effect on 1D intensity representation

Fig. 4.12 shows the effect of the average displacement field discussed in the previous chapter and in section. 4.2.1. When the dislocation density is small (loop with 32 voxels size), we assumed that the effect of the average displacement field can be neglected. The diffraction peak is not shifted using the periodic or the full displacement field. For high dislocation density the diffraction peak is shifted if the average displacement field is not considered.

4.3 X-ray diffraction analysis

Different X-ray diffraction analysis techniques were developed by several authors, most of whom belong to the Budapest school. Some of these methods were discussed in the first chapter. The aim of this analysis is to determine the microstructure characteristic parameters such as dislocation density and dislocation spatial distri-

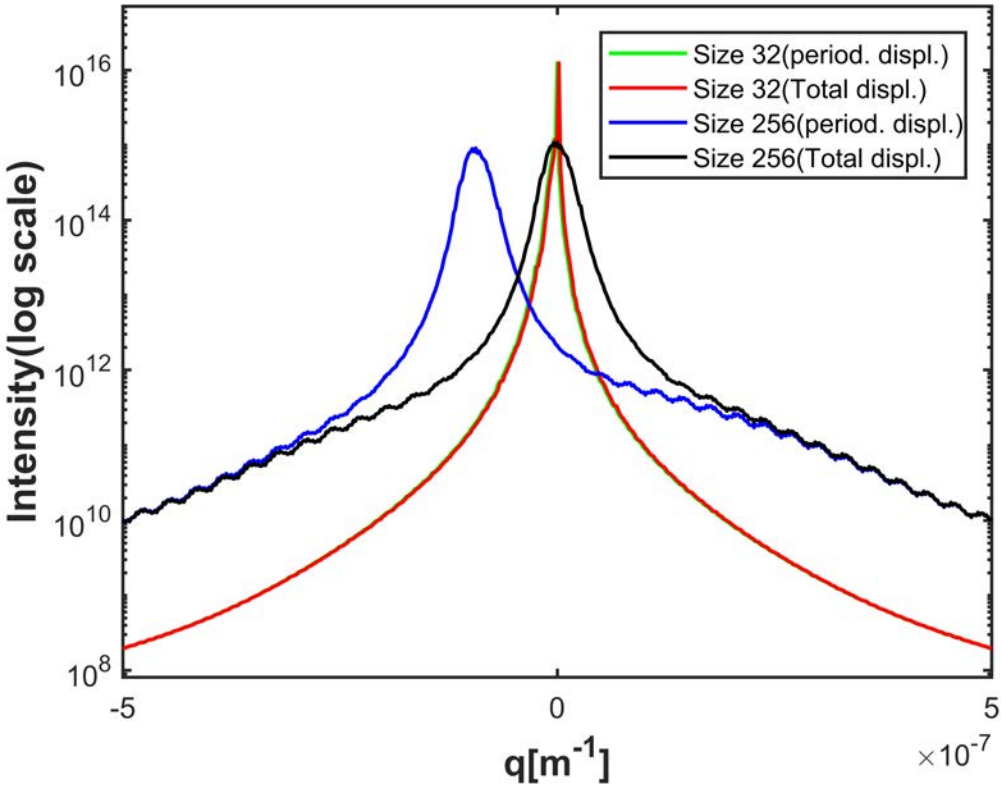


FIGURE 4.12 – 1D peak profiles computed for 64 random distributed hexagonal loop for 32 and 128 voxels side of loops.

bution parameters. Prior to analysis, the diffraction peaks are slightly shifted (less than a voxel) in order to correct the residual part of the translation and rotation of the **g** vector (see section. 4.2.1). The first moment of the peaks is then zero.Two analysis techniques will be used : the Fourier transform method, then the moments method. Both methods build upon the large **q** behavior of the peaks, i.e. depend on the variations of the strain field near the dislocation cores.

4.3.1 Fourier transform of the 1D diffraction peak

The model was proposed by Krivoglaz and Ryaboshapka [71] and improved by Wilkens [154]. Fig. 4.13 shows the real and imaginary parts of the FFT of the 1D (200) diffraction peak simulated for 64 hexagonal loops at random positions within the $1\mu m^3$ RVE (each side is $64\sqrt{2}$ voxels long). As expected, the real part is symmetric with a broad parabolic maximum : $A_0 = 1.8 \times 10^{16} \sim 512^6$. The imaginary part is antisymmetric, and falls to zero on both sides because of the periodicity of the FFT. The slope at zero is naught, and apparently follows a power

law before oscillating.

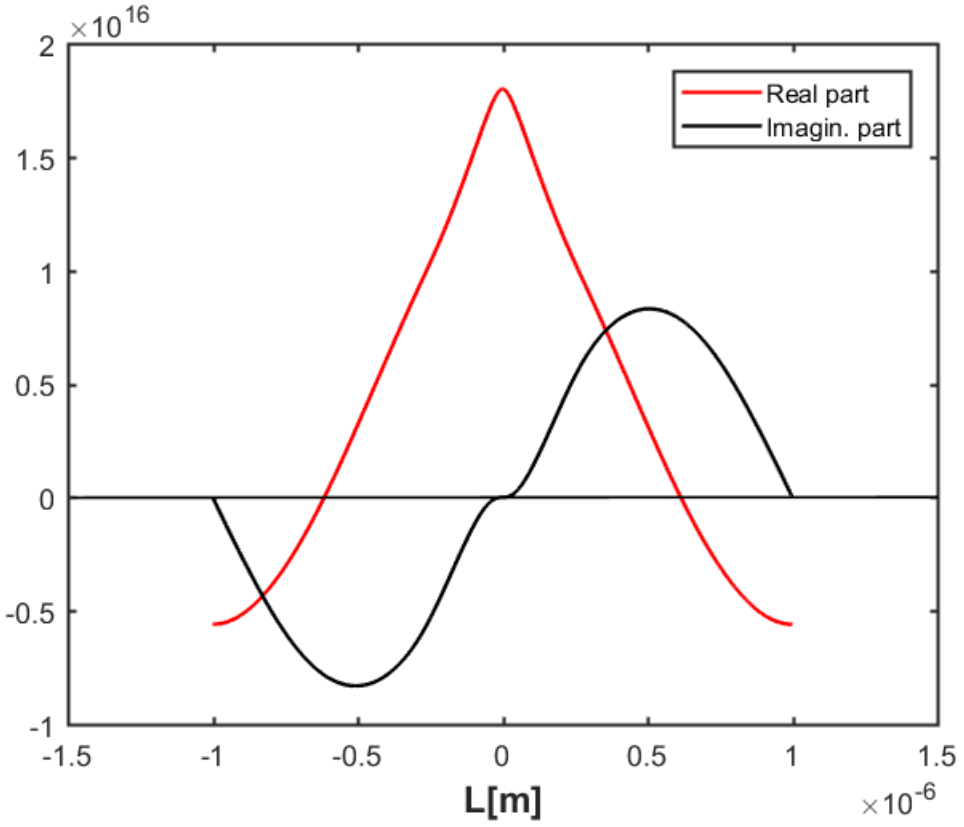


FIGURE 4.13 – Plot of the real and imaginary parts of the 1D (200) diffraction peak simulated for 64 loops.

4.3.1.1 Fit of the real part

As seen in the first chapter eq. 1.8, for a restricted random distribution of parallel straight dislocations [154], we expect the real part of the Fourier transform A_L to follow the relation [154] :

$$\frac{1}{L^2} ln \frac{A_L}{A_0} = -\frac{\pi}{2} \mathbf{g}^2 \mathbf{b}^2 C \rho f^*(\frac{L}{R_e^*}) \tag{4.6}$$

where $\mathbf{b}$, ρ , C , are the Burgers vector of the dislocations, their density, and the contrast factor. In the case of screw or edge dislocations in cubic crystals, representative values of the contrast factors as a function of the elastic anisotropy is given by Ungar et al. in [132]. Groma [51] also gives an expression of the contrast

factor for the screw dislocations :

$$C = cos^2\phi$$

and for edge dislocations :

$$C = sin^2\phi \frac{1}{8(1-\nu)}[1 - 4\nu + 8\nu^2 + 4(1-2\nu)cos^2\gamma]$$

where ν is the Poisson ratio, ϕ is the angle between $\mathbf{g}$ and the dislocation line vector $\mathbf{l}$ and γ is the angle between the vectors $\mathbf{b} - \mathbf{l}(\mathbf{l}.\ \mathbf{b})$ and $\mathbf{g} - \mathbf{l}(\mathbf{l}.\mathbf{g})$). The hexagonal dislocation considered in fig. 4.3 have mixed dislocation segments. The contrast factor of these segments is taken as the average of the screw and edge segments. The contrast of the hexagonal loop is taken as the average of the two screw dislocation segments and the four mixed dislocation segments. The result is $C \sim 0.3$.

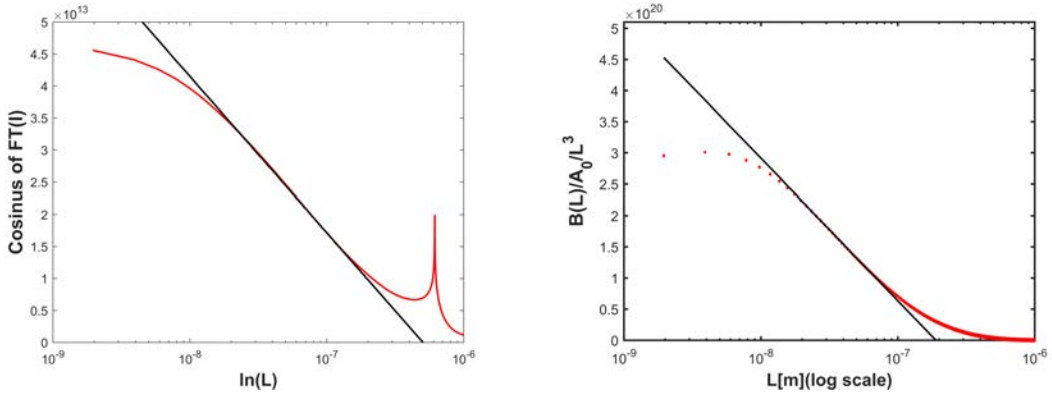
In the 10^{-8} to 10^{-7} m range the Wilkens function $f^*(\frac{L}{R_e^*})$ can be approximated by :

$$f^*\left(\frac{L}{R_e^*}\right) = 2 - ln\left(\frac{L}{R_e^*}\right) \tag{4.7}$$

i.e. the plot of $\frac{1}{L^2} ln \frac{A_L}{A_0}$ vs. L (logarithmic scale) should be a straight line which intersects the x axis at $L_0 = exp(2)R_e^*$. As shown in Fig. 4.14(a), this is indeed the case : the straight line going through the red points (at positions 3×10^{-8} m and 10^{-7} m) follows the plot. At large distance ($log(L) > 10^{-7}$), some peaks oscillations appear on the plot. The number and the magnitude of the peaks oscillations depend on the dislocations density or the size of the dislocations loops (see next sections). This part is not considered in the fit. We determine the dislocation density ρ and the distribution parameter (the cut-off radius of the dislocation distribution) R_e^* using this linear fit eq. 4.8. To summarize the fitting procedure of the real part :

-Compute the Fourier transform of the 1D plot. Thus determine and normalize the real part.

-Divide the logarithm of the normalized real part by L^2. The obtained function is fitted by a linear function. The dislocation density ρ and the cut off radius of dislocation R_e^* are given as function of the slope A_{sp} and intersection L_0 of the



(a) (b)

FIGURE 4.14 – Linear fit of the real and imaginary part of the FFT of peaks for 64 randomly distributed hexagonal loops of size 32 voxels. The slope and the intersection with the *xaxis* of the linear function are used to determine characteristic parameters.

linear function as :

$$\begin{aligned} \rho &= \frac{A_{sp}}{\pi C \mathbf{g}^2 \mathbf{b}^2} \\ R_e^* &= L_0 exp(-2) \end{aligned} \tag{4.8}$$

4.3.1.2 Fit of the imaginary part

As shown by Groma [51], and Groma and Monnet [53], the imaginary part B_L of the Fourier transform of the intensity should vary as :

$$ln\frac{B_L}{A_0} = \langle s^{(2)} \rangle L^3 ln(\frac{L}{R_2}) \tag{4.9}$$

where $\langle s^{(2)} \rangle$ is a function of the 2D two-particle density function related to the polarization of the distribution of dislocations. In the plot of $B_L^S/A_0/L^3$ vs. L (logarithmic scale) we indeed find a linear behavior fig. 4.14(b). To summarize the fitting procedure of the imaginary part :

-Compute the Fourier transform of the 1D plot. Thus determine and normalize the imaginary part.

-Divide the normalized imaginary part by L^3. The obtained function is fitted by a linear function. $\langle s^{(2)} \rangle$ and R_2 are respectively equal to the slope and the intersection with the x *axis* of the linear function.

4.3.2 Analysis method based on the momentum

A powerful analysis method based on the momentum (or the variance) of the peak profile is proposed by Groma [51]. This method was described in the first chapter. After normalization by their integrated intensity I_S, the different variances of the diffraction peaks were computed as :

$$v_k = \int_{-q'}^{q'} \frac{I(q)}{I_s} q^k \mathrm{d}q \tag{4.10}$$

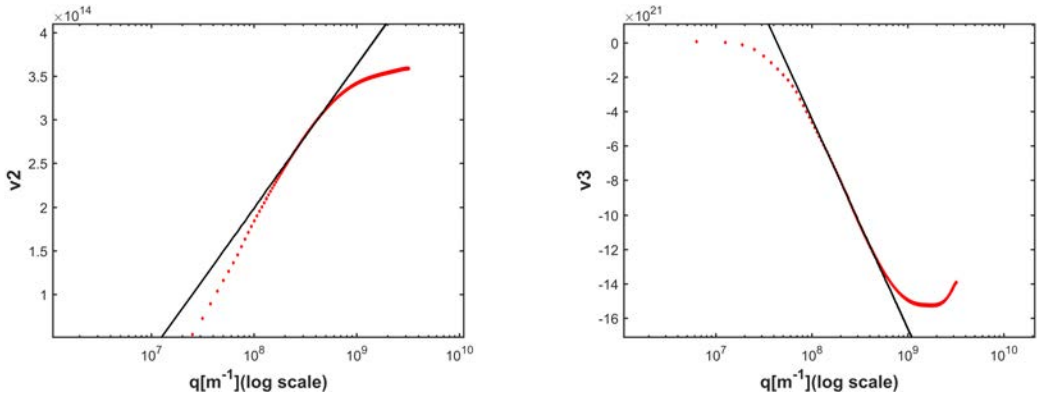
Fig. 4.15 shows the evolution with q of the second and third variances of the peaks (in red). The second and third variances vary linearly with the logarithm of $\mathbf{q}$ after normalization of the intensity for values of $\mathbf{q}$ within the 10^8 range. Thus, they can be fitted to the relations given in eq. 4.11. The fit results are also shown in fig. 4.15.

$$\begin{aligned} v_2(q') &= 2\Lambda \langle \rho \rangle ln\left(\frac{q'}{q_0}\right) \\ v_3(q') &= -6\langle s^{(2)} \rangle ln\left(\frac{q'}{q_1}\right) \end{aligned} \tag{4.11}$$

The constant Λ is defined as : $\Lambda = \frac{\pi}{2} C \mathbf{b}^2 \mathbf{g}^2 sin^2\phi$ (ϕ is the angle between $\mathbf{g}$ and the dislocation line vector $\mathbf{l}$). In the case of hexagonal dislocation considered, $\Lambda \sim 1$. The evolution of the fourth variances with q is shown in fig. 4.16(b). The fit of the fourth variance is more difficult, as there are four fit parameters $\langle \rho' \rangle, \langle \rho^{(2)} \rangle, q_2$ and q_3 :

$$v_4(q) = \Lambda \langle \rho \rangle q^2 + 12\Lambda \langle \rho'^{(2)} \rangle ln\left(\frac{q}{q_2}\right) ln\left(\frac{q}{q_3}\right) \tag{4.12}$$

As can be seen in fig. 4.16(a), the variations of v_4 (blue dots) and $\Lambda \langle \rho \rangle q^2$ (black curve) are large compared to their difference (green curve) : a small error on $\Lambda \langle \rho \rangle$ will



(a) (b)

FIGURE 4.15 – Second (a) and third (d) order variance and their fit for 64 randomly distributed hexagonal loops (size 32 voxels).

result in a large one on $\Lambda\langle\rho'^{(2)}\rangle$ We can see that the second term on the right-hand side (red curve) can be written as :

$$12\Lambda\langle\rho'^{(2)}\rangle ln\left(\frac{q}{q_2}\right) ln\left(\frac{q}{q_3}\right) = 12\Lambda\langle\rho'^{(2)}\rangle \left(ln(q) - ln(q_2)\right)\left(ln(q) - ln(q_3)\right) \qquad (4.13)$$

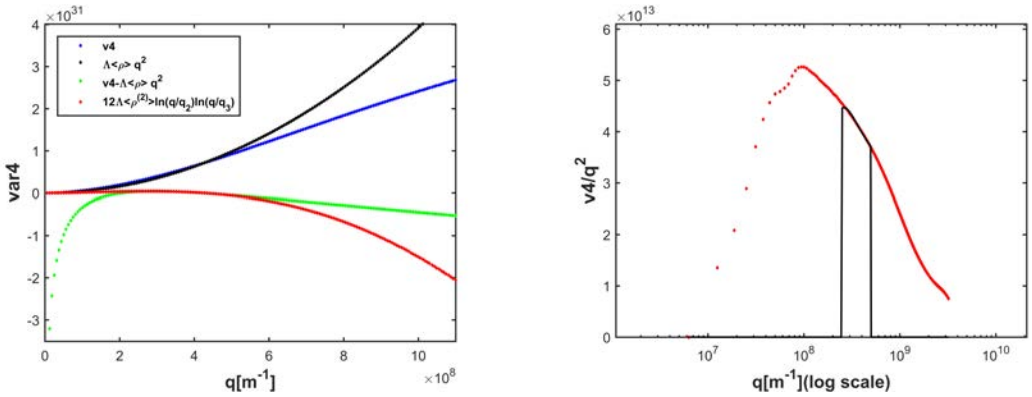
i.e. its plot would be parabolic on a logarithmic horizontal axis, and one of the two constants is determined by the intersection of the blue and black curves. The final $\langle\rho'^{(2)}\rangle$ results of the fit was found quite sensitive to the value of $\langle\rho\rangle$ deduced from v_2 and to the limits of the fit domain. However, as seen on fig. 4.16(b), the $v_4(q)/q^2$ plot can be fitted on a reasonable interval. To summarize the moments method :

-Compute the second, third and the fourth order from the 1D plot.

-The second and the third variances, v_2 and v_3 respectively, are fitted with linear function fig. 4.15. The slope of the linear fitting function allow to compute the dislocation density (with v_2) and $\langle s^{(2)}\rangle$ (with v_3).

-The normalized fourth order variance $v_4(q)/q^2$ is fitted on fig. 4.16 and $\langle\rho'^{(2)}\rangle$ is calculated.

The results of the analysis are represented in next sections and in Appendix. D for randomly distributed hexagonal loops with different size and for dislocation dipoles. The effect of the diffraction vector, the size of the loops or the dislocations density will be presented and commented.



(a) (b)

FIGURE 4.16 – (a) Different steps in the fit of v_4. (b) Fourth-order variance and it fit for 64 randomly distributed hexagonal loops (size 32).

4.4 Results

4.4.1 Effect of the diffraction vector g

Fig.4.17 shows the 1D diffraction peaks simulated for the (200), (020), and (002) **g** vectors, for a random distribution of 64 hexagonal loops with the same 128 voxels side (each side is $3.54 \times 10^{-7}m$ long, and the total dislocation density is $1.36 \times 10^{14}m^{-2}$). The (200) and (020) peaks, corresponding to $\mathbf{g}.\mathbf{b} = \pm 1$ are slightly asymmetric, each one being symmetric of the other. The third peak ($\mathbf{g}.\mathbf{b} = 0$) is much thinner and symmetric. Fig.4.18 is a plot of the (200), (400), and (600) peaks : as expected, the peak width increases with the magnitude of **g**.

Fig. 4.19 and fig. 4.20 show plots of $ln(A_L/A_0)/L^2$ and $B_L/A_0/L^3$, the normalized real and imaginary part of the FFT of the peaks. On the left side, the plots for (200) and (020) are nearly identical, except the positions and sizes of the oscillations. The (002) peak is symmetric. Both for the real and imaginary parts, the (002) plots are much lower : about one order of magnitude in the first case, and three orders of magnitude in the second. On the right side, both slopes of the fit line increase with the magnitude of **g**, while the oscillations (the first peak) shift to the left.

4.4.2 Effect of the dislocation loop's sizes

We now consider a random distribution of 64 hexagonal loops having the same voxels side. Five configurations are studied : 32, 64,128, 196, 256 voxels side of the loops. In all configurations, the dislocation loops are located at the same position

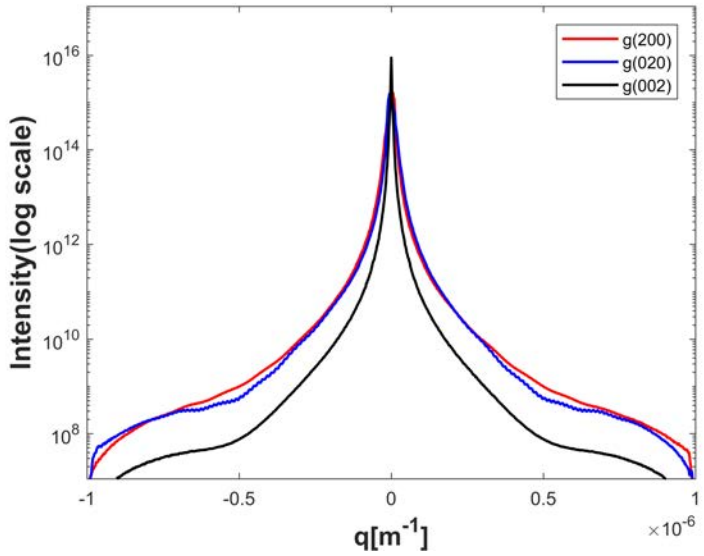


FIGURE 4.17 – 1D diffraction peaks respectively for the (200), (020), and (002)**g** vectors, for a random distribution of 64 hexagonal loops with the same 128 voxels side

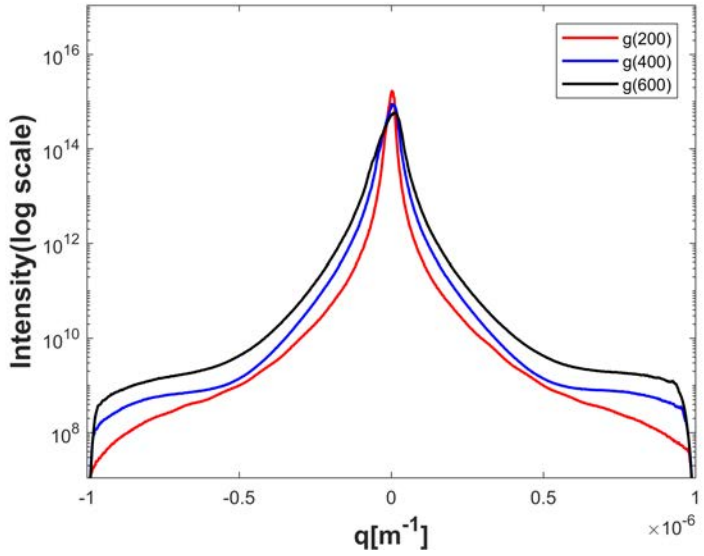
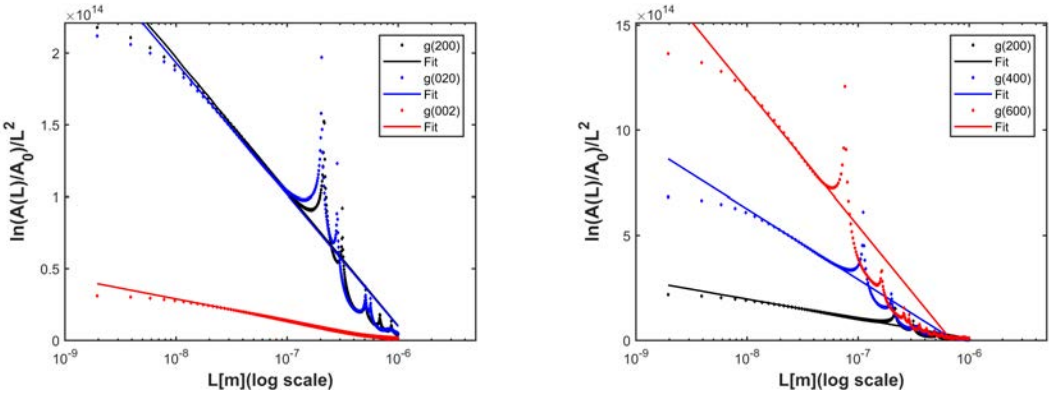


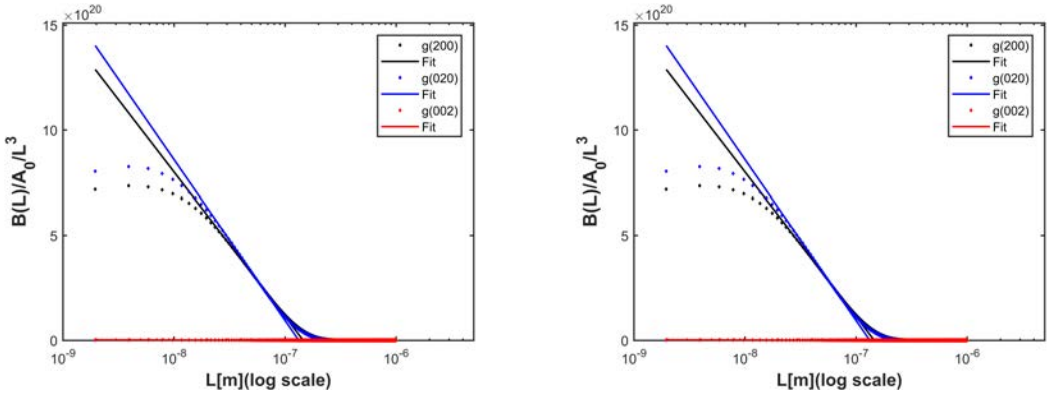
FIGURE 4.18 – 1D diffraction peaks simulated respectively for the (200), (400), and (600) **g** vectors, for a random distribution of 64 hexagonal loops with the same 128 voxels side

within the material. Fig. 4.21 shows a plot of $ln(A_L/A_0)/L^2$, the normalized real part of the FFT of the peaks for these configurations for the $g(200)$ diffraction vector. The slopes of the fit lines and the number and the magnitude the oscillations increase



(a) (b)

FIGURE 4.19 – The normalized real part $ln(A_L/A_0)/L^2$ of the FFT of the peaks for the (200), (020), and (002) **g** vectors (a) and for the (200), (400), and (600)**g** vectors (b).



(a) (b)

FIGURE 4.20 – The normalized imaginary part $(B_L/A_0/L^3)$ of the FFT of the peaks for the (200), (020), and (002) **g** vectors (a) and for the (200), (400), and (600) **g** vectors (b).

with the number of loops. Fig. 4.22 shows a plot of $B_L/A_0/L^3$, the normalized imaginary part of the FFT of the peaks.

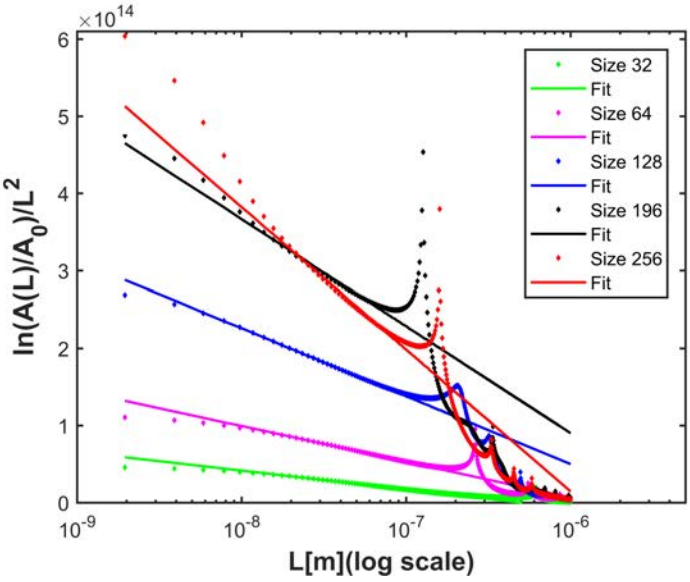


FIGURE 4.21 – Normalized real part $ln(A_L/A_0)/L^2$ of the FFT of the peaks for the (200) **g** vector for 64 random distribution of hexagonal loops with the same voxels side : 32, 64,128, 196, 256 voxels configurations are represented.

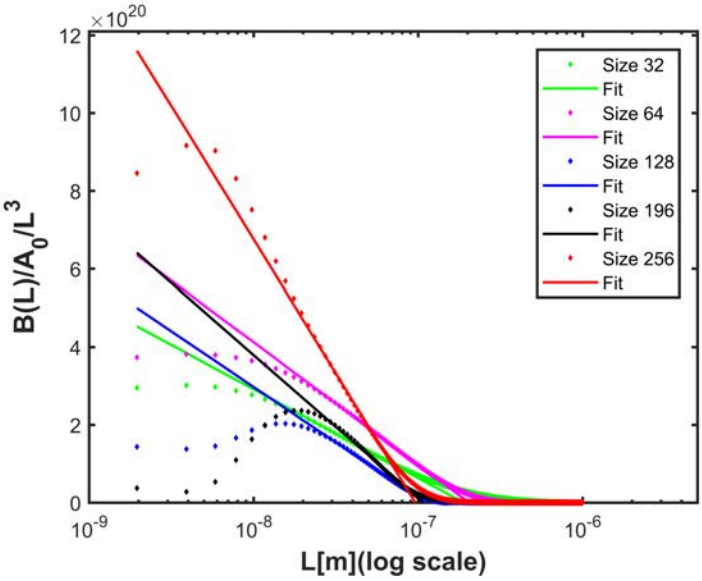


FIGURE 4.22 – Normalized imaginary part $B_L/A_0/L^3$ of the FFT of the peaks for the (200) **g** vector for 64 random distribution of hexagonal loops with the same voxels side : 32, 64,128, 196, 256 voxels configurations are represented.

Fig.4.23 shows the fitting of the second, third and fourth order variance for the 32 and 128 loops side configurations. The fit for other configurations is shown in Appendix D : fig. D.1 and fig. D.2.

The characteristic parameters computed with the fits are given in table 4.1 and are discussed in the next section.

	Fourier transform				Moments		
Size	$\rho[10^{13}]$	$R_e^*[10^{-8}]$	$\langle s^{(2)} \rangle [10^{19}]$	$R_2[10^{-8}]$	$\rho[10^{13}]$	$\langle s^{(2)} \rangle [10^{19}]$	$\langle \rho'^{(2)} \rangle [10^{30}]$
32	3.35	6.69	9.36	2.12	2.83	88.2	3.27
64	6.32	18.6	13.8	2.01	5.66	100	7.06
128	12.8	69.3	11.9	11.7	13.5	77	4.86
196	19.1	117	16.2	10.5	24.6	80.7	1.23
256	26.4	16.3	29.9	9.64	36.3	235	8.50

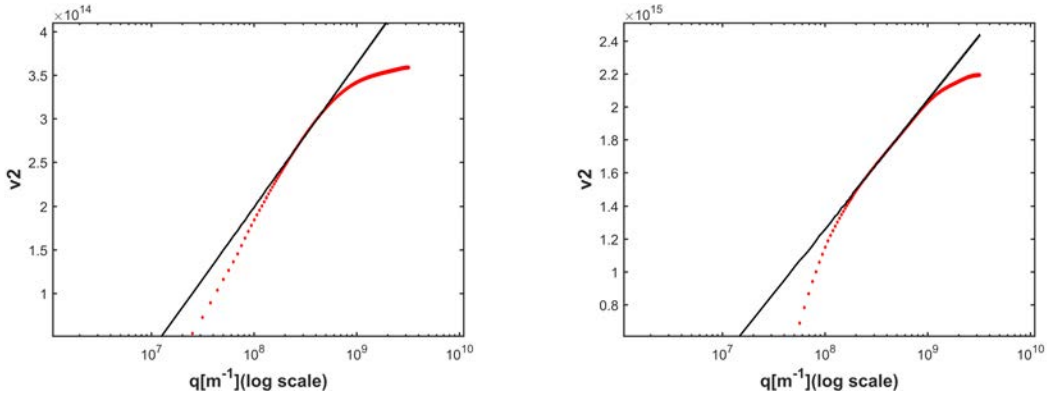
TABLE 4.1 – Characteristics parameters computed with the analysis methods for different size of 64 random distributed hexagonal loops.

4.4.3 Effect of the dislocation density

Now, we consider a random distribution of hexagonal loops with the same 64 voxels side (each side is $1.77 \times 10^{-7} m$ long). Five configurations are studied : 64, 128, 256, 512, and 4096 loops with correspond to different dislocation densities. Fig. 4.24 shows a plot of $ln(A_L/A_0)/L^2$, the normalized real part of the FFT of the peaks for theses configurations for the $g(200)$ diffraction vector (the 4096 loops configuration is represented alone for the sake of clarity). The slopes of the fit lines increase with the number of loops. Fig. 4.25 shows a plot of $B_L/A_0/L^3$, the normalized imaginary part of the FFT of the peaks. The slopes of the fit lines also increase with the number of loops. The characteristic parameters computed which these plots are represented on table. 4.4.3.

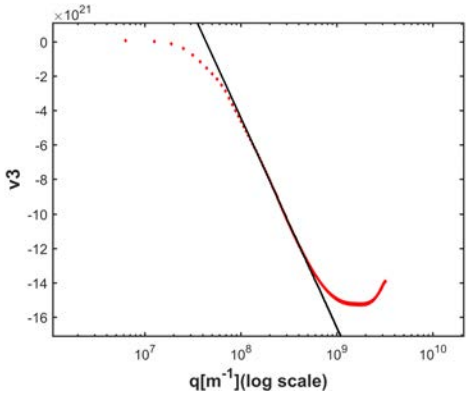
Fig.4.26 shows the fitting of the second and the third order third variance for the 64 and 256 loops configurations. The other plots are presented in Appendix D : fig. D.3 and fig. D.4.

The characteristic parameters ρ, R_e^*, $\langle S \rangle$ and R_2 computed with this fit are given in table. 4.4.3 and are discussed in the next section.

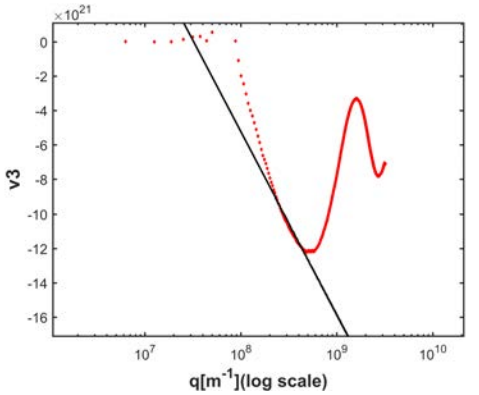


(a)

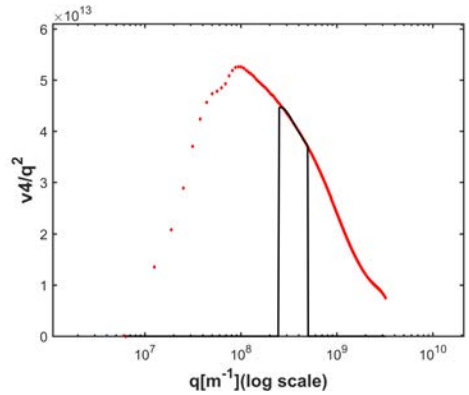
(b)



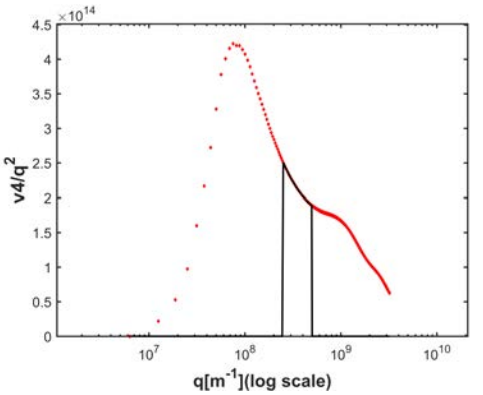
(c)



(d)

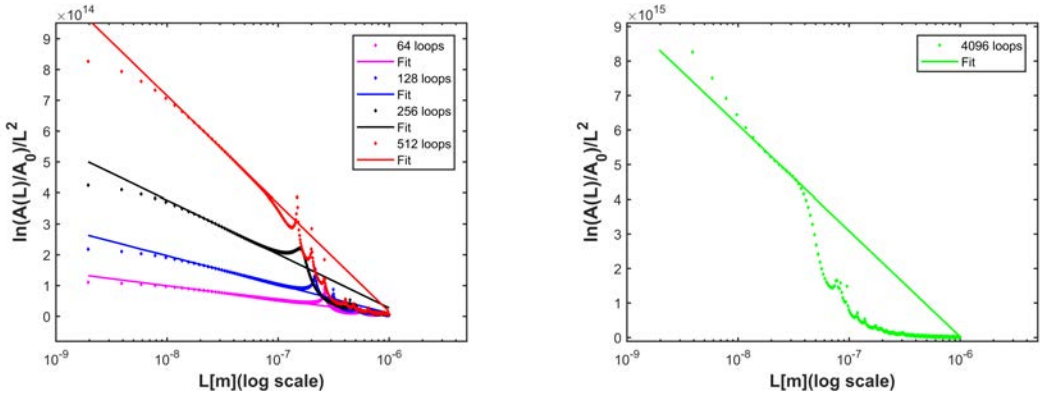


(e)



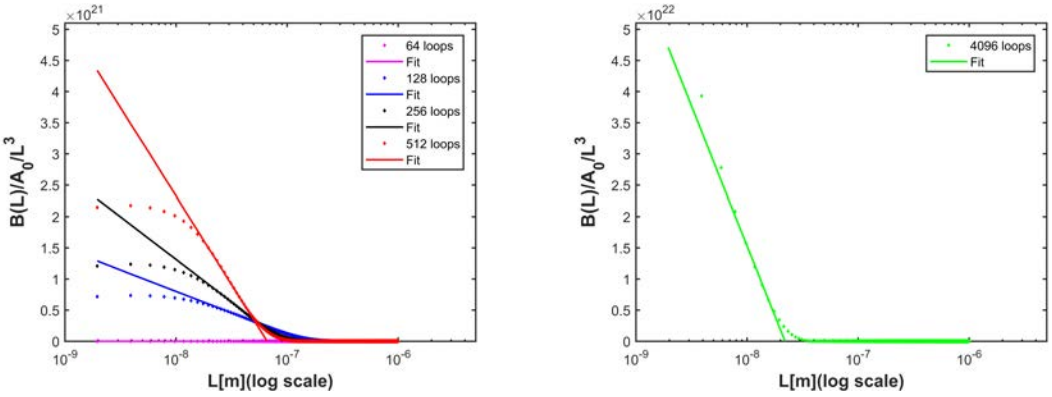
(f)

FIGURE 4.23 – Different variance orders for the (200)**g** vector for a 64 random distribution of hexagonal loops with the same voxels side. Second order (a) and (b), third order (c) and (d), fourth order (e) and (f), for the 32 and 128 loops side configuration respectively.



(a) (b)

FIGURE 4.24 – The normalized real part $ln(A_L/A_0)/L^2$ of the FFT of the peaks for the (200)**g** vector for a random distribution of hexagonal loops with the same 64 voxels side. Five configurations are represented : (a) 64, 128, 256 and 512 loops. (b) 4096 loops



(a) (b)

FIGURE 4.25 – The normalized imaginary part $B_L/A_0/L^3$ of the FFT of the peaks for the (200)**g** vector for a random distribution of hexagonal loops with the same 64 voxels side. Five configurations are represented : (a) 64, 128, 256 and 512 loops. (b) 4096 loops

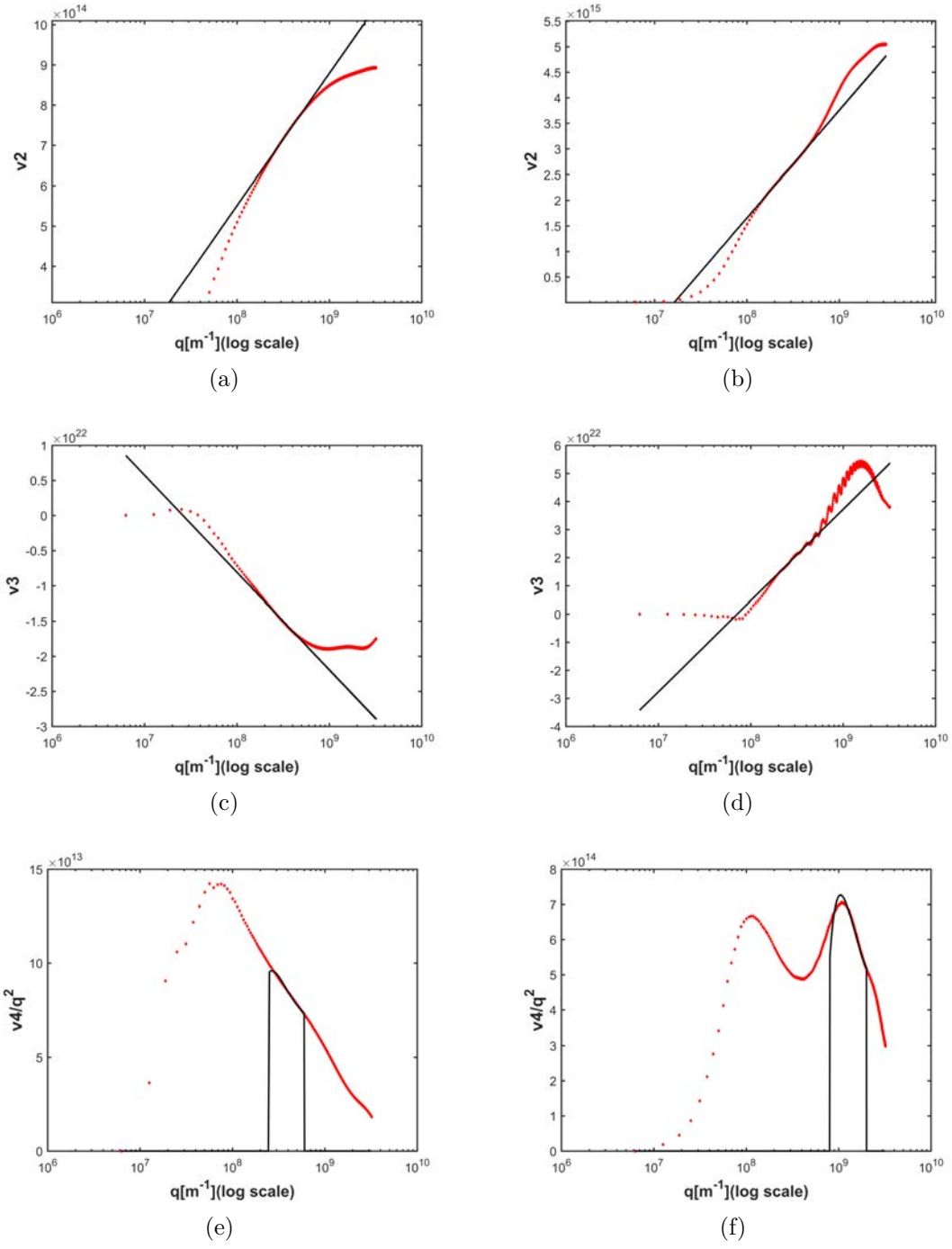


FIGURE 4.26 – Different variance orders for the (200)**g** vector for a random distribution of hexagonal loops with the same 64 voxels side : 64 (left) and 128 (right) loops.

	Fourier transform				Moments		
Loops	$\rho[10^{13}]$	$R_e^*[10^{-8}]$	$\langle s^{(2)}\rangle[10^{19}]$	$R_2[10^{-8}]$	$\rho[10^{13}]$	$\langle s^{(2)}\rangle[10^{19}]$	$\langle \rho'^{(2)}\rangle[10^{30}]$
64	6.32	18.6	13.8	2.01	5.66	100	7.06
128	13.5	17.4	29.8	14.6	15.4	215	1.06
256	25.6	18.6	61.6	8.82	32.6	510	219
512	50.7	15.0	123	6.63	80.6	1.29	523
4096	428	13.8	1940	2.20	1550	22400	4020
4096					463		

TABLE 4.2 – Characteristics parameters computed with the analysis methods for 64, 128, 256, 512 or 4096 random distribution of hexagonal loops with the same 64 voxels side

4.4.4 Dislocation dipoles

Now we consider dislocation dipoles. The first configuration is a single centered dislocation dipole and the effect of its size will be studied. The second configuration is the random distribution of 64 or 256 dipole dislocations with 64 voxels side.

Single dislocation dipole

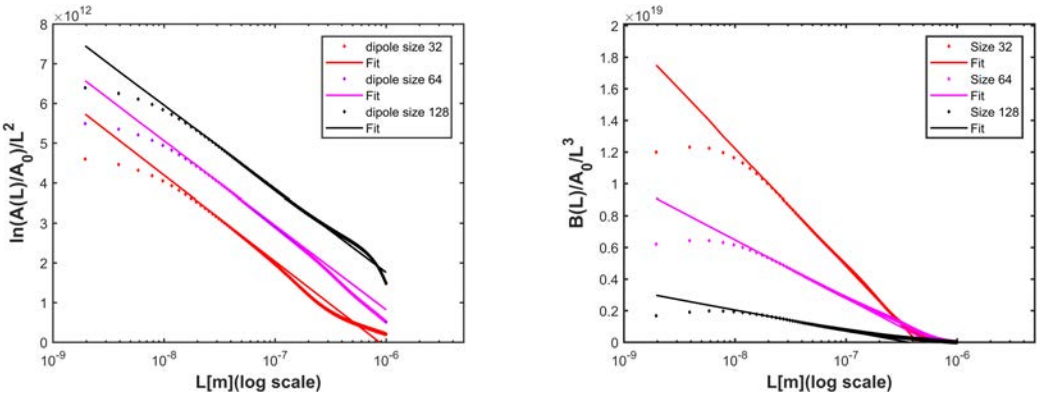
Fig. 4.27 shows a plot of $ln(A_L/A_0)/L^2$ and $B_L/A_0/L^3$, the normalized real and imaginary part of the FFT of the peaks for the $g(200)$ diffraction vector for the single dislocation dipole with different size. The slopes of the fit lines in fig.4.27(a) are almost equal.

Fig. 4.28 show the fitting of the different order variance for a single dipole dislocation with 32 voxels side. The other plots are presented in Appendix D fig. D.5.

The characteristic parameters ρ_{num}, R_e^*, $\langle S\rangle$ and R_2 computed with this fit are given in table. 4.3 and are discussed in the next section.

	Fourier transform				Moments		
Size	$\rho[10^{12}]$	$R_e^*[10^{-7}]$	$\langle s^{(2)}\rangle[10^{16}]$	$R_2[10^{-7}]$	$\rho[10^{12}]$	$\langle s^{(2)}\rangle[10^{16}]$	$\langle \rho'^{(2)}\rangle[10^{29}]$
32	2.98	81.0	53.8	4.44	3.19	2780	1.59
64	2.93	2.24	26.7	5.72	3.30	1390	1.81
128	2.90	6.22	9.45	3.65	3.30	573	1.80

TABLE 4.3 – Characteristics parameters computed with the analysis methods for a single dislocation dipole with different sizes



(a) (b)

FIGURE 4.27 – The normalized real part $ln(A_L/A_0)/L^2$ (a) and imaginary part $B_L/A_0/L^3$ (b) of the FFT of the peaks for the (200)**g** vector for a single dislocation dipole with different size : 32, 64 and 128 voxels

A random distribution of dislocation dipole

Fig. 4.29 shows a plot of $ln(A_L/A_0)/L^2$ (a) and $B_L/A_0/L^3$ (b), the normalized real and imaginary part of the FFT of the peaks for the $g(200)$ diffraction vector for a random distributed dislocation dipoles with 64 voxels size. The characteristic parameters ρ_{num}, R_e^*, $\langle S \rangle$ and R_2 computed with the fits are given in table. 4.4

Fig. 4.28 show the fitting of the different order variance for a random distribution of dipole dislocation with 64 and 256 voxels side.

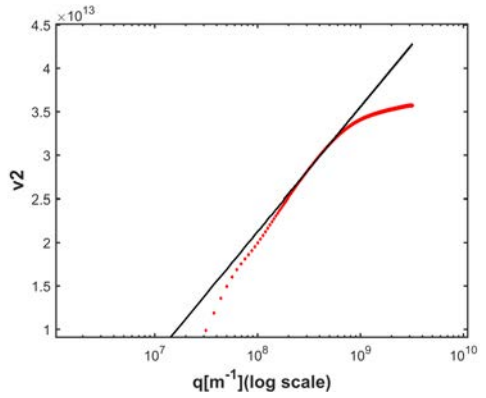
The characteristic parameters ρ_{num}, R_e^*, $\langle S \rangle$ and R_2 computed with this fits are given in table. 4.4 and are discussed in the next section.

	Fourier transform				Moments		
dipole disl.	$\rho[10^{14}]$	$R_e^*[10^{-7}]$	$\langle s^{(2)} \rangle [10^{20}]$	$R_2[10^{-8}]$	$\rho[10^{14}]$	$\langle s^{(2)} \rangle [10^{21}]$	$\langle \rho'^{(2)} \rangle [10^{32}]$
64	1.754	5.654	5.78	12.5	2.41	1.65	1.85
256	7.124	2.604	10.3	6.74	15	9.75	11.1

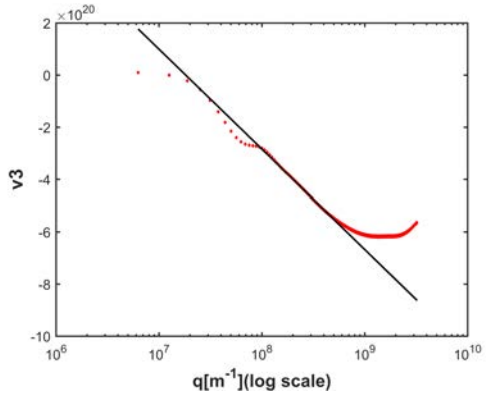
TABLE 4.4 – Characteristics parameters computed with the analysis methods for random distribution of 64 or 256 dislocation dipoles with 64 voxels side

4.4.5 Analysis of the results

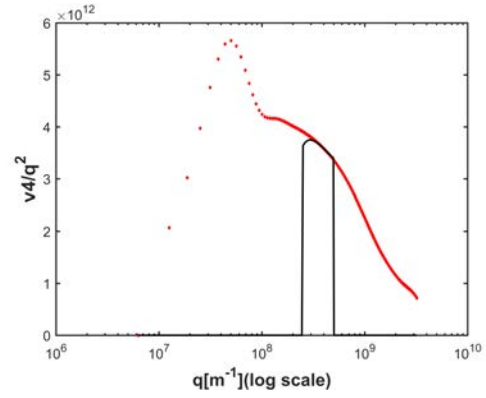
The characteristic parameters extracted from the analysis (dislocation densities, cut off parameters etc.) using the Fourier transform and the moments methods are



(a)

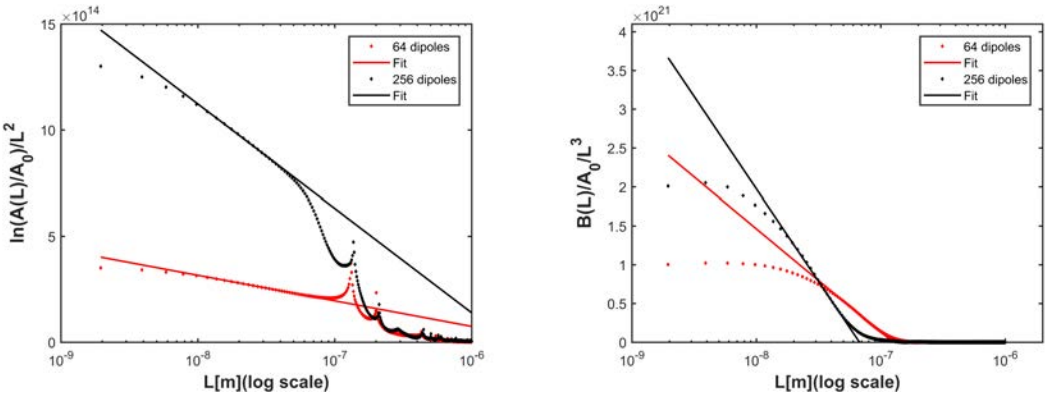


(b)



(c)

FIGURE 4.28 – Different variance orders for a single dislocation dipole with 32 voxels side : Second order (a) second order (b), third order c)



(a) (b)

FIGURE 4.29 – The normalized real part $ln(A_L/A_0)/L^2$ (a) and imaginary part $B_L/A_0/L^3$ (b) of the FFT of the peaks for the (200)**g** vector for random distribution of 64 or 256 dislocation dipoles with 64 voxels side

presented in the tables above. The results given by the Fourier transform method seems to be consistent for all the parameters specially for $\langle s^{(2)} \rangle$ and $\langle \rho'^{(2)} \rangle$. It is necessary to carefully choose the better interval for the fit to obtain a consistent result. For example, in table .4.4.3, the value of the dislocation density given in the last line (for 4096 loops) is obtained with a fit on a different interval. It is more close to the excepted value when the value just above in the table is more important. The analysis below is essentially based on the results obtained with the Fourier transform method.

The dislocation density ρ

The average dislocation density was calculated for all fits above. For a $1\mu m^3$ RVE divided in 512^3 voxels containing n_l hexagonal loops of side V_s (in voxels) its theoretical value is :

$$\langle \rho_{th-l} \rangle = 6\sqrt{2}\frac{n_l V_s}{512}10^{12} \tag{4.14}$$

For a RVE containing n_d dislocation dipoles :

$$\langle \rho_{th-d} \rangle = 2\sqrt{2}10^{12} n_l$$

Fig.4.31 compares the theoretical and the computed value as function of the number or the size of the dislocation loop. The computed value is almost equal to

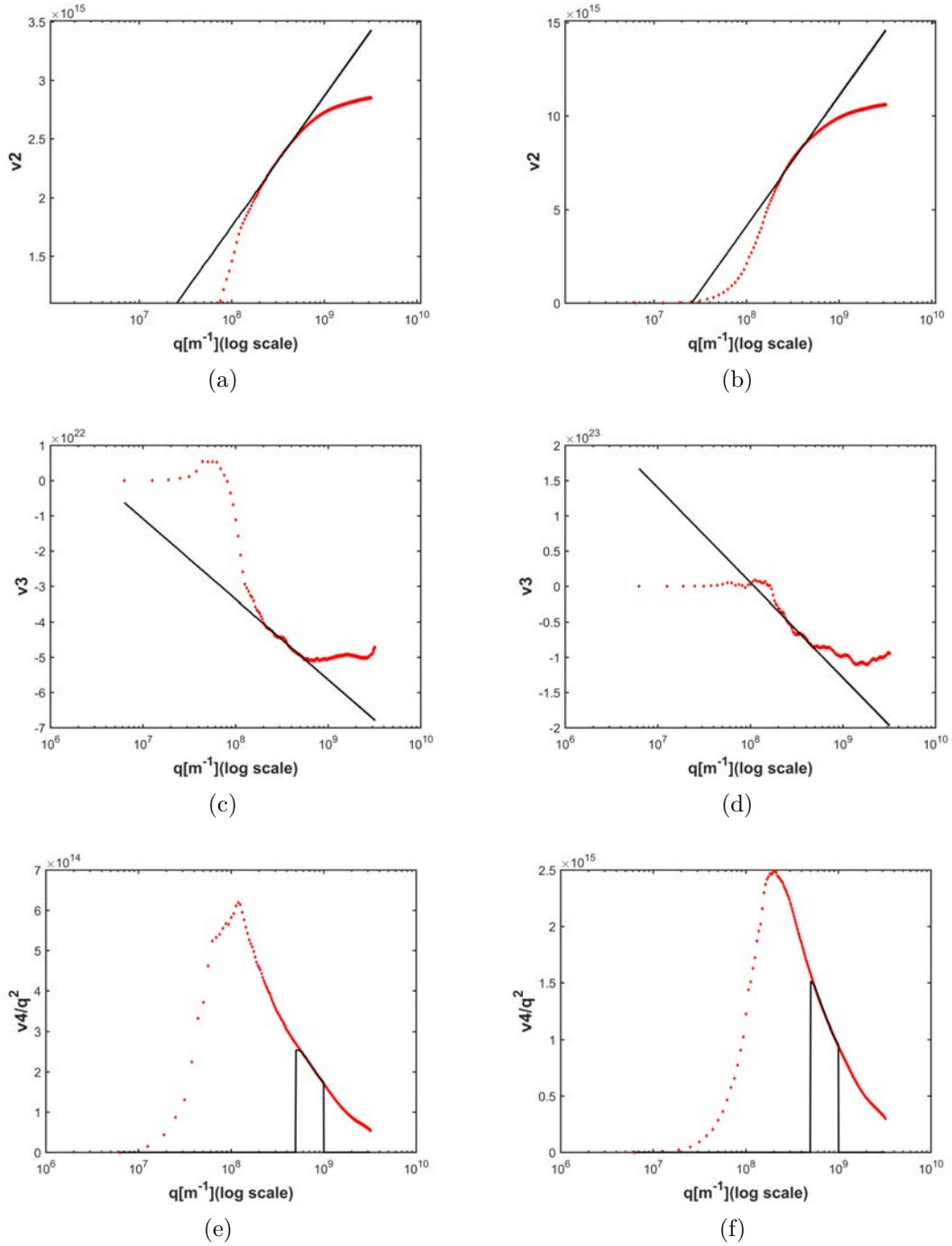
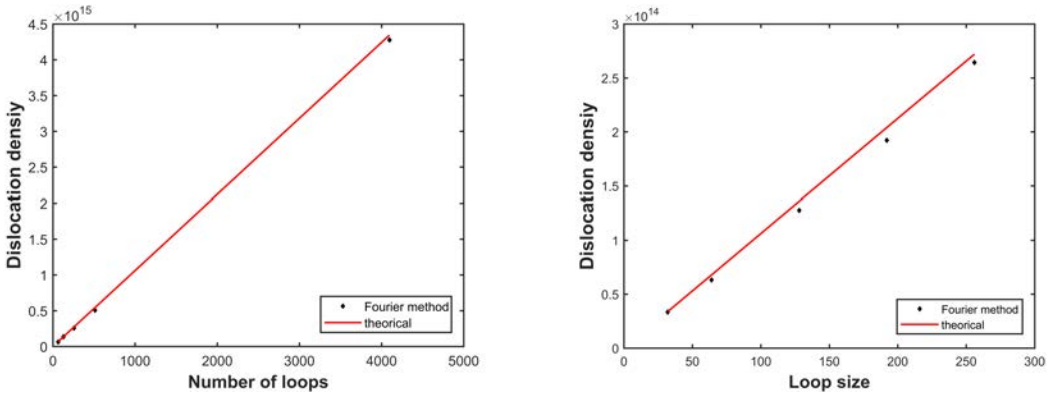


FIGURE 4.30 – Different variance orders for the (200)**g** vector for a random distribution of dipole dislocation with 64 (left) and 256 (right) voxels side



(a) (b)

FIGURE 4.31 – Comparison between the theoretical and the computed dislocation densities for a randomly distributed dislocation loops.(a) Variation of the number of dislocation loops. (b) Variation of the dislocation loop size

the theoretical one. The maximum error is 6%.

Another interesting way to validate our method is to study the dislocation dipoles. Indeed, the dislocation density does not change when the distance between the dislocations forming the dipole size increases. This is observed on fig. 4.32 which compares the computed dislocation density of a single dipole with the theoretical value. The computed dislocation density are almost equal with a maximal error of 5.5% with respect to the theoretical value.

The cut-off radius R_e^*

For a 2D distribution of infinite dipoles the theoretical value of the cut-off radius is defined by Wilkens [154] as the radius of a cylindrical domain which always contains the same number of dislocations of both signs. For a single dipole or a random distribution of dipoles with the same small distance d (i.e. $d << 1\mu m$ and $d << \rho^{-1/2}$) we expect a value $R_e^* \sim d$. When d is much larger than $\rho^{-1/2}$, the dislocation distribution can be taken as random, and the average distance between a dislocation and the nearest dislocation with opposite sign should be of the same order of magnitude as $\rho^{-1/2}$.

The same line of argument can be followed for dislocation loops. For a low density of small dislocation loops, we expect values of R_e^* of the same order of magnitude as the loop diameter. For a high density of dislocation loops with a large diameter $d >> 1\mu m$, we also expect : $R_e^* \sim \rho^{-1/2}$. Using eq. 4.14, we find :

$$R_e^* \sim (6\sqrt{2}\frac{n_l V_s}{512}10^{12})^{-1/2}$$

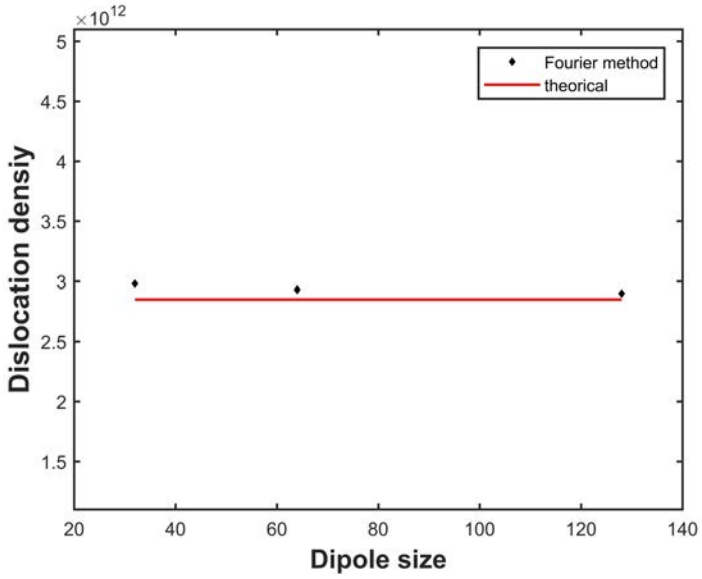


FIGURE 4.32 – Comparison between the theoretical and the computed dislocation density for a single dislocation dipole

Let us consider fig. 4.33 which shows R_e^* as function of loop size (left) or the number (right) of dislocation loops. When the size of the dislocation increases, the cut off radius increases as expected (left plot). But it decreases for 256 voxels side of the loop.

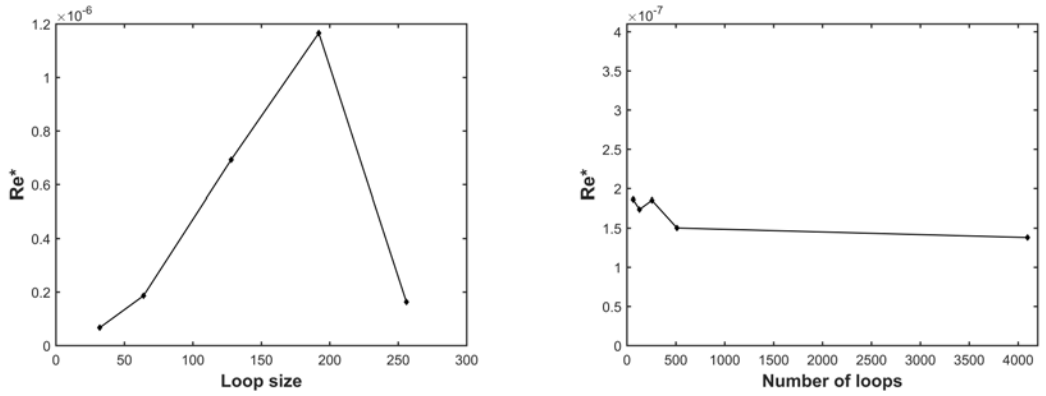
The characteristic value $\langle s^{(2)} \rangle$

The derivation of an analytic value of $\langle s^2 \rangle$ was proposed by Groma and Monnet in [53] for randomly distributed polarized dipoles. This analytic value is not computed here. However from the derivation of Groma and Monnet [53], $\langle s^2 \rangle$ must vary as :

$$\langle s^2 \rangle = \alpha_s \frac{\rho}{d} \tag{4.15}$$

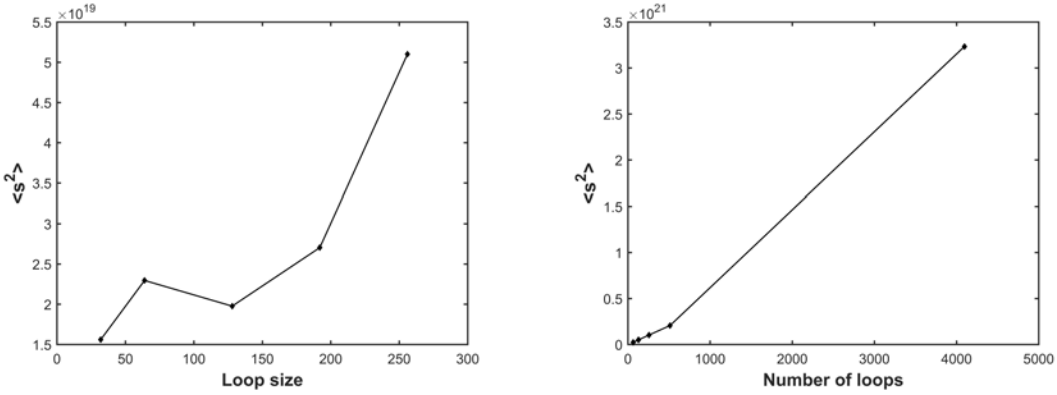
where α_s is a constant and d is the diameter of loops. Let us consider fig. 4.34 which show $\langle s^2 \rangle$ as function of size (left) or the number of dislocation loops (right) . When d and ρ increase simultaneously (left plot), $\langle s^2 \rangle$ increases smoothly as expected. When d is constant and ρ increases (right plot) $\langle s^2 \rangle$ increases almost linearly as expected.

It is interesting to study the variation of $\langle s^2 \rangle$ for dislocation dipole. Fig. 4.35 is a plot of $\langle s^2 \rangle$ for different value of a single dislocation dipole (a) and random



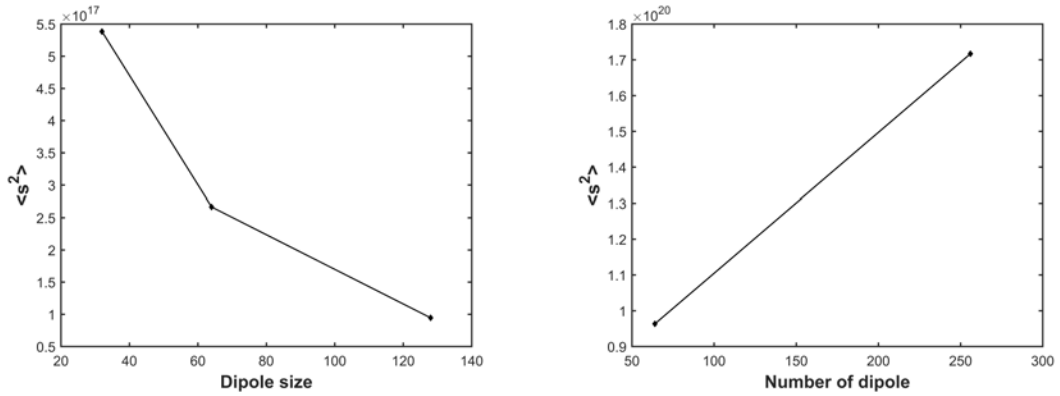
(a) (b)

FIGURE 4.33 – The cut off radius R_e^* for a random distribution of dislocation loop. (a) Variation of the dislocation size. (b) Variation of the number of dislocation loop



(a) (b)

FIGURE 4.34 – $\langle s^2 \rangle$ for a random distribution of dislocation loop of dislocation. (a) Variation of the dislocation size. (b) Variation of the number of dislocation loop



(a) (b)

FIGURE 4.35 – $\langle s^2 \rangle$ for a single dislocation dipole with different size (a) and for a random distribution of dislocation dipoles (b)

distributed dislocation dipole (b). $\langle s^2 \rangle$ decreases when the size of the dislocation dipole increases. Indeed, it increases when the number of dislocation dipole increases.

4.5 Conclusion

In this chapter, we developed a numerical method to generate virtual diffraction peaks in the vicinity of a diffraction vector **g**. The input data of this method is the displacement field. The simulated peaks exhibit the main features expected from diffraction peaks from a material containing dislocations : a broad and asymmetric maximum (proportional to the Burgers vector of the dislocation loops and depending on the number and sign of the loops), a streak perpendicular to the dislocation loop plane, and a symmetry which reflects the shape of the loops. After summing the intensities in order to obtain a 1D profile which may be compared to a simple $(\theta, 2\theta)$ diagram, we have obtained realistic shapes with tails following the expected laws : q^{-3} for perfect dislocations (due to the distribution of strain near the dislocation cores), and q^{-2} for stacking faults. If we do not take into account the voxel with the highest intensity (which would anyway be smeared in real cases), the calculated diffracted intensities span six orders of magnitude : this is larger than the peak to background ratio of most experiments. The diffraction peaks computed with the corrected displacement field for dislocation dipoles and dislocation loops exhibit the properties expected from the analytical computations using the Wilkens model and the moments method :

- The dislocation densities $\langle \rho \rangle$ resulting from the fits are correct within a few percents.

- The cut-off parameter R_e^* has the expected behavior, at least for small dislocation loops.

- The $\langle s^2 \rangle$ parameter varies approximately as ρ/d, where d is the half distance between the dislocations of a narrow dipole or a small dislocation loop

Both methods of analysis of the diffraction peaks (Fourier transform and moments) are based on the properties of 2D distributions of dislocations. Analytic solutions for the mechanical fields (strain, stress, and displacement) due to single dislocations in anisotropic elasticity are available. It is thus possible to calculate the contribution of the areas in the vicinity of dislocation cores to the tails of the diffraction peaks (i.e. large $\mathbf{q}$ and small $\mathbf{L}$ for the Fourier transform). By pairing dislocations of opposite signs into dipoles or using two-dislocations density functions it is possible to get expressions of the long range fields which converge faster, and obtain analytical expressions for peak parameters related to further parameters of the dislocation distribution such as R_e^*, $\langle s^2 \rangle$ etc. Further refinements such as using n dislocations density functions are possible, but their physical meaning is less obvious.

An obvious question is : can the same computation be done for dislocation loops ?. Analytic solutions for the strain field and the displacement field of piecewise straight loops are available at least in the elastically isotropic case [57]. The displacement field can be written as a sum on all corners of the loops. However, some of the properties of the displacement field of infinite straight dislocations used to obtain analytical results [51] are no longer valid for dislocation loops. Another interesting feature is that the 2D n-dislocations density functions used in [51] would need to be rewritten, perhaps as a 3D n-loops density function. Last, unlike the 2D case, the elastic fields generated by dislocation loops are polarized, especially if we assume that the loops have grown under the influence of an external stress and have the same sign. This has consequences on the long range stress field, and the diffraction peaks in $\mathbf{g}.\mathbf{b} \neq 0$ conditions are asymmetric. It might be worth to do a systematic study of these consequences.

General conclusion and perspectives

General conclusion

In this work, a Fast Fourier Transform (FFT) based method for the simulation of the diffraction peaks using the displacement field was developed and applied to references cases.

We developed an expression for a new consistent periodized discrete Green fourth order operator for FFT-based algorithms. This operator allows to compute the stress/strain field in periodic heterogeneous media with eigenstrain fields by solving the Lippmann-Schwinger equation in the Fourier space. The computation was tested on inclusions with different shapes, eigenstrains and elastic properties (cubic-shaped inclusion, spherical Eshelby inclusions and spherical inhomogeneity) and compared to analytical and computational results from scientific literature. The main results are that the mechanical fields computed with the new operator are accurate and oscillation-free. The main drawback is that the computation of the operator involves a 3D infinite sum (in practice $3N$ terms which can be computed by parallel computing) with an accuracy which varies as $1/N$.

We also developed an expression for a new consistent periodized discrete third order Green operator to compute the displacement field in the same heterogeneous material. The numerical results were compared to analytical ones and good accuracy were observed. In a material containing elastic singularities (i.e. dislocation loops) laying in planes inclined vs. the reference grid residual oscillations (or artifacts) are observed. We showed that these oscillations are due to the voxellisation of the eigenstrain field and we developed a post treatment sub voxelization method to suppress them. The resulting discontinuity of the displacement field in an inclined loop's plane is equal to the loop's Burgers vector.

The computation method was tested on the case of a homogeneous material containing single dislocation loops of different shapes and Burgers vectors lying in 111 slip planes, as well as random arrays of hexagonal dislocation loops with

different sizes and densities. We showed that the displacement fields computed with the classical Green operator or without the sub voxellisation correction give rise to phantom peaks in the simulation, and that these peaks disappear when both the modified operator and sub voxellisation method are used.

The 3D diffracted intensity was summed to compute 1D diffraction peaks which were analyzed with standard profile analysis techniques (Fourier method and the moments methods). The characteristic parameters extracted from the analysis (dislocation densities, cut off parameters etc.) were found consistent with the input parameters of the simulation within a few percent. Residual differences, especially at short length scale, are believed to result from physical reasons such as dislocation loops' corners.

Perspectives

The techniques developed in this thesis open the way to the following perspectives :

The fixed-point algorithm used with the fourth order Green operator diverges for large mechanical contrasts in a heterogeneous material. A more refined study on the choice of the homogeneous reference medium stiffness or on the numerical implementation can improve the abilities of this operator.

The slow convergence of the 3D sum involved in the computation of the Green operator may curb its use in cases where numerical oscillations are not a problem. However, alternative methods can be used to accelerate the convergence of the 3D sum. First tests show that a factor of 100 in the computing time can be easily achieved.

The analysis techniques used to deduce the dislocation microstructure from the 1D peaks parameters rely on analytical solutions for 2D distributions of infinite straight dislocations. However, real dislocation configurations are three dimensional, and this should have consequences on the 1D and even more the 3D distribution of the diffracted intensity in the vicinity of a peak's maximum. Trying to extend Wilken's or Groma's formalism to 3D cases might be an interesting challenge, and the present simulation method could be helpful.

Last, the ultimate aim of the present thesis was to simulate real experimental cases such as the diffraction peaks recorded during in situ tests on single crystal superalloys. Unfortunately solving preliminary questions as seen above was not an easy task and took much more time than expected. Thus, realistic simulations remain to be done.

Bibliographie

[1] A. Acharya. A model of crystal plasticity based on the theory of continuously distributed dislocations. *Journal of the Mechanics and Physics of Solids*, 49(4) :761–784, 2001.

[2] P.M. Anderson. Crystal-based plasticity. *Fundamentals of Metal Forming ; Wagoner, RH, Chenot, J.-L., Eds*, pages 263–293, 1982.

[3] B. S. Anglin, R. A. Lebensohn, and A. D. Rollett. Continuous distributions of dislocations : a new application of the methods of non-riemannian geometry. *Proc. Roy. Soc. London A*, 231 :263–273, 2014.

[4] L. Balogh, L. Capolungo, and C.N. Tomé. On the measure of dislocation densities from diffraction line profiles : A comparison with discrete dislocation methods. *Acta Materialia*, 60(4) :1467–1477, 2012.

[5] B. W. Batterman and H. Cole. Dynamical diffraction of x rays by perfect crystals. *Reviews of modern physics*, 36(3) :681, 1964.

[6] S. Berbenni, V. Taupin, K S. Djaka, and C. Fressengeas. A numerical spectral approach for solving elasto-static Field Dislocation and G-Disclination Mechanics. *Int. J. Solids Struct.*, 51 :4157–4175, 2014.

[7] S. Berbenni, V. Taupin, C. Fressengeas, and L. Capolungo. A fast Fourier transform-based approach for generalized disclination mechanics within a couple stress theory. *Generalized Continua as Models for Classical and Advanced Materials, Advanced Structured Materials,H. Altenbach and S. Forest (eds.), Springer International Publishing*, pages 47–75, 2016.

[8] S. Berbenni, V. Taupin, and R. A. Lebensohn. A fast fourier transform-based mesoscale
field dislocation mechanics study of grain size effects and reversible plasticity in polycrystals. *Journal of the Mechanics and Physics of Solids*, 135, 2020.

[9] E.F. Bertaut. Raies de debye–scherrer et repartition des dimensions des domaines de bragg dans les poudres polycristallines. *Acta Crystallographica*, 3(1) :14–18, 1950.

[10] F. Bertaut. Signification de la dimension cristalline mesuree dapres la largeur de raie debye-scherrer. *Comptes Rendus Hebdomadaires Des Seances De L Academie Des Sciences*, 228(2) :187–189, 1949.

[11] N. Bertin and W. Cai. Computation of virtual x-ray diffraction patterns from discrete dislocation structures. *Computational Materials Science*, 146 :268–277, 2018.

[12] N. Bertin, M.V. Upadhyay, C. Pradalier, and L. Capolungo. A fft-based formulation for efficient mechanical fields computation in isotropic and anisotropic periodic discrete dislocation dynamics. *Modelling and Simulation in Materials Science and Engineering*, 23, 2015.

[13] A. Borbély and I. Groma. Variance method for the evaluation of particle size and dislocation density from x-ray bragg peaks. *Applied Physics Letters*, 79(12) :1772–1774, 2001.

[14] R. N. Bracewell. *The Fourier Transform and Its Applications (2nd ed., revised)*. McGraw-Hill, New York, 1986.

[15] R. Brenner, R. A. Lebensohn, and O. Castelnau. Elastic anisotropy and yield surface estimates of polycrystals. *International Journal of Solids and Structures*, 46(16) :3018–3026, 2009.

[16] S. Brisard and L. Dormieux. FFT-based methods for the mechanics of composites : A general variational framework. *Comp. Mater. Sci.*, 49 :663–671, 2010.

[17] S. Brisard and L. Dormieux. Combining Galerkin approximation techniques with the principle of Hashin and Shtrikman to derive a new FFT-based numerical method for the homogenization of composites. *Comp. Meth. Appl. Mech. Eng.*, 217-220 :197–212, 2012.

[18] S. Brisard and F. Legoll. Periodic homogenization using the lippmann-schwinger formalism. *archives ouvertes*, 2014.

[19] G. Cailletaud, S. Forest, D. Jeulin, F. Feyel, I. Galliet, V. Mounoury, and S. Quilici. Some elements of microstructural mechanics. *Computational Materials Science*, 27(3) :351–374, 2003.

[20] Y. P. Chiu. Stress-field due to initial strains in a cuboid surrounded by an infinite elastic space. *J. Appl. Mech. - Trans. ASME*, 44 :587–590, 1977.

[21] H. Cole. Bragg's law and energy sensitive detectors. *Journal of Applied Crystallography*, 3(5) :405–406, 1970.

[22] F. F. Csikor and I. Groma. Probability distribution of internal stress in relaxed dislocation systems. *Physical Review B*, 70(6) :064106, 2004.

[23] T. W. DeGeus, J. Vondrejc, J. Zeman, H. Peerlings, and G.D. Geers. Finite strain FFT-based non-linear solvers made simple. *Comp. Meth. Appl. Mech. Eng.*, 318 :412–430, 2017.

[24] F. Delaire, J. L. Raphanel, and C. Rey. Plastic heterogeneities of a copper multicrystal deformed in uniaxial tension : experimental study and finite element simulations. *Acta Materialia*, 48(5) :1075–1087, 2000.

[25] L. Dirand. *Fluage à haute température d'un superalliage monocristallin : expérimentation in situ en rayonnement synchrotron.* PhD thesis, Institut National Polytechnique de Lorraine, 2011.

[26] L. Dirand, J. Cormier, A. Jacques, J. Chateau-Cornu, T. Schenk, O. Ferry, and P. Bastie. Measurement of the effective γ/γ' lattice mismatch during high temperature creep of ni-based single crystal superalloy. *Materials Characterization*, 77 :32–46, 2013.

[27] L. Dirand, A. Jacques, J. P. Chateau-Cornu, T. Schenk, O. Ferry, and P. Bastie. Phase-specific high temperature creep behaviour of a pre-rafted ni-based superalloy studied by x-ray synchrotron diffraction. *Philosophical Magazine*, 93(10-12) :1384–1412, 2013.

[28] K. S. Djaka, S. Berbenni, V. Taupin, and R. A. Lebensohn. A fft-based numerical implementation of mesoscale field dislocation mechanics : Application to two-phase laminates. *International Journal of Solids and Structures*, 2019.

[29] K. S. Djaka, V. Taupin, S. Berbenni, and C. Fressengeas. A numerical spectral approach to solve the dislocation density transport equation. *Modell. Simul. Mater. Sci. Eng.*, 23 :065008(27pp), 2015.

[30] K. S. Djaka, A. Villani, V. Taupin, L. Capolungo, and S. Berbenni. Field Dislocation Mechanics for heterogeneous elastic materials : A numerical spectral approach. *Comp. Meth. Appl. Mech. Eng.*, 315 :921–942, 2017.

[31] Komlan Sénam Djaka. *Développement et applications dune technique de modélisation micromécanique de type" FFT" couplée à la mécanique des champs de dislocations.* PhD thesis, Université de Lorraine, 2016.

[32] S P. Donegan and A D. Rollett. Simulation of residual stress and elastic energy density in thermal barrier coatings using fast Fourier transforms. *Acta Mater.*, 96 :212–228, 2015.

[33] W. Dreyer, W H. Muller, and J. Olschewski. An approximate analytical 2D-solution for the stresses and strains in eigenstrained cubic materials. *Acta Mech.*, 136(3-4) :171–192, 1999.

[34] M. Dupraz, G. Beutier, D. Rodney, D. Mordehai, and M. Verdier. Signature of dislocations and stacking faults of face-centred cubic nanocrystals in coherent

x-ray diffraction patterns : a numerical study. *Journal of applied crystallography*, 48(3) :621–644, 2015.

[35] J. N. Eastabrook and A. J . C. Wilson. The diffraction of x-rays by distorted-crystal aggregates iii : remarks on the interpretation of the fourier coefficients. *Proceedings of the Physical Society. Section B*, 65(1) :67, 1952.

[36] P. Eisenlohr, M. Diehl, R A. Lebensohn, and F. Roters. A spectral method solution to crystal elasto-viscoplasticity at finite strains. *Int. J. Plast.*, 46 :37–53, 2013.

[37] K S. Eloh, A. Jacques, and S. Berbenni. Development of a new consistent discrete green operator for fft based methods to solve heterogeneous problems with eigenstrains. *IJP*, 11 :1669 ; doi :10.3390/ma11091669, 2019.

[38] K S. Eloh, A. Jacques, G. Ribarik, and S. Berbenni. The effect of crystal defects on 3D high-resolution diffraction peaks : A FFT-based method. *Materials*, 11 :1669 ; doi :10.3390/ma11091669, 2018.

[39] D. J. Eshelby. The determination of the elastic field of an ellipsoidal inclusion and related problems. *Proceedings of the Royal Society A*, 241 :376–396, 1957.

[40] D. J. Eshelby. The elastic field outside an ellipsoidal inclusion. *Proceedings of the Royal Society A*, 252 :561–569, 1959.

[41] P. P. Ewald. X-ray diffraction by finite and imperfect crystal lattices. *Proceedings of the Physical Society*, 52(1) :167, 1940.

[42] D. J. Eyre and G. W. Milton. A fast numerical scheme for computing the response of composites using grid refinement. *The European Physical Journal-Applied Physics*, 6(1) :41–47, 1999.

[43] C. Fressengeas, V. Taupin, and L. Capolungo. An elasto-plastic theory of dislocation and disclination fields. *International Journal of Solids and Structures*, 48(25-26) :3499–3509, 2011.

[44] M. Frigo and S G. Johnson. An adaptive software architecture for the FFT. *Proc. Int. Conf. Acoust. Speech Sig. Process.*, 3 :1381–1384, 1998.

[45] I Gaal. De hass-van alphen effect in dislocated crystals. *Acta Physica Academiae Scientiarum Hungaricae*, 33(3-4) :411–418, 1973.

[46] I Gaal. Dissertation to the hungarian academy of sciences. 1976.

[47] L. Gélébart and R. Mondon-Cancel. Non-linear extension of FFT-based methods accelerated by conjugate gradients to evaluate the mechanical behavior of composite materials. *Comp. Mater. Sci.*, 77 :430–439, 2013.

[48] R. Glowinski and P. Le Tallec. *Augmented Lagrangian and operator-splitting methods in nonlinear mechanics*, volume 9. SIAM, 1989.

[49] J T. Graham, A D. Rollett, and R. LeSar. Fast fourier transform discrete dislocation dynamics. *Modell. Simul. Mater. Sci. Eng.*, 8 :085005, 2016.

[50] F. Grennerat, M. Montagnat, O. Castelnau, P. Vacher, H. Moulinec, P. Suquet, and P. Duval. Experimental characterization of the intragranular strain field in columnar ice during transient creep. *Acta Materialia*, 60(8) :3655–3666, 2012.

[51] I Groma. X-ray line broadening due to an inhomogeneous dislocation distribution. *Physical Review B*, 57(13) :7535, 1998.

[52] I. Groma, F. F. Csikor, and M. Zaiser. Spatial correlations and higher-order gradient terms in a continuum description of dislocation dynamics. *Acta Materialia*, 51(5) :1271–1281, 2003.

[53] I Groma and G Monnet. Analysis of asymmetric broadening of x-ray diffraction peak profiles caused by randomly distributed polarized dislocation dipoles and dislocation walls. *Journal of applied crystallography*, 35(5) :589–593, 2002.

[54] C. Hammond and C. Hammond. *The Basics of Cristallography and Diffraction*, volume 214. Oxford, 2001.

[55] S. Haouala, S. Lucarini, J LLorca, and J Segurado. Simulation of the hall-petch effect in fcc polycrystals by means of strain gradient crystal plasticity and fft homogenization. *Journal of the Mechanics and Physics of Solids*, 134 :103755, 2020.

[56] E. Hewitt and R. E. Hewitt. The gibbs-wilbraham phenomenon : An episode in fourier analysis. *Archive for History of Exact Sciences*, 21 :129–160 ; doi :10.1007/BF00330404, 1979.

[57] J P. Hirth and J. Lothe. *Theory of Dislocations (2nd ed.)*. Wiley, New York, 1982.

[58] F. Hofmann, S. Keegan, and A. M. Korsunsky. Diffraction post-processing of 3d dislocation dynamics simulations for direct comparison with micro-beam laue experiments. *Materials Letters*, 89 :66–69, 2012.

[59] S Y. Hu and L Q. Chen. Solute segregation and coherent nucleation and growth near a dislocation : a Phase-Field Model integrating defect and phase microstructure. *Acta Mater.*, 49 :463–472, 2001.

[60] A. Jacques. From modelling of plasticity in single crystal superalloys to high resolution X-rays three-crystals diffractometer peaks simulation. *Metall. Mater. Trans.*, 47 :5783–5805, 2016.

[61] A Jacques and P Bastie. The evolution of the lattice parameter mismatch of a nickel-based superalloy during a high-temperature creep test. *Philosophical Magazine*, 83(26) :3005–3027, 2003.

[62] Claus Jönsson. Elektroneninterferenzen an mehreren künstlich hergestellten feinspalten. *Zeitschrift für Physik*, 161(4) :454–474, 1961.

[63] Claus Jönsson. Electron diffraction at multiple slits. *American Journal of Physics*, 42(1) :4–11, 1974.

[64] J. W. Ju and L. Z. Sun. Effective elastoplastic behavior of metal matrix composites containing randomly located aligned spheroidal inhomogeneities. Part i : micromechanics-based formulation. *Int. J. Solids Struct.*, 38 :183–201, 2001.

[65] M. Kabel, T. Boehlke, and M. Schneider. Efficient fixed point and Newton-Krylov solvers for FFT-based homogenization of elasticity at large deformation. *Comp. Mech.*, 6 :1497–1514, 2014.

[66] M. Kabel, S. Fliegener, and M. Schneider. Mixed boundary conditions for FFT-based homogenization at finite strains. *Comp. Mech.*, 57 :193–210, 2016.

[67] M. Kabel, D. Merkert, and M. Schneider. Use of composite voxels in FFT-based homogenization. *Comp. Meth. Appl. Mech. Eng.*, 294 :168–188, 2015.

[68] S. Kassbohm, W.H. Muller, and R. Fessler. Improved approximations of Fourier coefficients for computing periodic structures with arbitrary stiffness distribution. *Comp. Mater. Sci.*, 37 :90–93, 2006.

[69] s. Kaßbohm, W.H. Müller, and Feßler R. Fourier series for computing the response of periodic structures with arbitrary stiffness distribution. *Computational Materials Sciences*, 32 :387–391, 2005.

[70] M. A. Krivoglaz. Theory of x-ray and thermal-neutron scattering by real crystals. 1969.

[71] M. A. Krivoglaz and K. P. Ryaboshapka. Theory of x-ray scattering by crystals containing dislocations, screw and edge dislocations randomly distributed throughout the crystal. *Fiz. Metallov. Metalloved*, 15 :18–31, 1963.

[72] Ekkehart Kröner. *Statistical continuum mechanics*. Number 92. Springer, 1972.

[73] R. Lebensohn, A. Kanjarla, and P. Eisenlohr. An elasto-viscoplastic formulation based on fast Fourier transforms for the prediction of micromechanical fields in polycrystalline materials. *Int. J. Plast.*, 32-33 :59–69, 2012.

[74] R. Lebensohn, A. Rollett, and P. Suquet. Fast fourier transform-based modeling for the determination of micromechanical fields in polycrystals. *J. Mater.*, 13 :13–18, 2011.

[75] R. A. Lebensohn. N-site modeling of a 3d viscoplastic polycrystal using Fast Fourier Transform. *Acta Mater.*, 49 :2723–2737, 2001.

[76] R. A. Lebensohn, R. Brenner, O. Castelnau, and A. D. Rollet. Orientation image-based micromechanical modeling of subgrain texture evolution in polycrystalline copper. *Acta Mater.*, 56 :3914–3926, 2008.

[77] R. A. Lebensohn, O. Castelnau, R. Brenner, and P. Gilormini. Study of the antiplane deformation of linear 2-d polycrystals with different microstructures. *International journal of solids and structures*, 42(20) :5441–5459, 2005.

[78] R. A Lebensohn, J. P Escobedo, E. K Cerreta, D. Dennis-Koller, C. A Bronkhorst, and J. F. Bingert. Modeling void growth in polycrystalline materials. *Acta Materialia*, 61(18) :6918–6932, 2013.

[79] R A. Lebensohn and A. Needleman. Numerical implementation of non-local polycrystal plasticity using fast Fourier transforms. *J. Mech. Phys. Solids*, 97 :333–351, 2016.

[80] A Leineweber and EJ Mittemeijer. Notes on the order-of-reflection dependence of microstrain broadening. *Journal of Applied Crystallography*, 43(5) :981–989, 2010.

[81] C Lemarchand, B Devincre, and LP Kubin. Homogenization method for a discrete-continuum simulation of dislocation dynamics. *Journal of the Mechanics and Physics of Solids*, 49(9) :1969–1982, 2001.

[82] K. Levenberg. A method for the solution of certain non-linear problems in least squares. *Quarterly of applied mathematics*, 2(2) :164–168, 1944.

[83] J. Li, X. Tian, and R. Abdelmoula. A damage model for crack prediction in brittle and quasi-brittle materials solved by the fft method. *International journal of fracture*, 173(2) :135–146, 2012.

[84] Q. Li and P. M. Anderson. A compact solution for the stress field from a cuboidal region with a uniform transformation strain. *J. Elasticity*, 64 :237–245, 2001.

[85] C. Licht and P. Suquet. Augmented lagrangian method applied to a problem of incompressible viscoplasticity arising in homogenization. *Numerical Methods for Nonlinear Problems, Taylor C.(ed.). Pineridge Press : Swansea*, pages 106–114, 1986.

[86] K. Liss, A. Bartels, A. Schreyer, and H. Clemens. High-energy x-rays : a tool for advanced bulk investigations in materials science and physics. *Texture, Stress, and Microstructure*, 35(3-4) :219–252, 2003.

[87] K-D Liss, A Royer, T Tschentscher, P Suortti, and AP Williams. On high-resolution reciprocal-space mapping with a triple-crystal diffractometer for high-energy x-rays. *Journal of Synchrotron Radiation*, 5(2) :82–89, 1998.

[88] S. Liu, X. Jin, Z. Wang, L M. Keer, and Q. Wang. Analytical solution for elastic fields caused by eigenstrains in a half-space and numerical implementation based on FFT. *Int. J. Plast.*, 35 :135–154, 2012.

[89] F. Livet. Diffraction with a coherent x-ray beam : dynamics and imaging. *Acta Crystallographica Section A : Foundations of Crystallography*, 63(2) :87–107, 2007.

[90] S. Lucarini and J. Segurado. On the accuracy of spectral solvers for micromechanics based fatigue modeling. *Computational Mechanics*, 63(2) :365–382, 2019.

[91] D. W. Marquardt. An algorithm for least-squares estimation of nonlinear parameters. *Journal of the society for Industrial and Applied Mathematics*, 11(2) :431–441, 1963.

[92] J. C. Michel, H. Moulinec, and P. Suquet. A computational scheme for linear and non-linear composites with arbitrary phase contrast. *Int. J. Num. Meth. Eng.*, 52 :139–160, 2001.

[93] D. P. Mika and P. R. Dawson. Effects of grain interaction on deformation in polycrystals. *Materials Science and Engineering : A*, 257(1) :62–76, 1998.

[94] G. W. Milton and K. Golden. Representations for the conductivity functions of multicomponent composites. *Communications on Pure and Applied Mathematics*, 43(5) :647–671, 1990.

[95] V. Monchiet and G. Bonnet. A polarization based FFT iterative scheme for computing the effective properties of elastic composites with arbitrary contrast. *Int. J. Num. Meth. Eng.*, 89 :1419–1436, 2012.

[96] V. Monchiet and G. Bonnet. Numerical homogenization of nonlinear composites with polization-based fft iterative scheme. *Computational Materials Science*, 79 :276–283, 2013.

[97] H. Moulinec and F. Silva. Comparaison of three accelerated FFT-based schemes for computing the mechanical response of composite materials. *Int. J. Num. Meth. Eng.*, 97 :960–985, 2014.

[98] H. Moulinec and P. Suquet. A fast numerical method for computing the linear and non linear properties of composites. *C. R. Acad. Sci. Paris II*, 318 :1417–1423, 1994.

[99] H. Moulinec and P. Suquet. A numerical method for computing the overall response of nonlinear composites with complex microstructure. *Comp. Meth. Appl. Mech. Eng.*, 157 :69–94, 1998.

[100] H Mughrabi, T Ungar, W Kienle, and M Wilkens. Long-range internal stresses and asymmetric x-ray line-broadening in tensile-deformed [001]-orientated copper single crystals. *Philosophical magazine A*, 53(6) :793–813, 1986.

[101] W. Muller. Fourier transforms and their application to the formation of textures and changes of morphology in solids. *Journal de Physique IV*, 6 :139–148, 1997.

[102] W H. Muller. Mathematical vs. experimental stress analysis of inhomogeneities in solids. *J. Phys. IV*, 6(C1) :139–148, 1996.

[103] WH Müller and S Neumann. An approximate analytical 3-d solution for the stresses and strains in eigenstrained cubic materials. *International journal of solids and structures*, 35(22) :2931–2958, 1998.

[104] T. Mura. *Micromechanics of defects in solids*. Kluwer Academic Publishers, Dordrecht, The Netherlands, 1987.

[105] J.F. Nye. Some geometrical relations in dislocated crystals. *Acta metallurgica*, 1(2) :153–162, 1953.

[106] T. Otsuka, R. Brenner, and B. Bacroix. Fft-based modelling of transformation plasticity in polycrystalline materials during diffusive phase transformation. *International Journal of Engineering Science*, 127 :92–113, 2018.

[107] A. Prakash and R. Lebensohn. Simulation of micromechanical behavior of polycrystals : finite elements versus fast Fourier transforms. *Modell. Simul. Mater. Sci. Eng.*, 17 :64010–64016, 2009.

[108] W H. Press, S A. Teukolsky, W T. Vetterling, and B P. Flannery. *Numerical recipes in C++. The art of scientific computing (2nd ed.)*. Cambridge University Press, 2002.

[109] S. Ravy. La diffraction cohérente des rayons x. *Reflets physique*, (34-35) :60–64, 2013.

[110] G. Ribárik. Modeling of diffraction patterns based on microstructural properties. *Material Science and Solid State Physics Program. Eötvös Loránd University Institute of Physics Department of Materials Physics*, 2008.

[111] G. Ribárik. Modeling of diffraction patterns based on microstructural properties. *Material Science and Solid State Physics Program. Eötvös Loránd University Institute of Physics Department of Materials Physics*, 2008.

[112] G. Ribárik, J. Gubicza, and T. Ungár. Correlation between strength and microstructure of ball-milled al–mg alloys determined by x-ray diffraction. *Materials science and engineering : A*, 387 :343–347, 2004.

[113] G. Ribárik, T. Ungár, and J. Gubicza. Mwp-fit : a program for multiple whole-profile fitting of diffraction peak profiles by ab initio theoretical functions. *Journal of Applied Crystallography*, 34(5) :669–676, 2001.

[114] A. W. Richards, R. A. Lebensohn, and K. Bhattacharya. Interplay of martensitic phase transformation and plastic slip in polycrystals. *Acta Materialia*, 61(12) :4384–4397, 2013.

[115] AD Rollett, RA Lebensohn, M Groeber, Y Choi, J Li, and GS Rohrer. Stress hot spots in viscoplastic deformation of polycrystals. *Modelling and Simulation in Materials Science and Engineering*, 18(7) :074005, 2010.

[116] F. Roters, P. Eisenlohr, L. Hantcherli, D. D. Tjahjanto, T. R. Bieler, and D. Raabe. Overview of constitutive laws, kinematics, homogenization and multiscale methods in crystal plasticity finite-element modeling : Theory, experiments, applications. *Acta Materialia*, 58(4) :1152–1211, 2010.

[117] A. Rovinelli, Y. Guilhem, H. Proudhon, R. A Lebensohn, W. Ludwig, and M. D. Sangid. Assessing reliability of fatigue indicator parameters for small crack growth via a probabilistic framework. *Modelling and Simulation in Materials Science and Engineering*, 25(4) :045010, 2017.

[118] A. Rovinelli, M. D. Sangid, H. Proudhon, Y. Guilhem, R. A. Lebensohn, and W. Ludwig. Predicting the 3d fatigue crack growth rate of small cracks using multimodal data via bayesian networks : In-situ experiments and crystal plasticity simulations. *Journal of the Mechanics and Physics of Solids*, 115 :208–229, 2018.

[119] M. Schneider, D. Merkert, and M. Kabel. Fft-based homogenization for microstructures discretized by linear hexahedral elements. *Int. J. Num. Meth. Eng.*, 109 :1461–1489, 2017.

[120] M. Schneider, F. Ospald, and M. Kabel. Computational homogenization of elasticity on a staggered grid. *Int. J. Num. Meth. Eng.*, 105 :693–720, 2016.

[121] C Seitz, M Weisser, M Gomm, R Hock, and A Magerl. A high-energy triple-axis x-ray diffractometer for the study of the structure of bulk crystals. *Journal of applied crystallography*, 37(6) :901–910, 2004.

[122] P. Shanthraj, P. Eisenlohr, M. Diehl, and F. Roters. Numerically robust spectral methods for crystal plasticity simulations of heterogeneous materials. *Int. J. Plast.*, 66 :31–45, 2015.

[123] L. Sharma, R. H. Peerlings, P. Shanthraj, F. Roters, and M. G. Geers. Fft-based interface decohesion modelling by a nonlocal interphase. *Advanced Modeling and Simulation in Engineering Sciences*, 5(1) :7, 2018.

[124] D. Smilgies, D. R. Blasini, S. Hotta, and H. Yanagi. Reciprocal space mapping and single-crystal scattering rods. *Journal of synchrotron radiation*, 12(6) :807–811, 2005.

[125] X. Song, F. Hofmann, and A. M. Korsunsky. Dislocation-based plasticity model and micro-beam laue diffraction analysis of polycrystalline ni foil : A forward prediction. *Philosophical Magazine*, 90(30) :3999–4011, 2010.

[126] A. R. Stokes and A. J. C. Wilson. The diffraction of x rays by distorted crystal aggregates-i. *Proceedings of the Physical Society*, 56(3) :174, 1944.

[127] P. Suquet, H. Moulinec, O. Castelnau, M. Montagnat, N. Lahellec, F. Grennerat, P. Duval, and R. Brenner. Multi-scale modeling of the mechanical behavior of polycrystalline ice under transient creep. *Proc. IUTAM*, 3 :76–90, 2012.

[128] T. Tran, V. Monchiet, and G. Bonnet. A micromechanics-based approach for derivation of constitutive coefficients of strain-gradient media. *Int. J. Solids Struct.*, 5 :783–792, 2012.

[129] R. Tréhorel. *Comportement mécanique haute température du superalliage monocristallin AM1 : étude in situ par une nouvelle technique de diffraction en rayonnement synchrotron*. PhD thesis, 2018.

[130] R. Tréhorel, G. Ribarik, T. Schenk, and A. Jacques. Real-time study of transients during high-temperature creep of an ni-base superalloy by far-field high-energy synchrotron x-ray diffraction. *Journal of Applied Crystallography*, 51(5), 2018.

[131] T Ungár and A Borbély. The effect of dislocation contrast on x-ray line broadening : a new approach to line profile analysis. *Applied Physics Letters*, 69(21) :3173–3175, 1996.

[132] T Ungár, I Dragomir, Á Révész, and A Borbély. The contrast factors of dislocations in cubic crystals : the dislocation model of strain anisotropy in practice. *Journal of applied crystallography*, 32(5) :992–1002, 1999.

[133] T. Ungár, J. Gubicza, G. Ribárik, and A. Borbély. Crystallite size distribution and dislocation structure determined by diffraction profile analysis : principles and practical application to cubic and hexagonal crystals. *Journal of applied crystallography*, 34(3) :298–310, 2001.

[134] T Ungar, H Mughrabi, D Rönnpagel, and M Wilkens. X-ray line-broadening study of the dislocation cell structure in deformed [001]-orientated copper single crystals. *Acta Metallurgica*, 32(3) :333–342, 1984.

[135] M. V. Upadhyay, L. Capolungo, and L. Balogh. On the computation of diffraction peaks from discrete defects in continuous media : comparison of

displacement and strain-based methods. *Journal of Applied Crystallography*, 47(3) :861–878, 2014.

[136] M. V. Upadhyay, L. Capolungo, V. Taupin, and C. Fressengeas. Elastic constitutive laws for incompatible crystalline media : the contributions of dislocations, disclinations and g-disclinations. *Philosophical Magazine*, 93(7) :794–832, 2013.

[137] M V. Upadhyay, L. Capolungo, V. Taupin, C. Fressengeas, and R A. Lebensohn. A higher order elasto-viscoplastic model using fast Fourier transforms : effects of lattice curvatures on mechanical response of nanocrystalline metals. *Int. J. Plast.*, 83 :126–152, 2016.

[138] A. Utkarsh. *The ParaView Guide : A Parallel Visualization Application, ISBN 978-1930934306*. Kitware Inc., 2015.

[139] G. Vainikko. Fast solvers of the lippmann-schwinger equation. In *Direct and inverse problems of mathematical physics*, pages 423–440. Springer, 2000.

[140] J. G. M. Van Berkum, R. Delhez, T. H. De Keijser, and E. J. Mittemeijer. Diffraction-line broadening due to strain fields in materials ; fundamental aspects and methods of analysis. *Acta Crystallographica Section A : Foundations of Crystallography*, 52(5) :730–747, 1996.

[141] N. Vaxelaire, H. Proudhon, S. Labat, C. Kirchlechner, J. Keckes, V. Jacques, S. Ravy, S. Forest, and O. Thomas. Methodology for studying strain inhomogeneities in polycrystalline thin films during in situ thermal loading using coherent x-ray diffraction. *New Journal of Physics*, 12(3) :035018, 2010.

[142] A. Vidyasagar, W L. Tan, and D M. Kochmann. Predicting the effective response of bulk polycrystalline ferroelectric ceramics via improved spectral phase field methods. *J. Mech. Phys. Solids*, 106 :133–151, 2017.

[143] A. Vidyasagar, A D. Tutcuoglu, and D M. Kochmann. Deformation patterning in finite-strain crystal plasticity by spectral homogenization with application to magnesium. *Comp. Meth. Appl. Mech. Eng.*, 335 :584–609, 2018.

[144] V. Vinogradov and G W. Milton. An accelerated FFT algorithm for thermoelastic and non-linear composites. *Int. J. Num. Meth. Eng.*, 76 :1678–1695, 2008.

[145] V. Volterra. Sur l'équilibre des corps élastiques multiplement connexes. In *Annales scientifiques de l'École normale supérieure*, volume 24, pages 401–517, 1907.

[146] J. Vondřejc, J. Zeman, and I. Marek. An FFT-based Galerkin method for homogenization of periodic media. *Comp. Math. Appl.*, 68 :156–173, 2015.

[147] Z. Wang, H. Yu, and Q. Wang. Analytical solutions for elastic fields caused by eigenstrains in two joined and perfectly bonded half-spaces and related problems. *Int. J. Plast.*, 76 :1–28, 2016.

[148] B. E. Warren. X-ray studies of deformed metals. *Progr. in Metal Phys.*, 8, 1959.

[149] B. E. Warren. X-ray difiraction. *Addison Wesley Pub. Co., Reading, MA*, 375 :379–388, 1969.

[150] B. E. Warren. *X-ray Diffraction*. Courier Corporation, 1990.

[151] B. E. Warren and B. L. Averbach. The separation of cold-work distortion and particle size broadening in x-ray patterns. *Journal of applied physics*, 23(4) :497–497, 1952.

[152] B.E. Warren. X-ray diffraction methods. *Journal of applied physics*, 12(5) :375–384, 1941.

[153] M Wilkens. X-ray diffraction line broadening and crystal plasticity. In *Strength of Metals and Alloys (ICSMA 8)*, pages 125–130. Elsevier, 1989.

[154] M. I. Wilkens. Theoretical aspects of kinematical x-ray diffraction profiles from crystals containing dislocation distributions(fourier transform of x ray diffraction line profiles from crystals with dislocations). *NBS Fundamental Aspects of Dislocation Theory*, 2, 1970.

[155] G. K. Williamson and W. H. Hall. X-ray line broadening from filed aluminium and wolfram. *Acta metallurgica*, 1(1) :22–31, 1953.

[156] F. Willot. Fourier-based schemes for computing the mechanical response of composite with accurate local field. *C. R. Mecanique*, 343 :232–245, 2015.

[157] F. Willot, B. Abdallah, and Y P. Pellegrini. Fourier-based schemes with modified Green operator for computing the electrical response of heterogeneous media with accurate local fields. *Int. J. Num. Meth. Eng.*, 98 :518–533, 2014.

[158] F. Willot and Y P. Pellegrini. Fast Fourier transform computations and build-up of plastic deformation in 2D, elastic-perfectly plastic, pixelwise disordered porous media. *Continuum Models and Discrete Systems, D. Jeulin and S. Forest (eds.), CMDS11, Presse Ecole des Mines Paris*, pages 443–449, 2008.

[159] Arthur James Cochran Wilson. The reflexion of x-rays from the anti-phase nuclei of aucu3. *Proceedings of the Royal Society of London. Series A. Mathematical and Physical Sciences*, 181(987) :360–368, 1943.

[160] S. L. Wong, J. Park, M. P. Miller, and P. R. Dawson. A framework for generating synthetic diffraction images from deforming polycrystals using crystal-based finite element formulations. *Computational Materials Science*, 77 :456–466, 2013.

[161] X. Wu. An efficient antialiasing technique. In *Acm Siggraph Computer Graphics*, volume 25, pages 143–152. ACM, 1991.

[162] G. Xiong, O. Moutanabbir, M. Reiche, R. Harder, and I. Robinson. Coherent x-ray diffraction imaging and characterization of strain in silicon-on-insulator nanostructures. *Advanced Materials*, 26(46) :7747–7763, 2014.

[163] J. Zeman, J. Vondrejc, J. Novak, and I. Marek. Accelerating a FFT-based solver for numerical homogenisation of periodic media by conjugate gradients. *J. Comp. Phys.*, 229 :8065–8071, 2010.

Annexe A

Crystalline material and X-ray diffraction

A.1 Crystalline material

A.1.0.1 Crystalline structure

A material has a crystalline structure when its atoms have an ordered spatial arrangement. This ordered spatial arrangement is often periodic. The smallest periodic unit is the unit cell. The unit cell is represented using three vectors $(\mathbf{a}_1, \mathbf{a}_2, \mathbf{a}_3)$. They are characterized by their norms and directions. The elementary mesh is then identified by six parameters : vectors length and the three angles which they make between them. In the coordinate system formed by the elementary cell, the atoms are defined by position vectors. Figure fig. A.1 below shows an example of a simple mesh in a 2D representation.

The infinite repetition by translation of the elementary mesh constitutes the crystal lattice. The above figure shows an example of a crystal lattice in a 2D representation. In a 3D representation, the elementary mesh forms a rectangular or cubic parallelepiped. The arrangement of atoms in this parallelepiped allows to differentiate crystalline materials. In a cubic material for example, the atoms are located only at the cube's corners. When the atoms are located at the cube's corners and at the face centers, it is a face centered cubic material. In the crystal lattice, atoms form equidistant atomic planes. The distance d between these planes is an important parameter in crystallography.

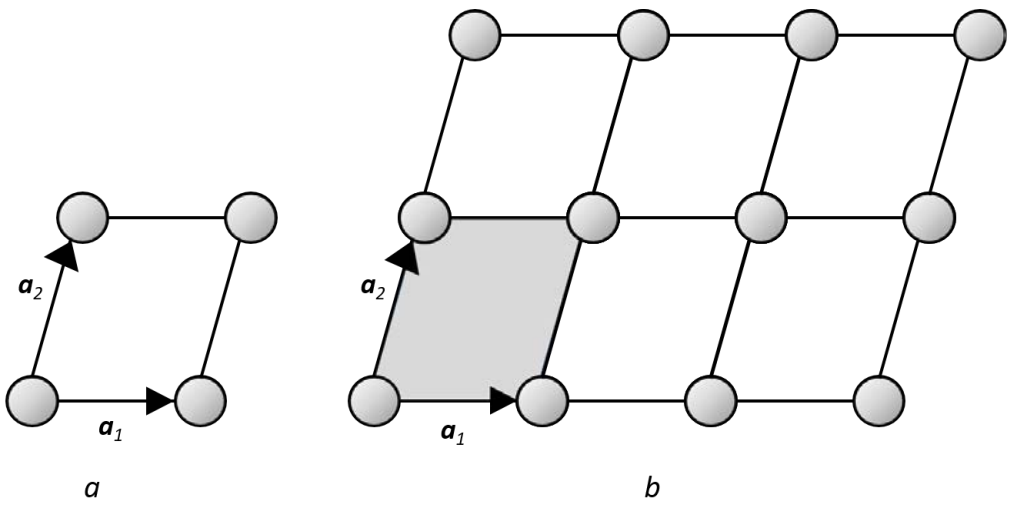


FIGURE A.1 – (a)Definition of the unit cell. (b) The infinite repetition by translation of the unit cell gives the crystal lattice.

A.1.0.2 Direct and reciprocal lattice

The direct lattice is associate to the crystal lattice. It allows to define atoms position, the atomic planes in the crystal etc. In the direct lattice the position of each atom is defined as :

$$\mathbf{r} = m\mathbf{a}_1 + n\mathbf{a}_2 + p\mathbf{a}_3 \tag{A.1}$$

Where m, n, p are integers. Note that $(\mathbf{a}_1, \mathbf{a}_2, \mathbf{a}_3)$ is a direct trihedron. Three angles are defined using these vectors : $\alpha = mes(\mathbf{a}_1, \mathbf{a}_2)$, $\beta = mes(\mathbf{a}_2, \mathbf{a}_3)$, $\gamma = mes(\mathbf{a}_3, \mathbf{a}_1)$. In a cubic material $\alpha = \beta = \gamma = 90°$. In the direct lattice, the atomic planes are described by the three integers called the Miller-indices denoted h, k, l(negative indices have horizontal bars, for example $1\bar{2}3$). The inverses of h, k, l are proportional to the intercepts of the atomic plane with the unit cell vectors $\mathbf{a}_1, \mathbf{a}_2, \mathbf{a}_3$ respectively. The distance d between these planes is denoted d_{hkl}.

The reciprocal lattice is related to the direct lattice. The unit vectors of reciprocal lattice are denoted $\mathbf{b}_1, \mathbf{b}_2, \mathbf{b}_3$ and are given by :

$$\mathbf{b}_1 = \frac{\mathbf{a}_2 \wedge \mathbf{a}_3}{V}, \mathbf{b}_2 = \frac{\mathbf{a}_3 \wedge \mathbf{a}_1}{V}, \mathbf{b}_3 = \frac{\mathbf{a}_1 \wedge \mathbf{a}_2}{V} \tag{A.2}$$

Where V is the volume of the unit cell. Others relations define theses vectors :

$$\mathbf{a}_i.\mathbf{b}_j = 1 \quad if \quad i = j$$

$$\mathbf{a}_i.\mathbf{b}_j = 0 \quad if \quad i \neq j$$

In diffraction theory, the reciprocal lattice is the Fourier transform of the direct lattice. For a (h, k, l) plan define in the direct lattice, one denotes $\mathbf{g}_{hkl}$ the shortest reciprocal lattice vector orthogonal to this plane. The distance d_{hkl} is then given by

$$d_{hkl} = \frac{1}{\sqrt{\mathbf{g}_{hkl} \cdot \mathbf{g}_{hkl}}}$$

.

A.2 Diffraction basis

In this section, we give some basic definitions in diffraction theory. We consider a crystalline material diffracting a monochromatic beam. This corresponds to the most studied applications of X-ray diffraction.

A.2.0.1 Diffraction by an atom

Let's consider fig. A.2 showing the principle of diffraction. The incident beam has a wave vector $\mathbf{k}$. The wavelength is λ and the length $\mathbf{k}$ (pulsation) of this beam is $2\pi/\lambda$. The wave function of this incident beam is (i is the complex imaginaryi $= \sqrt{-1}$) :

$$A(\mathbf{r}) = e^{\mathrm{i}2\pi\mathbf{kr}} \tag{A.3}$$

This incident beam is diffracted by the atom located in point O. The diffracted beam wave vector is $\mathbf{k}'$. For the X-ray beam, the diffraction is assumed to be elastic such as $\mid \mathbf{k} \mid = \mid \mathbf{k}' \mid$. The diffraction introduces a shift phase :

$$\phi_j = e^{\mathrm{i}2\pi\mathbf{k}'\mathbf{r}_j} . e^{-\mathrm{i}2\pi\mathbf{k}\mathbf{r}_j}$$

where $\mathbf{r}_j$ is the position of the atom. The wave function of the diffracted beam is :

$$A_j(\mathbf{r}) = e^{\mathrm{i}2\pi\mathbf{k}'\mathbf{r}} . e^{\mathrm{i}2\pi(\mathbf{k}'-\mathbf{k})\mathbf{r}_j} \tag{A.4}$$

There is constructive interference only if $e^{\mathrm{i}2\pi(\mathbf{k}-\mathbf{k}')\mathbf{r}_j} = 1$. This means that $(\mathbf{k} - \mathbf{k}')\mathbf{r}_j$ must be an integer. The vector $\mathbf{r}_j$ is defined in the direct lattice, therefore the

previous condition is satisfied only if $(\mathbf{k}' - \mathbf{k})$ is a vector of the reciprocal lattice. This condition is the so called Laue condition.

$$\mathbf{g}_{hkl} = \mathbf{k}' - \mathbf{k}$$

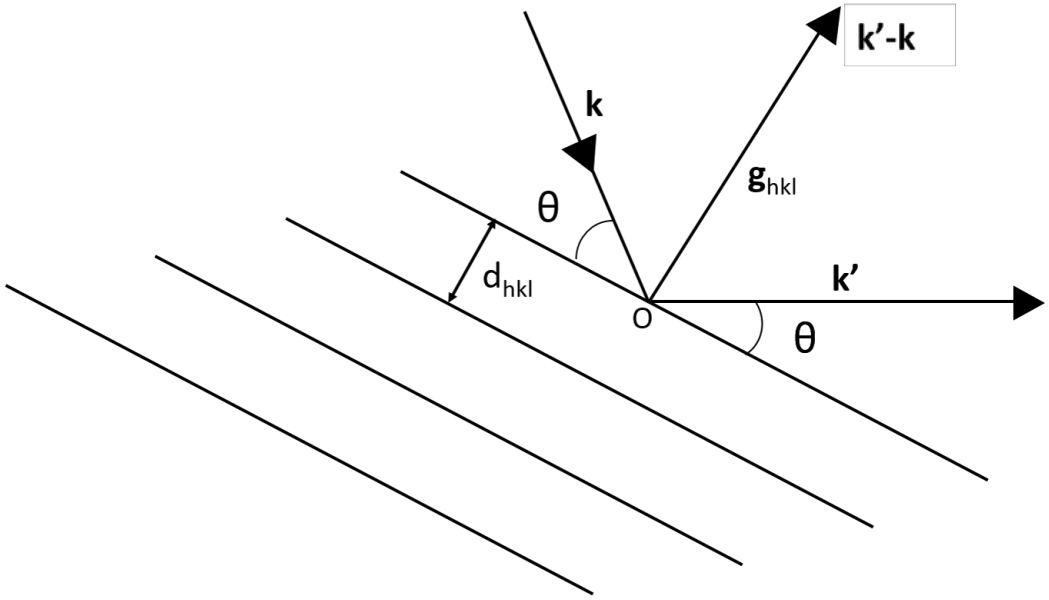


FIGURE A.2 – Schematic view of the diffraction showing the incident wave vector $\mathbf{k}$, the diffraction wave vector $\mathbf{k}'$ and the diffraction vector $\mathbf{g}_{hkl}$

The Ewald construction [41, 54, 124] derives from the Laue condition and is used to determine which lattice plane of a crystal will diffract an incident beam. The Ewald sphere is the sphere defined by the place of the possible extremities of vector $\mathbf{g}$ for all possible directions of the diffracted beam. The radius of the Ewald sphere is $1/\lambda$. One example of this construction is shown in fig.A.3.

A.2.0.2 Bragg's law

Let us assume that the X-ray beam crosses a perfect monocrystal and let assumed that the planes d_{hkl} diffract fig. A.3. While $\mid \mathbf{k} \mid = \mid \mathbf{k}' \mid$, the incident angle θ is equal to the exit angle, figA.2 and one can write :

$$\frac{1}{2d_{hkl}} = \frac{1}{\lambda} sin\theta$$

which leads to :

$$2d_{hkl} sin(\theta) = \lambda \tag{A.5}$$

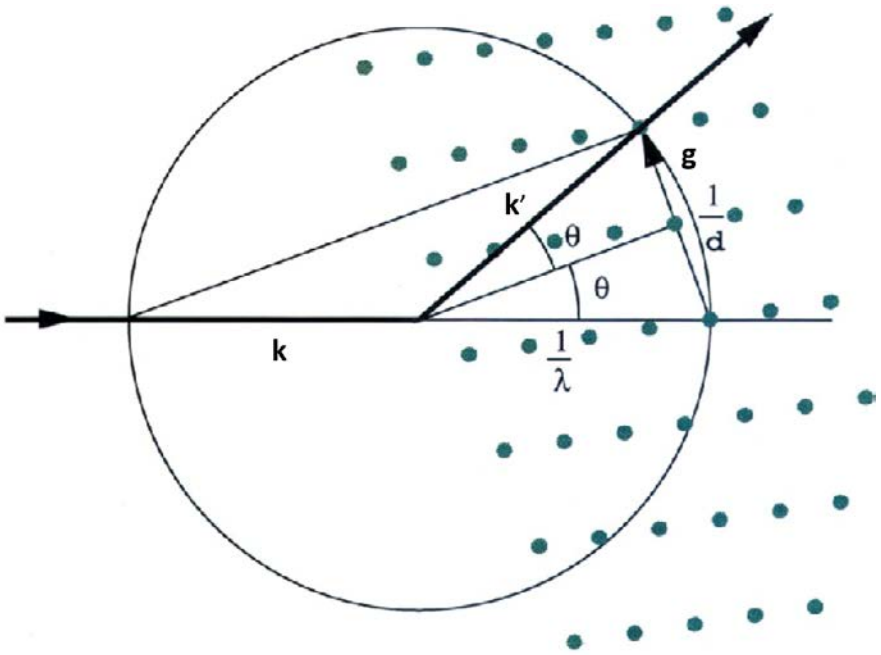


FIGURE A.3 – Ewlad's construction. The atoms located on the Ewald sphere can diffract the incident beam

This last relation is the so called Bragg's law and is the most in X-ray diffraction [152, 149, 150, 5, 21, 54]. It allows for example to compute the distance d_{hkl} for (hkl) plane when the other parameters are known. It is similar to the *Laue condition* which is an equation giving a necessary and sufficient condition for an incident beam to be diffracted by a crystal lattice.

A.2.0.3 Amplitude and Intensity

Amplitude

Let'us consider the schematic view of Fig.A.2. The position vector $\mathbf{r}_j$ of an atom can be written as function of it unit cell $m_1 m_2 m_3$ as :

$$\mathbf{r}_j = m_1\mathbf{a}_1 + m_2\mathbf{a}_2 + m_3\mathbf{a}_3 + \mathbf{r}_{jm} \tag{A.6}$$

where $\mathbf{r}_{jm}$ is the position of the atom in the unit cell. The scattering amplitude Λ_j of a single atom at position $\mathbf{r}_j$ is [150] : (for the sake of simplicity, $\mathbf{g}_{hkl}$ will be

denoted $\mathbf{g}$) :

$$\mathbf{\Lambda}_j(\mathbf{g}) = \Lambda_0 f_j e^{i2\pi \mathbf{g}\mathbf{r}_j/\lambda} \tag{A.7}$$

The constant Λ_0 is proportional to the amplitude of the incident beam. f_j is the scattering factor of the atom located in $\mathbf{r}_j$. The total amplitude is obtained by summing $\mathbf{\Lambda}_j(\mathbf{g})$ over all the atoms of the unit cell $m_1 m_2 m_3$ and by summing over all the unit cells. Let's assume that the crystal shape is a parallepiped with dimensions $N_1 a_1$, $N_2 a_2$, $N_3 a_3$ parallel to axes $\mathbf{a}_1$, $\mathbf{a}_2$,$\mathbf{a}_3$ of the crystal. The total amplitude reads :

$$\mathbf{\Lambda}(\mathbf{g}) = \Lambda_0 \sum_j f_j e^{i2\pi \mathbf{r}_{jm}/\lambda} \sum_{m_1=0}^{N_1-1} e^{i2\pi \mathbf{g} m_1 \mathbf{a}_1/\lambda} \times \sum_{m_2=0}^{N_2-1} e^{i2\pi \mathbf{g} m_2 \mathbf{a}_2/\lambda} \times \sum_{m_3=0}^{N_3-1} e^{i2\pi \mathbf{g} m_3 \mathbf{a}_3/\lambda} \tag{A.8}$$

The first summation over the atoms of the unit cell is different from one structure to another. This is called the structure factor. It designated by F and is written :

$$\mathbf{F} = \sum_j f_j e^{i2\pi/\lambda \mathbf{r}_{jm}} \tag{A.9}$$

An analytical expression can be determined for each of the remaining sums using geometric progression :

$$\sum_{m_1=0}^{N_1-1} e^{i2\pi \mathbf{g} m_1 \mathbf{a}_1/\lambda} = \frac{1 - e^{i2\pi \mathbf{g} N_1 \mathbf{a}_1}}{1 - e^{i2\pi \mathbf{g}\mathbf{a}_1}}$$

After derivation, the complex scattered amplitude is given by (for 1 dimensional application) :

$$\Lambda(\mathbf{g}) = \Lambda_0 F \frac{sin(\pi \mathbf{g} N_1 \mathbf{a}_1/\lambda)}{sin(\pi \mathbf{g}\mathbf{a}_1/\lambda)} \tag{A.10}$$

Intensity

The scattering amplitude is not experimentally accessible. So it is more convenient to study the expression for scattering intensity. The scattered intensity is

proportional to the square of the amplitude :

$$\begin{aligned} I(\mathbf{g}) &\sim \mathbf{\Lambda}(\mathbf{g}) \times \bar{\mathbf{\Lambda}}(\mathbf{g}) \\ I(\mathbf{g}) &= I_0 F^2 \sum_m \sum_{m'} e^{(i2\pi/\lambda)\mathbf{g}(\mathbf{r}_m - \mathbf{r}_{m'})} \end{aligned} \tag{A.11}$$

where $\bar{\Lambda}(\mathbf{g})$ is the complex conjugate of $\Lambda(\mathbf{g})$. With the previous 1D consideration, the scattered intensity is :

$$I(\mathbf{g}) = I_0 \mathbf{F} \times \bar{\mathbf{F}} \frac{sin^2(\pi \mathbf{g} N_1 \mathbf{a}_1/\lambda)}{sin^2(\pi \mathbf{g}\mathbf{a}_1/\lambda)} \tag{A.12}$$

Let define a variable $x = \pi \mathbf{g}\mathbf{a}_1/\lambda$, the final expression of the scattered intensity is [150, 111] :

$$I(\mathbf{g}) = \frac{sin^2(N_1 x)}{sin^2(x)} \tag{A.13}$$

This expression allows to study explicitly the diffracted intensity [149]. This function is governed by two variables : the number of atoms N in a row and x [110, 51]. This expression shows that the intensity is maximal when $sin(x) = 0$. The value x_0 satisfying this condition is :

$$\begin{aligned} x_0 &= k\pi \\ \mathbf{g}\mathbf{a}_1 &= k\lambda \end{aligned}$$

This last equation is equivalent to the Bragg's law [149]. One defines variable of the intensity profiles $\mathbf{q}$ as $\mathbf{q} = \mathbf{g} - \mathbf{g}_B$, where $\mathbf{g}_B$ is the exact Bragg's position. Two characteristic parameters are defines as :

The maximum intensity

$$I_0 = max\{I(\mathbf{q})\} \tag{A.14}$$

The Full Width at Half Maximum (FWHM) :

$$FWHM\{I(\mathbf{q})\} = \mathbf{q}_2 - \mathbf{q}_1, \quad with \quad \mathbf{q}_1 < \mathbf{q}_2 \quad and \quad I(\mathbf{q}_1) = I(\mathbf{q}_2) = \frac{I_0}{2} \tag{A.15}$$

One can add to these characteristic parameters, the position of the maximum intensity or the the area of the intensity curve which can be used for some studies. The variable N is related to the size of the diffracting crystal and x is related to an uniform or local deformation of the crystal.

A.2.0.4 The size of the crystal

The influence of the crystal size is containing in the variable N which is the number of atoms in the crystal. The maximum intensity I_0 is given by :

$$\lim_{x \to 0} \frac{sin^2(Nx)}{sin^2(x)} = N^2$$

The maximum value of the peak is then proportional to the square of the crystal volume. FigA.4, shows that when N increases (the size of the crystal increases), the width of the curve decreases and it becomes a delta function. For large values of N the intensity function can be approximated :

$$\frac{sin^2(Nx)}{sin^2(x)} = N^2 \left(\frac{sin(Nx)}{Nx} \right)^2$$

The FWHM value of this function can be determined by resolving the equation

$$\frac{sin(Nx)}{Nx} = \frac{1}{\sqrt{2}}$$

The numerical resolution of this equation lead to : $FWHM = 2.78\frac{1}{N}$. This expression corroborate the fact that when the crystal size decreases the peak broadens.

As X-ray diffraction experiments are performed for fixed volume (N fixed), the influence of the parameter $x = \pi \mathbf{g} \mathbf{a}_1 / \lambda$ is often studied. For a given diffraction vector $\mathbf{g}$, it is the variation of the unit cell vector $\mathbf{a}_1$ which affects the diffraction function. The unit cell vector $\mathbf{a}_1$ varies when the atoms are moved from their initial position. Hence, all uniform or local deformation affects the x-ray diffraction profile

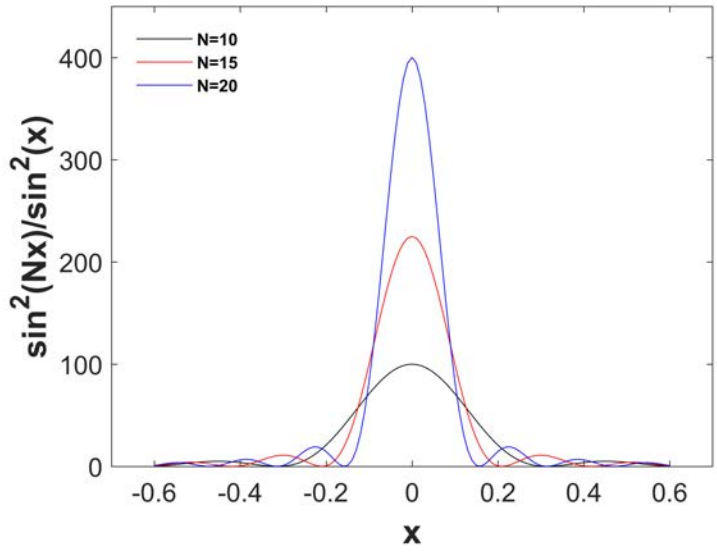


FIGURE A.4 – The function $\frac{sin^2(Nx)}{sin^2(x)}$ plotted close to its first maximum for different values of N. As N tends to infinity, the curve becomes a delta function

A.2.0.5 Uniform deformation

A uniform deformation is often due to an applied strain/stress or uniform dilatation. Such deformation lead to a uniform variation of the unit cell vector $\mathbf{a}_1$. As shown in fig.A.5, the maximum intensity does not change but it shifted from $-\frac{\delta \mathbf{a}_1}{\mathbf{a}_1}$ his initial position.

A.2.0.6 A non uniform deformation

A local deformation in the crystal is often due to line defects such as dislocations, cracks. To study their effect on peak profile it is important to evaluate the distribution of the displacement or the deformation field due to such defects.

Let's consider the unit cell denoted $m_1m_2m_3$. We denote $\mathbf{u}(m_1, m_2, m_3)$ the displacement field which is different for each unit cell. Therefore, the position of unit cell, assimilated to one of it origin reads :

$$\mathbf{r}_m = m_1\mathbf{a}_1 + m_2\mathbf{a}_2 + m_3\mathbf{a}_3 + \mathbf{u}(m_1, m_2, m_3) \tag{A.16}$$

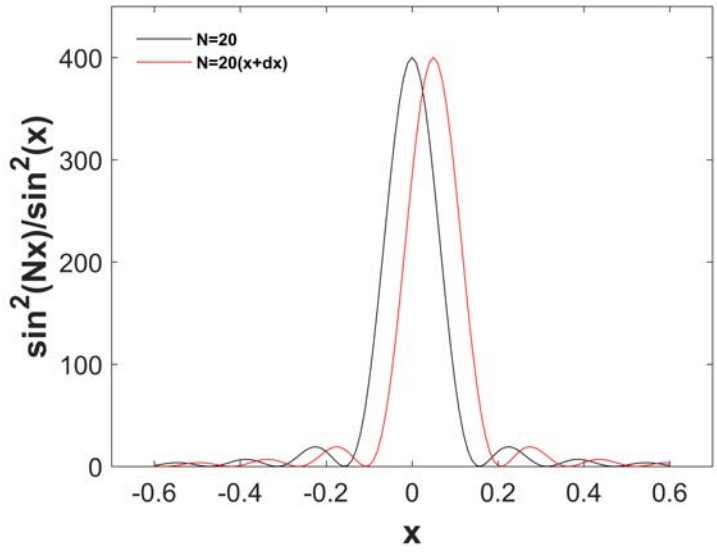


FIGURE A.5 – The effect of a uniform deformation on the intensity line profile. This uniform deformation does not change the maximum intensity but it position is shifted

with

$$\mathbf{u}(m_1, m_2, m_3) = X_m \mathbf{a}_1 + Y_m \mathbf{a}_2 + Z_m \mathbf{a}_3 \tag{A.17}$$

Let's consider a $00l$ reflection (the general formulation is given bellow) :

$$\begin{aligned} &\frac{\mathbf{g}}{\lambda} = l\mathbf{b}_3 \\ &\frac{\mathbf{g}}{\lambda}.\mathbf{u} = lZ_m \\ &I(\mathbf{g}) = I_0 F^2 \sum_m \sum_{m'} e^{(i2\pi)(m_3 - m_{3'} + l(Z_m - Z_{m'}))} \end{aligned} \tag{A.18}$$

To carry this integration a useful separation of the crystal is suggested [10, 9, 150]. The crystal is separated in columns along the $\mathbf{a}_3$ (or along the crystal vector parallel to the diffraction vector) as shown in the figure bellow (fig. A.6) [150]. The integration is carried like this : for a given $m_1 m_2$, the sum over m_3 and m'_3 is the contribution of all pairs in the column $m_1 m_2$ and the sums over m_1 and m_2 is the columns contribution. Using the notations in eq. A.19 and after caring this integration and other derivations, the final expression of the intensity obtained as

Fourier series eq. A.20 :

$$\begin{aligned} n &= m_3 - m_3' \\ Z_n &= Z(m_3') - Z(m_3) \\ L &= na_3 \end{aligned} \tag{A.19}$$

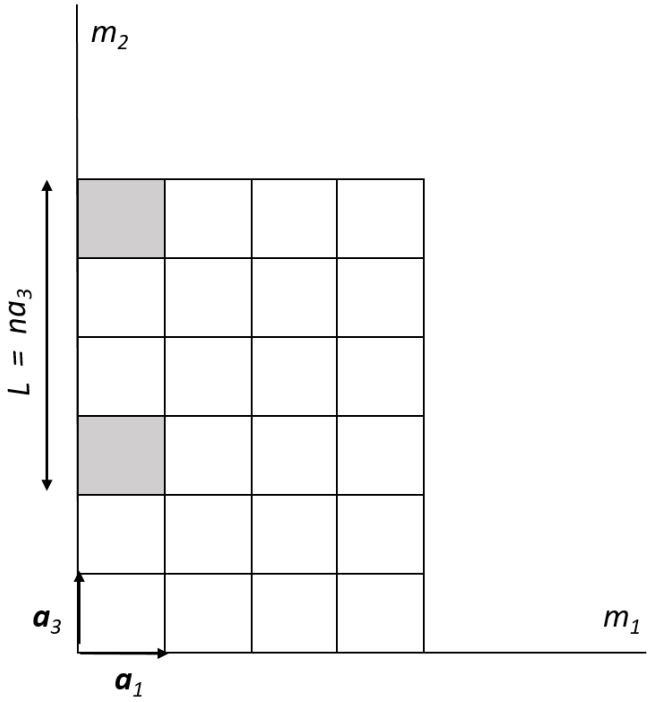


FIGURE A.6 – 2D representation of the crystal divided in columns along the direction of the direction vector

$$I(\mathbf{g}) = I_0 \sum_{n=-\infty}^{+\infty} (A_n cos(2\pi n h_3) + B_n sin(2\pi n h_3)) \tag{A.20}$$

where $h_3 = \frac{|\mathbf{a}_3|}{d}$ (a_3 is the unit cell vector and d is the distance between reflection planes). The Fourier coefficients are defined as :

$$\begin{aligned} A_n &= \frac{N_n}{N_3}\langle cos(2\pi l Z n)\rangle, \\ B_n &= -\frac{N_n}{N_3}\langle sin(2\pi l Z_n)\rangle \end{aligned} \tag{A.21}$$

N_n is the average number of pair per column and N_3 is the average number of cells per column [150, 135]. The sinus coefficient B_n is less studied because its value

is very small and is difficult to determine with experiment. The coefficient A_n is determined by experiment. It is the product of $\frac{N_n}{N_3}$ and $\langle cos(2\pi l Z_n)\rangle$. $\frac{N_n}{N_3}$ depends only on the size of the crystal and $\langle cos(2\pi l Z_n)\rangle$ depends on the distortion due to Z_n. $\frac{N_n}{N_3}$ is represented by A_n^S and $\langle cos(2\pi l Z_n)\rangle$ by A_n^D (eq. A.22). For small values of n and l, the logarithm of A_n is given in eq. A.25 :

$$A_n = A_n^S A_n^D \tag{A.22}$$

$$lnA_n(l) = lnA_n^S - 2\pi^2 l^2 \langle Z_n^2\rangle \tag{A.23}$$

This last expression allows to determine the size effect and distortion effect [150, 110]. We will focus of the determination of the the distortion effect which will be related to the dislocation effect or distribution in the material. However the size effect can be determined with a logarithmic representation of the measured $A_n(l)$ against l^2 for several value of n fig.A.7 [150]. Since the size coefficient A_n^S is independent of l, intercepts at $l = 0$ is A_n^S.

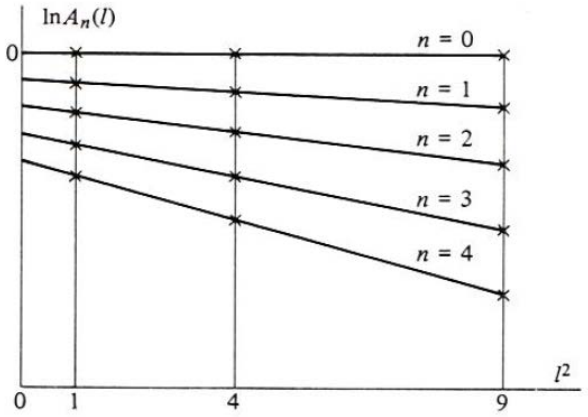


FIGURE A.7 – The logarithmic plot of $lnA_n(l)$ [150]. The plot is used to separate size and distortion effect

In fig. A.7, we note that the slope of $lnA_n(l)$ is $-2\pi^2\langle Z_n^2\rangle$ with corresponds to the distortion effect. The strain along a_3 direction is denoted ε_L and given in eq. A.24. From the slope of $lnA_n(l)$, the means square values of average strain $\langle \varepsilon_L^2\rangle$ can be computed.

$$\varepsilon_L = \frac{\Delta L}{L} = \frac{Z_n}{n} \tag{A.24}$$

To summarize this section, we note that for a $00l$ reflection, it is possible to

determine the square value of average strain using the plotting of fig. A.7. In [150], the authors showed that the result of eq. A.25 can be generalized for any reflection :

$$lnA_L = lnA_L^S - 2\pi^2 L^2 \langle \varepsilon_L^2 \rangle / d^2 \tag{A.25}$$

When the means square values of average strain is determined from the measured intensity, the next step is to determine the dislocation parameters such as density or distribution using this value. To do this, different formulation of the means square $\langle \varepsilon_L^2 \rangle$ is proposed in the literature and are discussed in the first chapter [71, 70, 154, 153, 52, 22].

Annexe B

Equivalence between DGO_k on a set of N points and CGO on a set of $2kN$ points

As in section 2.4.1, a discrete stepwise function $t^d(x_i)$ is considered with $x_i = \frac{id}{N} + \frac{d}{2N}$, where i varies from 0 to $N-1$. With N points, the discrete Fourier transform (DFT) $\widehat{T^D}$ of t^d is given in Eq. 2.15 :

$$\widehat{T^D}(\xi_h) = \sum_{i=0}^{N-1} t^d(x_i) exp(-j2\pi\xi_h x_i) \tag{B.1}$$

with $\xi_h = \frac{h}{d}, h = 0, ..., N-1$. The DFT denoted $\widehat{T^D}$ was given in Eq. 2.24 as a function of the Fourier transform $\widehat{T^d}$:

$$\widehat{T^D}(\xi_h) = N \sum_{m=-\infty}^{\infty} (-1)^m \widehat{T^d}(\xi_{mN+h}) \tag{B.2}$$

Choosing a finer discretization, the period d can be divided into $2kN$ points $y_l = \frac{ld}{2kN}$ where l varies from 0 to $2kN-1$. Let us now define the DFT denoted $\widehat{T^D}_{2kN}$ as follows :

$$\widehat{T^D}_{2kN}(\xi_o) = \sum_{l=0}^{2kN-1} t^d(y_l) exp(-j2\pi\xi_o y_l) \tag{B.3}$$

with $\xi_o = \frac{o}{d}, o = 0, ..., 2kN-1$. The zero shift of the y_l points is chosen so that the x_i points are included in the y_l set. Using the inverse FT yields :

$$t^d(y_l) = \sum_{q=0}^{2kN-1} \sum_{n=-\infty}^{\infty} \widehat{T^d}(\xi_{2knN+q}) exp(j2\pi\xi_{2knN} y_l) exp(j2\pi\xi_q y_l) \tag{B.4}$$

Then, from $exp(j2\pi\xi_{2knN} y_l) = 1$, we get :

$$t^d(y_l) = \sum_{q=0}^{2kN-1} exp(j2\pi\xi_q y_l) \sum_{n=-\infty}^{\infty} \widehat{T^d}(\xi_{2knN+q}) \tag{B.5}$$

Now, $\widehat{T^D}_{2kN}$ is calculated as follows :

$$\widehat{T^D}_{2kN}(\xi_q) = 2kN \sum_{n=-\infty}^{\infty} \widehat{T^d}(\xi_{2knN+q}) \tag{B.6}$$

Therefore, there are two alternative descriptions of the step function t^d, either with initial N points, or with $2kN$ points (i.e. finer discretization). $\widehat{T^D}$ and $\widehat{T^D}_{2kN}$ can both be expressed as infinite sums of components of $\widehat{T^d}$. The values of t^d computed by inverse DFT should be equal for $y_l = x_i$. Using the inverse DFT of $\widehat{T^D}$ to compute the step function t^d can also be seen as an alternative way to compute the DFT of $\widehat{T^D}_{2kN}$ with the same accuracy but on a subset of the y_l points.

$$\widehat{T'^D}(\xi_h) = N \sum_{m=-k}^{k-1} (-1)^m \widehat{T^d}_{2kN}(\xi_{mN+h}) \tag{B.7}$$

We also restrict the $\widehat{T^D}_{2kN}$ sum (Eq. B.6) to its first term, i.e. $\widehat{\mathbf{\Gamma}}$ truncated to $-kN, ., kN-1$. The inverse DFT of the truncated $\widehat{\mathbf{\Gamma}}$, computed on $2kN$ points, will exhibit Gibbs oscillations at discontinuities, i.e. at points $y_l = x_i + \frac{d}{2N}$. However, these oscillations should be damped for $y_l = x_i$, where t^d is actually computed, thus the inverse DFT of $\widehat{T'^D}_k$ is free of the Gibbs oscillations.
The whole proof of section 2.4.1 can now be performed again for $\widehat{T^D}_{2kN}$ instead of $\widehat{T^D}$. As a conclusion, the discrete operator DGO_k with truncation order k is thus equivalent to use the CGO (i.e. the classic $\widehat{\mathbf{\Gamma}}$ operator) on a $2k$ times finer resolution. The main advantage to use the DGO_k is thus both decreases of memory storage and CPU time for a same accuracy as compared to the CGO.

Annexe C

Analytical stress and displacement components for periodic distributions of cubic-shaped inclusions with eigenstrains in isotropic elasticity

Stress components

First of all, the analytical stress solution for the stress field due to an eigenstrain ε^*_{ij} in a cubic-shaped isotropic elastic inclusion embedded in an infinite isotropic elastic medium was reported by [20, 84]. The cuboidal inclusion dimensions are $2a_1$, $2a_2$, $2a_3$ in the x, y, z directions, respectively. We consider the following homogeneous elastic properties in the medium : shear modulus μ, Young's modulus E and Poisson ratio ν. In the case where the only non zero eigenstrain component is ε^*_{33},

the analytical solution reads (see eq. (5) in [84]) :

$$
\begin{aligned}
\frac{\sigma_{12}(\mathbf{x})}{\mu\varepsilon^*_{33}} &= \frac{1}{4\pi(1-\nu)}\sum_{n=1}^{8}(-1)^n[-2\nu\ln(2R_n+2C_{n3})+\frac{C_{n3}}{R_n}] \\
\frac{\sigma_{13}(\mathbf{x})}{\mu\varepsilon^*_{33}} &= \frac{1}{4\pi(1-\nu)}\sum_{n=1}^{8}(-1)^n[-\ln(2R_n+2C_{n2})-\frac{C_{n2}}{R_n}+\frac{C_{n1}^2C_{n2}}{[C_{n1}^2+C_{n3}^2]R_n}] \\
\frac{\sigma_{23}(\mathbf{x})}{\mu\varepsilon^*_{33}} &= \frac{1}{4\pi(1-\nu)}\sum_{n=1}^{8}(-1)^n[-\ln(2R_n+2C_{n1})-\frac{C_{n1}}{R_n}+\frac{C_{n1}C_{n2}^2}{[C_{n2}^2+C_{n3}^2]R_n}] \\
\frac{\sigma_{11}(\mathbf{x})}{E\varepsilon^*_{33}} &= \frac{1}{8\pi(1-\nu^2)}\sum_{n=1}^{8}(-1)^n[-2\nu\arctan\frac{C_{n1}C_{n3}}{C_{n2}R_n}-\frac{C_{n1}C_{n2}C_{n3}}{[C_{n1}^2+C_{n3}^2]R_n}] \\
\frac{\sigma_{22}(\mathbf{x})}{E\varepsilon^*_{33}} &= \frac{1}{8\pi(1-\nu^2)}\sum_{n=1}^{8}(-1)^n[-2\nu\arctan\frac{C_{n2}C_{n3}}{C_{n1}R_n}-\frac{C_{n1}C_{n2}C_{n3}}{[C_{n2}^2+C_{n3}^2]R_n}] \\
\frac{\sigma_{33}(\mathbf{x})}{E\varepsilon^*_{33}} &= \frac{1}{8\pi(1-\nu^2)}\sum_{n=1}^{8}(-1)^n[-2\arctan\frac{C_{n1}C_{n3}}{C_{n2}R_n}+\frac{C_{n1}C_{n2}C_{n3}}{[C_{n1}^2+C_{n3}^2]R_n} \\
&\qquad -2\arctan\frac{C_{n2}C_{n3}}{C_{n1}R_n}+\frac{C_{n1}C_{n2}C_{n3}}{[C_{n2}^2+C_{n3}^2]R_n}]
\end{aligned}
\tag{C.1}
$$

In this expression, the distance R_n between the position vector $\mathbf{x}(x_1,x_2,x_3)$ and the n^{th} corner of the cuboidal inclusion ($n=1,...,8$) is defined as :

$$R_n(\mathbf{x}) = \sqrt{C_{n1}^2+C_{n2}^2+C_{n3}^2}$$

where the components C_{nj} are given by :

$$
[C_{nj}] = \begin{bmatrix}
x_1-a_1 & x_2-a_2 & x_3-a_3 \\
x_1+a_1 & x_2-a_2 & x_3-a_3 \\
x_1+a_1 & x_2+a_2 & x_3-a_3 \\
x_1-a_1 & x_2+a_2 & x_3-a_3 \\
x_1-a_1 & x_2+a_2 & x_3+a_3 \\
x_1-a_1 & x_2-a_2 & x_3+a_3 \\
x_1+a_1 & x_2-a_2 & x_3+a_3 \\
x_1+a_1 & x_2+a_2 & x_3+a_3
\end{bmatrix}
\qquad j=1,2,3
$$

In order to derive the analytical stress solution to be compared with the FFT-based results, an infinite periodic distribution of cuboidal inclusions with the same periods as in the FFT-based calculations should be considered, which theoretically corresponds to an infinite sum of individual stress contributions using Eq. (C.1). In order to reduce the computations, we first calculate in the unit cell the total stress given by the superposition of $27\times27\times27$ periodically distributed cuboidal inclusions. Then, this truncated infinite sum solution is corrected by substracting the average residual stress given by $fC_{ijkl}\varepsilon^*_{kl}$ where f is the volume fraction of periodic eigenstrained inclusions in the infinite medium. Such truncation and correction were considered as satisfactory enough to be used an analytical solution that has been compared to FFT results for the local stress field (see Figs. 2.8 and 2.9).

Displacement components

Let us consider again the cuboidal configuration with same dimensions and same elastic moduli, eigenstrain as before. Assuming that the eigenstrain field ε^*_{ij} is due to an array of rectangular dislocation loops with general equivalent Burgers vector denoted $\mathbf{b}(b_1, b_2, b_3)$, this eigenstrain is responsible for a displacement vector field $\mathbf{u}(\mathbf{x})$ that can be calculated (after lengthy derivations) from the Burgers displacement formula, see [57]. Therefore, the first component $u_1(\mathbf{x})$ related to the x direction writes :

$$u_1(\mathbf{x}) = \frac{1}{8\pi(1-\nu)} \sum_{n=1}^{8} (-1)^n \{\varepsilon^*_{11}[(2\nu-3)(C_{n3}\log(R_n+C_{n3})+C_{n2}\log(R_n+C_{n2}))+ 2(1-\nu)C_{n1}\arctan\frac{C_{n2}C_{n3}}{C_{n1}R_n}]+\varepsilon^*_{22}[(1-2\nu)(C_{n2}\log(R_n+C_{n3}))+2\nu(C_{n1}\arctan\frac{C_{n2}C_{n3}}{C_{n1}R_n} - C_{n3}\log(R_n+C_{n2})]+\varepsilon^*_{33}[(1-2\nu)(C_{n3}\log(R_n+C_{n2}))+2\nu(C_{n1}\arctan\frac{C_{n2}C_{n3}}{C_{n1}R_n}- C_{n2}\log(R_n+C_{n3})]\} \quad \text{(C.2)}$$

The eigenstrains are related to the Burgers vector components as follows :

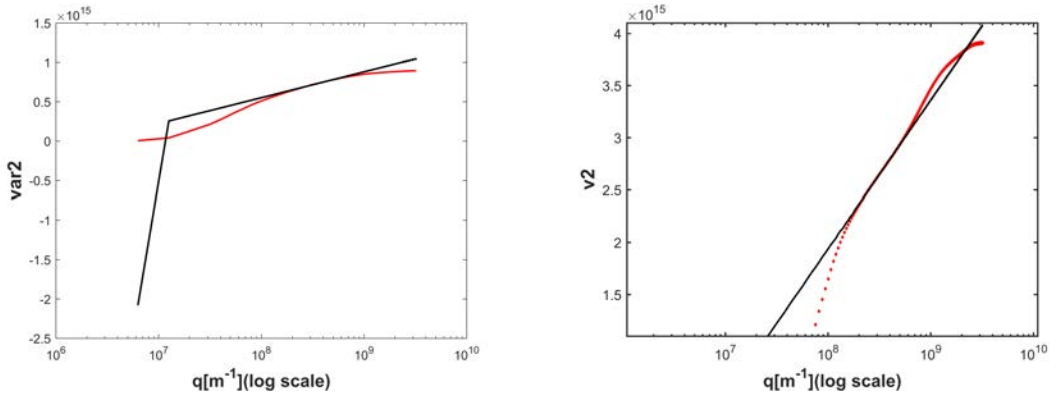
$$\varepsilon^*_{11} = b_1/(2a_1) \qquad \varepsilon^*_{22} = b_2/(2a_2) \qquad \varepsilon^*_{33} = b_3/(2a_3)$$

The other components of the displacements fields are obtained by cyclic permutation. Let us note that for the numerical applications presented in this thesis, the only non zero eigenstrain component is ε^*_{33}, i.e. only $b_3 \neq 0$.

In order to derive the analytical displacement solution to be compared with the FFT-based results, an infinite periodic distribution of cuboidal inclusions with the same periods as in the FFT-based calculations should be considered, which theoretically corresponds to an infinite sum of individual displacement contributions using Eq. (C.2). In order to reduce the computations, we first calculate in the unit cell the total displacement given by the superposition of a finite number of $27 \times 27 \times 27$ periodically distributed cuboidal inclusions. Then, this truncated infinite sum solution is corrected by substracting the overall displacement given by $f\varepsilon^*_{ij}x_j$ where f is the volume fraction of periodic eigenstrained inclusions in the infinite medium. Such truncation and correction were considered as satisfactory enough to be used an analytical solution that has been compared to FFT results for the local displacement field (see Fig. 3.1).

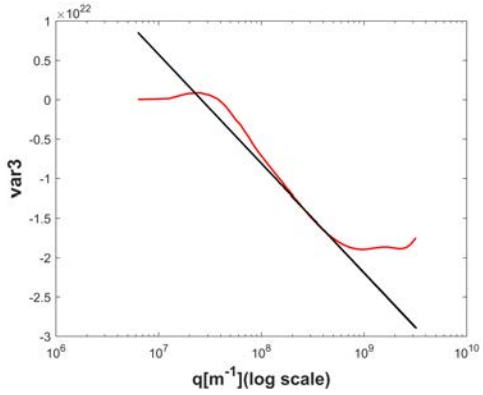
Annexe D

Peaks analysis results

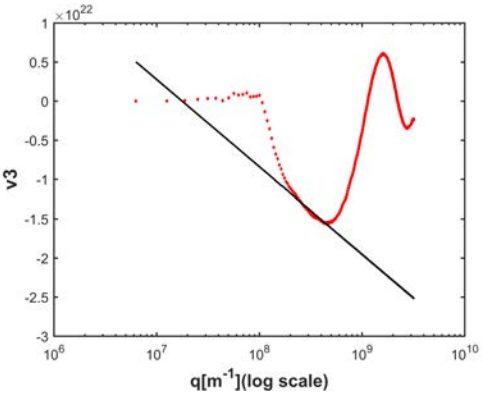


(a)

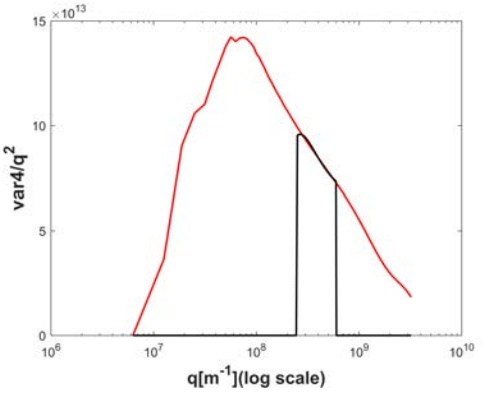
(b)



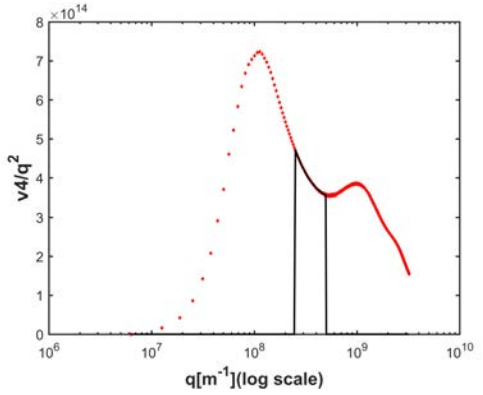
(c)



(d)

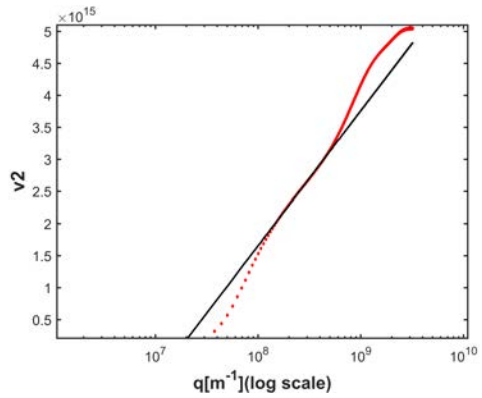


(e)

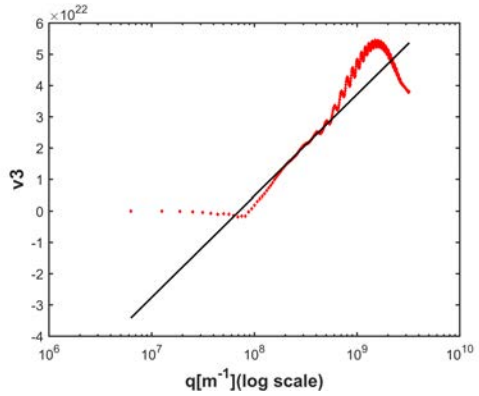


(f)

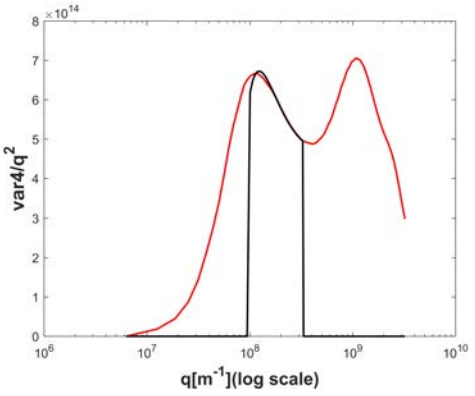
FIGURE D.1 – Different variance order for the (200)**g** vector for a 64 random distribution of hexagonal loops with the same voxels side. Second order (a) and (b), third order (c) and (d), fourth order (e) and (f), for the 64 and 196 loops side configuration respectively.



(a)



(b)



(c)

FIGURE D.2 – Different variance order for the (200)**g** vector for a 64 random distribution of hexagonal loops with the same voxels side. Second order (a), third order (b), fourth order (c) for the 256 loops side.

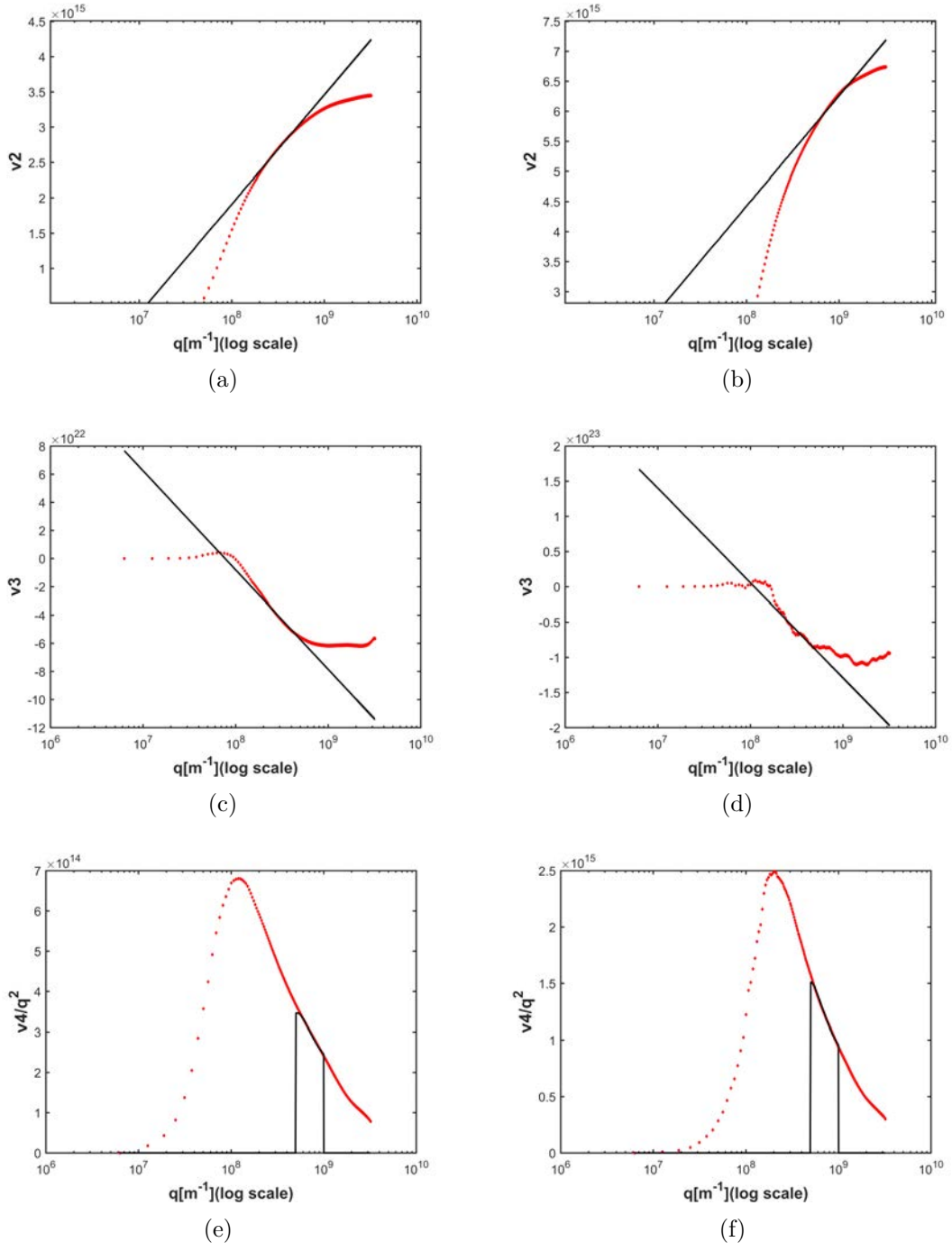
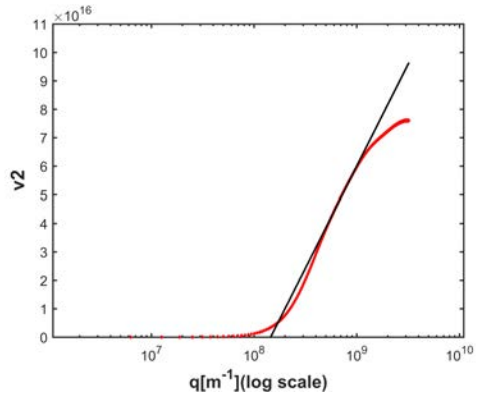
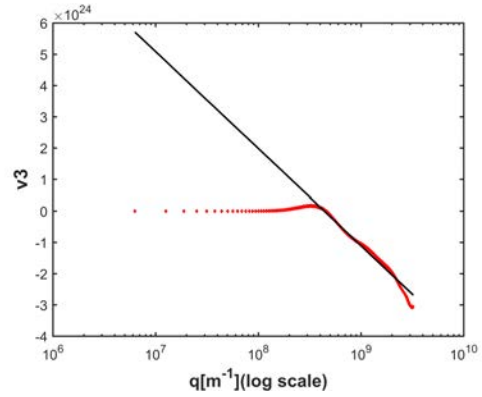


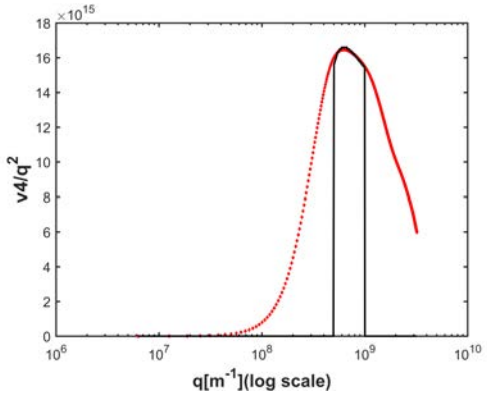
FIGURE D.3 – Different variance order for the (200)**g** vector for a random distribution of hexagonal loops with the same 64 voxels side : 256 (left) and 512 (right) loops.



(a)



(b)



(c)

FIGURE D.4 – Different variance order for the (200)**g** vector for4096 distribution of hexagonal loops with the same 64 voxels side

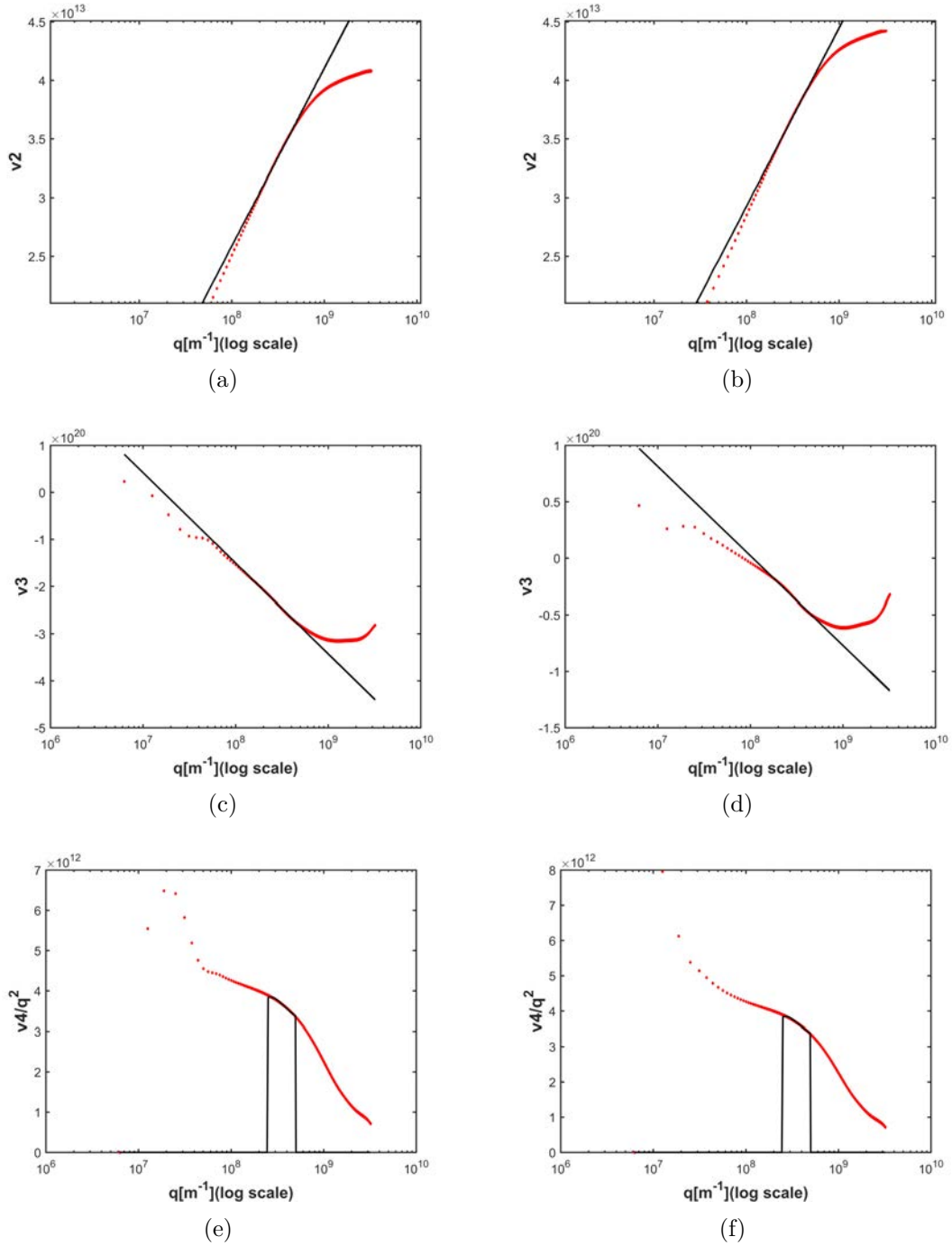


FIGURE D.5 – Different variance orders for a single dislocation dipole with 64 (left) or 128 (right) or voxels side